PHYSIK-DEPARTMENT

Precision Meson Spectroscopy:

Diffractive Production at COMPASS and Development of a GEM-based TPC for PANDA

Dissertation

von

Quirin Weitzel

TECHNISCHE UNIVERSITÄT
MÜNCHEN

TECHNISCHE UNIVERSITÄT MÜNCHEN
Physik-Department E18

Precision Meson Spectroscopy:

Diffractive Production at COMPASS and Development of a GEM-based TPC for PANDA

Quirin Weitzel

Vollständiger Abdruck der von der Fakultät für Physik der Technischen Universität München zur Erlangung des akademischen Grades eines

Doktors der Naturwissenschaften (Dr. rer. nat.)

genehmigten Dissertation.

Vorsitzender: Univ.-Prof. Dr. W. Weise

Prüfer der Dissertation:

1. Univ.-Prof. Dr. St. Paul
2. Hon.-Prof. A. C. Caldwell, Ph.D.

Die Dissertation wurde am 05.08.2008 bei der Technischen Universität München eingereicht und durch die Fakultät für Physik am 24.09.2008 angenommen.

Summary

Meson spectroscopy is a unique way to access Quantum Chromo Dynamics (QCD) and learn about its properties. Due to the non-Abelian structure, QCD predicts new states of matter with gluonic degrees of freedom. In particular $q\bar{q}g$ hybrids, which can have spin-exotic quantum numbers forbidden for conventional $q\bar{q}$ mesons, are expected to exist. Such states were searched for in the past, mostly in the light-quark sector. However, the experimental situation is still ambiguous and needs to be clarified. Further insights will certainly also come from the heavy-quark spectroscopy. Several new charmonium-like resonances were for example discovered during the last years, which have to be studied in more detail by future experiments to reveal their nature.

Diffractive dissociation reactions at COMPASS provide clean access to meson resonances with masses below $2.5\,\mathrm{GeV}/c^2$. During a pilot run in 2004 using pion beams on lead targets, a competitive number of $\pi^-\pi^-\pi^+$ final state events were recorded within a few days of data taking. A full partial wave analysis (PWA) of these data has been performed for this dissertation, concentrating on the kinematic domain of large momentum transfer ($t' \in [0.1, 1.0]\ \mathrm{GeV}^2/c^2$). While well-known mesons are resolved with high quality, also a strong signal consistent with the much disputed hybrid candidate $\pi_1(1600)$ is observed in the spin-exotic $J^{PC} = 1^{-+}$ partial wave. A Breit-Wigner parameterization yields a mass and width of $1.660^{+0.010}_{-0.074}$ and $0.269^{+0.063}_{-0.085}\,\mathrm{GeV}/c^2$, respectively. In addition, a first PWA of events with small momentum transfer ($t' \in \left[10^{-3}, 10^{-2}\right]\ \mathrm{GeV}^2/c^2$) has been carried out, yielding several high-mass radial-excitation states.

In the future, the PANDA experiment at the FAIR facility will perform high-precision spectroscopy in the charm-sector employing $\bar{p}p$ annihilations. Due to its excellent tracking capabilities for charged particles, a time projection chamber (TPC) has been proposed for the central tracker of PANDA. A continuous operation without ion gate is foreseen, which constitutes a novel development in high-rate particle physics experiments. Gas Electron Multiplier (GEM) foils offer an intrinsic ion back-flow suppression combined with high gains, and will therefore be used for gas amplification. A small-size GEM-TPC test chamber has been constructed during this thesis and commissioned using both X-rays and muons from cosmic-ray air-showers. From the latter data, a spatial resolution down to 140 µm has been achieved. The detector has been operated stably for many months with Ar/CO_2 (70/30) and at typical gas amplification factors of (5-10)$\cdot 10^3$.

Zusammenfassung

Die Spektroskopie von Mesonen stellt einen einzigartigen Zugang zur Quanten Chromo Dynamik (QCD) dar. Aufgrund ihrer nicht-Abelschen Struktur sagt diese Theorie neue Materiezustände voraus, insbesondere $q\bar{q}g$ Hybridstrukturen bestehend aus Konstituenten-Quarks und -Gluonen. Hybride können am besten über exotische Spin- und Paritäts-Quantenzahlen nachgewiesen werden, also solche die für konventionelle $q\bar{q}$ Mesonen nicht erlaubt sind. Trotz einiger experimenteller Evidenzen im Bereich der leichten Hadronen ist die Existenz von Hybriden immer noch nicht zweifelsfrei anerkannt und bedarf weiterer Beweise. Neue Erkenntnisse sind sicherlich auch aus dem Charm-Sektor zu erwarten. Hier wurden in den letzten Jahren mehrere neue, schmale Resonanzen entdeckt, deren Natur noch unklar ist und die genauer vermessen werden müssen.

COMPASS ermöglicht durch diffraktive Reaktionen die Produktion von Mesonen mit Massen unterhalb von $2.5\,\mathrm{GeV}/c^2$. Bereits während einer Teststrahlzeit wurde innerhalb von wenigen Tagen eine beeindruckende Zahl von $\pi^-\pi^-\pi^+$ Ereignissen aufgezeichnet. Für die vorliegende Doktorarbeit ist eine Partialwellenanalyse (PWA) dieser Daten durchgeführt worden, mit Schwerpunkt auf Ereignissen mit hohem Impulsübertrag ($t' \in [0.1, 1.0]\ \mathrm{GeV}^2/c^2$). Zusätzlich zu etablierten Mesonen werden auch weitere Resonanzen beobachtet, unter anderem in der Spin-exotischen $J^{PC} = 1^{-+}$ Welle. Letzteres Signal lässt sich durch eine Breit-Wigner-Funktion beschreiben, resultierend in einer Masse von $1.660^{+0.010}_{-0.074}$ und einer Breite von $0.269^{+0.063}_{-0.085}\,\mathrm{GeV}/c^2$. Auch für kleinere Impulsüberträge ($t' \in \left[10^{-3}, 10^{-2}\right]\ \mathrm{GeV}^2/c^2$) ist eine erste PWA ausgearbeitet worden. Mehrere radiale Mesonenanregungen werden in diesen Daten beobachtet.

Das PANDA Experiment am zukünftigen Beschleunigerkomplex FAIR wird mit Hilfe von $\bar{p}p$-Annihilationen präzise Messungen an Charm-haltigen Mesonen durchführen. Eine TPC ("Time Projection Chamber") ist als zentraler Spurdetektor für geladene Teilchen vorgeschlagen worden. Völlig neu ist der Modus, in dem eine TPC bei PANDA betrieben werden muss: ohne Trigger und damit ohne explizites Startsignal sowie kontinuierlich laufend. Letzteres erfordert eine Unterdrückung der Ionen-Rückdrift, weshalb GEM-Folien ("Gas Electron Multiplier") zur Gasverstärkung geplant sind. Im Rahmen der vorgestellten Promotion ist eine GEM-TPC Testkammer gebaut und sowohl mit Röntgenstrahlung als auch mit kosmischen Myonen in Betrieb genommen worden. Ortsauflösungen bis zu $140\,\mu\mathrm{m}$ wurden dabei erreicht. Der Detektor lief während dieser Messungen über viele Monate hinweg stabil, bei Verstärkungen von (5-10)$\cdot 10^3$ und mit einem $\mathrm{Ar}/\mathrm{CO}_2$ (70/30) Gasgemisch.

Contents

1 Introduction **1**

2 Spectroscopy: Mesons and Exotics **5**

2.1 Phenomenology and Theoretical Concepts 5

2.2 Experimental Methods 11

2.3 Diffractive Dissociation 13

2.4 Experimental Status 17

3 The COMPASS Experiment at CERN **23**

3.1 Overview of the Physics Program 24

3.2 Setup during the 2004 Pilot Hadron Run 26

3.3 Data Taking and Event Reconstruction 30

4 Partial Wave Analysis **35**

4.1 Physics Assumptions and Implications 36

4.2 Spin Formalisms and Decay Amplitudes 40

4.3 Technique of Mass-Independent PWA 42

4.4 Output Parameters and Quality Assurance 45

4.5 Mass-Dependent Fit 49

5 Analysis of $\pi^-\pi^-\pi^+$ Events from Diffractive Dissociation **51**

5.1 Data Set and Event Selection 51

5.2 Mass Spectra, Dalitz Plots and Kaon Background 60

5.3 Monte Carlo Simulations 64

5.4 Mass-Independent Partial Wave Analysis 71

5.5 Intensities, Phases and Mass-Dependent Fit 83

5.6 Systematic Studies 96

5.7 Leakage Study for Exotic Wave at "High-t'" 99

5.8 First Glimpse at the $\pi^-\pi^-\pi^-\pi^+\pi^+$ Data 100

6 The PANDA Experiment at FAIR **103**
6.1 Physics Objectives 103
6.2 In-Beam Installation at the Storage Ring 106
6.3 Detector Components 107

7 A High-Rate TPC for PANDA based on the GEM **111**
7.1 Technological Challenges 111
7.2 The GEM Solution 114
7.3 TPC Design and Integration into PANDA 116
7.4 Research and Development towards a PANDA TPC 118

8 Test Chamber Measurements **119**
8.1 Detector Description and Operation 119
8.2 Construction and Component Tests 127
8.3 X-Ray Commissioning and Gain Calibration 131
8.4 Electronics, Data Acquisition and Trigger for Cosmic Muons Detection . . 135
8.5 Event Reconstruction and Analysis 141
8.6 Results from Measurements with Cosmic Muons 147
8.7 Future Prospects 150

9 Conclusions and Outlook **151**

A Software Versions **153**
A.1 Real Data Processing 153
A.2 Simulations 153
A.3 PWA Program 154

B Recalculation of Beam Energy **155**

C Simulations Supplement **157**
C.1 Event Generator Tuning 157
C.2 Further PWA Quality Distributions 158

Bibliography **161**

Own Contributions **177**

Acknowledgements **179**

Chapter 1

Introduction

One of the most important questions in contemporary particle physics is to understand the phenomena related to the dynamics of the strong force. The accepted underlying theory is Quantum Chromo Dynamics (QCD) [1], which describes the interaction between point-like quarks by the exchange of gluons. Due to the non-Abelian SU(3) structure of QCD [2, 3], these bosonic field quanta carry themselves strong charge, which comes in three colors. QCD therefore predicts and implicates a series of new effects, but many of these have not yet been completely understood or have simply not been observed unambiguously. It is an experimental fact that quarks are always confined within color-neutral compounds, unless extremely high densities and temperatures are created. This behavior can be modelled and even simulated based on QCD assumptions [4], but it is very difficult to calculate a binding quark potential from first principles. Experiments in turn have failed so far to prove the existence of objects with explicit gluonic degrees of freedom, so-called hybrids and glueballs. Owing to the self-coupling of gluons such exotics should exist and, in principle, also be observable. To this end spectroscopy is the key experimental tool to study the spectrum of strongly interacting particles and search for new states. However, excellent setups are needed, pushing for the limits of achievable luminosities and resolutions.

In the light meson sector the observed particles can be very well sorted and to some extent also understood according to the $\mathrm{SU}(3)_{\mathrm{flavor}}$ constituent quark model [5]. This approach does not contain any dynamics and describes mesons as bound states of a quark q and an antiquark $\bar{q}$ with quark flavors u, d and s. In addition to these conventional states, QCD-based models predict several hybrids and glueballs with masses below $2.5\,\mathrm{GeV}/c^2$ [6, 7]. Consequently, their detection is a prime goal of hadron physics, but due to the high density of ordinary mesons in that mass range they are difficult to identify. The most promising way out is to search for states with spin-parity quantum numbers forbidden for $q\bar{q}$ systems, e. g. $J^{PC} = 0^{--}, 0^{+-}, 1^{-+}, 2^{+-}, \ldots$. Such spin-exotic objects could only be interpreted in terms of gluonic excitations or tetraquarks and would provide an important confirmation of QCD and derived theories beyond the static $\mathrm{SU}(3)_{\mathrm{flavor}}$ model. They were searched for in the past and indeed first evidences for light 1^{-+} $q\bar{q}g$ candidates, called $\pi_1(1400)$ and $\pi_1(1600)$, were reported in different channels [8, 9, 10, 11].

However, many of these results are still heavily disputed and even counter statements have been published [12]. Further high-statistics experiments are therefore much needed to clarify the situation.

The COMPASS experiment at CERN [13, 14] is unique in the sense that it offers different mechanisms to produce mesons and exotics. It combines high intensities with a large acceptance and an excellent resolution for both neutral and charged final state particles. Most of the data taking since the startup in 2001 was performed with muon beams and a polarized target, mainly to investigate the spin structure of the nucleon. In fall 2004 also a first run using pion beams impinging on nuclear targets took place, dedicated among other things to light hadron spectroscopy. In particular diffractive dissociation reactions were recorded, during which the beam pions hit the target very peripherally and get excited to some resonance X. The study of the states produced through this mechanism at COMPASS is one of the two topics of this thesis. Due to the excellent quality of the data, the technique of Partial Wave Analysis (PWA) could be employed, allowing the identification of the quantum numbers of X and thus the search for spin-exotic states.

Switching from light quarks to the charm sector, a completely new field for spectroscopy opens. In 1974 the discovery of the narrow resonance J/ψ revolutionized particle physics [15, 16], and marked the beginning of charmonium physics. It took more than 30 years, but with the recent discoveries of η_c' [17] and h_c [18, 19] the complete $c\bar{c}$ spectrum below the $D\bar{D}$ threshold, as expected from early theory models [20, 21], is nowadays known. However, above this threshold several new narrow states were discovered over the last years [22, 23, 24, 25], which do not quite fit into the predicted scheme. They triggered a big activity among theorists and experimentalists and their interpretation as $c\bar{c}$ states, tetraquarks, $(q\bar{q})(q\bar{q})$ molecules or $q\bar{q}g$ hybrids is hotly debated [26, 27]. Also several new open-charm mesons were found [28, 29, 30, 31], the decays and properties of which add important information to the overall picture. Coming back to the initially raised question about quark confinement, the charm sector provides an ideal environment to study what happens if the two quarks of a meson are pulled apart and "string breaking" (hadron fragmentation from the vacuum) sets in.

Discovering new states is always only a first step, which has to be followed by a second one, namely precision measurements. Without the knowledge of natural resonance widths and branching ratios, no stringent constraints can be set for theoretical models and thus the insight obtained is limited. This is especially true for the revived spectroscopy in the charm sector, since it gets more and more clear that the interpretation of the objects found suffers from poor statistics and insufficient resolutions. A direct formation and scanning of the resonances is needed, which is only possible from in-flight $p\bar{p}$ annihilations. The PANDA experiment at FAIR [32] will take over this task, presumably from 2015 onwards. Designed as an internal target spectrometer at an antiproton storage ring, PANDA will reach unmatched luminosities. This, however, poses a big challenge to the detectors since they have to cope with interaction rates of up to $2 \cdot 10^7$ /s. For the central tracker of PANDA a TPC (Time Projection Chamber [33]) has been proposed [34]. In addition to an excellent tracking performance, such a device allows the identification of charged particles via $\mathrm{d}E/\mathrm{d}x$ measurements, in particular in the momentum range be-

low 1 GeV/c. In order to be able to make an optimum use of the continuous antiproton beam, the TPC has to be operated in an ungated mode, which has never be done in any high intensity experiment before. Due to their intrinsic ion back-flow suppression, GEM structures (Gas Electron Multiplier [35]) are foreseen for gas amplification. Currently, a lot of research and development activities are ongoing to evaluate the feasibility of a TPC for PANDA. The first step in that line has been the construction and commissioning of a small-size test chamber employing the GEM technology, which is the second topic of this thesis.

The presented dissertation can be divided into three main parts. The first part, chapter 2, is meant to serve as a general introduction to meson spectroscopy. Both theoretical concepts and experimental techniques are briefly discussed and the most important meson properties are introduced. Special attention is paid to the diffractive dissociation production mechanism. At the end an overview of the current experimental situation is given, focussing on the search for spin-exotic objects and the newly discovered charmonium states. In a second part the analysis of $\pi^-\pi^-\pi^+$ events, diffractively produced at COMPASS, is presented. As a preparation, chapters 3 and 4 introduce the COMPASS experiment and the PWA technique utilized, respectively. All necessary information about the setup, the data taking and the performed PWA fits can be found there. The actual results are shown in chapter 5, which comprises the event selection, the simulations for the acceptance corrections, the fit outcomes and the estimates of the systematic errors. The third part of this thesis is concerned with the TPC development for PANDA. After a description of the current experimental design of PANDA in chapter 6, the idea of using a GEM-based TPC as central tracker is explained in chapter 7. The main challenges of operating such a device are reviewed, and solutions are discussed. In chapter 8 the construction and commissioning of the small-size TPC test chamber is detailed and first measurements with this detector are presented. Finally, the main results and conclusions of the presented work are summarized in chapter 9.

Chapter 2

Spectroscopy: Mesons and Exotics

In order to provide the necessary background knowledge for the physics results presented in this thesis and to motivate the technological developments for future efforts, this chapter covers topical features in meson spectroscopy[1]. First the main properties of mesons are summarized and exotic states are introduced (section 2.1). This is mostly done on a phenomenological basis, but also theory models and predictions are detailed. In section 2.2 the experimental approaches are treated by going through the possible mechanisms to produce mesons and a selection of experiments, which have been performed in this field. Diffractive dissociation reactions are discussed in a dedicated part (section 2.3), including the definition of all involved kinematical variables. Those are later on used consistently in the analysis description (chapter 5). Finally, a brief review of the experimental status concerning the search for spin-exotic states and the recent findings in the charmonium sector is given (section 2.4). It is pointed out that for all subjects of this chapter an enormous number of papers exists and that the selection of topics and references naturally has to be incomplete. Recent reviews of meson spectroscopy with a focus on exotic non-$q\bar{q}$ objects can be found in [26, 36, 37]. The common prime source of information is, of course, the Review of Particle Physics, the 2006 version [38] of which has been used for this thesis.

2.1 Phenomenology and Theoretical Concepts

The goal of this section is to summarize the properties and features of mesons and exotic states. This includes the introduction of the basic quantum numbers as well as of dynamical Breit-Wigner functions to describe particle resonances. In addition, a brief overview of theoretical models and predictions is given, in particular concerning hybrid mesons and charmonium. It goes without saying that only some of the concepts can be detailed, for a more complete review please refer to e. g. [26].

[1] To keep this chapter reasonably short, baryons are not treated here at all.

2.1.1 Meson Quantum Numbers and Exotic States

Mesons are usually characterized by their total angular momentum J, their parity P and their charge conjugation parity C. Thereby J is composed from the total spin S and the relative orbital angular momentum L of the $q\bar{q}$ pair, respectively. Strictly speaking C is only a good quantum number for neutral mesons (like π^0 or J/ψ), however, for charged ones made up from u and d quarks only it can be defined through the neutral component of the corresponding isospin multiplet[2]. More precisely the G-parity is introduced as a charge conjugation operation followed by a rotation in isospin space about the y axis. Both isospin I and G-parity are conserved in strong interactions and, in summary, the following relations hold:

$$P = (-1)^{L+1} \quad ; \quad C = (-1)^{L+S} \quad ; \quad G = (-1)^I C = (-1)^{L+S+I} \quad . \tag{2.1}$$

Mesons fulfilling $P = (-1)^J$ belong to the natural spin-parity series and have a positive naturality $\eta = +1$ with

$$\eta = P(-1)^J \quad . \tag{2.2}$$

From equation (2.1) it is apparent that J^{PC} quantum numbers like $0^{+-}, 1^{-+}, 2^{+-}, \ldots$ are not accessible in $q\bar{q}$ systems. The establishment of such spin-exotic states would be a direct hint for the existence of objects with either gluonic excitations or more than two quarks involved. In that context hybrids ($q\bar{q}g$), glueballs (gg) or tetraquarks ($qq\bar{q}\bar{q}$) are mostly discussed, which are in general referred to as exotics. This should not be confused with spin-exotics, because also a hybrid for example can have normal quantum numbers allowed for any $q\bar{q}$ system. This brings up a general feature of mesons, namely that those with identical external quantum numbers can mix, even if they have a different internal flavor structure. In fact many of the physically observed particles like the ω or the η have $u\bar{u}$, $d\bar{d}$ and even $s\bar{s}$ components. This composes a big challenge for the detection of exotics with normal quantum numbers since they would most likely mix with ordinary $q\bar{q}$ states and it is extremely difficult to prove this small admixture. Thus it is much more encouraging to look for spin-exotic states.

2.1.2 Description of Resonances

The mass dependence of a resonance (e. g. a short-lived meson) is usually parameterized by means of a relativistic Breit-Wigner (BW) function,

$$\mathrm{BW}(m, M_0, \Gamma_0) \sim \frac{1}{M_0^2 - m^2 - iM_0\Gamma_\mathrm{T}(m)} \quad , \tag{2.3}$$

where M_0 and Γ_0 are the mass and the width of the resonance, respectively. This formula takes a mass dependent total width into account,

$$\Gamma_\mathrm{T}(m) = \sum_n \Gamma_{0\,n} \frac{M_0}{m} \frac{q_n}{q_{0\,n}} \frac{F_{L\,n}^2(q_n)}{F_{L\,n}^2(q_{0\,n})} \quad \text{with} \quad \Gamma_0 = \Gamma_\mathrm{T}(M_0) \quad , \tag{2.4}$$

[2]Representation of the $\mathrm{SU(2)_{flavor}}$ group describing the symmetry between u and d quarks in hadrons; by moving on to the $\mathrm{SU(3)_{flavor}}$ group, also s quarks can be included and the whole light meson sector be described in terms of singlet and octet groups [5].

which represents a sum over all possible decay channels n (partial width $\Gamma_{0\,n}$) of the resonance. Here q_n denotes the break-up momentum of the particular (two-body) decay[3] and $q_{0\,n} = q_n(M_0)$. The functions $F_{L\,n}$ are the so-called Blatt-Weisskopf barrier factors, which are connected to the spherical Hankel functions [39]. From those they carry over an asymptotic behavior when q_n approaches the threshold defined by the mass of the decay particles, which can effect the resonance shape. If the partial widths (branching ratios) $\Gamma_{0\,n}$ of a resonance are not known, a constant width BW is usually assumed as best approximation by replacing $\Gamma_{\mathrm{T}}(m)$ in equation (2.3) with Γ_0.

In a spectroscopy analysis like the one presented in this work, BW functions are fundamental in two respects. First of all the mesons (and exotics) under investigation are parameterized according to equations (2.3) and (2.4), and their masses and widths determined from a fit. Secondly, the reconstructed decay chains contain intermediate states, which are specified as BW resonances with pre-known parameters (see section 4.1.3). For illustrations resonances are also often described in terms of a real amplitude and a phase $\phi(m)$. Compared to the phase appearing in the polar representation of complex numbers, however, $\phi(m)$ contains an indeterminable shift. Only if the interference of two resonances produced through the same reaction mechanism is considered, this shift cancels and the relative phase is observable (cf. section 4.4.3).

2.1.3 QCD, Derived Models and Regge Theory

The fundamental gauge theory behind strong interactions is Quantum Chromo Dynamics (QCD) [1]. To this end the QCD Lagrangian is derived from the Dirac equation for free particles by requiring invariance under a local $\mathrm{SU}(3)_{\mathrm{color}}$ transformation:

$$\mathcal{L}_{\mathrm{QCD}} = \bar{q}_i \left(i\partial_\mu \gamma^\mu \delta_{ij} + g\frac{\lambda^a_{ij}}{2} A^a_\mu \gamma^\mu - m\delta_{ij} \right) q_j - \frac{1}{4} F^a_{\mu\nu} F^{a\,\mu\nu} \quad , \tag{2.5}$$

with the field strength

$$F^a_{\mu\nu} = \partial_\mu A^a_\nu - \partial_\nu A^a_\mu + g f_{abc} A^b_\mu A^c_\nu \quad , \tag{2.6}$$

where q_i are the quark fields with color indices $i = 1, 2, 3$, λ^a are the Gell-Mann matrices, A^μ_a are the gluon fields with $a = 1, \ldots, 8$, g is the coupling constant and m the quark mass. Equations (2.5) and (2.6) show that quarks couple to gluons but, in addition, also trilinear and quadratic pure gluon vertices exist [2, 3]. It is due to this fact that QCD implies the existence of new forms of hadronic matter like hybrids or glueballs[4]. On the other hand, the gluon self-coupling makes the theory very difficult to solve and approximate solutions have to be found. The non-observation of free quarks has led to the general belief that color is confined in QCD, but the mechanism behind this confinement still has to be demonstrated.

[3] Absolute value of the momentum of the decay particles in the resonance rest frame.

[4] First suggested in the framework of the so-called Bag Model [40, 41]; the lightest hybrid was predicted to have a mass of 1.3-1.4 GeV/c^2.

The theory which is maybe closest to QCD is Chiral Perturbation Theory (χPT) [42]. It relies on an effective Lagrangian and respects all QCD symmetries. Instead of quarks and gluons, π, K and η mesons are the fundamental ingredients, arising as Goldstone bosons of a spontaneous breaking of chiral symmetry. χPT works for low energies and can precisely determine quark mass ratios in the u, d and s sector. However, no predictions for glueball, hybrid or charmonium states have been made so far. In the following some of the QCD-based theories which do so are introduced and, at the end, also the main ideas of Regge theory are discussed.

2.1.3.1 Lattice QCD

A very promising approach to obtain hadron properties from the QCD Lagrangian is Lattice QCD (LQCD) [4]. This technique aims for simulating QCD on a discrete space-time lattice and has progressed very rapidly during the last years. The main remaining obstacles are that light quarks come out too massive from the calculations (by a factor ~ 10) and that it is very computer-time consuming to include quark loops in the simulations[5]. Nevertheless, very important milestones have been achieved by reproducing for example the confining linear part of the $q\bar{q}$ potential from the flux-tube model [43] (see also below). Even the decay of mesons, the string breaking so to say, can be simulated. One of the early achievements of LQCD was the calculation of the glueball spectrum, including many spin-parity configurations [44]. The lowest mass glueball $J^{PC} = 0^{++}$ is expected to have a mass between 1.6 and 1.8 GeV/c^2 followed by a 2^{++} and a 0^{-+} state around 2.5 GeV/c^2. Besides for conventional mesons, detailed predictions exist now also for $q\bar{q}g$ hybrids, in particular with exotic 1^{-+} quantum numbers (like studied in the analysis presented in chapter 5). The lightest ones should have masses between 1.7 and 2.2 GeV/c^2 [45, 46, 47] and decay preferentially into $b_1\pi$ (partial width 400 ± 120 MeV/c^2) and $f_1\pi$ (90 ± 60 MeV/c^2) [48]. In the charmonium sector exotics are predicted above 4 GeV/c^2, in particular a 1^{-+} $c\bar{c}g$-hybrid with a mass around 4.3 GeV/c^2 [49] and a 0^{+-} glueball state around 4.5 GeV/c^2 [44, 50].

2.1.3.2 The Flux-Tube Model

The most intuitive picture concerning hybrids comes from the flux-tube model [6]. It describes mesons as $q\bar{q}$ pairs, connected by a string of mass points with a linear confining potential between the masses. A non-relativistic Hamiltonian is constructed, including terms for the free quark and antiquark, a Coulomb-like potential between them and a part for the flux tube. The latter accounts for possible transverse displacements of the mass points and contains several parameters to tune the string tension. When the flux tube is in its ground state, the conventional $q\bar{q}$ spectrum is obtained. However, the Schrödinger equation can also be solved corresponding to flux-tube (string) excitations, and this additional degree of freedom opens up the possibility to describe hybrids even with exotic J^{PC} quantum numbers. The lightest hybrid states predicted from this model have masses

[5] Neglecting quark loops is also referred to as the quenched approximation.

between 1.8 and 2 GeV/c^2 [51, 52]. While mesons can decay via flux-tube breaking at any point along its length, hybrids have a node along the $q\bar{q}$ axis leading to a suppression of decays into two mesons with identical spatial wave function. Thus the probability for decays into two pseudoscalar mesons or one pseudoscalar and one vector meson is expected to be significantly smaller than into one pseudoscalar and one pseudovector meson. Typical partial widths for a 1^{-+} hybrid decay in the flux-tube model are 170, 60 and 5-20 MeV/c^2 for $b_1\pi$, $f_1\pi$ and $\rho\pi$ final states, respectively [53]. Other channels like $\eta\pi$ and $\eta'\pi$ contribute only with 0-10 MeV/c^2. Adding these numbers, a total width of the order of 200-250 MeV/c^2 is expected.

2.1.3.3 Quark Models

Several QCD-inspired models exist, which are based on the assumption of constituent quarks (e. g. [54]). The mass of these effective particles is often an open parameter and a confining potential is introduced. Differences between the models are related to the description of the exchange process and they compete in reproducing (or predicting) the conventional meson spectrum. In particular for the charmonium spectrum below and also above the $D\bar{D}$ threshold[6] very precise predictions exist. A minimal non-relativistic central potential $V(r)$ for the $c\bar{c}$ system comprises a Coulomb-like (one-gluon exchange) part plus a linear term to model confinement:

$$V(r) = -\frac{4}{3}\frac{\alpha}{r} + br \quad , \tag{2.7}$$

where α (the strong coupling constant) and b are fitting parameters. Usually a hyperfine interaction is furthermore introduced, by adding a term proportional to $\vec{S}_c \cdot \vec{S}_{\bar{c}}$, and also other spin-dependent terms (like L-S, spin-orbit coupling). This increases the number of parameters for the models by two, e. g. the charm-quark mass enters now.

Figure 2.1 presents as an example a compilation of predicted and observed charmonium states from [55], sorted by the orbital angular momentum L between the c and the $\bar{c}$ quark. Also the total angular momentum J and the parity P are denoted next to the mass levels. Two quark models (half dashed and dotted lines) are compared to the experimental measurements (solid lines): a non-relativistic model (left half lines) and a relativistic one (right half lines [54]). For further details see the figure caption.

2.1.3.4 Regge Theory

Already during the late 1950's and early 1960's, Regge theory was developed as one of the first efficient tools for the description of hadronic interactions [56, 57]. In contrast to the other models and theories described in this section it is not based on QCD, which was actually developed about ten years later. It is not really a predictive theory but more phenomenological in character, in the sense that it was developed and modified under the influence of experimental results. Nevertheless, the Regge framework is still very

[6] About 3.73 GeV/c^2, defined by the mass of the two lightest open-charm mesons D^0 and $\bar{D}^0$.

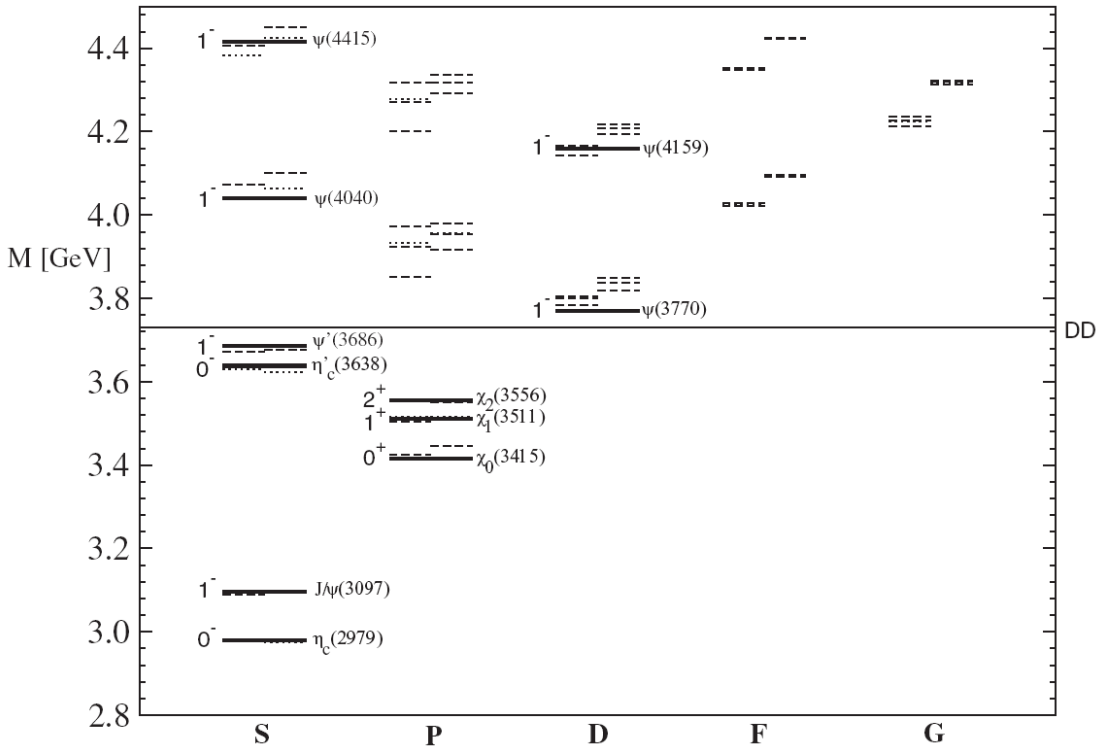

Figure 2.1: Predicted and observed spectrum of charmonium states from [55] (2005). Solid lines represent experimental data, broken (half) lines two different quark model calculations (see text). Spin-triplet levels are dashed and spin-singlet dotted lines. The $D\bar{D}$ threshold at 3.73 GeV is also shown.

popular and its terminology often used. In the following some of the main concepts are introduced, for detailed reviews see for example [58, 59].

Regge theory is concerned with the link between the observed spectrum of hadrons and the strong interaction of particles at high energies. It is based on relativistic scattering theory, in particular on the ideas of crossing symmetry and partial wave expansions. Consider a two-body reaction[7] $a + b \rightarrow c + d$ as depicted in figures 2.2 (left) and 2.3 and, in addition, the crossed-channel reaction $a + \bar{c} \rightarrow \bar{b} + d$. The scattering amplitude $F(s,t)$ can be written as a series of partial wave amplitudes f_l, which are multiplied on Legendre-Polynomials P_l:

$$F(s,t) \sim \frac{\sqrt{s}}{p} \sum_{l=0}^{\infty} (2l+1) f_l(s) P_l(\cos\theta) \quad , \tag{2.8}$$

where s is the square of the center-of-mass (CM) energy, t the squared 4-momentum transfer, p the absolute value of the momentum of particles a and b in the CM system and θ the scattering angle. Note that, depending on the masses of the involved particles, only certain regions in the 2-dim. s-t plane are physical, corresponding to the crossed reactions.

[7] Or quasi two-body if one of the final state particles further decays.

In the vicinity of a resonance r, $F(s,t)$ will have a pole and Regge theory states now that by introducing a complex angular momentum l an analytic extension between the physical regions can be found:

$$f(l,s) \sim \frac{1}{l-\alpha_r(s)} \quad \text{with} \quad f(l,s) = f_l(s) \quad \text{for} \quad l = 0,1,2,\ldots \quad . \tag{2.9}$$

$f(l,s)$ is called a Regge pole and $\alpha_r(s)$ a Regge trajectory. For the process $a + \bar{c} \to \bar{b} + d$ (s-channel) l takes integer values and $l = \alpha_r(m_r^2)$ describes distinct physical states with spin $J = l$, lying on a straight line in the J-m^2 plane. A trajectory r is thereby usually associated with a set of internal quantum numbers like parity and isospin. In this context one speaks e. g. of a ρ trajectory. The parameters (slope and intersection point) of the different α_r can be obtained from experiments.

For the t-channel scattering process $a + b \to c + d$, however, l is non-integer (in general even complex) and α_r connects it to the mass m of the (virtual) exchange particle through $l = \alpha_r(m^2)$. It can be shown that for high beam energies the scattering amplitude takes the form

$$F(s,t) \sim \sum_r \gamma_{ac}^r(t)\gamma_{bd}^r(t)s^{\alpha_r(t)} \quad , \tag{2.10}$$

where $\gamma_{ac}^r(t)$ and $\gamma_{bd}^r(t)$ may be interpreted as coupling constants (see figure 2.2, left) and $\alpha_r(t)$ as the trajectory of an exchanged Reggeon (e. g. a ρ). Thus Regge theory allows to use a relatively simple exchange picture, where in fact a tremendous averaging over elementary processes would be necessary. A special role is played by the Reggeon with the quantum numbers of the vacuum, which is discussed in the context of diffractive reactions in section 2.3.4.

2.2 Experimental Methods

A variety of techniques have been developed to produce and study meson resonances. They can be roughly divided into so-called production and formation reactions, which are briefly described in this section. Some examples of experiments are given throughout the discussion, focussing on those which are often cited in this thesis.

2.2.1 Production Experiments

In production experiments the total energy is shared between a recoil particle and a multi-meson final state. Angular momentum can be transfered and the quantum numbers of the final state system are restricted only by conservation laws. In particular exotic quantum numbers (see section 2.1.1) are allowed. The drawback is a worse mass resolution compared to formation experiments, thus natural widths of narrow resonances are determined with lower precision. Diffractive (see section 2.3) and charge-exchange reactions (e. g. $\pi^- p \to \eta\pi^0 n$) are classical examples for this type, but also central production and $\bar{p}p$ annihilations at fixed beam momentum (e. g. at rest). The former two can be modelled as one Reggeon exchange processes (with e. g. a P or ρ trajectory, cf. section 2.1.3.4), which

is illustrated in figure 2.2 (left). The CERN experiments WA3[8], GAMS[9] and COMPASS[10] employe(d) this technique, important representatives are also VES[11] and BNL-E852[12]. In central production reactions two Reggeons fuse to form a meson [64] (right of figure 2.2), which was exploited by e. g. WA76 [65] and WA102 [66] and which is also one possible mechanism for COMPASS to search for glueballs [67]. In $\bar{p}p$ annihilations at fixed beam momentum or at rest, mesons can be studied recoiling against another meson, often a pion. The Crystal Barrel[13] and the Obelix [70] experiments can partly be classified to belong to this category. Finally, the general purpose detectors BaBar [71] and BELLE [72] at the SLAC[14] and KEK[15] B-factories turned out to be powerful tools to study resonances in the charmonium sector. Although operating at the $\Upsilon(4S)$ bottonium resonance to produce $B\bar{B}$ mesons for CP violation measurements, lower mass states are accessible through several mechanisms like B-decays, two-photon fusion [73], initial state radiation [74] and even double-charmonium production [75]. In fact most of the observations concerning the new charmonium-like states (see section 2.4.2) have come from these two experiments.

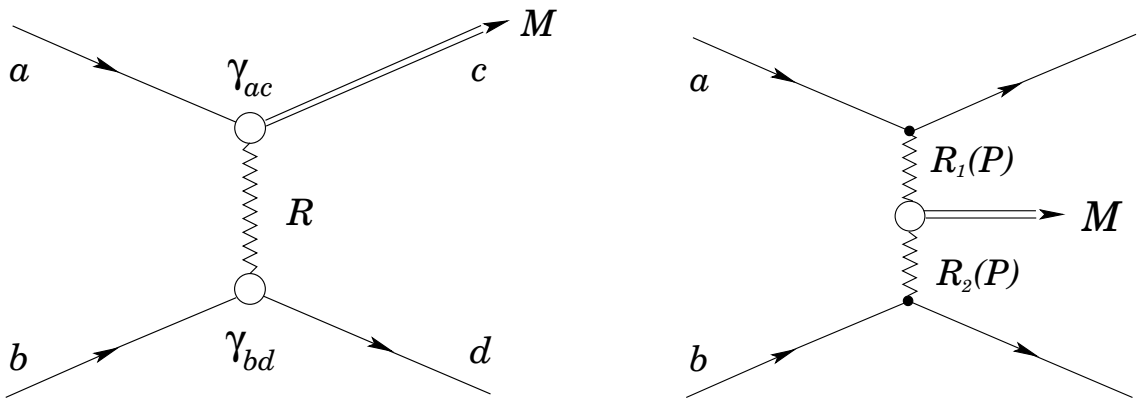

Figure 2.2: Left: Diagram for a two-body scattering reaction with Reggeon exchange and produced mesonic system (mass M). Right: Central production of a mesonic system of mass M.

[8]Carried out by the ACCMOR collaboration in the CERN West Area [60].

[9]Joint project of CERN and Protvino/Serpukov [61] (and references therein).

[10]See chapter 3; COMPASS is unique in the sense that it offers many mechanisms to produce mesons.

[11]VErtex Spectrometer (VES) at Institute for High Energy Physics (IHEP), Protvino [62].

[12]Experiment 852 (E852) at Brookhaven National Laboratory (BNL) [63].

[13]This spectrometer started to take data at the Low Energy Antiproton Ring (LEAR) at CERN in 1989 [68, 69] and went through several upgrades and relocations since then. It is now set up in Bonn at the ELSA ring and will have the large prototype of the PANDA TPC be installed to support the charged particle tracking (cf. section 7.4).

[14]Stanford Linear Accelerator Center, California, US; PEP-II e^+e^- collider.

[15]National Laboratory for High Energy Physics, Tsukuba, Japan; KEK-B e^+e^- collider.

2.2.2 Formation Experiments

In formation experiments there is no recoil particle and the mass and the quantum numbers of the final state are defined by the initial state. Thus direct formation of mesons with exotic quantum numbers is in general not possible. Typical examples are e^+e^- or $\bar{p}p$ annihilations at storage rings, where the center-of-mass energy can be varied. By performing a scan of the latter, narrow resonances can be measured with high precision, limited only by the momentum resolution of the storage ring and not by the capability of the spectrometer to reconstruct the recoil particle. The advantage of the e^+e^- variant is the rather "clean" reaction, since leptons are point like and do not undergo strong interactions. However, only states with the quantum numbers of the photon $J^{PC} = 1^{--}$ can be produced directly. Others are obtained though secondary interactions like radiative decays, thus the good resolution is lost. To this end $\bar{p}p$ annihilations have the upper hand, but there the drawback is a comparatively high background from which the interesting events have to be separated. Many past and recent experiments have made use of the e^+e^- technique to study charmonium states, e. g. DASP I-II at DESY[16], MARK I-III and Crystal Ball at SLAC[17], BES I-III at IHEP[18] and CLEO-c at Cornell [80]. On the $\bar{p}p$ side less experiments took place so far, examples are R704 at CERN[19] and E760 and E835 at Fermilab[20]. Especially the latter demonstrated in an impressive way the advantage of formation experiments by determining precisely the mass and widths of the χ charmonium states ($L = 1, J = 0, 1, 2$, see figure 2.1) [84]. The future will be PANDA at FAIR [32], where both the luminosity and the accessible center-of-mass energy will be extended compared to the Fermilab experiments (see chapter 6).

2.3 Diffractive Dissociation

This section details some of the aspects of diffraction in hadron physics, in particular the dissociation of pions to mesons. The topic is very interesting in itself, however, since it is "only" the production mechanism for the mesons studied later on, in chapter 5, the descriptions are kept short. First the analog situation in optics is recapitulated, the concepts of which are then applied to the hadron case. Next the extension to dissociation processes is made and the involved kinematic variables are introduced. Furthermore, the Regge theory view of diffraction is briefly touched. At the end, the possibility of double dissociation and the Deck effect are discussed. Detailed reviews on the field of diffractive interactions of hadrons can be found in [85, 86, 87].

[16] Deutsches Elektronen-SYnchrotron, Hamburg; Double Arm Spectrometer (DASP) at DORIS ring [76].

[17] Set up at the Stanford Positron Electron Accelerating Ring (SPEAR), see e. g. [77, 78].

[18] BEijing Spectrometer at the Institute of High Energy Physics (IHEP), Beijing, China [79].

[19] Using the Intersecting Storage Rings (ISR), the first hadron collider in the world. Major technological developments for $\bar{p}$ physics were employed, including stochastic cooling [81] and internal targets [82].

[20] Fermi National Accelerator Laboratory, Batavia, US; Experiments 760 and 835 at the Antiproton Accumulator [83].

2.3.1 Analogy: Diffraction and Polarization in Optics

In optics the diffraction of a plane wave of light, with wave number $k = 2\pi/\lambda$, on an absorbing disc with radius R is usually treated in the Fresnel-Kirchhoff approximate method. Two conditions have to be satisfied: $kR \gg 1$ (short wavelength) and $R/D \ll 1$ (large distance D of screen behind the disc). While in geometrical optics $kR^2/D \gg 1$ is furthermore assumed, Frauenhofer diffraction applies when $kR^2/D \ll 1$. The latter case is of importance for this discussion. A complex scattering amplitude $f(q)$ is introduced as Fourier transform of the profile function Γ describing the shape of the absorber. q represents here the two-dimensional momentum transfer in the black-disc plane, given by $q = k \sin\theta$ with θ being the angle of deflection. The optical theorem relates the imaginary part of $f(q)$ to the total flux σ_{T} collected by the screen: $\sigma_{\mathrm{T}} = 4\pi\Im(f(0))/k$. By extending the discussion from scalar to vector amplitudes, polarization effects in optics can be described, too. If the absorbing disc has for example different indices of refraction for right and left polarized light, "diffractive production" occurs: 100% linearly-polarized incident light will have an admixture of a rotated polarization component after the disc. This phenomena is possible because of the additional degree of freedom due to the vector nature of light waves.

2.3.2 Application to Hadronic Waves

Hadrons propagate in free space according to relativistic wave equations, where the wave number k is related to the momentum p by $k = p/\hbar$. For $p = 190\,\mathrm{GeV}/c$ in the laboratory system, for example, $k \approx 10^{18}\,\mathrm{m}^{-1}$. If the interaction of a beam pion of this momentum with a stationary target is considered, the short-wavelength condition introduced in the previous section can be probed. However, the reaction has to be seen in the overall center-of-mass system, which is illustrated on the left of figure 2.3. For e. g. a lead nucleus or a proton target, $k_{\mathrm{cm}} = 6 \cdot 10^{17}$ or $5 \cdot 10^{16}\,\mathrm{m}^{-1}$, respectively. Neglecting the dimensions of the pion, R can be roughly estimated by the expression $\sqrt[3]{A}$ and $k_{\mathrm{cm}}R \approx 3\,500$ or 50 is obtained. Thus even the latter case satisfies the short-wavelength condition. The large-distance condition is always fulfilled due to the small dimensions of the target, and also kR^2/D is much smaller than one (Frauenhofer diffraction). Typical diffraction patterns appear in experimental data as a function of momentum transfer[21]. Assuming a Gaussian profile function Γ for very forward scattering events, the radius of the "black disc" (the target) can approximately be calculated by $R = 0.3\sqrt{b}\,\mathrm{fm}$, where b in $(\mathrm{GeV}^2/c^2)^{-1}$ is the slope of the logarithm of the t distribution for small t [85][22]. For lead and protons this relation gives $b \approx 400$ and $\approx 10\,(\mathrm{GeV}^2/c^2)^{-1}$, respectively.

So far only elastic hadronic interactions have been considered in the sense that both the beam particle and the target stay intact. However, there exists also the analogon to optical polarization effects in hadronic interactions, namely the so-called diffractive dissociation [89]. The state $|i\rangle$ of a hadron passing a nucleus can be viewed as a linear combination of

[21] See e. g. figure 5.5 for the COMPASS case, to which the given numerical example applies.

[22] Theories can treat the t spectrum also well above the forward peak, thus extending into the regime of the minima and maxima in figure 5.5 [88].

states $|X\rangle$ that have the same intrinsic quantum numbers[23]: $|i\rangle = \sum_X C_X|X\rangle$. The profile functions Γ_X are in general not equal for all these states[24] and, in particular, different from the elastic scattering profile function Γ. Thus the diffracted wave does not coincide with the incident physical hadron, but is a superposition of the states $|X\rangle$. The amplitude of each state after the target is proportional to the difference between Γ_X and Γ . Diffractive dissociation is thus expected to be small where these differences are small, for instance at the center of a heavy nucleus. It is therefore a peripheral interaction or, in other words, a "grazing shot". An important prerequisite is coherent production, meaning that the different waves $|X\rangle$ have to stay in phase inside the nucleus. This translates into the condition that the mass of a diffractively produced resonance cannot be much larger than e. g. the mass of the beam particle: $(M^2 - m^2)c^4 \leq 2p\hbar/R$ [85]. From a 190 GeV/c beam pion scattering off a lead nucleus, for example, only mesons up to $\approx$ 3.5 GeV/c^2 are accessible. Early measurements of pion dissociation can be found in [90].

2.3.3 Kinematics of Meson Production from Pion Dissociation

Summarizing the previous section, diffractive dissociation of pions is, with some limitations, a convenient method to produce hadrons with the same internal quantum numbers as a pion. On the right of figure 2.3 this reaction is presented from a kinematical point of view: The incoming pion scatters off the target and gets excited (dissociates) to some state c (X). X than decays into n bodies, three pions in the case of the analysis presented in this thesis:

$$\pi^- + A \rightarrow X + A' \rightarrow \pi^-\pi^-\pi^+ + A' \quad . \tag{2.11}$$

Such a reaction is, of course, non-elastic, but exclusive in the sense that the target stays intact and transfers only momentum and angular momentum to the beam pion. Thus the kinetic energy of the recoil particle added up to the total energy of the three pions E_c is equal to the beam energy E_a. The interaction is assumed to proceed via an effective Reggeon exchange (cf. sections 2.1.3.4 and 2.3.4).

The process can be characterized by two kinematical variables: s and $t' = |t| - |t|_{min}$, where $s = (p_a + p_b)^2$ is the square of the total center-of-mass energy and $t = (p_a - p_c)^2$ is the square of the four momentum transferred from the incoming beam to the outgoing system c. The minimum value of $|t|$ which is allowed by kinematics for a given m_c is called $|t|_{min}$. It is different from zero because a minimum longitudinal momentum transfer is necessary to produce the high-mass state c. In the overall center-of-mass frame (see figure 2.3 left), a simple kinematical calculation shows that

$$t' = |t| - |t|_{min} = 2|\vec{p}_a||\vec{p}_c|(1 - \cos\theta_0) \geq 0 \quad , \quad |t|_{min} = 2(E_a E_c - |\vec{p}_a||\vec{p}_c|) - m_a^2 - m_c^2 \quad . \tag{2.12}$$

$\vec{p}_a$ and $\vec{p}_c$ are the 3-momenta of the beam and the diffractively produced system in the center-of-mass system, respectively. In the laboratory system the following approximate

[23]Like electric charge, isospin and C-parity. However, they don't have to keep spin and parity if some angular momentum is transferred during the reaction.

[24]Corresponding to the different indices of refraction in optics.

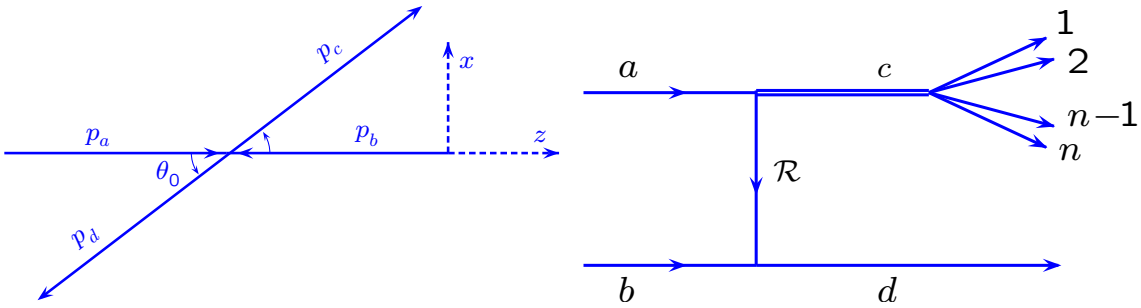

Figure 2.3: Left: The reaction $a + b \to c + d$ in the overall center-of-mass frame. a is the incoming beam particle (in z direction), b the target, c the scattered object, d the recoil particle and θ_0 the scattering angle. Right: Diffractive production of the system c (also referred to as X later on) with invariant mass m_c, decaying to n bodies. R stands for the exchanged Reggeon.

formula works well for high beam energies:

$$t' = |t| - |t|_{min} \quad ; \quad |t|_{min} \approx \frac{(m_c^2 - m_a^2)^2}{4|\vec{p}_a|^2_{\text{lab}}} \quad . \tag{2.13}$$

In order to fully describe the three-body decay of the state X for a fixed mass m_c, five phase-space variables are needed. They are collectively denoted as τ within this thesis, in particular during the PWA description in chapter 4. Different possibilities to chose these five variables exist, depending on the application and choice of reference frames. An example of a concrete representation is given in section 4.2.

2.3.4 The Pomeron Picture

In section 2.1.3.4 Regge trajectories have been introduced to describe hadronic scattering processes. Most of them have similar slopes, and intersection points $0 < \alpha(0) < 1$. An exception is the Pomeron [91]. This special case of a Reggeon was introduced historically to explain the slowly rising cross-sections of hadronic collisions at high energies. Its intersection point is $\alpha(0) = 1.08$, and it is still a debated question whether such an object can be linked to any physical resonance (e. g. a glueball) in the crossed-channel.

The Pomeron carries no internal quantum numbers like electric charge or isospin. It has furthermore $C = G = 1$ and is associated with a natural-parity exchange: $P_{\text{exchange}} = (-1)^{J_{\text{exchange}}}$ (or $\eta_{\text{exchange}} = +1$, cf. section 2.1.1). Thus the diffractive dissociation process can be described by the exchange of one or more Pomerons [85]. According to equation (2.10) this comes with the assumption that the two vertices in figure 2.2 (left) factorize, which was experimentally well confirmed [92].

2.3.5 Possibility of Double-Dissociation

So far it has been assumed in the discussion that the dissociation process only takes place at the "upper" vertex in figure 2.3 (right) and that the target stays intact. In case of a

proton target, however, also the proton could be excited during the reaction to a N^* resonance[25]. This is referred to in the literature as double-dissociation [85, 87]. It has been observed experimentally and, importantly, it has been verified that the Regge factorization of the two vertices still holds [92]. Thus for the PWA presented in this thesis such a reaction constitutes possible background only in the sense that the exclusivity condition is not strictly valid anymore[26].

2.3.6 The Deck Effect

In the study of diffractive dissociation reactions one has to take into account not only the production of resonances and their decays, but also non-resonantly produced final states. This is illustrated in figure 2.4. The left diagram shows the previously discussed one-Reggeon exchange mechanism for the case when a beam pion gets excited to e. g. the $a_1(1260)$ resonance with $J^{PC} = 1^{++}$. This meson subsequently decays into $\rho(770)$ and a pion. Such events proceeding through a produced resonance are the "intended" ones, which one wants to analyze by means of a PWA. However, a $\rho\pi$ final state with the same quantum numbers can also result from the process shown in the right diagram of figure 2.4, which involves a pion exchange. The corresponding two amplitudes will interfere and, in general, the properties of e. g. $a_1(1260)$ can change due to that. This effect is treated within the framework of the Deck Model [93] and was verified in experiments [94]. It concerns mostly $a_1(1260)$, but also other $\rho\pi$ final states preferentially in S-waves.

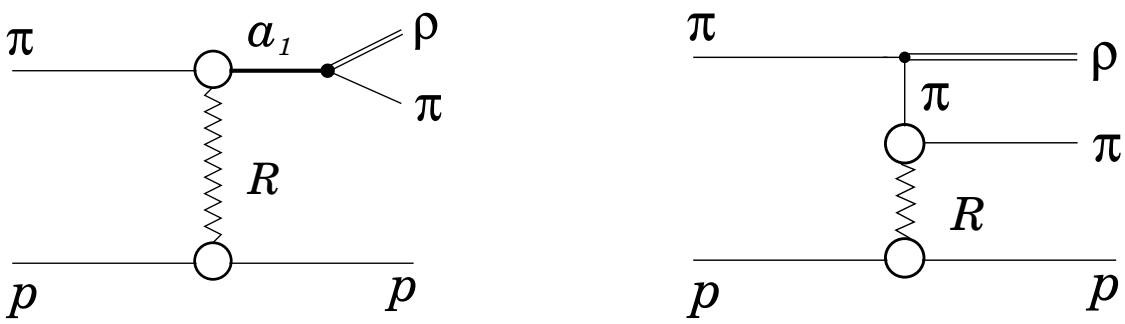

Figure 2.4: Illustration of the Deck effect. Left: Resonant production of $a_1(1260)$ decaying to $\rho\pi$. Right: Non-resonant process with the same final state.

2.4 Experimental Status

This section briefly reviews the experimental situation of the search for spin-exotic mesons and the newly discovered narrow-width states in the charmonium sector. Especially in the latter case it has become difficult to keep track on all recent findings, since more and more resonances above the $D\bar{D}$ threshold show up. The summary on these

[25] Like e. g. $N(1440)$; Δ resonances are excluded due to isospin conservation.
[26] Because the decay products of N^* are not detected, cf. section 5.1.4.

states is therefore kept rather short, topical review articles about that field are for example [27, 95, 96, 97]). A nice and comprehensive discussion of the exotic signals in the light-quark sector can be found in [26].

2.4.1 Mesons with Spin-Exotic Quantum Numbers $J^{PC} = 1^{-+}$

According to theory models (cf. section 2.1.3) the lightest objects with $J^{PC} = 1^{-+}$ could decay to $\eta\pi, \eta'\pi, \rho\pi, b_1\pi, f_1\pi, \rho'\pi, a_0\rho$ and $a_1\eta$. Many of these channels were studied at various places and using different production mechanisms[27] (see section 2.2). Table 2.1 gives an overview of most of the experiments, including the employed production mechanisms and analyzed decay channels. In most of the cases at least a "discussible" signal was observed, but often the conclusions were rather controversial. Some of the measurements are discussed in the following, using from time to time already the Partial Wave Analysis (PWA) language. For more details on PWA please refer to chapter 4.

Experiment	Production Mechanism	1^{-+} Decay Channel
BNL-E852	diffraction, charge exchange	$\eta\pi, \eta'\pi, \rho\pi, f_1\pi, b_1\pi$
VES	diffraction, charge exchange	$\eta\pi, \eta'\pi, \rho\pi, f_1\pi, b_1\pi$
KEK-E179	diffraction	$\eta\pi$
GAMS/NA12	charge exchange	$\eta\pi$
Crystal Barrel	$\bar{p}d$, $\bar{p}p$ annihilation	$\eta\pi, \rho\pi, b_1\pi$
Obelix	$\bar{p}p$ annihilation	$\rho\pi$

Table 2.1: Overview of past experimental searches for states with spin-exotic quantum numbers 1^{-+}; for references see text.

2.4.1.1 The $\eta\pi$ Channel

After a very early study from Serpukov in 1981 [98], the GAMS collaboration at CERN was the first to claim a 1^{-+} signal at a mass of about $1.4\,\mathrm{GeV}/c^2$ in the $\eta\pi^0$ channel [8]. At the beginning of the 1990's, high statistics became available from VES and KEK-E179 [99, 100], supporting this observation. In both cases diffractive reactions were exploited, using a π^- beam of 18-37 GeV/c and 6.3 GeV/c, respectively. The VES results were nicely confirmed by BNL-E852 [9, 101] and the name $\pi_1(1400)$ was assigned to the claimed resonance. It was mostly seen in a P_+ wave[28] and its interference studied w. r. t. $a_2(1320)$ (D_+). Also in charge-exchange processes this exotic $1^{-+}P_+$ wave was seen, but the results were not conclusive [102, 103]. In a completely different reaction the Crystal Barrel and the Obelix collaboration confirmed the existence of the exotic P_+ wave in the $\eta\pi$ system, namely by studying $\bar{p}n \to \pi^-\pi^0\eta p$ [10] and/or $\bar{p}p \to 4\pi$ [70, 104]. In general

[27] So far, no evidence for spin-exotic states with quantum numbers different from 1^{-+} exists.

[28] Referring to orbital angular momentum $L = 1$ and spin projection $M = 1$; in chapter 4 spin states are described in the reflectivity basis (see equation (4.3)).

the claim for an exotic $\pi_1(1400)$ is doubted[29], in particular its interpretation as a hybrid: Based on $SU(3)_{flavor}$ arguments it has been demonstrated [107] that the $\eta\pi$ decay channel contradicts the hybrid hypothesis and that $\pi_1(1400)$ is more likely a tetraquark state.

2.4.1.2 The $\eta'\pi$ Channel

Based on studies of the $\eta'\pi^-$ channel, the $\pi_1(1600)$ emerged as most promising hybrid candidate. In diffractive reactions at $37\,\mathrm{GeV}/c^2$ and $18\,\mathrm{GeV}/c^2$ the experiments VES and BNL-E852, respectively, obtained similar results from a PWA [99, 108]. The signal survived even harshest tests [106]. GAMS, BNL-E852 and VES also studied $\eta'\pi^0$ final states produced from charge-exchange reactions, but in contrast to the $\eta'\pi^-$ case no signal was observed.

2.4.1.3 Partial Wave Analysis of the $\pi^-\pi^-\pi^+$ System

The published analyses of the 1^{-+} wave in the $\pi^-\pi^-\pi^+$ channel are highly controversial. This channel was studied in the past only by two experiments[30], namely VES [109, 110, 111, 112] and BNL-E852 [11, 12, 113]. Both made use of diffractive dissociation from pion beams ($37\,\mathrm{GeV}/c$ on nuclear targets and $18\,\mathrm{GeV}/c$ on a proton target, respectively). Many of the basic parameters of the PWA models were similar in the listed analyses, however, they differed substantially in the chosen wave sets. In [109, 110, 111, 112] up to 42 waves were used, 21-27 in [11, 113] and 36 in [12]. Several 1^{-+} waves were included with different spin projections M. BNL-E852 initially published a clear evidence for $\pi_1(1600)$ [11, 113], with a mass and width of $M = (1593 \pm 8^{+29}_{-47})\,\mathrm{MeV}/c^2$ and $\Gamma = (168 \pm 20^{+150}_{-12})\,\mathrm{MeV}/c^2$. This signal is shown on the left of figure 2.5. But a few years later, a second BNL-E852 analysis based on 10 times more statistics and an increased wave set contradicted these results and claimed the absence of $\pi_1(1600)$ in the data [12] (right of figure 2.5). The conclusion of the authors was that two important $2^{-+}F$-waves had been missing in the first analysis and that the initially observed signal had been faked by leakage[31]. Also at VES the signal was unstable [110, 112] and no clear conclusions could be drawn[32]. The PWA presented in this thesis based on the COMPASS data ($190\,\mathrm{GeV}/c$ on lead targets), however, shows a strong exotic 1^{-+} signal consistent with the $\pi_1(1600)$ resonance (see section 5.5.1.7). A major advantage of COMPASS is its excellent acceptance, corresponding to little leakage (see section 5.7).

[29] There are e. g. suggestions that the VES and BNL-E852 signal is an interference of non-resonant Deck-like background and a hybrid resonance at $1.6\,\mathrm{GeV}/c^2$ [105]; also other interpretations exist [106].

[30] Thus the COMPASS analysis presented in this thesis represents the third independent experimental contribution to this field. For more details on PWA see chapter 4.

[31] Migration of events from dominant waves to small waves, usually caused by a wrong or insufficient acceptance description.

[32] In the VES PWAs the instabilities arose from different ranks of the spin density matrix used in the fits (cf. section 5.6.1).

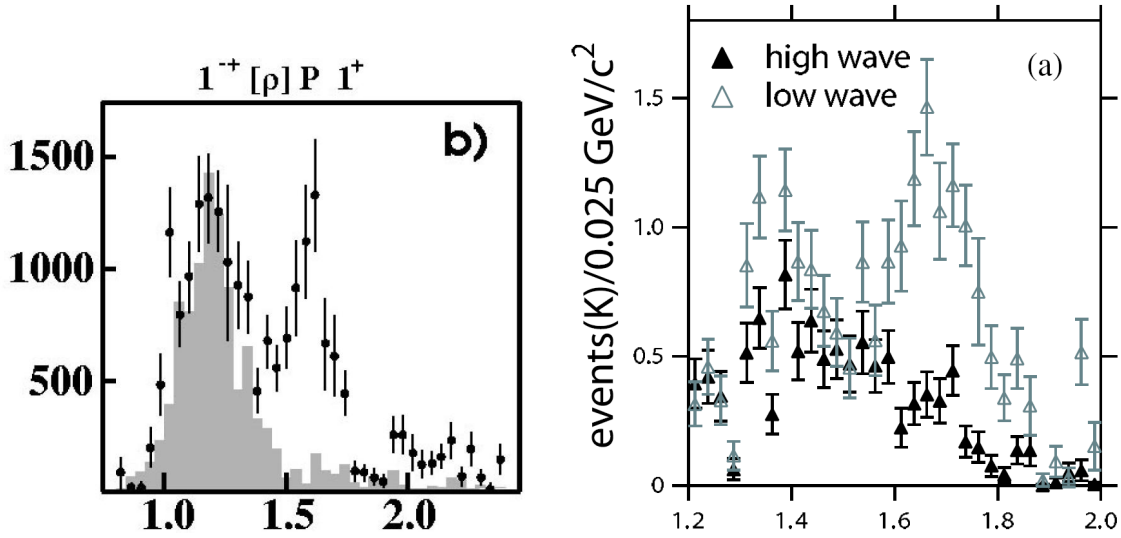

Figure 2.5: The disputed 1^{-+} signals from the two BNL-E852 analyses. Left: 21-wave PWA (40 MeV/c^2 mass bins) from which evidence for $\pi_1(1600)$ was claimed [113]; the bump around 1.2 GeV/c^2 was understood from simulations as leakage (grey-shaded histogram). Right: Higher statistics PWA (25 MeV/c^2 mass bins) [12] using either the same waves as in [113] (low wave set) or 36 waves (high wave set); in the latter case $\pi_1(1600)$ disappeared.

2.4.1.4 The $\omega\pi\pi$ Channel

VES [112, 114, 115] and BNL-E852 [116] also studied the 1^{-+} wave in the $\omega(\pi^-\pi^-\pi^+)\pi^-\pi^0$ channel, thus with five pions in the final state. A PWA model including $\omega\rho$, $b_1\pi$ and $\rho_3\pi$ intermediate states was tried and a clear $\pi_1(1600)$ signal was seen in $b_1\pi$. Its mass and width was determined by BNL-E852 to $M = (1664 \pm 8 \pm 10)\,\mathrm{MeV}/c^2$ and $\Gamma = (184 \pm 25 \pm 28)\,\mathrm{MeV}/c^2$. VES got a consistent mass but a larger width (330 MeV/c^2). Further evidence for $\pi_1(1600) \to \omega\pi\pi$ was reported from $\bar{p}p$ annihilations into $\omega 3\pi$ [117].

2.4.1.5 The $f_1\pi$ Channel

The results from BNL-E852 on the reaction $\pi^- p \to \eta\pi^+\pi^-\pi^- p$ are published in [118] and those from VES on $\pi^- A \to \eta\pi^+\pi^-\pi^- A$ in [112]. Both experiments obtained a similar picture from a PWA, including a broad $1^{-+}(f_1\pi)$ signal. In case of BNL-E852 a Breit-Wigner parameterization gave a mass and width of $M = (1709 \pm 24 \pm 41)\,\mathrm{MeV}/c^2$ and $\Gamma = (403 \pm 80 \pm 115)\,\mathrm{MeV}/c^2$.

2.4.2 New Charmonium-Like States above the $D\bar{D}$ Threshold

While a few years ago the charmonium sector above the $D\bar{D}$ threshold was a virgin territory, recently several new resonances have been discovered. Most of them have been

observed with weak statistical evidence only and their quantum numbers are often unknown[33]. A common tendency is that all these states are surprisingly narrow, which motivated their interpretation as tetraquark compounds, hadronic molecules[34] or hybrids. Most of the signals were seen at BELLE and BaBar (cf. section 2.2.1), but also other experiments contributed. In the following only the "established" new states are presented, some more are currently discussed (e. g. $X(4160)$ [119] and $Y(4325)$ [120]) or in the stage of being published.

2.4.2.1 $X(3872)$

The best studied of the new resonances is called $X(3872)$. It was discovered by BELLE in the reaction chain $B^{\pm} \rightarrow K^{\pm}X(3872), X(3872) \rightarrow \pi^{+}\pi^{-}J/\psi$ [22] and confirmed by BaBar [121], CDF [122] and D0 [123][35]. The average mass and width assigned by the PDG are $M = 3871.2 \pm 0.5\,\mathrm{MeV}/c^2$ and $\Gamma < 2.3\,\mathrm{MeV}/c^2$ [38]. Further decay modes of the $X(3872)$ were observed, and the quantum numbers 1^{++} emerged as most probable ones. The nature of this hadron is still unclear and several interpretations as molecule, tetraquark, glueball or hybrid (see [26] and references therein) or as $\chi_{1c}(2P)$ charmonium state [55] exist.

2.4.2.2 The X, Y, Z resonances around 3940 MeV$/c^2$

$X(3940), Y(3940)$ and $Z(3930)$ were all first observed by the BELLE collaboration [24, 25, 124]. $X(3940)$ would be a good candidate for the $\eta_c(3S)$ $c\bar{c}$ state, because it is produced in the same way like $\eta_c(1S)$ and $\eta_c(2S)$ and shows up together with these states in a J/ψ recoil spectrum. However, its mass of $(3943 \pm 6 \pm 6)\,\mathrm{MeV}/c^2$ is significantly smaller than the predictions for $\eta_c(3S)$ [55]. The situation for $Y(3940)$, $M = (3943 \pm 11 \pm 13)\,\mathrm{MeV}/c^2$, is even more complicated due to its OZI-forbidden[36] $J/\psi\omega$ decay mode [26]. The $Z(3930)$ has a mass of $(3929 \pm 5 \pm 2)\,\mathrm{MeV}/c^2$ and could maybe be identified with the predicted $\chi_{c2}(2P)$ $c\bar{c}$ state [55, 126].

2.4.2.3 $Y(4260)$ and $Z^{\pm}(4430)$

Both these states are astonishing and hotly debated. $Y(4260)$ was discovered by BaBar [23] and already confirmed by e. g. CLEO [127]. It is believed to be a vector state with $J^{PC} = 1^{++}$ and various explanations for its nature have been proposed. A long discussion on this particle including many references can be found in [26]. The $Z^{\pm}(4430)$ was first observed by BELLE in $\psi'\pi^{\pm}$ from $B \rightarrow K\psi'\pi^{\pm}$ decays [128] and constitutes the first known charged resonance with hidden charm. It evidently cannot belong to the charmonium family and is a candidate for a tetraquark with content $c\bar{c}u\bar{d}$ (Z^{+}) or $c\bar{c}\bar{u}d$ (Z^{-}).

[33] Which is why high-statistics and precision experiments like PANDA (see chapter 6) are much-needed.
[34] Also composed of four quarks, but the total wave function is decomposed into two colorless ($q\bar{q}$) parts.
[35] Both CDF and D0 are located at the Tevatron accelerator at Fermilab.
[36] Okubo, Zweig and Iizuka rule: Decays proceeding through disconnected quark lines in the Feynman-diagram picture are suppressed; see e. g. [125].

Chapter 3

The COMPASS Experiment at CERN

COMPASS (COmmon Muon and Proton Apparatus for Structure and Spectroscopy) is a fixed-target experiment at CERN[1], which studies how hadrons are made up from quarks and gluons [13, 14]. Making use of the SPS (Super Proton Synchrotron) high-intensity muon and hadron beams, a variety of physics topics is addressed. Among other things, the program comprises the investigation of nucleon structure functions (e. g. ΔG), of hadron polarizabilities and of the hadron spectrum itself. To this end COMPASS covers a large kinematical regime including quasi-elastic measurements as well as deep-inelastic reactions where the target nucleons are completely destroyed. A key element of the whole physics program is to understand the role of gluons, namely how they contribute to the nucleon spin and how their excitations and self-coupling can possibly lead to states like glueballs and hybrids. In particular the existence of mesons with exotic quantum numbers is studied from diffractive dissociation processes (cf. sections 2.1.1 and 2.3), which is also the topic of the analysis presented in this thesis (see chapter 5). An overview of a selected subset of the COMPASS physics program is given in section 3.1.

Depending on the particular beam conditions and physics measurements, different targets are employed in COMPASS. For the data taking with muons for example, a large polarized target has so far been used. Outgoing particles are detected by a two-stage spectrometer, which covers a large range of scattering angles and particle momenta. Both stages are equipped with a dipole magnet and several types of tracking detectors, which are adapted to the expected rates, the spatial resolutions required and the solid angles to be covered. Figure 3.1 presents an artists view of the experiment. A novum in particle physics experiments is the usage of micro-pattern gaseous tracking detectors, which are based on GEM foils for charge amplification only[2]. Particle identification is performed using a Ring Imaging Cherenkov (RICH) Counter as well as hadronic and electromagnetic calorimetry. The setup has been successfully operated since 2002 mostly with muon beams devoted to the study of nucleon structure functions. During a two-week pilot run in 2004, for the first time data were recorded also with a pion beam addressing the po-

[1] European Organization for Nuclear Research, Geneva, Switzerland.

[2] The success, in particular the high-rate capability, of these devices had a substantial influence on the design of the proposed TPC for PANDA; for further details about the GEM technology see section 7.2.

larizability of pions and their dissociation into mesons[3]. A comprehensive description of the COMPASS experiment, both for data taking with muons and hadrons, can be found in [14] including the performance of all detector systems. In section 3.2 only the particular setup used during the 2004 pilot hadron run is summarized, focussing on the details which are important for the presented analysis. To lead over to the latter, section 3.3 introduces the functionality and terminology of the data acquisition system and offline event reconstruction.

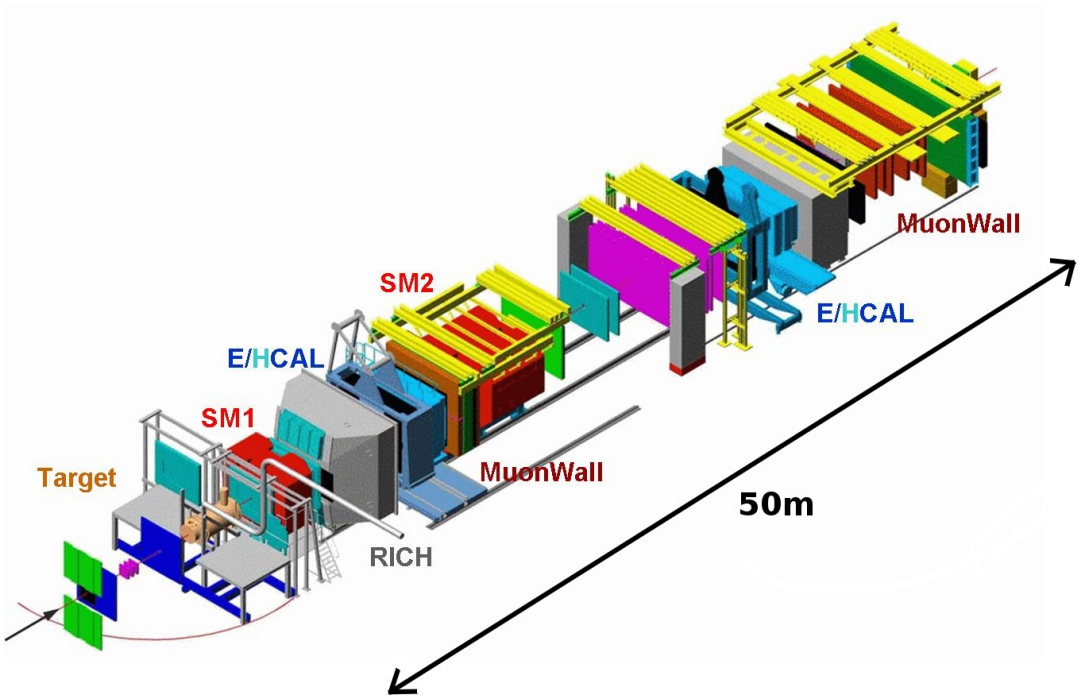

Figure 3.1: Artists view of the COMPASS experiment at CERN; setup corresponding to data taking with the polarized target (light brown color) shown. The beam is coming from the left. For further details see text and [14].

3.1 Overview of the Physics Program

In the following, the COMPASS physics program is summarized. First some of the main aspects of the data taking with muons are outlined (sections 3.1.1 to 3.1.3), mostly referring to papers published by the COMPASS collaboration. Afterwards some selected topics of the hadron program are briefly discussed (sections 3.1.4 to 3.1.6), for a full review please refer to [67]. To keep this overview section short, in general no results are stated or discussed. If available, they can be found in the cited references.

[3]Currently a long-term hadron run is ongoing using a liquid hydrogen target. At the point of writing this thesis, however, no data had yet been ready for physics analysis.

3.1.1 Longitudinal Spin Structure of the Nucleon

In the late 1980's the so-called spin crisis arose, when it was discovered that only part of the proton spin is carried by the quarks [129]. This triggered a great activity among both experimentalists and theorists, which has continued down to the present day. In the line of these experiments COMPASS investigates the polarization of quarks [130, 131, 132, 133] and gluons inside nucleons from the analysis of deep inelastic muon scattering events. In particular the gluon contribution $\Delta G/G$ to the total nucleon spin is directly measured. Three approaches are pursued to extract $\Delta G/G$ by analyzing events with either D mesons (open-charm), hadron pairs with large transverse momenta (high-p_T) [134] or single high-p_T hadrons [135] being produced.

3.1.2 Transverse Spin Distributions

Only in the early 1990's it was worked out that to fully describe the quark state inside the nucleon also the transverse spin distributions $\Delta_T q(x)$ are needed [136]. They are accessible via Collins and Sivers asymmetries, which have been measured by COMPASS with a transversely polarized target [137, 138].

3.1.3 Lambda Polarization

In addition to the valence quark distributions also the polarization of sea quarks[4] is subject of ongoing investigations. In case of a polarized target, the virtual photon exchanged during the deep inelastic scattering process can transfer the polarization to a detectable Λ baryon. If the target is unpolarized, also the spontaneous polarization of the latter is examined. First results from COMPASS on Λ polarizations can be found in [139, 140, 141, 142].

3.1.4 Pion Polarizabilities and Chiral Anomaly

The response of pions or kaons to an external electromagnetic field is described by their electric and magnetic polarizabilities $\bar{\alpha}$ and $\bar{\beta}$, respectively. These are fundamental quantities within the theory of strong interactions, in particular regarding chiral symmetry conservation. On the theory side, Chiral Perturbation Theory (χPT, see section 2.1.3) is able to make accurate predictions for $\bar{\alpha}_\pi$ and $\bar{\beta}_\pi$ [143, 144], which are so far not in agreement with experimental results [145, 146]. At COMPASS both pion and kaon polarizabilities can be measured by employing the Primakoff reaction and making use of the intense hadron beams available at the CERN SPS. During the 2004 pilot run, Primakoff events were recorded using pion scattering on lead targets. These data are currently being analyzed [147].

The decay of neutral pions $\pi^0 \to \gamma\gamma$ and the reaction $\gamma\pi^\pm \to \pi^\pm\pi^0$ involve anomalous vertices, which can also be treated in the framework of χPT [148]. Especially for

[4] $q\bar{q}$ fluctuations inside the nucleon, including heavy quark flavors like s or c.

$\gamma\pi^{\pm} \rightarrow \pi^{\pm}\pi^{0}$ precise experimental data are needed to catch up with the more and more progressing theory predictions. At COMPASS this channel is accessible in a similar way as the Primakoff reaction, thus by the scattering of high-energetic (negative) pions on solid state targets at momentum transfers close to zero. A first analysis based on the 2004 pilot run data is ongoing [149].

3.1.5 Exotic Mesons

The motivation and techniques to search for non-$q\bar{q}$ hadrons such as glueballs, hybrids or $q\bar{q}q\bar{q}$ states is discussed in detail in chapter 2. The existence of these objects is the most important qualitative open question in QCD. Due to the availability of π, K, p and μ beams, COMPASS is in a unique position to contribute to this field by making use of different production mechanisms. In particular peripheral hadron scattering, namely diffractive and central production (see section 2.2.1), are employed as part of the hadron program. While the latter will be studied at COMPASS for the first time from the data taken in 2008, the diffractive dissociation of pions into mesons has already been successfully tested in 2004 during the pilot run. For this thesis $\pi^{-}\pi^{-}\pi^{+}$ final state events from only about two days of data taking have been analyzed (see chapter 5), showing clear evidence for the hybrid candidate $\pi_1(1600)$ with exotic quantum numbers 1^{-+}. To precisely determine its properties, study different branching ratios and possibly map out the full light-hybrid spectrum, part of the 2008 beam time will again be dedicated to diffractive meson production.

3.1.6 Doubly Charmed Baryons

From the beginning on the search for doubly charmed baryons has been a topic for COMPASS [13]. Little is known about these particles [150] although more and more signals have been reported during the last years (see for example [151]). Thus it would be a great opportunity for a high-rate experiment like COMPASS to do spectroscopy in this sector. However, an optimized setup including high-precision vertex reconstruction and advanced trigger schemes are needed. Therefore this physics has so far not been addressed yet, but is postponed to the future.

3.2 Setup during the 2004 Pilot Hadron Run

Figure 3.2 presents the schematic layout of the 2004 COMPASS hadron setup. From left to right the experiment can be divided into three parts, corresponding to the target region and the first and second spectrometer stage, respectively. In the drawing the beam enters from the left, parallel to the z-axis of a right-handed coordinate system, which is defined according to the indicator in the lower left corner. Since the target region had many significant modifications compared to the muon run of the same year, it is detailed, together with the beam, in section 3.2.1. Following the design idea of COMPASS, however, not many changes had to be done for the spectrometer itself. In particular the two magnets

(SM1 and SM2) were running at their maximum currents. SM1, which defines the first (large angle) spectrometer stage, has a vertical field integral of 1 Tm corresponding to a deflection of 300 mrad for particles with a momentum of 1 GeV/c. In order to ensure the required polar acceptance of 180 mrad with respect to the target, the tracking detectors of this stage therefore have to cover an acceptance of 250 mrad. The RICH counter was on purpose not active during the 2004 pilot hadron run and the rather heavy chamber gas replaced by nitrogen to save material and avoid secondary interactions and photon conversions. For the same reason three scintillating fiber stations were removed from the beam: FI04 at $z \sim 2.15$ m, FI06 at $z \sim 15.0$ m and FI07 at $z \sim 21.3$ m (all still indicated in figure 3.2). Instead the centers of three GEM detectors were activated: GM06 at $z \sim 15.8$ m, GM07 at $z \sim 20.2$ m and GM09 at $z \sim 20.8$ m.

The third part of the setup shown in figure 3.2 represents the second (small angle) spectrometer stage, which detects particles with small angles (± 30 mrad) and large momenta (5 GeV/c and higher). Its central element is the 4 m long SM2 magnet, which has a field integral of 4.4 Tm. For the 2004 hadron run the central hole of the electromagnetic calorimeter of this stage (ECAL2) was reduced from 380×380 to 76×76 mm^2 to adapt to the more focussed pion beam. For the Primakoff measurements also an additional trigger hodoscope was installed in front of ECAL2. The trigger concept which was chosen to select diffractive dissociation events is discussed in section 3.2.2.

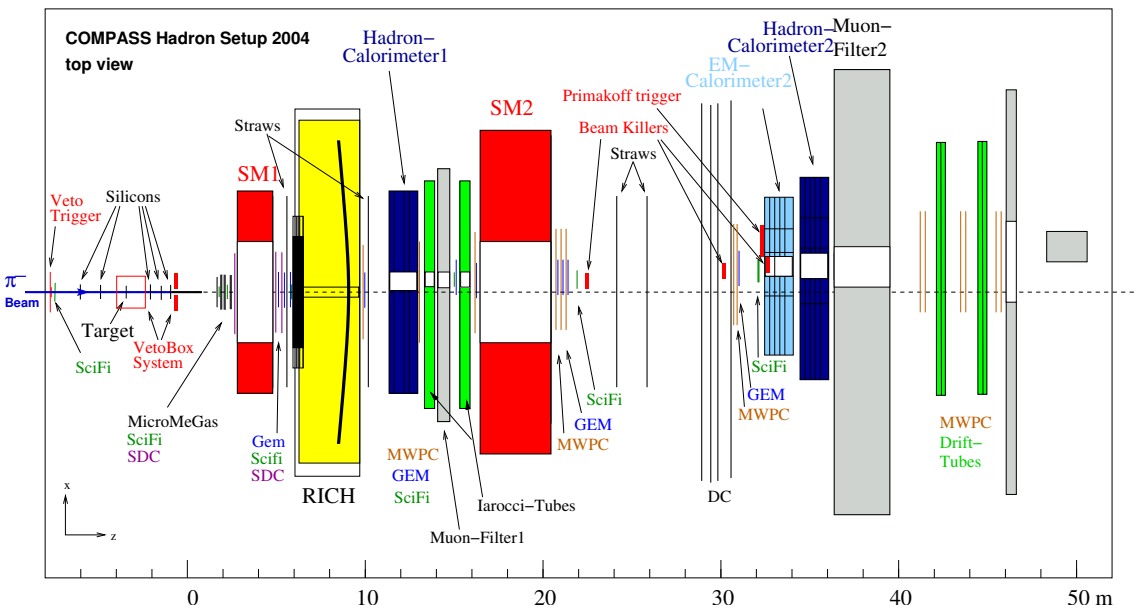

Figure 3.2: Schematic view of the COMPASS pilot hadron run setup in 2004 (without beam line); spectrometer magnets indicated in red color. For details on the different components (including their abbreviations) see text and [14].

3.2.1 Beam Properties and Target Region

The COMPASS hall is connected to the SPS by means of a 600 m long beam line. At its beginning, the intense primary proton beam[5] impinges on a beryllium production target with a thickness of 500 mm. From the produced particles, secondary hadrons (mainly pions) up to 280 GeV/c can be selected by tuning a series of focussing and bending magnets. The maximum hadron flux allowed by radiation safety is 10^8 particles per SPS cycle (16.8 s), however, during the pilot run it was about an order of magnitude lower. Table 3.1 lists all important beam parameters of the 2004 π^- beam. It should be noticed that the proportions of particles are given right after the production target. At the position of the COMPASS target, the fraction of K^- was only about 2-3% due to the kaon decays during the transportation in the beam line.

Beam Parameter	Measured Value
Beam momentum	190 GeV/c
Hadron flux at COMPASS per SPS cycle	$1\text{-}2 \cdot 10^7$
Proportion of negative pions	95%
Proportion of negative kaons	4.5%
Other components (mainly antiprotons)	0.5%
Spot size at COMPASS target ($\sigma_x \times \sigma_y$)	$3.5 \times 2.8\,\text{mm}^2$

Table 3.1: Parameters and performance of the 2004 hadron beam.

For the identification of the individual beam particles, in principle a pair of Differential Cherenkov (CEDAR) counters was foreseen in the final section of the beam line. However, these devices were not operating reliably in 2004 due to pressure instabilities. Therefore no beam tagging could be performed. In addition, it turned out later that some of the beam particles suffered an energy loss of a few GeV during the transportation. Instead of being blocked by scrapers, they re-scattered into the beam line and accidentally reached the COMPASS target [152]. Since the Beam Momentum Station (BMS) [14], which measures the beam energy E_a (cf. figure 2.3) on an event by event basis, was on purpose removed from the beam line to save material, this problem has actually been verified only using the three pion events of the analysis presented in this thesis. Their total energy sum E_c is to a very good approximation equal to the beam energy and can be correlated to the well reconstructed x-y position of the primary vertex. Taking into account even the momentum transfer from the target, E_a can be precisely recalculated (cf. section 5.1.4). Its distribution clearly exhibits a low energy shoulder (see for example figure 5.4) corresponding to the discussed energy loss in the beam line. It was carefully tested that these events do not impose any systematics on the analysis.

During the 2004 hadron run, COMPASS collected data with several solid-state targets, different in material and width, which are listed in table 3.2. All targets consisted of simple discs with a diameter of 3 cm, corresponding to more than 3σ of the beam width. To

[5] Up to $1.2 \cdot 10^{13}\,p/s$, delivered with a cycle structure of 4.8 s spills of beam followed by breaks of 12 s.

measure the direction of the incoming beam particle, one scintillating fiber detector and two stations of silicon micro-strip detectors were placed before the target (cf. figure 3.2). Three more such stations were present after the target, which have been crucial for the reconstruction of primary vertices. Several trigger components were installed close to the target, too (see section 3.2.2).

Material	Thickness x	x/X_0	x/λ_I	Atomic Mass
Lead	1.6 mm	0.28	0.015	207.2
Lead	3 or 2 + 1 mm	0.53	0.029	207.2
Copper	3.5 mm	0.24	0.037	63.55
Carbon	23 mm	0.12	0.086	12.01

Table 3.2: Targets during the 2004 hadron run [14]; X_0 denotes the radiation length and λ_I the nuclear interaction length. Most of the events analyzed in chapter 5 were recorded with a segmented 2+1 mm lead target (natural isotopic mixture: 52.4% ^{208}Pb ($J = 0$), 24.1% ^{206}Pb ($J = 0$), 22.1% ^{207}Pb ($J = 1/2$) and 1.4% ^{204}Pb ($J = 0$) [153]).

3.2.2 Diffractive Trigger

The 2004 diffractive trigger (Diff$_1$) consisted of several hardware components, which are illustrated in figure 3.3. Most of them belonged to the common trigger system shared with the Primakoff measurement. First of all, incoming beam particles were detected by the coincidence of two scintillators with a diameter of 5 cm (beam counter). Both were located before the target and centered on the beam axis. Complementary, a veto detector with a central hole of 4 cm in diameter rejected beam particles not crossing the target material. Two additional veto counters made of lead-scintillator sandwiches and located downstream of the target were used to suppress events with particles emitted under large angles and falling outside of the spectrometer acceptance. A system of three beam killers placed between the second magnet (SM2) and the hadronic calorimeter (HCAL2) rejected non-interacting beam particles. A further barrel-shaped veto system was installed around the target to detect hard scattering events with large momentum transfers and to provide this information either directly to the trigger logic or to the offline analysis. However, due to not understood threshold behaviors and missing calibrations it has never been used, neither on the trigger level nor in the reconstruction or analysis.

In addition to these general components, two elements were included in the Diff$_1$ trigger to enhance the fraction of diffractive dissociation events. The first one was a scintillator with a diameter of 5 cm, which was used as multiplicity counter (MPC). It was set up to trigger on at least two crossing charged particles[6]. Secondly, a maximum cluster of at least 6 GeV was required in HCAL2. Both the MPC and HCAL2 condition have been modelled in the simulations as described in section 5.3, however, their influence on the overall acceptance has been found to be on the percent level only. During the 2004 hadron

[6] To cover the $\pi^-\pi^-\pi^+$ and the $\eta\pi^-$ channels.

data taking, typical diffractive trigger rates of about $2 \cdot 10^4$/spill were reached.

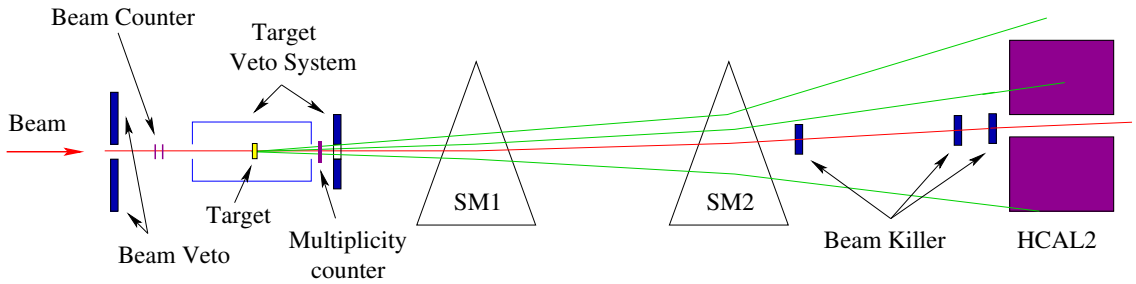

Figure 3.3: Sketch of the 2004 diffractive trigger scheme (see text); veto components are drawn in blue, others in magenta. Shown are a 3π event (green lines) fulfilling all trigger requirements and a single pion event (red line) corresponding to a non-interacting beam particle; the latter case is vetoed by the beam killers.

3.3 Data Taking and Event Reconstruction

In order to close the gap between the description of the experimental setup and the physics analysis, this section briefly summarizes the functionality and terminology of the COMPASS data acquisition (DAQ) and event reconstruction. Starting from the processing which takes place right at the detectors themselves, the data flow and concentration until the point of storage to disc is depicted. A rather new development in this line is the online filter, which is discussed separately because it also has some direct impact for the analyzed diffractive events. Finally, the offline event reconstruction and analysis tools are explained, based on which any physics analysis starts out. Of course, all these technologies and techniques have a much deeper level of complexity than could be described here. For further details and references to more sources of information, please refer to [14, 135, 140, 154]. Concerning technical matters of the employed software, like particular versions, see also appendix A.

3.3.1 Readout Electronics and Data Acquisition System

The hardware trigger (cf. section 3.2.2) defines the point in time when an interesting event occurred. This information is distributed by a Trigger Control System (TCS) to the detector frontend electronics with an overall latency of about 1.5 µs and synchronous to a reference clock of 38.88 MHz. Also a unique identification number for the events is assigned at this level. It is foreseen that different hardware triggers are active at the same time, for example during the 2004 hadron run the Primakoff and the diffractive trigger were running in parallel. Usually a minimum time interval of 5 µs is required between two different triggers and not more than three events within 75 µs or ten within 250 µs can be processed. This leads to 5% dead time at a trigger rate of 10 kHz. For each event about

250 000 detector channels have to be read at COMPASS. Of course, only a small fraction contain actual information corresponding to signals created by traversing particles. Therefore at the earliest possible stage, namely the frontend electronics mounted close to the detectors, the signals are separated from the noise by means of applied thresholds. The remaining digitized data are encoded and sent via optical fibers (up to 40 MB/s) to the next readout chain level consisting of several concentrator modules. The programming of both the frontends and the concentrators for the various detector types is based on a central database and performed by a dedicated software (Configuration Server).

The data from the concentrators is, again via optical fibers (up to 160 MB/s), transmitted to readout buffer (ROB) computers placed inside a counting room. Thus from this moment on, all readout steps are performed in software[7]. The ROBs, which are still attached to certain detector systems, are connected through a network switch to the so-called event builder (EVB) computers[8]. These machines collect the data belonging to single events from the ROBs and send the whole event to the central data storage at CERN. Usually the events are grouped to runs of 100 or 200 spills (cf. section 3.2.1) corresponding to data taking periods of 30-60 minutes. Up to 580 TB of data have been recorded by COMPASS per year in the past, during beam times of typically five months.

3.3.2 Online Filter

To increase the purity of the hardware trigger and allow for a cost effective reduction of the amount of needed storage tapes, a dedicated online filtering program has been developed for COMPASS. It is running on the previously introduced EVB computers and works on the complete events. More precisely it is inserted into the event stream, which is produced by each EVB, and performs the filtering before the data are stored to local discs awaiting the transfer to the central CERN storage. Depending on the trigger rate and the number of active EVBs, the allowed average decision making time is 4 ms per event. Thus only a partial decoding of the data is possible excluding the possibility of charged particle tracking in regions where a magnetic field is present. However, apart from purely technical checks, information about hits in the silicon micro-strip or scintillating fiber detectors for example can be extracted and evaluated online. The filter offers several modes of operation, in which it either just passes the events through, checks them and marks bad ones or actually really filters out bad ones.

For the pilot hadron run in 2004, the filter supported the diffractive trigger by probing the track multiplicity in the three silicon stations downstream of the target. The applied algorithm calculated the number of hits for each of the twelve detector planes and sorted the planes accordingly. In order not to be effected by noise or individual efficiencies, the four planes with the biggest and the four planes with the smallest number of hits were not considered for the filter decision. The number of hits in the remaining four planes were summed up and required to be greater than five. By this 45% of the events were discarded, which enabled the retirement of a pre-scaler with factor 2 for the diffrac-

[7] DATE software package, developed for the ALICE experiment at CERN.
[8] In 2004, 19 ROB and 12 EVB computers were employed.

tive trigger. In order to take the online filter into account for the acceptance corrections needed for the partial wave analysis (cf. section 4.3), the described algorithm has been modelled for the simulations (see section 5.3).

3.3.3 Event Reconstruction and Analysis Environment

Before a physics analysis can take place, the complex step of event reconstruction has to be done. It involves several processing steps, during which the raw detector information is transformed into tracks, vertices and particle identification hypotheses. This task requires a detailed knowledge of the apparatus taking all the employed equipments and detector functionalities as well as all materials and detector positions into account. A dedicated software package, the COMPASS Reconstruction and Analysis Library (CORAL), has therefore been developed since about ten years. In parallel, a ROOT-based [155] analysis framework has been made available to all COMPASS members, which allows for an efficient access to the features of the reconstructed events. These Physics Analysis Software Tools (PHAST) [156] also provide the user with a variety of standardized selection routines and act as an interface to CORAL. The output from the reconstruction is stored as so-called mDST (mini Data Summary Table)[9] files in the PHAST format. The mDST production is done centrally at CERN on a batch system, where COMPASS has a share of about 1 000 processor units. Several iterations are needed until a final production of a certain data taking period is available, because for example the exact position of the detectors have to be established (alignment procedure). Since for the analysis presented in chapter 5 mainly the track and vertex finding and fitting parts of the reconstruction are important, these two CORAL steps are detailed in the following.

The first preparatory step for the tracking is the "decoding", where the raw data of all detector channels are mapped from abstract electronics identification numbers to real positions (3-dim. coordinates). If appropriate, calibrations are applied and, finally, hits are produced with a time and an amplitude associated. Neighboring hits, which are assumed to belong to one and the same particle crossing, are then combined by "clustering" algorithms. The next step is a preliminary pattern recognition (the "pre-pattern"), during which track segments are searched for in five zones of the spectrometer, where charged particles can be expected to travel along straight lines. This is done in projections first[10] and then continued in 3-dim. space. The result of the "pre-pattern" are lists of track segment candidates for each zone, which are above all subjected to a cleaning[11].

The remaining candidates are inter-connected in the so-called "bridging", a process which loops over the candidate lists and tries to match track segments from different zones. The combinations found are sorted according to their quality and number of associated hits and, iteratively, condensed into complete tracks. Finally, a Kalman fit [157] is employed to calculate the optimum track parameters (x and y positions, $\mathrm{d}x/\mathrm{d}z$ and $\mathrm{d}y/\mathrm{d}z$ slopes, inverse momentum $1/p$) and the corresponding error matrices. At this

[9] ROOT trees containing PHAST events with tracks, vertices and information from the RICH, the trigger, the calorimeters and so on; the mDST size is reduced by a factor ~ 80 compared to the raw data.

[10] Utilizing a pivot-plane algorithm [14].

[11] Using a dictionary (look-up table) of example track pieces, generated from Monte Carlo simulations.

stage the multiple scattering due to traversed material and the precise magnetic field maps are taken into account.

After a successful track reconstruction CORAL initiates the "vertexing" stage. In a two-step process primary and secondary interaction points as well as decay vertices are searched for. The aim is to get the best estimate of the three coordinates of the vertex positions and of the momentum vectors of all connected tracks at this point. In general a vertex is called primary when it contains a beam track. First a fast pre-selection based on a Point-Of-Closest-Approach algorithm is performed, during which groups of tracks are defined which have most likely the same origin. Also an estimate for the vertex parameters is carried out. These parameters are then precisely calculated in a second step, using an inverse Kalman filter algorithm: Step by step it is tried to remove a track from the vertex and, if a track was removed, the vertex is re-fitted. While in the direction perpendicular to the beam axis this method achieves vertex resolutions of about 0.1 mm, along this axis the resolution depends strongly on the z position itself and the opening angle of the outgoing particles. In case of the diffractively produced 3π events with momentum transfers greater than $0.1\,\mathrm{GeV}^2/c^2$ and primary vertex z positions around $-310\,\mathrm{cm}$ (see figure 3.2), this resolution is for example 4-5 mm.

Chapter 4

Partial Wave Analysis

The most important analysis tool for meson spectroscopy and, in particular, the search for spin-exotic states is the partial wave analysis (PWA). With this technique, a given data set containing final state decay products of some (possibly unknown) resonances can be exploited and the resonance parameters be determined. Those include the mass, the width and the J^{PC} quantum numbers as they have been introduced in section 2.1. To identify the spin properties, an evaluation of the angular distributions of the final state particles is the key. The PWA furthermore takes interferences between different, in their masses overlapping, states into account. In fact it is often solely this interference behavior, which leads to the undoubtful discovery of a new resonance.

Depending on the particular production mechanism and reaction chain, different PWA implementations are usually employed. This can be due to computing performance reasons, but also principle physics arguments can play a role. Most likely one would use for example another approach to analyze the $\bar{p}p$ annihilation data obtained with the future PANDA experiment (see chapter 6) than to analyze the diffractive dissociation data which are recorded at COMPASS (see chapters 3 and 5). Only the latter case is described in this chapter, focussing on the PWA of $\pi^-\pi^-\pi^+$ events.

Each PWA starts out with some physics assumptions concerning the reaction process. Section 4.1 summarizes them for the analysis presented in this work and also points out their implications. Furthermore, a PWA is always based on a so-called spin formalism, which employs certain reference frames and decides on the concrete representation of spin states and angular distributions. A very common approach, namely the Zemach formalism, is briefly introduced in section 4.2. The computational techniques of the performed PWA, namely a mass-independent extended maximum likelihood fit followed by a mass-dependent χ^2 fit, are detailed in sections 4.3 to 4.5. All output parameters obtained from the fits are explained and the quality assurance of the whole procedure is discussed.

4.1 Physics Assumptions and Implications

The performed PWA relies on a couple of physics assumptions, which are described in this section. They lead to a parameterization of the reaction cross-section and are therefore crucial for the whole procedure. Some of the assumptions are connected to the production process and are therefore very specific to the diffractive dissociation case (see section 2.3). The one-Reggeon exchange is an example for this. Others like the isobar model are very common and used in most PWA nowadays. As far as possible, the actual impact of each assumption is addressed, whereas some of the technical points have to be resumed later in this chapter again after more details about the analysis have been explained. To provide a basis for the following discussions, figure 4.1 illustrates in a simplified way the diffractive resonance production, focussing on the features relevant for the PWA. In particular all involved quantum numbers and notations are introduced (see figure caption).

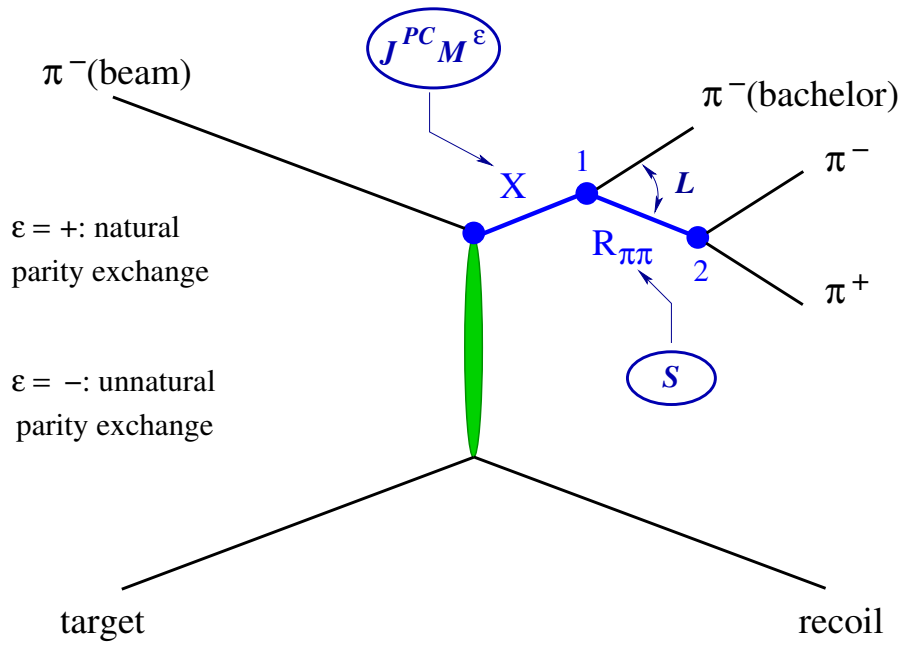

Figure 4.1: Overview of the $\pi^- + A \rightarrow X + A' \rightarrow \pi^-\pi^-\pi^+ + A'$ diffractive dissociation process, illustrating the physics assumptions and quantum numbers which enter the PWA. All initial and final state particles are drawn in black, the intermediate states in blue color. The produced resonance X has spin J, parity P, charge conjugation C, spin projection M and reflectivity ϵ (cf. section 4.2.1). It is assumed to decay at point 1 into a di-pion resonance $R_{\pi\pi}$ (also called isobar) and a π^-, with a subsequent decay of $R_{\pi\pi}$ into a $\pi^+\pi^-$ pair at point 2 (isobar model). The spin of $R_{\pi\pi}$ is denoted by S and the relative orbital angular momentum between $R_{\pi\pi}$ and the bachelor π^- by L. Depending on the reflectivity ϵ of the state X, the interaction involves a natural or unnatural parity exchange (see section 4.1.2).

4.1.1 Exclusivity and Regge-Exchange Reaction

In order to be able to exploit the angular distributions of an event in the PWA fit, it is of course a prerequisite that all final state particles have been measured by the experiment. In the most general case this should include not only the resonance decay products (upper part of figure 4.1) but also the recoil particle (lower part). However, in the case of diffractive dissociation at high beam energies the recoil can be regarded as completely separated (large rapidity gap). The π^- projectile only grazes the target and the resonance X is purely produced from the upper vertex. Thus its properties can in fact be studied from the knowledge of the 4-momenta of the decay products only. In other words, it is assumed that the total reaction cross-section factorizes in products corresponding to a projectile/resonance and a target/recoil vertex without any further final state interactions. The target just acts as a strong interaction partner and provides momentum and angular momentum transfer to the beam projectile. Neither it breaks up nor it is excited and its mass stays therefore the same throughout the whole reaction[1]. It is in that sense that exclusivity is required in the analysis (cf. section 5.1.4).

Thinking in terms of exchange reactions (cf. figure 2.2 (left)), the separation between the upper and the lower part of figure 4.1 is formalized as a (space-like) Regge process. As discussed in section 2.3.4, the Pomeron is the most prominent trajectory. It carries angular momentum and helicity and thus the beam pions with $J^P = 0^-$ may be excited to different J^P states X. No isospin or electric charge is transferred from the target to the projectile. It should be emphasized at this point that the performed PWA does not directly take the quantum numbers of the target (recoil) into account. The inserted waves refer only to the state X and its decay. The fact that the (unpolarized) target might have spin (nucleon case) or not (lead case) is only reflected in the number of fit parameters, more precisely in the rank of the spin density matrix [158, 159] (cf. equations (4.1) and (4.9)).

4.1.2 Parity Conservation and Naturality-Reflectivity Correspondence

In strong interactions parity is conserved. This is in particular true for the diffractive meson production, and therefore the PWA has to take it into account. As will be introduced in section 4.2.1, it has become a common practice to describe the state X in terms of the reflectivity $\epsilon = \pm 1$ quantum number, limiting at the same time the spin projection to values $M \geq 0$. This turns out to be a very convenient description, since parity conservation can be translated into the fundamental constraint that waves with opposite ϵ are not allowed to interfere [158]. Thus much less free parameters have to be used in the PWA fit, which makes it more stable and also more fast.

A second important, although again not trivial topic connected to the reflectivity is its correspondence to the exchanged naturality η (see [160] or appendix 1 of [161]). Since diffractive reactions are dominated by a Pomeron exchange ($\eta = +1$, section 2.3.4), only

[1] This is actually not perfectly true in case of high momentum transfers t', since there is a certain probability to excite the target nucleons; see also the discussion in sections 2.3.5 and 5.1.4.

$\epsilon = +1$ waves are expected to contribute significantly to the PWA fit. Therefore, from the beginning on, much less $\epsilon = -1$ waves compared to $\epsilon = +1$ waves are considered.

4.1.3 The Isobar Model and Di-Pion Parameterizations

Before it is possible to write down a decay amplitude using a particular spin formalism (see section 4.2), it has to be defined how the final state particles are grouped to construct the decay chain. The most popular approach, which is followed also by the employed PWA program, is the so-called isobar model. In this model it is assumed that all subsequent decays appear to be two-body decays as visualized by the blue part of figure 4.1 for the case of $\pi^-\pi^-\pi^+$ final states. More precisely, the produced state X decays at point 1 into a di-pion resonance $R_{\pi\pi}$ (also referred to as isobar) and a bachelor π^-. $R_{\pi\pi}$ subsequently decays itself at point 2 into a $\pi^+\pi^-$ pair. In general, the isobar model has been found to work extremely well in very different environments and for most of the known hadrons. Exceptions may of course be direct decays in more than two particles (like $\omega \to 3\pi$) or decay chains involving rescattering processes of the final state particles.

To build up the spin J (with projection $M \geq 0$ and reflectivity $\epsilon = \pm 1$) of the state X, L-S coupling is assumed: First the spins of the isobar and the bachelor particle are added, which is, of course, equal to the spin S of $R_{\pi\pi}$ in case of a bachelor pion with spin 0. Next the orbital angular momentum L as defined in figure 4.1 is added to S following the usual rules of angular momentum summations. The full description of the state X includes in addition to J, M and ϵ also its parity P and charge conjugation C (cf. section 2.1). One particular set of these quantum numbers in combination with the specification of $R_{\pi\pi}$, L and S defines a decay amplitude[2] ψ. Which ones have been considered for the different fits presented in this work is discussed in section 5.4.1.

As can be motivated from the data, the most important di-pion resonances to be considered are the $\rho(770)$ and the $f_2(1270)$. Furthermore the $f_0(980)$ and $\rho_3(1690)$ have been added but they play only a minor role. All these isobars are described as relativistic Breit-Wigner functions with dynamical total width including Blatt-Weisskopf barrier factors (cf. section 2.1.2). Their parameters, namely mass and width, have been taken from the Particle Data Group (PDG) [38]. In case of the $f_0(980)$ a width of 40 MeV has been assumed, which corresponds to the lower PDG limit.

In addition to the listed rather narrow isobars a broad $(\pi^+\pi^-)$ s-wave amplitude has been included. It contains two broad spin-0 resonances, which are difficult to separate since they strongly overlap: $f_0(600)$ (also called $\sigma(600)$) and $f_0(1370)$. In principle the above mentioned $f_0(980)$ could have been added here as well, but due to its narrow width it has been taken out and treated as a single isobar (following the approaches by BNL-E852 [113] and VES [109]). In general the parameterization of the $(\pi\pi)_s$ state is subject to ongoing discussions and different approaches exist.

[2]Instead of decay amplitude the term partial wave is also often used; e. g. the number of events going through a given ψ is called intensity of this partial wave.

4.1.4 Parameterization of the Reaction Cross-Section

Summarizing all the physics assumptions which have been discussed in this section, the following formula can be written down to parameterize the cross-section σ of the diffractive dissociation process for the PWA fit:

$$\sigma(\tau, m, t') = \sum_{\epsilon=\pm 1} \sum_{r=1}^{N_r} \left| \sum_i \sum_k C^{\epsilon}_{ikr} \, \mathrm{BW}_k(m, M_{0\,k}, \Gamma_{0\,k}) \, f^{\epsilon}_i(t') \, \psi^{\epsilon}_i(\tau, m) \right|^2 \quad . \tag{4.1}$$

In this expression τ and m stand for the five phase space parameters occurring in a 3-body decay and the invariant mass of the $\pi^-\pi^-\pi^+$ system[3], respectively, while t' denotes the 4-momentum transfer according to equation (2.12). The fact that partial waves with opposite reflectivity ϵ are not allowed to interfere is taken into account by putting the corresponding sum outside of the absolute squares. Similarly the rank N_r is treated (cf. section 4.3.1), which indeed increases the number of parameters C^{ϵ}_{ikr} (complex production amplitudes) but doesn't introduce any further interference terms. The mass dependence of the produced state X is described by Breit-Wigner (BW) functions[4] according to equation (2.3). It is foreseen that for a certain decay amplitude ψ^{ϵ}_i several BW functions might be needed, which is reflected by the index k. In turn the same BW shape might be used for different ψ^{ϵ}_i in case of a resonance having different decay channels. Each ψ^{ϵ}_i is a function of τ and m and is constructed based on the isobar model including the parameterizations of the involved di-pion resonances $R_{\pi\pi}$ (see also section 4.2). Thus the index i collects all quantum numbers $J^{PC}M^{\epsilon}[\text{isobar } \pi]L$, where [isobar π] specifies the decay. The t' dependence of σ is described by an independent set of real functions f^{ϵ}_i, which are discussed below. They as well as the decay amplitudes are fixed during the whole PWA procedure and do not contain any fitting parameters.

The superior goal of the PWA is to digest from a given data sample the complex production amplitudes C^{ϵ}_{ikr} and the Breit-Wigner parameters M_0 and Γ_0 for all produced resonances. For practical reasons[5] this task is split into two parts involving a partitioning of the data. First a mass-independent fit is performed in narrow m bins as described in section 4.3. Since the cross-section σ introduced by equation (4.1) is always a fast-varying function of m and, in addition, not to destroy the mass resolution for narrow resonances, the bin size is chosen as small as allowed by the available statistics (e. g. 40 MeV for the presented analysis). In a second step, a mass-dependent fit then determines the BW parameters based on the results obtained for the individual mass bins (see section 4.5).

In principle a fine binning not only in m but also in t' could be considered. However, this requires large statistics and, of course, also the number of fits increases drastically. Instead rather big t' intervals are used (at least for the "high-t'" analysis, see section 5.4), in which the cross-section dependence on t' can be reasonably described by the functions f^{ϵ}_i. It is assumed that only for different $J^{PC}M^{\epsilon}$ states different $f^{\epsilon}_i(t')$ are needed and that,

[3] In section 2.3.3 m is called m_c, but the index is dropped here for simplicity.
[4] In general also coherent background is meant here, which has to be added sometimes; see section 4.5.
[5] Like a complicated PWA model or too many events.

depending on the spin projection M, they have the following shape [60]:

$$M = 0: \quad a \cdot e^{-bt'} \quad ; \quad M = 1: \quad a \cdot t' e^{-bt'} \quad . \tag{4.2}$$

In particular the additional factor t' in case of $M = 1$ waves is important to take into account. The parameters a and b have once to be obtained from the data itself[6] and are then kept fixed during all fits. Thus the $f_i^\epsilon(t')$ can be regarded in a similar way as the decay amplitudes $\psi_i^\epsilon(\tau, m)$, which are also considered as known and do not contain any fitting parameters during the standard analysis.

4.2 Spin Formalisms and Decay Amplitudes

The topic of describing the spin state of a system consisting of several particles is fundamental in particle physics. Of particular importance for the PWA is the question how to construct decay amplitudes ψ, which apply for example to the case of a resonance decay as depicted in figure 4.1. During the last more than 50 years several formalisms have been developed, which can roughly be divided into two groups: tensor and spin-projection formalisms[7]. In both cases the starting point for an experimentalist is usually a Lorentz transformation from the laboratory system to a rest system of the resonance X, which is in case of the performed PWA the so-called Gottfried-Jackson frame. In this context also the reflectivity quantum number ϵ is introduced. Two representative spin formalisms, one for each mentioned group, are the Zemach and the helicity formalism. The former has been used for almost all presented fits and is briefly discussed below. Fast algorithms can be built on it, but it gets complicated when high spin states are involved. The helicity formalism has been employed only for cross-checks. Its advantage is for example that relativistic extensions can be easily added [164, 165]. A comprehensive and detailed introduction to spin formalisms containing many references to further publications can be found for example in [166].

4.2.1 Gottfried-Jackson Frame and Reflectivity Basis

For each event the Gottfried-Jackson frame (GJF) is defined as illustrated in figure 4.2 [159, 167]. The starting point are the 3-momenta $\vec{p}_a, \vec{p}_b = \vec{0}, \vec{p}_c = \vec{p}_X$ and $\vec{p}_d$ of the beam particle, the target, the produced resonance X and the recoil particle in the laboratory system, respectively. First a Lorentz transformation to the rest frame of X is performed, in which the target is moving away from the origin with momentum $\vec{p}'_b$. The z_{GJ} axis is chosen parallel to the beam direction $\vec{p}'_a$ and the y_{GJ} axis defined as normal to the production plane. The latter is spanned by the direction of the 3-momentum of the target $\vec{p}'_b$ and the recoil particle $\vec{p}'_d$. Finally, the new x_{GJ} axis is determined by $x_{\mathrm{GJ}} = y_{\mathrm{GJ}} \times z_{\mathrm{GJ}}$.
Having the isobar model for the 3-body decay of the system X in mind (see figure 4.1), two important angles are usually introduced in the GJF: $\cos\theta$ denotes the cosine of the

[6] By using broad mass intervals and narrow t' bins; see section 5.4 and [60].
[7] Two of the original publications on these subjects are [162] and [163], respectively.

polar angle θ of the added momentum vector of a $\pi^+\pi^-$ pair (the isobar) and ϕ_{TY} the corresponding azimuthal angle[8]. Typical distributions of these two angles are shown for example in figure 5.40. To fully describe the phase-space kinematics of a 3-body decay, three more variables are needed. They can be chosen as the mass of the isobar $R_{\pi\pi}$ and two more angles describing the orientation of one of the decay products of the isobar. The latter is often done in a rest frame of the isobar (e. g. the helicity frame [166]).

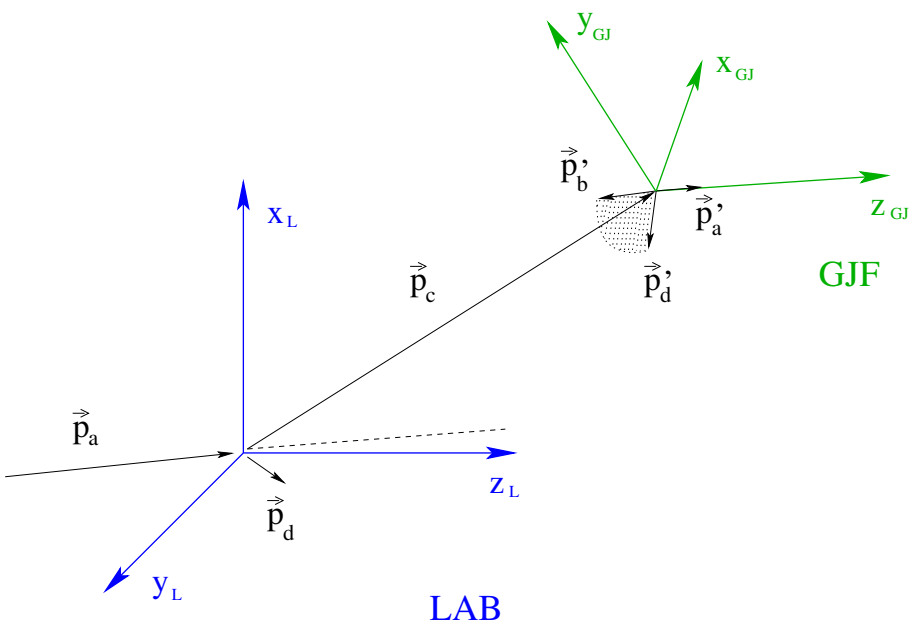

Figure 4.2: Definition of Gottfried-Jackson frame (see text).

As pointed out already in section 4.1.2, it is convenient to introduce the reflectivity basis to describe the spin projection of the produced resonance X [158]. Linear combinations of the quantum number M are formed such that the resulting amplitude is either even or odd under reflection in the production plane:

$$\psi^{\epsilon}_{JM}(\tau, m, t') = c(M)\left[\psi_{JM}(\tau, m, t') - \epsilon P(-1)^{J-M}\psi_{J(-M)}(\tau, m, t')\right] \quad , \tag{4.3}$$

where $c(M)$ is given by

$$\begin{aligned} c(M) &= 1/\sqrt{2}, \quad M > 0 \\ &= 1/2, \quad M = 0 \\ &= 0, \quad M < 0 \quad . \end{aligned}$$

The quantum number $\epsilon = \pm 1$ is called reflectivity.

[8]Named after S. B. Treiman and C.-N. Yang [168].

4.2.2 Non-Relativistic Zemach Tensors

The basic concept of this formalism is that every angular momentum j involved in a decay is represented by a symmetric and traceless[9] tensor of rank j in a 3-dim. space [169, 170]:

$$T^j_{m_1 m_2 \cdots m_j} \quad \text{with} \quad T^j_{\cdots m \cdots m' \cdots} = T^j_{\cdots m' \cdots m \cdots} \quad \text{and} \quad \sum_m T^j_{\cdots m \cdots m \cdots} = 0 \quad \text{for} \quad m_i = 1, 2, 3 \quad . \tag{4.4}$$

The coupling of angular momenta, like the spin S of a particle and its orbital angular momentum L relative to another spinless particle, is then done by multiplying the corresponding tensors together, followed by a contraction.
For $j \leq 2$ the tensors T^j are

$$j = 0: \quad T^0 = 1 \tag{4.5}$$

$$j = 1: \quad T^1_{m_1} = p_{m_1} \tag{4.6}$$

$$j = 2: \quad T^2_{m_1 m_2} = \frac{1}{2}(p_{m_1} q_{m_2} + q_{m_1} p_{m_2}) - \frac{1}{3}\delta_{m_1 m_2} \quad , \tag{4.7}$$

where $\vec{p}$ and $\vec{q}$ are two arbitrary vectors. For example the decay amplitude $a_2(1320)(\vec{p}) \to \pi^-(\vec{p}_1) + \rho(\vec{p}_{23}) \to \pi^-(\vec{p}_1) + \pi^-(\vec{p}_2) + \pi^+(\vec{p}_3)$ could be constructed from these tensors in the GJF. This is demonstrated e. g. in [166]. Two more things have to be taken into account here, namely the fact that ρ is a resonance and that the two negative pions cannot be distinguished by the experiment. The former is covered by multiplying the corresponding tensor with a Breit-Wigner function $\mathrm{BW}(w_{23})$, where w_{23} denotes the invariant mass of the $\pi^+\pi^-$ system. The second topic is respected by considering also the amplitude $a_2(1320)(\vec{p}) \to \pi^-(\vec{p}_2) + \rho(\vec{p}_{13})$ and sum over the two possibilities (Bose symmetrization).

4.3 Technique of Mass-Independent PWA

This section introduces the first step of the PWA procedure employed for the analysis presented in this thesis, namely the mass-independent fit. As discussed in section 4.1.4 it involves a partitioning of the data in bins of the invariant mass m of the produced system X. Thus the global cross-section σ introduced by equation (4.1) has to be adapted, in particular with re-defined fitting parameters (production amplitudes). For each mass bin one individual extended likelihood fit is then performed using several stages of computational processing. Special attention is paid to the possibility of multiple solutions, which cannot be distinguished based on the fit performance. The following descriptions are closely connected to the employed PWA program, which is detailed in section 4.3.3.

[9] But, in general, not covariant with respect to Lorentz transformations.

4.3.1 Mass-Independent Cross-Section and Spin Density Matrix

In a reasonably narrow m bin and t' range, the mass-independent cross-section σ_{indep} can be expressed as

$$\sigma_{\text{indep}}(\tau, m, t') = \sum_{\epsilon=\pm 1} \sum_{r=1}^{N_r} \left| \sum_i T_{ir}^{\epsilon} \, f_i^{\epsilon}(t') \, \psi_i^{\epsilon}(\tau, m) \Big/ \sqrt{\int \left| f_i^{\epsilon}(t') \right|^2 \mathrm{d}t'} \sqrt{\int \left| \psi_i^{\epsilon}(\tau, m) \right|^2 \mathrm{d}\tau} \right|^2 . \tag{4.8}$$

Identical to the global cross-section σ it contains the two non-coherent sums for the reflectivity ϵ and the rank N_r. However, this time no Breit-Wigner shapes for the system X are included, thus it is assumed that σ_{indep} is basically constant over the whole fitted mass bin. Apart from the computational necessity to subdivide the data, this has also the advantage that in equation (4.8) no assumptions about non-resonant contributions (e. g. from Deck-like backgrounds, see section 2.3.6) are contained. In order to distinguish the new production amplitudes from those used for σ, they are renamed as T_{ir}^{ϵ} in σ_{indep}. It is stressed that these complex numbers are the only fitting parameters. By dividing each decay amplitude by its normalization integral (integral over τ, but not m), its dependence on m inside each mass bin is compensated. Similarly the functions f_i^{ϵ} are normalized (integral over t'). This stabilizes the fitting procedure because now the expression $\sum_r |T_{ir}^{\epsilon}|^2$ is proportional to the number of events decaying through $\psi_i^{\epsilon}(\tau, m)$ and thus the parameters T_{ir}^{ϵ} have a compatible scale. Normalized decay amplitudes and t' functions are denoted in the following as $\bar{\psi}(\tau, m)$ and $\bar{f}(t')$, respectively.

The second summation in equation (4.8) (index r) incoherently adds several coherent cross-section terms, in which the same vectors of decay amplitudes ψ_i^{ϵ} (vector index i) are multiplied on different independent complex vectors T_{ir}^{ϵ} enumerated by $r = 1 \ldots N_r$. The latter are also referred to as production vectors. By summing over r, the spin density with maximal rank N_r can be introduced (one for each reflectivity ϵ), and σ_{indep} be rewritten accordingly:

$$\rho_{ij}^{\epsilon} = \sum_{r=1}^{N_r} T_{ir}^{\epsilon} T_{jr}^{\epsilon *} \quad ; \quad \sigma_{\text{indep}}(\tau, m, t') = \sum_{\epsilon} \sum_{ij} \rho_{ij}^{\epsilon} \, \bar{f}_i^{\epsilon}(t') \, \bar{\psi}_i^{\epsilon}(\tau, m) \, \bar{f}_j^{\epsilon *}(t') \, \bar{\psi}_j^{\epsilon *}(\tau, m) \quad . \tag{4.9}$$

As addressed in section 4.1.1, the motivation to eventually increase the rank of the spin density matrix is connected with the spin degrees of freedom of the target. It turns out that for its parameterization it is convenient to use "pseudo-orthogonal" production vectors T_{ir}^{ϵ} with the first $r-1$ elements set to zero ($T_{ir}^{\epsilon} = 0$ for $i = 1 \ldots r-1$). In addition, the first non-zero element T_{rr}^{ϵ} is taken as purely real. This approach to describe ρ_{ij}^{ϵ} is called Chung-Trueman parameterization [158].

It should be noticed that the definition of the production vectors T_{ir}^{ϵ} is sensitive to the order of the decay amplitudes ψ_i^{ϵ} used in a certain PWA model. Individual T_{ir}^{ϵ} cannot be interpreted as physics parameters, only density matrix elements obtained by summing over r according to equation (4.9) have a meaning[10]. When both the target and the recoil particles are nucleons ("high-t'" case in the presented analysis) $N_r = 2$, reflecting the

[10] This fact is sometimes formulated such that it is not possible to perform an amplitude analysis [159].

possibility to have a helicity-flip or not at the baryon vertex (cf. figure 4.1). In case of diffraction on a nucleus with spin 0 (mostly true for the "low-t'" lead data, see caption of table 3.2) the rank can be limited to $N_r = 1$, and then only coherent amplitudes are measured. However, these limitations work only in the ideal case and different values of N_r should always be tried.

4.3.2 Method of Optimization

During the mass-independent fit, the production vectors T^{ϵ}_{ir} in equation (4.8) are optimized until a dependence of σ_{indep} on the phase-space variables τ as close as possible to the real data is achieved. This is done within each mass bin and thus independent parameter sets are obtained. The optimization is performed using an extended maximum-likelihood method, by finding the maximum of the following functional over T^{ϵ}_{ir}:

$$\ln L = \sum_{n=1}^{N_{\text{events}}} \ln \sigma_{\text{indep}}(\tau_n, m_n, t'_n) - \int\int_{m_1}^{m_2}\int \sigma_{\text{indep}}(\tau, m, t')\, \text{Acc}(\tau, m, t')\, \mathrm{d}\tau\, \mathrm{d}m\, \mathrm{d}t' \quad . \tag{4.10}$$

The summation runs over all available real events in a particular mass bin (with lower and upper limit m_1 and m_2, respectively), in which σ_{indep} is assumed to be a constant function of m. The second term in equation (4.10) is the so-called normalization integral of the cross-section and takes the acceptance of the experimental setup into account[11]. It is a feature of the extended maximum-likelihood method [171], that for the finally optimized parameters this integral is equal to the number of events,

$$N_{\text{events}} = \int\int_{m_1}^{m_2}\int \sigma_{\text{indep,opt}}(\tau, m, t')\, \text{Acc}(\tau, m, t')\, \mathrm{d}\tau\, \mathrm{d}m\, \mathrm{d}t' \quad . \tag{4.11}$$

Merging equations (4.9) and (4.10), $\ln L$ can be expressed by

$$\ln L = \sum_{n=1}^{N_{\text{events}}} \ln \sum_{\epsilon}\sum_{ij} \rho^{\epsilon}_{ij}\, \bar{f}^{\epsilon}_i(t'_n)\, \bar{\psi}^{\epsilon}_i(\tau_n, m_n)\, \bar{f}^{\epsilon *}_j(t'_n)\, \bar{\psi}^{\epsilon *}_j(\tau_n, m_n) - \sum_{\epsilon}\sum_{ij} \rho^{\epsilon}_{ij}\, \text{IA}^{\epsilon}_{ij} \quad , \tag{4.12}$$

which is more suitable from the computational point of view. The integrals

$$\text{IA}^{\epsilon}_{ij} = \int\int_{m_1}^{m_2}\int \bar{f}^{\epsilon}_i(t')\, \bar{\psi}^{\epsilon}_i(\tau, m)\, \bar{f}^{\epsilon *}_j(t')\, \bar{\psi}^{\epsilon *}_j(\tau, m)\, \text{Acc}(\tau, m, t')\, \mathrm{d}\tau\, \mathrm{d}m\, \mathrm{d}t' \tag{4.13}$$

do not contain any fitting parameters and are defined independently for each mass bin.

4.3.3 PWA Program and Computational Stages

The employed mass-independent PWA program is based on the "Ascoli fitter" [172], which was developed in the 1970's. Since then it has undergone a series of tests, modifications and improvements [159] by groups from the University of Illinois (USA), the

[11] Obtained from Monte Carlo simulations independently for each mass bin; cf. section 5.3.

Joint Institute for Nuclear Research in Dubna (Russia) and the Institute for High Energy Physics in Protvino (Russia). The version which has finally been utilized for the presented analysis has been further developed and maintained by Dmitri Ryabchikov[12]. It is contained in a framework which, in addition, also offers tools to visualize the fit results, generate Monte Carlo phase-space events and perform mass-dependent fits. Compared to older versions, the current program has the Chung-Trueman spin density matrix parameterization implemented (see section 4.3.1). Its standard spin formalism is built on non-relativistic Zemach tensors (see section 4.2.2), which have been used for all fits presented in this work. However, also the helicity formalism based on Wigner D-functions (see introduction to section 4.2), including optionally relativistic corrections, has recently been implemented.

To perform a mass-independent fit, the program comprises two major computational stages, which are both optimized for speed. During the first stage, the integrals $\mathrm{IA}^{\epsilon}_{ij}$ (see equation (4.13)) are calculated for each mass bin and stored. They do not contain any fitting parameters, but use the acceptance information from simulated Monte Carlo phase space events (cf. section 5.3). Only in case of a change in the acceptance description and/or a change in the event selection they need to be recalculated[13]. The second stage is then the actual fit, where in addition to $\ln L$ also its first and second derivatives on the fitting parameters are analytically calculated during each step of the fit. This is possible due to the rather special (bi-linear) dependence of $\ln L$ on the parameters T^{ϵ}_{ir} (see equations (4.9) and (4.12)) and significantly speeds up the procedure. Of the order of 20 - 50 steps are typically needed by a fit to converge.

4.4 Output Parameters and Quality Assurance

The basic output parameters from the mass-independent PWA fit are the complex production amplitudes T^{ϵ}_{ir} and their errors for each mass bin. They define the spin density matrix according to equation (4.9), from which in turn the physics output characteristics are derived. Most prominent to mention here are the intensities and relative phases of the partial waves. A crucial step of the whole analysis procedure is the quality assurance, which tests the PWA and the acceptance description by comparing several real data distributions to those predicted by the obtained fit model.

4.4.1 Error Propagation and Treatment of Multiple Solutions

The statistical errors of the production amplitudes T^{ϵ}_{ir} are defined and propagated in the standard way[14]. First the Hesse matrix $\mathbf{H}$ with the second derivatives of the functional

[12] Institute for High Energy Physics, 142284 Protvino, Russia, Dmitri.Riabchikov@cern.ch.

[13] For the acceptance corrected number of events similar integrals with the acceptance put to one are needed; see section 4.4. They are also already calculated at this stage.

[14] It should be remembered, however, that the T^{ϵ}_{ir} are actually complex numbers, which is ignored here for simplicity. An elegant way to take this into account for the error definition and propagation is to represent complex numbers by 2×2 matrices, which is outlined for example in [173].

$\ln L$ (see equation (4.12)) on the T^{ϵ}_{ir} is calculated and evaluated at the point of optimization. Then the covariance matrix $\mathbf{V}$ is obtained by a matrix inversion $\mathbf{V} = \mathbf{H}^{-1}$ and the square root of its diagonal elements are taken as 1σ errors of the parameters T^{ϵ}_{ir}. This corresponds to a systematic variation of each parameter out of the maximum until a change in the log-likelihood of $\Delta \ln L = 0.5$ is seen. Of course, $\mathbf{V}$ contains in general not only diagonal but also non-diagonal elements, thus correlations between the different T^{ϵ}_{ir}. They are respected during the propagation of the errors to the elements of the spin density matrix (see equation (4.9)) and also during the further propagation to the errors of the derived physics observables introduced in the following sections. In general, all plots presented in chapter 5 with results from the mass-independent PWA show these statistical errors in black color. It is stressed at this point that the mass-dependent fit, which follows the mass-independent one (see section 4.5), gets only the spin density matrix elements and their errors for each mass bin forwarded, but not the correlations between them.

In principle the log-likelihood fit for one particular mass bin can converge to a local maximum, which is different from the global one corresponding to the optimum parameters T^{ϵ}_{ir}. This can especially happen for small signals (partial waves), where statistical fluctuations are high. Thus depending on the starting parameters, different solutions might be obtained, which could be equally good in terms of the maximum $\ln L$. To estimate and account for this possibility of multiple solutions, a dedicated method has been developed and integrated to the PWA program. It foresees that for each PWA model (set of partial waves) and each mass bin in fact many (~ 30) fit attempts with different random starting parameters are performed. Out of them, the best one (max. $\ln L$) is chosen as solution including the obtained statistical errors. However, if there exist within one particular mass bin one or more other solutions which differ from the best fit only by one unit of $\ln L$, the situation is reevaluated taking them into account: For each physics parameter (spin density matrix element) the two extreme values are consulted and their difference defines an additional error. This error is added to the statistical one quoted by the best fit for this parameter, and the parameter value itself is redefined as the middle value between the two extreme solutions. To distinguish the additional errors due to multiple solutions from the purely statistical ones in the results plots, they are always shown as thick green lines. Of course, the mass-dependent fit gets in such a case the new spin density matrix element together with the enlarged error.

4.4.2 Intensity and Overlap

Once the optimized cross-section σ_{indep} is available, the number of acceptance corrected events in a mass bin $[m_1, m_2]$ is obtained as

$$N_{\text{corr}} = \int \int_{m_1}^{m_2} \int \sigma_{\text{indep,opt}}(\tau, m, t')\, \mathrm{d}\tau\, \mathrm{d}m\, \mathrm{d}t' = \sum_{\epsilon} \sum_{ij} \rho^{\epsilon}_{ij}\, \mathrm{I}^{\epsilon}_{ij} \quad . \tag{4.14}$$

Different to the integrals $\mathrm{IA}^{\epsilon}_{ij}$ introduced in equation (4.13) the integrals

$$\mathrm{I}^{\epsilon}_{ij} = \int\int_{m_1}^{m_2}\int \bar{f}^{\epsilon}_{i}(t')\ \bar{\psi}^{\epsilon}_{i}(\tau, m)\ \bar{f}^{\epsilon *}_{j}(t')\ \bar{\psi}^{\epsilon *}_{j}(\tau, m)\ \mathrm{d}\tau\ \mathrm{d}m\ \mathrm{d}t' \tag{4.15}$$

do not contain the experimental acceptance, thus integrate over the whole space space with $\mathrm{Acc}(\tau, m, t') = 1$. It should be noted that all diagonal integrals ($i = j$) in equation (4.13) are equal to one, because the normalized decay amplitudes $\bar{\psi}^{\epsilon}_{i}$ and t' functions $\bar{f}^{\epsilon}_{i}$ are used. Thus N_{corr} in equation (4.14) is a sum of diagonal elements ρ^{ϵ}_{ii} and non-diagonal elements ρ^{ϵ}_{ij} multiplied on $\mathrm{I}^{\epsilon}_{ij}$. In this context the terms intensity and overlap are introduced by[15]

$$\mathrm{Intens}^{\epsilon}_{i} = \rho^{\epsilon}_{ii} \quad \text{and} \quad \mathrm{Overlap}^{\epsilon}_{ij} = 2\,\Re(\rho^{\epsilon}_{ij}\mathrm{I}^{\epsilon}_{ij}) \quad . \tag{4.16}$$

In other words the total number of acceptance corrected events in one particular mass bin is the sum of all partial wave intensities and non-zero overlaps between them.

The intensity $\mathrm{Intens}^{\epsilon}_{i}$ can also be regarded as the (acceptance corrected) number of events, which proceed through the decay channel i (with reflectivity ϵ). Combining the results from all mass bins in one histogram, $\mathrm{Intens}^{\epsilon}_{i}$ will show a Breit-Wigner shaped bump if a resonance is present in the respective partial wave. $\mathrm{Overlap}^{\epsilon}_{ij}$ can be non-zero only if the waves i and j have the same quantum numbers $J^{PC}M$ (orthogonality of the decay amplitudes). However, $\mathrm{Overlap}^{\epsilon}_{ij} = 0$ doesn't imply that the waves i and j do not interfere, because interference is expressed by the non-diagonal elements of ρ^{ϵ}_{ij} alone without any multiplication on $\mathrm{I}^{\epsilon}_{ij}$ (cf. section 4.4.3).

4.4.3 Interference, Coherence and Phase Motion

The interference between two partial waves i and j is defined by the non-diagonal complex spin density matrix element ρ^{ϵ}_{ij}. Compared to the intensity $\mathrm{Intens}^{\epsilon}_{i}$ introduced in section 4.4.2, which is one real number, ρ^{ϵ}_{ij} contains, of course, two real numbers ($\Re(\rho^{\epsilon}_{ij})$ and $\Im(\rho^{\epsilon}_{ij})$) and might therefore be even more important concerning the prove of existence of a resonance. It is stressed again that interference is not the same as overlap and that only the latter contributes to the total number of events used in the fit. Usually the coherence $\mathrm{Coh}^{\epsilon}_{ij}$ and the phase ϕ^{ϵ}_{ij} are displayed instead of $\Re(\rho^{\epsilon}_{ij})$ and $\Im(\rho^{\epsilon}_{ij})$[16], which are derived quantities defined by

$$\rho^{\epsilon}_{ij} = r^{\epsilon}_{ij}\, e^{i\phi^{\epsilon}_{ij}} \quad \text{and} \quad \mathrm{Coh}^{\epsilon}_{ij} = \frac{r^{\epsilon}_{ij}}{\sqrt{\rho^{\epsilon}_{ii}\rho^{\epsilon}_{jj}}} = \frac{\sqrt{\Re(\rho^{\epsilon}_{ij})^2 + \Im(\rho^{\epsilon}_{ij})^2}}{\mathrm{Intens}^{\epsilon}_{i}\ \mathrm{Intens}^{\epsilon}_{j}} \quad . \tag{4.17}$$

If the results from the fits in different 3π mass bins are combined in one histogram, the phase between two partial waves i and j can exhibit a characteristic dependence on m. More precisely, if one of the waves contains a resonance X with mass m_0 and width Γ_0,

[15] Note that $\rho^{\epsilon}_{ij} = \rho^{\epsilon *}_{ji}$ and, in general, $z + z^* = 2\,\Re(z)$ for $z \in \mathbb{C}$.

[16] For illustration reasons; however, for the mass-dependent fit (see section 4.5) $\Re(\rho^{\epsilon}_{ij})$ and $\Im(\rho^{\epsilon}_{ij})$ are used.

the phase will show a motion over 180° starting at $m_0 - \Gamma_0$, turning at m_0 and ending at $m_0 + \Gamma_0$. Usually the wave j would also contain a resonance X' itself and therefore the phase motion might be reduced or even completely compensated if X and X' overlap in mass. In any case a defined phase is a prerequisite for a possible existence of a resonance. An important cross-check is also to look at the degree of coherence $\mathrm{Coh}_{ij}^{\epsilon}$ between the amplitudes i and j, which should be close to one in the mass range of interest. This is particularly important in case of a rank $N_r > 1$, since then coherence is not self-evident.

4.4.4 Spin Totals

Adding all intensities $\mathrm{Intens}_i^{\epsilon}$ and non-zero overlaps $\mathrm{Overlap}_{ij}^{\epsilon}$ (see equation (4.16)) with the same quantum numbers J^{PC}, M and/or ϵ provides the spin-total intensities, the so-called spin-totals. Their advantage is that they have smaller statistical errors compared to the individual intensities, and therefore resonances might be better pronounced in them. In addition, the ratio $J^{PC}M^{\epsilon}[\text{isobar } \pi]L$ to $J^{PC}M^{\epsilon}$-total is sometimes the best way to estimate the fraction of $X \to [\text{isobar } \pi]$ to $X \to 3\pi$, where X is a dominant resonance in the waves with quantum numbers J^{PC}. In case of the presented analysis it has been particularly interesting to compare the $M = 0$ with the $M = 1$ spin-totals for certain J^{PC} states. In general positive and negative reflectivities ϵ have to be kept separately, because they correspond to different production mechanisms (see section 4.1.2).

4.4.5 Quality Assurance

After a mass-independent PWA based on a certain model (set of partial waves) has been performed, the obvious question is about the quality of the fit. One approach is to look at the log-likelihood $\ln L$ and compare it to fits using other models. However, since in fact for each mass bin a separate fit is done, it is likely to be that the results from different bins might lead to different conclusions[17]. A more global method is based on the comparison of certain kinematical distributions, once obtained from the real data and once predicted by the optimized cross-sections for all mass bins (equation (4.8)). Since it is this method which has been employed for the presented analysis, it is described in detail in the following.

The starting point are the simulated phase space events, which contain the information about the experimental acceptance (cf. section 5.3). They comprise flat distributions w. r. t. the five phase-space variables τ in the sense that no resonances are present. In other words they do not contain any structures in the angular distributions like for example in $\cos\theta_{GJ}$ or ϕ_{TY} (see section 4.2.1). The idea is now to sum over all available Monte Carlo events N_{MC}, calculate $\sigma_{\text{indep,opt}}$ and Acc for each of them and weight the events accordingly. Of course, depending on m, different cross-sections $\sigma_{\text{indep,opt}}$ have to be used. If then some distribution is histogrammed from the weighted events and normalized to N_{MC}, it can be compared to the corresponding real data distribution. The first distribution to check is naturally the 3π mass with the binning of the PWA fit. This serves as

[17] The possibility and treatment of multiple solutions within one mass bin is discussed in section 4.4.1.

a prove of principle of the method, because in this case the prediction and the real data have to have the same shape by definition[18].

It should be noted that this method always tests the PWA model and the acceptance description at the same time. The reason is that the optimized production vectors T^{ϵ}_{ir} in $\sigma_{\text{indep,opt}}$ are obtained taking the acceptance into account. Thus a poor acceptance description could in the worst case pull the fit into a wrong direction, which is of course also true for a poor PWA model. The prediction based on phase-space events weighted with both $\sigma_{\text{indep,opt}}$ and Acc shows therefore how the data are described by the PWA model in combination with the acceptance model.

4.5 Mass-Dependent Fit

The second step of the PWA method used for this thesis is the so-called mass-dependent fit, which is part of the software framework introduced in section 4.3.3. It is performed after the mass-independent analysis using the results obtained there for each mass bin. More precisely the spin density matrix elements ρ^{ϵ}_{ij} and their errors are considered (cf. sections 4.3.1 and 4.4.1). Coming back to the full, in particular mass-dependent cross-section introduced by equation (4.1), the goal is now to determine the production amplitudes C^{ϵ}_{ikr} as well as the masses $M_{0\,k}$ and widths $\Gamma_{0\,k}$ for all produced resonances. This is achieved by fitting a subset of the spin density matrix, as a function of the 3π mass m, including especially those ρ^{ϵ}_{ij} which express a strong resonating behavior[19]. As a preparatory step, the spin density matrix elements have to be decomposed in terms of Breit-Wigner and background functions. Based on this the method of least-squares (χ^2 fit) is then applied to find the model which best describes the data, in other words to obtain the parameters C^{ϵ}_{ikr}, $M_{0\,k}$ and $\Gamma_{0\,k}$ and their uncertainties.

4.5.1 Decomposition of the Spin Density Matrix

By comparing equations (4.9) and (4.1) the spin density matrix can be expressed through Breit-Wigner and background functions (both denoted as $\text{BW}_k(m)$) as[20]

$$\rho^{\epsilon}_{ij} = \sum_{r=1}^{N_r} \left(\sum_k C^{\epsilon}_{ikr} \text{BW}_k(m) \sqrt{\int |\psi^{\epsilon}_i(\tau)|^2 \mathrm{d}\tau} \right) \left(\sum_l C^{\epsilon}_{jlr} \text{BW}_l(m) \sqrt{\int |\psi^{\epsilon}_j(\tau)|^2 \mathrm{d}\tau} \right)^* \quad . \tag{4.18}$$

To be consistent with the mass-independent fit the same rank N_r is used in equation (4.18), and also the Chung-Trueman parameterization is respected for the parameters C_{ikr}. As mentioned already in section 4.1.4 several BW functions might be needed to describe one partial wave intensity ρ^{ϵ}_{ii} and its interferences ρ^{ϵ}_{ij}. On the other hand the same BW_k can be used for different partial waves i, reflecting different decay channels of one resonance. In general it is also possible to add incoherent k terms (non-interfering

[18] Because σ_{indep} doesn't depend on m within one PWA mass bin.

[19] How this subset has actually been chosen for the presented analysis is discussed in detail in section 5.5.1.

[20] The functions $f^{\epsilon}_i(t')$ are dropped in the following because they are not used in the mass-dependent fit.

resonances) in equation (4.18), however, this has never been done for any of the fits presented later. In case of resonances with known branching ratios, dynamic width BW functions are employed including Blatt-Weisskopf barrier factors (see section 2.1.2). Otherwise constant width BWs are used. The program furthermore offers the possibility to multiply an overall mass-dependence factor on each production amplitude C_{ikr}. Finally, the background is parameterized as $e^{-\alpha p^2}$ [60, 174], where p is the break-up momentum of a given decay of the resonance X (point 1 in figure 4.1) and α is a fitted parameter.

4.5.2 Fitting Method and Output

The mass-dependent fit is performed by employing the χ^2-method, which is applied based on equation (4.18). As a preparation for the fit, first of all the elements of the spin density matrix are selected, which are to be analyzed. In other words partial wave intensities and interferences between them are chosen. Furthermore, the fit model is specified by selecting a set of BW_k and eventually also background functions. From the beginning on it is fixed which ones are used to describe a particular partial wave i, thus only certain parameters C_{ikr} are kept as non-zero and are released[21]. For background functions as well as dynamic width BWs, the parameters of the involved isobars in the particular decay channels are needed to calculate the respective break-up momenta (cf. section 4.5.1). If in the latter case more than one decay channel is considered, also the corresponding branching ratios are fixed. Since the right hand side of equation (4.18) is a continuous function of m, it has to be specified how many interpolation points within each mass bin are used for the (numerical) calculation of the χ^2. Apart from some dedicated studies, however, usually just one point in the middle of the mass bin has been used. Finally, some starting values for all resonances are provided to the fit. All the settings, which have been used for the results shown in section 5.5, can be found at the beginning of that section.

As a minimizer of the assembled χ^2-function the MINUIT package is used [175]. To get reasonable starting parameters for the parameters C_{ikr}, the BW masses and widths are kept fixed first and the χ^2-function is minimized for the C_{ikr} only[22]. In a next step also the BW parameters are then released and MIGRAD is called allowing for $\sim 40\,000$ steps. Since depending on the convergence behavior MIGRAD doesn't necessarily involve the calculation of the Hesse matrix (second derivatives) during all steps, after a successful convergence HESSE is always called. From its output the symmetric statistical errors on the masses and widths are defined. It has been checked once that no significant asymmetric errors are present by comparing to MINOS.

[21] More precisely one should distinguish between the real and imaginary parts of the production amplitudes C_{ikr}, which comprise independent fit parameters.

[22] The default procedure of MINUIT is to use MIGRAD, eventually supported by SIMPLEX.

Chapter 5

Analysis of $\pi^-\pi^-\pi^+$ Events from Diffractive Dissociation

In this chapter the results from an analysis of $\pi^-\pi^-\pi^+$ final state events, diffractively produced at COMPASS (see section 2.3 and chapter 3), are presented. More precisely, the dissociation of beam pions into mesons has been investigated, including the search for the spin-exotic states. First the analyzed data set and the event selection are presented in section 5.1. At this level a fundamental distinction within the analysis is introduced, splitting up events depending on their momentum transfers from the target to the projectile. Based on this, the obtained $\pi^-\pi^-\pi^+$ mass spectra and Dalitz plots are shown (section 5.2), exhibiting already the dominantly produced resonances. Also background sources are discussed.

The actual decomposition of the data into events with produced resonances, described by Breit-Wigner parameterizations, is the task of the Partial Wave Analysis (PWA). Since it requires an acceptance correction, Monte Carlo simulations have been performed. They are described in section 5.3, proving the excellent acceptance and resolution of COMPASS for $\pi^-\pi^-\pi^+$ events. The PWA itself has been carried out in two steps as described in chapter 4: First a mass-independent PWA has been performed, followed by a mass-dependent fit from which the resonance properties have been determined. The results are displayed in sections 5.4 and 5.5. In order to be able to estimate systematic errors, several tests have been done, which are summarized in section 5.6. In addition, the possibility of leakage to the exotic 1^{-+} wave has been studied (see section 5.7). The chapter concludes with a very first look to events with five charged pions in the final state.

5.1 Data Set and Event Selection

The results of the PWA presented in this work are based on a data sample, which was recorded by the COMPASS collaboration in 2004 using a 190 GeV/c π^- beam on lead targets (see section 3.2). Within a few days of data taking, more than four million of exclusive $\pi^-\pi^-\pi^+$ events were recorded, covering a range in momentum transfer t' from 0 to a few GeV$^2/c^2$. Thus meson production can be studied in very different regimes. This

section describes step by step how the events have been selected and demonstrates the applied cuts. First a number of basic or loose cuts have been applied, to reduce the data set to a level such that parallel computing was not necessary anymore. This reduction is called "step 1" in the following. Afterwards the cuts have been tightened and the data eventually divided into intervals in momentum transfer t' ("step 2" followed by "step 3a" or "step 3b"). In particular the definition of exclusivity and the calculation of t' during "step 3b" involve some subtleties. Possible background to the analysis, which cannot be rejected by the cuts, is discussed. At the end of this section, the statistics of the selection process is summarized in tables 5.1 - 5.3.

5.1.1 Analyzed Data Set

From the about three weeks of data taking with a π^- beam at COMPASS in 2004 (27.10 - 15.11) less then three days have in the end been considered for the analysis. During this time the diffractive trigger was active and lead targets were inserted (see section 3.2). In fact the data belong to two different periods, one with a 1.6 mm thick[1] and one with a segmented 2+1 mm thick target installed. In between there was a break of six days, where other targets and beams were used. In many regards the data from the two periods are equivalent, just a few things were set up differently and had to be taken into account during the analysis. Whenever relevant this will be mentioned in the following sections, but in general the data have been combined. The first period (15 runs with numbers 42820-42840) thereby accounts for only $\sim$ 15% of the total statistics. This is partly due to the fact that the online filter (see section 3.3.2) was not yet switched on for these runs and therefore less triggered events survive the offline analysis cuts. Thus the majority of the finally analyzed $\pi^-\pi^-\pi^+$ events were recorded during the second period (58 runs with numbers 43191-43323), corresponding to data taking with the segmented target. Taking this into account, one arrives to the remarkable fact that the whole statistics of the presented analysis was recorded by COMPASS in only about two days.

The starting point of the presented analysis have been mDST files, which were produced centrally at CERN from November 2005 to April 2006 (see section 3.3.3 and appendix A). The files belonging to the two previously introduced run periods were copied from the CERN data storage to local discs at TU München (Physik-Department, E18), filtered and carefully checked to be unique. During the filtering, events without a primary vertex or without at least one track in the silicon stations approaching the target were sorted out. A total of 363 718 272 events remained after this step and have been further processed.

[1] Recently it has been shown [176] that this particular target was replaced without further notice by a 3 mm thick one during the beam time (same position and material, starting from run number 42743). This doesn't effect the event selection at all, however, the Monte Carlo simulations are slightly wrong for the corresponding 15% of the data (see section 5.3). To be on the save side, this effect has been included in the systematic error estimations (see section 5.6). In the following the terminology "1.6 mm" target will still be used to avoid confusions.

5.1.2 Trigger and Online Filter Requirements

The most basic event selection criterion is the requirement of the diffractive trigger bit set in the trigger mask[2]. This has not been demanded exclusively, but 3π events which were selected only by others than the diffractive trigger have been rejected. The reason is that in those cases the acceptance corrections for the PWA would have been much more complicated, especially if detectors like the electromagnetic calorimeter with its high energy threshold were included in the trigger. The diffractive trigger instead can be basically regarded as "minimum bias" in the sense that it almost did not cut into the acceptance of the 3π detection (cf. section 5.3). Its requirement has naturally been the first cut applied within the "step 1" reduction (see also table 5.1).

Following the logics of data taking, the next test should have been to look into the online filter information. As explained in section 3.3.2 the online filter checked for a certain truncated hit multiplicity n in the silicon stations after the target and rejected events with $n < 6$. The Monte Carlo studies confirm that, similar to the diffractive trigger, the filter acted basically with a "minimum bias" as intended. During the 1.6 mm period, however, it was still being tuned and therefore not active. This is why no online filter information has been taken into account for this period. Although in a stable configuration during the 2+1 mm period, the filter was also not always active then, but sometimes in "mark-only" mode[3]. To homogenize the 2+1 mm data set, the events from the corresponding runs have been subjected to an offline filtering using the "mark-only" information. Since it was not clear from the beginning on how this action will perform, it has been decided not to do it during "step 1" but shift it to a later stage of the selection process ("step 2", see table 5.2). In the Monte Carlo simulations both periods have been treated according to the respective real data conditions.

5.1.3 Reconstruction of Primary Vertex and Cut on its z Position

The diffractive dissociation of the beam particle as well as all subsequent resonance decays are strong interaction processes. Therefore all involved intermediate states have lifetimes of the order of 10^{-21} - 10^{-24} s, making it impossible for the tracking system to resolve secondary vertices. The three charged final state pions in contrast can be regarded as stable within the COMPASS spectrometer, because of their weak interaction decays. Thus the event signature for the presented analysis is simply a primary vertex with one incoming and three outgoing charged particles (charge $-, -, +$). During "step 1" of the selection it has been checked that exactly one such primary vertex within the target area (-309 ± 10 cm) exists. In principal it could have happened that within one trigger window two interactions took place, but for such events the risk of wrong combinatorics is high and also they are not included in the simulations. The efficiency of the vertexing part of the COMPASS reconstruction has been verified in a dedicated study. Only $\sim 5\%$ additional exclusive 3π events could be found, most of them ($\sim 50\%$) with tracks falling outside of the acceptance of the silicon detectors.

[2]Bitmap holding for each event the information of which trigger(s) fired.

[3]In this mode events with $n < 6$ were not rejected, but marked that they should have been.

It should be noticed that all four reconstructed particles could have been assumed only to be pions in the following. Neither for the beam line nor for the spectrometer itself a particle identification (PID) was available during the 2004 pilot hadron run (see section 3.2). Thus some of the events could be in reality composed of e. g. $\pi^-e^-e^+$ or $\pi^-K^-K^+$. The first case is not particularly dangerous for the PWA, because electrons and positrons undergo only electroweak interactions and are therefore much suppressed in resonance decays. Of course, an e^+e^- pair can also result from a γ conversion in some material, but in such a case no angular correlations are established. More thoughts have to be spent on the contamination by $\pi^-K^-K^+$ final states, for more details see section 5.2.4.

During "step 2" the cut on the primary vertex z position has been further tightened. This is less trivial than it might appear, because two competing optimizations enter. First of all this cut is supposed to improve the signal-to-background ratio for the PWA by rejecting e. g. $K^- \rightarrow \pi^-\pi^-\pi^+$ decays , which can occur everywhere along the beam (z) axis from the $\sim 2\%$ kaons present in the COMPASS beam (cf. section 5.2.3). Also vertices far away from the nominal target positions have to be discarded, because the whole event might be poorly reconstructed or even fake. On the other hand, the Monte Carlo simulations (see section 5.3) clearly showed that, since it suppresses small ($< 1\,\mathrm{GeV}/c^2$) 3π masses, this cut is the most critical one concerning the acceptance. To tune the limits of the vertex cut, therefore only events with low momentum transfer (later in this section introduced as "low-t'" data) have been considered, since there the acceptance effect is largest.

From the first data taking period, the position of the 1.6 mm target has been determined (-310.169 cm) as the mean of a fit of the vertex z position distribution with a single Gaussian from -325 cm to -295 cm. The obtained σ is 0.478 cm and has served as a scale for the cut optimization. Similarly the 2+1 mm target data have been treated, but in this case two Gaussians with disjoint ranges have been applied (division at -309 cm). Their means are -314.490 cm and -304.547 cm and the corresponding standard deviations 0.551 cm and 0.402 cm, respectively. From these values, finally, $\pm 4\sigma$ cuts around the mean target positions have been defined. As mentioned above, these limits worked out from the "low-t'" data have been used for the full t' range. They are demonstrated in figure 5.1, where for both target periods the z position of the primary vertices is shown in combination with the applied cuts. Both distributions have been obtained after "step 3a" (see below), just the cut on the vertex position has not been tightened.

5.1.4 Selection of t' Ranges and Definition of Exclusivity

As stressed in section 4.1.1 exclusive events are a prerequisite for the PWA. This is to be understood in the sense that the target (recoil) stays intact throughout the whole reaction without being excited or even destroyed. The kinetic energy of the recoil particle added up to the total energy of the three pions should then be equal to the beam energy. However, during the 2004 COMPASS pilot hadron run neither the beam energy was measured on an event by event basis nor was there a recoil detector present (see section 3.2). Only the direction of the incoming beam particle and thus the scattering angle θ was measured precisely by the silicon detectors around the target.

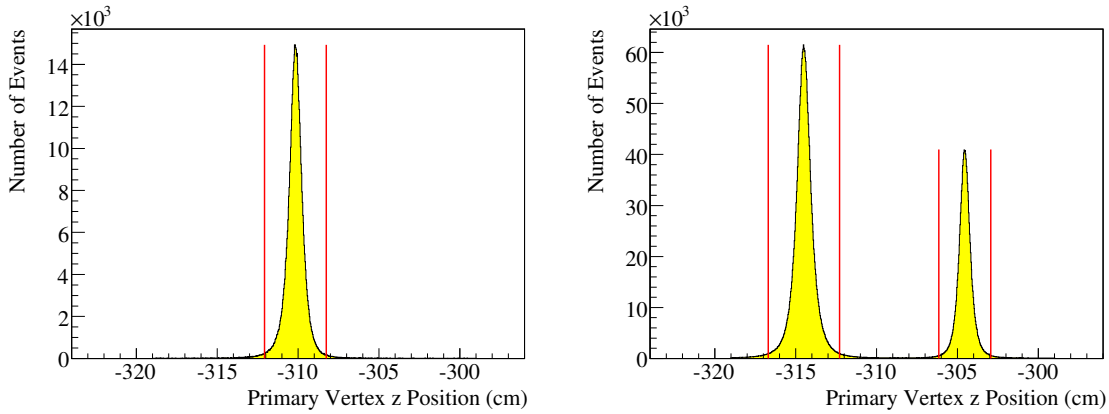

Figure 5.1: Distribution of primary vertices along z axis; $\pm 4\sigma$ cut marked by red lines. Left: 1.6 mm lead target from first data taking period. Right: 2+1 mm lead target.

In order to still be able to perform an exclusivity cut and calculate the momentum transfer t', two procedures have been established. The first one is a simplified approach, where the energy of the beam particle E_a is just set to be equal to the measured total energy of the three final state pions E_c (see figure 2.3). t' is then calculated according to equation (2.13) and the exclusivity cut[4] is defined by $185(159) < E_a = E_c < 193(219)$ GeV. This procedure works already remarkably well, the smaller t' the better. It has been employed during the selection stage "step 3a", which doesn't distinguish yet between different t' intervals. Figure 5.2 shows the corresponding overall t' distribution. It vanishes at $\sim 5\,\mathrm{GeV}^2/c^2$, which translates to a scattering angle of ~ 14 mrad for the total 3π momentum in the laboratory frame. The exclusivity cut based on the simplified approach is visualized in figure 5.3. Apparently, the exclusivity peak has in addition to the nominal 190 GeV beam energy a shoulder at about 187 GeV. As discussed in section 3.2 this has been traced back to a problem in the beam line between the CERN SPS and the COMPASS hall. Thus the shoulder was a feature of the 2004 beam and the respective events have been treated as the nominal ones. Consistently, the simulations have taken the true beam energy profile into account (see appendix C.1).

The second procedure to calculate E_a is more precise in the sense that it is based on the assumption that the target (recoil) mass stays the same during the whole diffractive process. Starting from this point, an expression for E_a can be derived, which contains the precisely measured quantities θ and p_c. It can be found together with the underlying calculations in appendix B. In contrast to the approach of "step 3a", a target mass has to be specified here, which is in general not known. While it is safe for events with $t' < 10^{-2}\,\mathrm{GeV}^2/c^2$ to assume coherent scattering off the lead nuclei as a whole (cf. section 2.3.2), for events with larger t' values the situation is not so clear. At some point only scattering off individual nucleons should take place. Comparing to other experiments which used either also nuclear targets (VES[5] [109]) or proton targets (BNL-E852 [113], see figure 5.9) it has

[4]The values in brackets denote the loose cut already applied during "step 1" (see table 5.1).

[5]This collaboration was actually facing exactly the same problem during their analysis and developed a

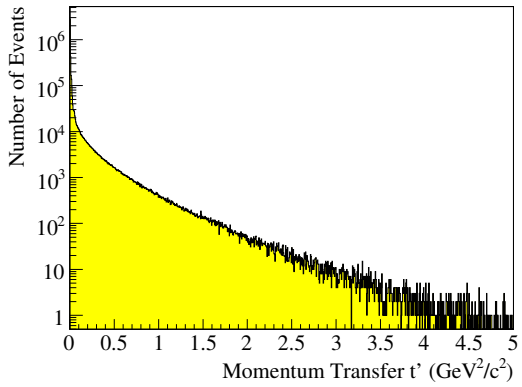

Figure 5.2: Overall t' distribution, obtained after "step 3a" (see text); logarithmic scale.

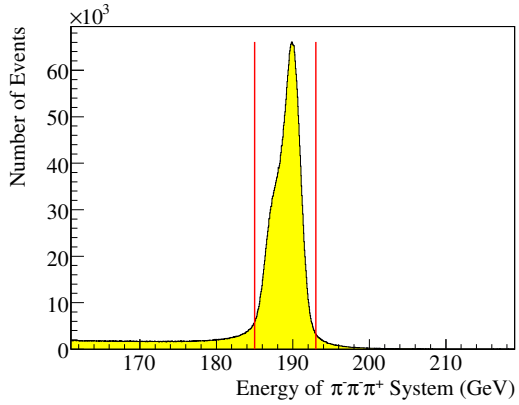

Figure 5.3: Exclusivity cut based on the total energy of the three final state pions ("step 3a"); no t' selection.

been decided to use a proton mass for the target for $t' > 0.1\,\mathrm{GeV}^2/c^2$. For the intermediate range from $10^{-2}\,\mathrm{GeV}^2/c^2$ to $0.1\,\mathrm{GeV}^2/c^2$ still a lead mass has been used. Thus this more precise procedure to calculate E_a and t' (according now to equation (2.12)) requires a partitioning of the data into t' ranges. This would have been done anyway for the PWA, since also the resonance production is t' dependent and it is better not to fit all data together (cf. section 4.1.4).

The selection of t' ranges in combination with the precise exclusivity cut is called "step 3b". In total five t' ranges have been defined, which are described in the following. For the first three a lead mass has been used for the target, while for the other two a proton mass has been assumed. The first range ($t' < 10^{-3}\,\mathrm{GeV}^2/c^2$) corresponds to momentum transfers, which are zero within the resolution of the experiment (see section 5.3.2). Here probably not only strong interaction events are present, but also mesons produced in photo-production. In addition, the reaction production plane is poorly defined for these events (see section 4.2). Therefore this range has not been analyzed in detail by means of a PWA[6]. The second range ($10^{-3}\,\mathrm{GeV}^2/c^2 < t' < 10^{-2}\,\mathrm{GeV}^2/c^2$), called "low-$t'$", corresponds to the coherent scattering of the beam pions off the lead nuclei and has been analyzed in a dedicated PWA fit. The beam energy distribution shown in figure 5.4 demonstrates how little background this "low-t'" data sample has and how well pronounced the exclusivity peak is. For the subsequent t' range ($10^{-2}\,\mathrm{GeV}^2/c^2 < t' < 10^{-1}\,\mathrm{GeV}^2/c^2$) it is not clear whether the target (recoil) is dominantly a lead nucleus or a nucleon and, following the discussions of sections 4.1.1 and 4.3, it is not well-defined which rank to use for the PWA. It has therefore been excluded from the analysis so far.

numerical solver for the kinematics. Their program was employed to cross-check the formula presented in appendix B and it gave consistent results.

[6]However, a preliminary PWA of these data has brought forward some $a_2(1320)$ mesons, which cannot be produced strongly at such small momentum transfers. If this is established, the radiative decay width of a_2 would be accessible, which is a poorly known quantity [177]; see also section 5.2.1.

Figure 5.5 presents the combined t' distribution for the three ranges using a lead mass, thus for $t' < 0.1\,\mathrm{GeV}^2/c^2$. A characteristic pattern is exhibited and the diffractive nature of the pion dissociation process becomes apparent[7]. From the steep slope $-b = 390 \pm 2\,(\mathrm{GeV}^2/c^2)^{-1}$ of the distribution at small t', the radius of the "black disc" (the strong interaction or lead nucleus radius, see also section 2.3.2) can be estimated using the relation $R = 0.3\sqrt{-b}$ fm [85]. The result is $R = (5.92 \pm 0.02)$ fm, which agrees within $10 - 20\%$ with the standard estimate $r_0\sqrt[3]{A}$ (with $A = 207$ and $r_0 = 1.1$-1.3 fm).

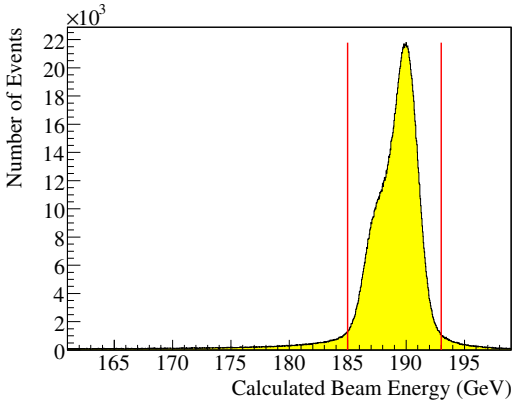

Figure 5.4: Beam energy spectrum with exclusivity peak for "low-t'" data ("step 3b"); cut shown in red color.

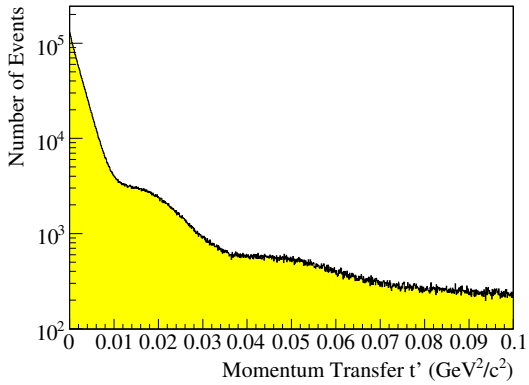

Figure 5.5: 4-momentum transfer t' for diffraction of beam pions on lead nuclei; logarithmic scale.

The so-called "high-t'" range from $0.1\,\mathrm{GeV}^2/c^2$ to $1.0\,\mathrm{GeV}^2/c^2$ has been subject to most of the performed PWA fits presented in this thesis. It is in this regime where candidates for spin exotic states in the $\pi^-\pi^-\pi^+$ channel have been reported in the past [110, 113]. Figure 5.6 shows the corresponding t' distribution assuming scattering of the beam pions off individual nucleons inside the lead nuclei. Since there are more than one exponential functions present in this histogram, an overall slope parameter has been estimated from a weighted sum of the individual slopes. A value for $-b$ of about $5\,(\mathrm{GeV}^2/c^2)^{-1}$ has been obtained, which translates into a radius of about 0.7 fm. This is roughly consistent with the assumption of a "nucleon black disc", but the estimate should be taken with care in this case. The reason is that a nucleon is not orders of magnitudes larger than a pion and therefore the pion form factor enters as well.

For the "high-t'" data set the exclusivity cut has been applied according to figure 5.7. Apparently there is much more non-exclusive background present compared to the "low-t'" data and also the exclusivity peak is broadened. The dominant part of the background are probably events with four or even five particles in the final state. For example one or two neutral pions could be present, which have in general not been searched for in this analysis. Those below the exclusivity peak would be anyway very difficult to detect since they have almost no energy. Also two charged pions could have escaped unde-

[7] Similar distributions including other target materials can be found in [178].

tected. In all such cases one or more particles are completely missing and therefore not only the energy balance is wrong but also the momentum transfer t' is systematically calculated to be too high[8]. A further disturbance at "high-t'" could arise from possible nucleon excitations to N^* resonances, a process which is introduced in section 2.3.5 as double dissociation. This would result in a small (several hundred MeV) shift to lower values due to an undetected soft pion from the N^* decay. Also the broadening of the exclusivity peak could be explained because several N^* resonances with different masses exist [38]. In contrast to the above described background, however, the meson vertex (upper part in figure 4.1) is not affected in such cases, just some energy is missing for the total balance. Thus all underlying assumptions of the PWA are valid (see section 4.1) and the standard techniques can be applied. The last (fifth) t' range collects all events with momentum transfers higher than 1 GeV$^2/c^2$ and is already dominated by background. It has therefore not been studied in more detail.

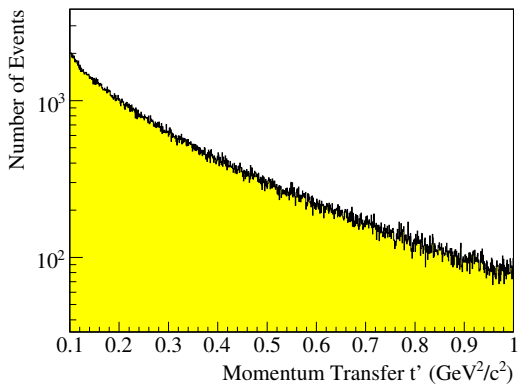

Figure 5.6: 4-momentum transfer t' for diffraction of beam pions on single nucleons within the lead target; logarithmic scale.

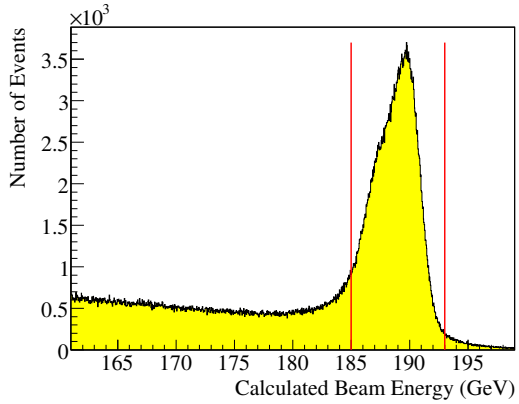

Figure 5.7: Beam energy spectrum with exclusivity peak for "high-t'" data ("step 3b"); cut shown in red color.

5.1.5 Summary of Selection Statistics

In this section the statistics of the event selection is presented. It is distinguished between the three introduced "steps", which are summarized again in the following. During "step 1" (table 5.1) the diffractive trigger cut has been applied first, followed by the requirement of one primary vertex within the target area ($|z + 309| < 10$ cm). Furthermore, the correct charge of the outgoing pions has been tested. Also a loose exclusivity cut based on the simplified approach ($|E_{3\pi} - 189| < 30$ GeV) has been applied. During the subsequent "step 2" (table 5.2) the online filter cut (see section 5.1.2) has been added and the cut on the vertex z position has been tightened according to section 5.1.3. While "step 1" and

[8]This is of course connected to the fact that the "low-t'" spectrum shown in figure 5.4 is so clean. In general, t' distributions are only shown after the exclusivity cut has been applied.

"step 2" have been always performed first, "step 3a" and "step 3b" are alternatives to each other. In "step 3a" no selection of the momentum transfer t' has been performed and the exclusivity cut has been tightened still based on the total energy of the three final state pions ($|E_{3\pi} - 189| < 4\,\text{GeV}$). During "step 3b" instead the five introduced t' ranges (see section 5.1.4) have been defined and the precise exclusivity cut based on the recalculated beam energy E_a has been performed ($|E_a - 189| < 4\,\text{GeV}$).

All PWA fits presented in this work are based on either the 427 897 "high-t'" events or the 2 130 556 "low-t'" events, both obtained after "step 3b" (table 5.3). It should be noticed that these numbers have been further decreased within the PWA program to 417 028 and 2 098 077, respectively. This is mostly due to the fact that only events with $\pi^-\pi^-\pi^+$ masses from $0.5\,\text{GeV}/c^2$ to $2.5\,\text{GeV}/c^2$ have finally been fitted. Also a small spike at ± 1 in the $\cos\theta$ distributions has been cut, where θ is in the $\pi^-\pi^-\pi^+$ rest frame the angle between a π^- and the recoil or the π^+ and the recoil, respectively (see figure 5.41, for which the cut has already been applied).

Requirement	Remaining Events (absolute number)	Remaining Events (percentage)	Reduction Factor (percentage)
Processed events	363 718 272	100.00%	0.00%
Diffractive trigger	87 668 309	24.10%	75.90%
One primary vertex	82 163 497	22.59%	6.28%
3 outgoing tracks	22 994 116	6.32%	72.01%
$(\|z + 309\| < 10)$ cm	13 386 779	3.68%	41.78%
Correct charge (-,-,+)	10 903 461	3.00%	18.55%
$(\|E_{3\pi} - 189\| < 30)$ GeV	5 599 550	1.54%	48.64%

Table 5.1: Selection statistics for "step 1". Absolute number and percentage of events remaining after the respective cuts shown; reduction factors (last column) are w. r. t. the previous cut.

Requirement	Remaining Events (absolute number)	Remaining Events (percentage)	Reduction Factor (percentage)
Online filter cut for 2+1 mm runs	5 574 339	1.53%	0.45%
$\pm 4\sigma$ cut around target z positions	5 417 724	1.48%	2.81%

Table 5.2: Selection statistics for "step 2", performed after "step 1" (see table 5.1). Absolute number and percentage of events remaining after the respective cuts shown; reduction factors (last column) are w. r. t. the previous cut.

t' interval (GeV$^2/c^2$)	Remaining Events (absolute number)	Remaining Events (percentage)	Reduction Factor (percentage)
"Step 3a", $(\lvert E_{3\pi} - 189\rvert < 4)$ GeV			
all t'	4 388 547	1.21%	19.00%
"Step 3b", $(\lvert E_a - 189\rvert < 4)$ GeV			
$0 \leq t' < 10^{-3}$	1 053 381	0.29%	80.56%
$10^{-3} \leq t' < 10^{-2}$	2 130 556	0.59%	60.67%
$10^{-2} \leq t' < 10^{-1}$	743 715	0.20%	86.27%
$10^{-1} \leq t' < 1$	427 897	0.12%	92.10%
$1 \leq t' < 10$	43 198	0.01%	99.20%

Table 5.3: Statistics for the two alternative selections "step 3a" and "step 3b", in both cases after "step 1" and "step 2" have already been applied (see tables 5.1 and 5.2). Absolute number and percentage of events remaining after the respective cuts shown; reduction factors (last column) are w. r. t. the previous cut.

5.2 Mass Spectra, Dalitz Plots and Kaon Background

After the final event selection ("step 3b", see section 5.1.5) has been performed, it is instructive to look at $\pi^-\pi^-\pi^+$ invariant mass spectra and Dalitz plots before actually performing a PWA fit. By this the dominantly produced resonances and eventually even their main decay channels already become apparent, which is a valuable input for the PWA and has to be reflected by the fit. The corresponding distributions are presented in this section, especially for the "high-t'" data set. At momentum transfers $t' \approx 0$, an interesting consistency check within the analysis is to find and study the small K^- signal from beam kaons decaying into three charged pions. Since these events have in reality $t' = 0$ and also the natural width of K^- is practically zero, both the t' and the mass resolution of COMPASS can be estimated and compared to the simulations. At the end of this section, backgrounds to the analysis involving kaons in the final state are discussed.

5.2.1 $\pi^-\pi^-\pi^+$ Mass Spectra for Different t' Ranges

Figure 5.8 presents the invariant mass of the $\pi^-\pi^-\pi^+$ system. Shown are the data without any t' selection (yellow color, "step 3a") as well as the data corresponding to the five t' ranges introduced in section 5.1.4 ("step 3b"). The "high-t'" histogram (light blue color) is shown separately again in figure 5.9 and compared to the corresponding plot from a BNL-E852 analysis [113], which was based on 250 000 events. This experiment had a li-

quid hydrogen (thus proton) target, used a 18 GeV/c π^- beam and analyzed a t' range from $\sim$ 0.08 - 1.0 GeV$^2/c^2$. Despite the difference in beam energy the two plots show a remarkable agreement, supporting the assumption that for high momentum transfers at COMPASS in 2004 the scattering took place mostly on the nucleons inside the lead targets. In particular the production of three major resonances is evident in both cases, namely of the well-known $a_1(1260)$, $a_2(1320)$ and $\pi_2(1670)$. For further reference their masses, widths and main decay channels are summarized in table 5.4. From figure 5.8 it is apparent that the production of $a_2(1320)$ depends strongly on t'. While $a_1(1260)$ and $\pi_2(1670)$ are present in all selected t' intervals, this rather sharp resonance shows up visibly only for events with $t' > 0.1$ GeV$^2/c^2$. An exception are the data from the lowest t' range ($< 10^{-3}$ GeV$^2/c^2$), which contain also several thousand $a_2(1320)$[9].

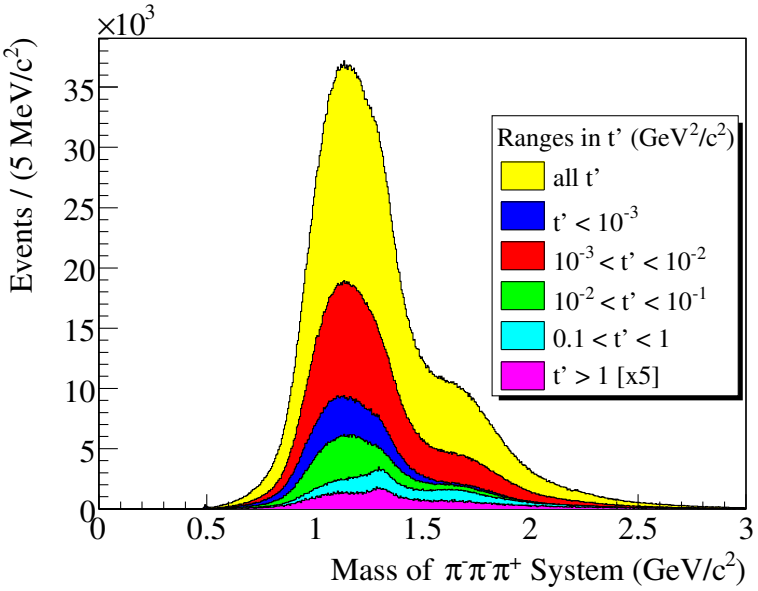

Figure 5.8: Invariant mass of $\pi^-\pi^-\pi^+$ final states for all t' (yellow) and different t' ranges. The histogram of the fifth range (purple) is scaled up by a factor of five.

State	J^{PC}	Mass m (GeV/c^2)	Width Γ (GeV/c^2)	Main Decay Channels
$a_1(1260)$	1^{++}	1.230 ± 0.040	0.250 to 0.600	$\rho\pi$
$a_2(1320)$	2^{++}	1.3183 ± 0.0006	0.107 ± 0.005	$\rho\pi$ ($\sim$ 70%), $\eta\pi$ ($\sim$ 15%)
$\pi_2(1670)$	2^{-+}	1.6724 ± 0.0032	0.259 ± 0.009	$f_2\pi$ ($\sim$ 60%), $\rho\pi$ ($\sim$ 30%)

Table 5.4: Properties of the $a_1(1260)$, $a_2(1320)$ and $\pi_2(1670)$ mesons; from PDG [38].

[9] Thus probably produced in photo-production, see also comments in section 5.1.4.

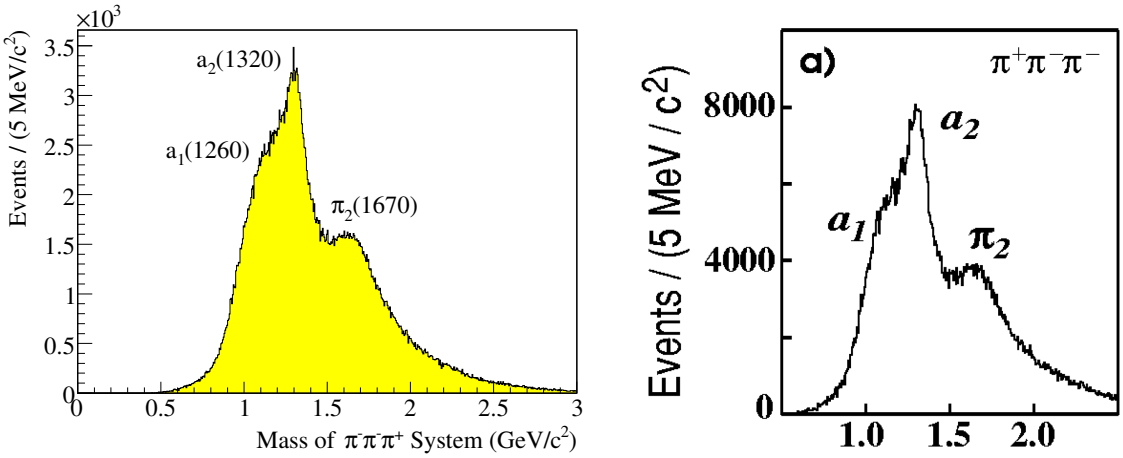

Figure 5.9: Invariant mass of the $\sim$ 425 000 $\pi^-\pi^-\pi^+$ events with $0.1 \leq t' < 1.0\,\mathrm{GeV}^2/c^2$ from COMPASS (left) and of $\sim$ 250 000 events with $0.08 \leq t' < 1.0\,\mathrm{GeV}^2/c^2$ from BNL-E852 (right) [113]. The BNL-E852 plot is acceptance corrected, i. e. the real number of events per mass bin is smaller.

5.2.2 Dalitz Plots for "High-t'" Data

To visualize the main decay channels of the produced resonances, Dalitz plots have been produced for the "high-t'" case. Thus for each $\pi^-\pi^-\pi^+$ event, the two possible $\pi^+\pi^-$ pairs have been defined and their invariant masses filled in a two-dimensional histogram[10]. Figure 5.10 shows the Dalitz plots for the $a_2(1320)$ and the $\pi_2(1670)$ mass regions. While the former has only $\rho\pi^-$ as dominant $\pi^-\pi^-\pi^+$ final state channel, the latter decays into $f_2\pi^-$ and $\rho\pi^-$ (cf. table 5.4).

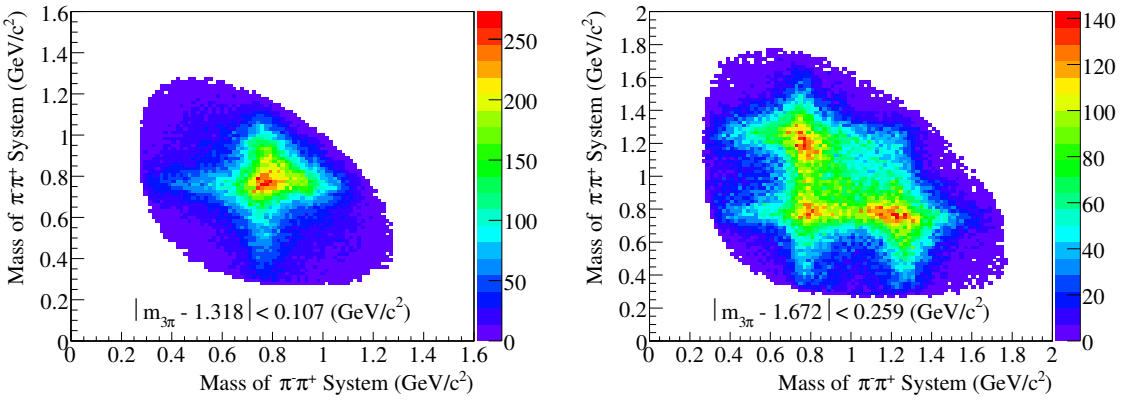

Figure 5.10: Dalitz plots for $a_2(1320)$ (left) and $\pi_2(1670)$ (right), both simply selected by a $\pm 1\Gamma$ cut around their nominal mass (cf. table 5.4 and figure 5.9).

[10] Usually the squared mass of the $\pi^+\pi^-$ pairs is plotted. However, since the phase space is not flat here anyway, the (non-squared) mass has been chosen.

5.2.3 $K^- \to \pi^-\pi^-\pi^+$ Signal

As discussed in section 3.2.1, about 2-3% of the 2004 COMPASS beam particles were in fact kaons (K^-, $1.2 \cdot 10^{-8}$ s life time). They could decay everywhere along the beam direction, thus also within the COMPASS spectrometer. The hadronic $K^- \to \pi^-\pi^-\pi^+$ decay mode has a branching ratio of 5.6% only, nevertheless, it should be possible to extract a clear K^- signal from the $\pi^-\pi^-\pi^+$ final state data. Since for a decay t' is zero, only events with very low momentum transfers ($< 10^{-3}\,\mathrm{GeV}^2/c^2$, cf. section 5.1.4) have been considered for this study. To further enhance the fraction of kaons compared to diffractive dissociation events, the cut on the primary vertex z position has been inverted (still based on 4σ, cf. section 5.1.3). Thus only vertices outside the targets have been accepted. Apart from that all other cuts have been applied as usual, in particular the exclusivity cut.

Figure 5.11 presents the obtained 3π invariant mass distribution in the low mass range, which contains the expected kaon peak. The histogram has been fitted with a signal Gaussian and a background polynomial, resulting in a kaon mass and experimental width of $(494.17 \pm 0.13)\,\mathrm{MeV}/c^2$ and $(4.1 \pm 0.2)\,\mathrm{MeV}/c^2$, respectively (statistical errors). The obtained mass is slightly higher than the PDG value of $(493.677 \pm 0.016)\,\mathrm{MeV}/c^2$ [38], but sub-MeV/c^2 shifts do not impose any danger for the later presented PWA. The reconstructed K^- width is a direct measure for the mass resolution of COMPASS[11]. If the kaons are selected from figure 5.11 by a cut around their nominal mass ($(494 \pm 5)\,\mathrm{MeV}/c^2$), the t' distribution shown in figure 5.12 is obtained. It has been fitted with a Gaussian to get an estimate for the t' resolution at $t' = 0$ and a value of $(0.34 \pm 0.02) \cdot 10^{-3}\,\mathrm{GeV}^2/c^2$ (statistical error) has been found.

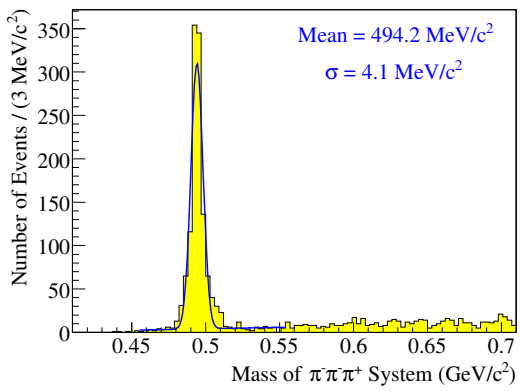

Figure 5.11: $K^- \to \pi^-\pi^-\pi^+$ signal, extracted at very low values of t' and outside the targets. The blue curve represents a fit to the data (see text).

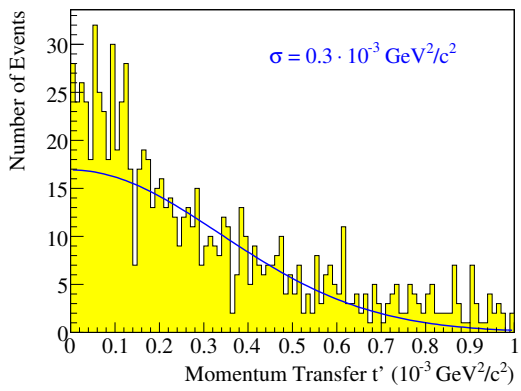

Figure 5.12: t' distribution for K^- decay events; Gaussian fit shown as blue curve (see text).

[11] However, at very low values of t' and $m_{3\pi}$, and for vertices outside the target material.

5.2.4 $K^-\pi^-\pi^+$ and $K^+K^-\pi^-$ Backgrounds

The presented analysis contains possible background due to missing particle identification, both for the beam and the final state particles (cf. section 3.2). First of all some of the $\sim 2-3\%$ kaons contained in the COMPASS beam could have been diffractively excited, resulting in $K^-\pi^-\pi^+$ final states [179, 180]. In that case $K^*(892)$ or $K^*(1430)$ for example should be present as isobars in the decay chain, which both decay into $K^-\pi$ with a branching ratio of $\sim 100\%$ and $\sim 50\%$, respectively. Most prominent should be the $K^*(892)$, having a width of $\Gamma \sim 50\,\mathrm{MeV}/c^2$. It has been searched for in the data by assigning a kaon mass to one of the nominal pions, but no signal has been observed.

A second source of background is related to the possible $K^+K^-\pi^-$ decays of the (unflavored) resonances produced from the pion beam. Some of the isobars considered for the PWA later in this work also decay into K^+K^-, however, these are always suppressed channels (e. g. 4.6% for $f_2(1270)$ or 1.6% for $\rho_3(1690)$ [38]). The dominant isobar $\rho(770)$, of course, is too light to decay into two kaons. Nevertheless the exercise has been done to also assign to two of the final state particles a kaon mass, but again nothing has been seen in the respective Dalitz plots. In particular the narrow $\phi(1020)$ ($\Gamma = 4.26\,\mathrm{MeV}/c^2$), which decays with a branching ratio of almost 50% into K^+K^-, has not shown up.

5.3 Monte Carlo Simulations

As explained in section 4.3.2, the PWA fit is able to take the experimental acceptance into account. To provide this information, the COMPASS 2004 hadron run setup has been simulated, distinguishing between the two different data taking periods (see section 5.1.1). The simulations are based on phase space distributed $\pi^-\pi^-\pi^+$ Monte Carlo (MC) events. They have been generated based on input from real data distributions, e. g. for E_a and t', and for both the "high-t'" and the "low-t'" case. It has been carefully checked that they are flat e. g. in the Dalitz plot variables. For more information about the event generator tuning and a summary of all input parameters see appendix C.1.

For the "high-t'" and the "low-t'" range 9 000 000 and 7 200 000 events have been generated, respectively. This is sufficiently more than the number of real events, and the statistical errors of the PWA are therefore not enlarged due to the acceptance corrections. All events have been processed with COMGEANT[12], reconstructed with CORAL (see section 3.3.3 and appendix A.) and, together with the acceptance information, passed to the PWA program. To illustrate the COMPASS performance, the obtained acceptances are shown for some key distributions. Also resolutions have been extracted for selected kinematical variables. Both the acceptances and the resolutions are presented for the "high-t'" and the "low-t'" range separately in the following. For simplicity, the results presented in this section have been obtained from the simulations of the 2+1 mm target period only.

[12]Geant-based simulation framework of COMPASS, for more details see appendix A.

5.3.1 Evaluation of Spectrometer Acceptance

For each simulated event the generated MC truth and, if available, the information from the reconstruction have been regarded. This includes the position of the primary vertex and the 4-momenta of the beam pion and the final state pions, respectively. In case of the beam pion, the same method as for the real data has been applied consistently to calculate its energy E_a (see section 5.1.4 and appendix B). In total four acceptance conditions have been worked out using the same cuts and requirements, which have also been used for the real data. The first one asks for a reconstructed primary vertex with three outgoing particles, which have the correct charges. Also the loose vertex and exclusivity cut according to "step 1" of the event selection (cf. section 5.1.5) have been applied on this level. This mandatory first acceptance condition is displayed in red color in all acceptance plots and accounts already for the largest fraction of the total acceptance. The tightening of the vertex and the exclusivity cut according to "step 3b" defines the next step (green color in the plots) and has been treated as an independent acceptance flag.

The two remaining conditions deal with the diffractive trigger and the online filter, which are discussed in sections 3.2.2 and 3.3.2. Concerning the hardware trigger, the MPC and HCAL2 have been treated (blue color). A multiplicity ≥ 2 has been required in the MPC, which has been evaluated based on the generated MC truth momenta of the three outgoing pions extrapolated to the position of the MPC. The 6 GeV threshold for the maximum cluster in HCAL2 has instead been tested with the information from the reconstructed clusters. While the MPC doesn't effect the acceptance at all, HCAL2 plays a small role on the % level. Concerning the online filter, the algorithm which was applied in 2004 has been repeated for the MC events using the MC truth hit information in the silicon detectors after the target. Again the observed effect is negligible, only for high masses ($> 2\,\mathrm{GeV}/c^2$) the filter cuts into the acceptance by a few %. However, this mass range is actually hardly accessible in the 3π analysis.

While the described acceptance conditions have been applied to the reconstructed events, the shown distributions themselves are based on the generated MC truth. For each variable several histograms have been filled, one for all generated events and others for those which passed the respective requirements. The latter histograms have then been normalized to the first one. To be close to the real physics data and not be biased by extreme cases, a cut on the 3π mass has been applied for all distributions as indicated in the figures, except for the 3π mass distribution itself.

5.3.1.1 "High-t'" Performance

In figure 5.13 to figure 5.16 the COMPASS 2004 "high-t'" acceptance is shown for the 3π mass, the $\pi^+\pi^-$ subsystem mass, $\cos\theta_{\mathrm{GJ}}$ and ϕ_{TY} (cf. section 4.2.1). Both angles have been evaluated here for the two possible $\pi^+\pi^-$ pairs of each event. The differently colored distributions within each figure demonstrate the effect of the applied requirements (see above), which accumulate to the final acceptance (yellow filled histogram). Compared to other experiments covering a similar momentum transfer range [113], COMPASS shows an excellent acceptance for diffractively produced 3π events,

which is mostly flat and of the order of 55-60%. The little drop for small 3π masses ($< 0.7\,\mathrm{GeV}/c^2$) is due to the vertex cut, while for high masses ($> 2\,\mathrm{GeV}/c^2$) the online filter requirement dominates. Of particular importance is the rather flat $\cos\theta_{\mathrm{GJ}}$ distribution, since sharp drops here could lead to leakage in the PWA, especially in regions where also the 3π mass acceptance drops. However, this seems not be a problem for COMPASS at "high-t'", as has been checked also in a dedicated leakage study (see section 5.7).

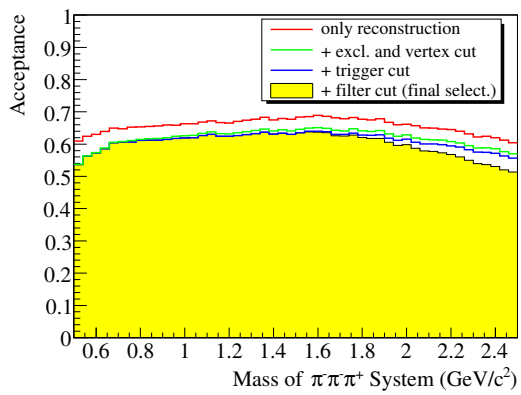

Figure 5.13: Acceptance for $\pi^-\pi^-\pi^+$ invariant mass between 0.5 and $2.5\,\mathrm{GeV}/c^2$ at "high-t'".

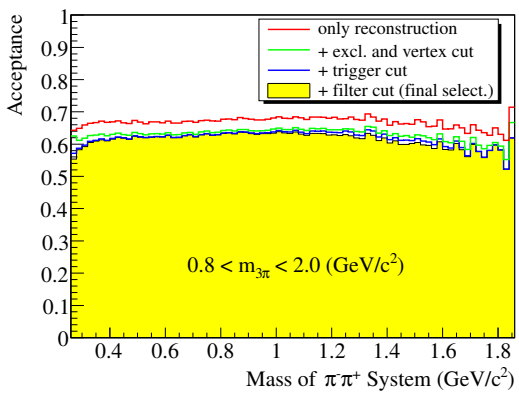

Figure 5.14: Acceptance for $\pi^+\pi^-$ subsystem mass ("high-t'"); 3π mass range limited as indicated.

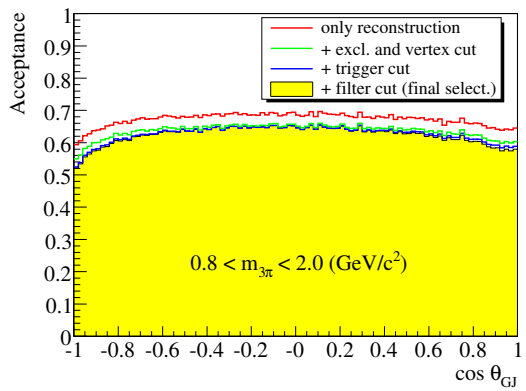

Figure 5.15: Acceptance for $\pi^+\pi^-$ polar angle in GJF ("high-t'"); 3π mass range limited as indicated.

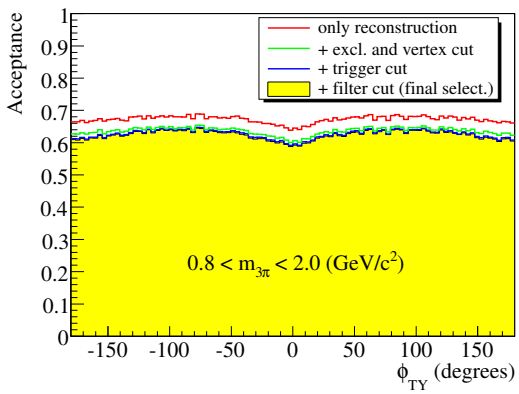

Figure 5.16: Acceptance for $\pi^+\pi^-$ azimuthal angle in GJF ("high-t'"); 3π mass range limited as indicated.

5.3.1.2 "Low-t'" Performance

Figure 5.17 to figure 5.20 present the same acceptance plots as in the previous section, but this time for the "low-t'" range. While the average acceptance is similar to the "high-t'" case, much more severe drops are observed in the 3π mass and $\cos\theta_{\mathrm{GJ}}$ distributions. In the former case the vertex cut accounts for the sharper drop at low masses, because the vertex resolution is in general worse if smaller scattering angles are involved. The decreases of up to 20% at $\cos\theta_{\mathrm{GJ}} = \pm 1$ instead seem to be an overall reconstruction feature and cannot be attributed to a particular acceptance condition. The ϕ_{TY} distribution is completely flat for "low-t'".

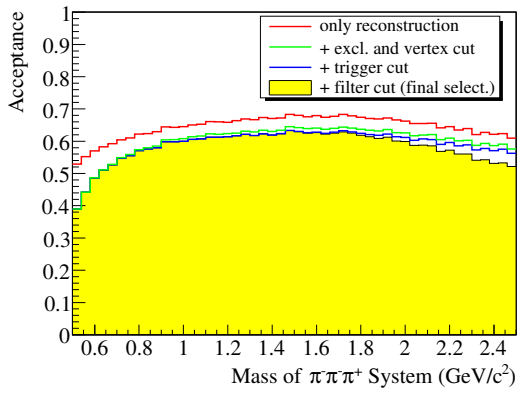

Figure 5.17: Acceptance for $\pi^-\pi^-\pi^+$ invariant mass between 0.5 and 2.5 GeV/c^2 at "low-t'".

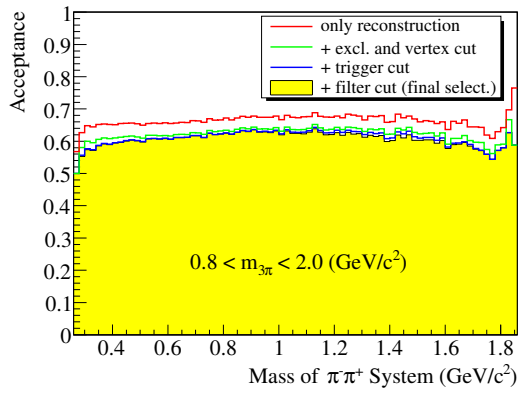

Figure 5.18: Acceptance for $\pi^+\pi^-$ subsystem mass ("low-t'"); 3π mass range limited as indicated.

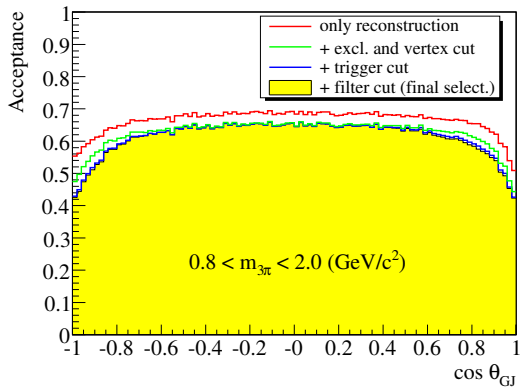

Figure 5.19: Acceptance for $\pi^+\pi^-$ polar angle in GJF ("low-t'"); 3π mass range limited as indicated.

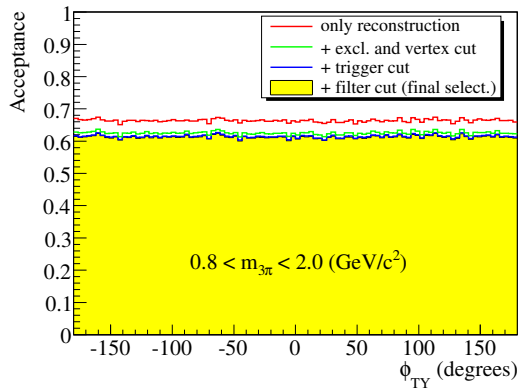

Figure 5.20: Acceptance for $\pi^+\pi^-$ azimuthal angle in GJF ("low-t'"); 3π mass range limited as indicated.

5.3.2 Experimental Resolution

In the following the resolutions for the $\pi^-\pi^-\pi^+$ mass, the beam energy E_a, the primary vertex z position and the momentum transfer t' are discussed. Again it is distinguished between "high-t'" and "low-t'" events. The technique to extract the presented resolutions is always the same, namely to plot the difference between the generated MC truth and the corresponding reconstructed values and to state the standard deviations (RMS) of the obtained residual histograms. This has been done for fully accepted events only (cf. section 5.3.1).

5.3.2.1 "High-t'" Performance

Figure 5.21 shows the 3π mass resolution for the "high-t'" case as obtained from the simulations with the 2+1 mm target (yellow histogram). Since this resolution depends both on the target width and z position, in addition, the 2 mm and the 1 mm parts alone are presented (colored histograms). An overall RMS resolution of 19 MeV/c^2 is obtained[13], which is of course dominated by the 2 mm part because twice as many events have been generated for this segment (see appendix C.1). It should be noticed that within the resolution no significant systematic shift of the reconstructed mass w. r. t. the generated MC truth is seen. Similarly to the 3π mass case the vertex z resolution is presented in figure 5.22, which is on average 5 mm. The resolution difference of 1.2 mm between the 1 mm and the 2 mm thick target segments is thereby mostly due to the different position along the z axis and not due to the target width.

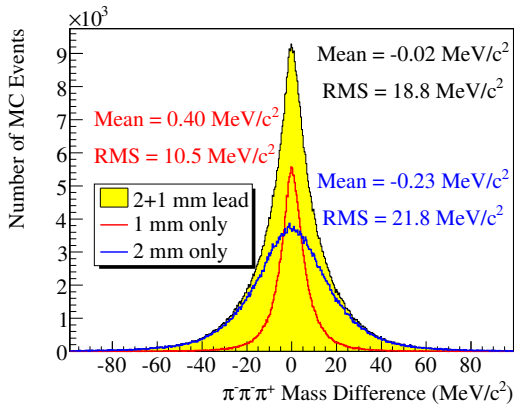

Figure 5.21: 3π mass resolution at "high-t'" for 2+1 mm target; standard deviations (RMS) given.

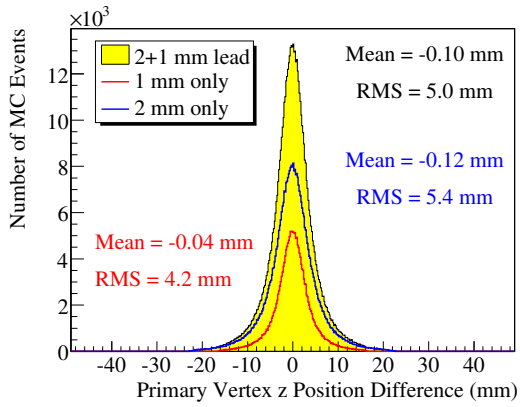

Figure 5.22: Vertex resolution at "high-t'" for 2+1 mm target; standard deviations (RMS) given.

According to figure 5.23 the RMS resolution for the beam energy E_a is about 0.8 GeV,

[13]Overall also in the sense that events with 3π masses between 0.5 and 2.5 GeV/c^2 have been generated. However, the resolution in the $a_2(1320)$ mass region (the most narrow resonance found in the PWA) is about the same.

where E_a has been calculated as described in section 5.1.4 and appendix B. Apparently the reconstructed value is systematically to low by about 60 MeV ($\sim$ 8% of the RMS), for which so far no reason could be found. The same shift occurs when instead of E_a just the total 3π energy E_c is examined, thus it is not due to the method of calculating E_a. The broadening of the beam energy profile is visualized in figure 5.24.

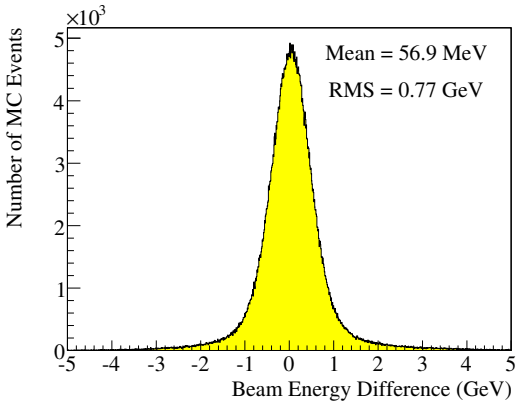

Figure 5.23: "High-t'" energy resolution; standard deviation (RMS) given.

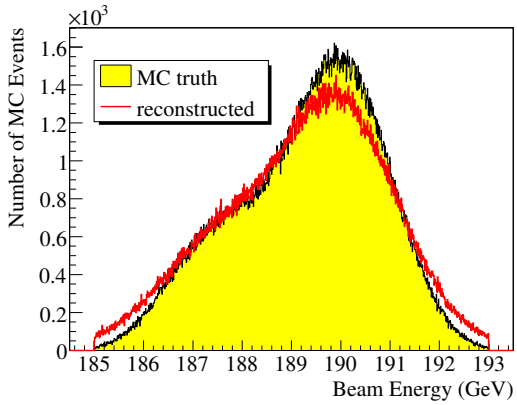

Figure 5.24: Beam energy broadening due to finite resolution.

Finally, figure 5.25 and figure 5.26 present the t' resolution and the corresponding broadening of the generated "high-t'" distribution, respectively. In a way t' is the most difficult case, because its resolution strongly depends on its value and at the same time its distribution falls exponentially. For the "high-t'" range the average absolute RMS resolution is about $23 \cdot 10^{-3}\,\mathrm{GeV}^2/c^2$, which translates into a relative resolution of the order of 10%.

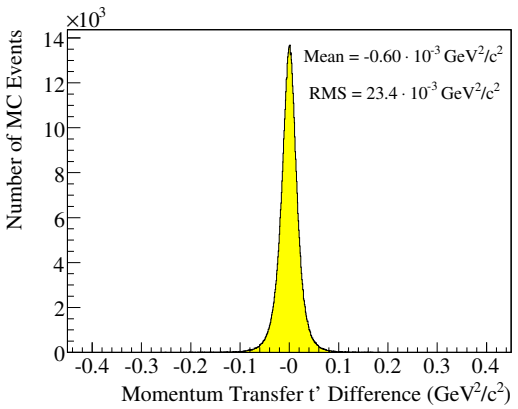

Figure 5.25: t' resolution at "high-t'"; standard deviation (RMS) given.

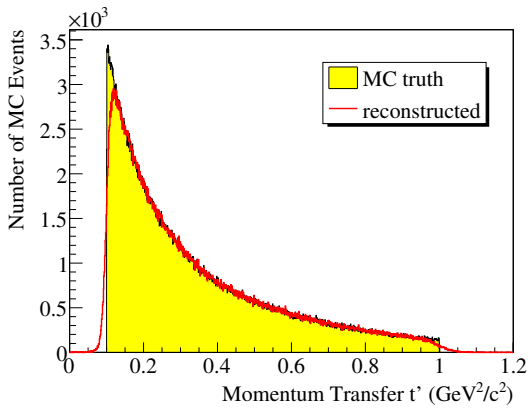

Figure 5.26: Broadening of t' distribution due to resolution.

5.3.2.2 "Low-t'" Performance

Figure 5.27 to Figure 5.30 present again the resolutions for the $\pi^-\pi^-\pi^+$ mass, the primary vertex z position, the beam energy E_a and the momentum transfer t', but this time for "low-t'" events. While the mass and the energy resolution are similar as for "high-t'" (also the energy shift), the vertex and the t' resolution differ. As mentioned before, the vertexing is worse the smaller the scattering angles are, thus the smaller t'. This is well reproduced by the simulations, in particular the individual RMS values for the different target segments (different colors in figure 5.28) are in good agreement with the σ parameters obtained from the real data (see section 5.1.3). Concerning the mass resolution a rough cross-check can be performed by comparing to the fitted kaon width from the $K^- \to \pi^-\pi^-\pi^+$ data ($\sigma \sim 4\,\mathrm{MeV}/c^2$, see section 5.2.3). Since kaons are stable within the COMPASS spectrometer, this width also reflects the mass resolution. However, to have a comparison on an equal footing, only generated events with a 3π mass of about $0.5\,\mathrm{GeV}/c^2$ should be considered. For those RMS resolutions of $3\,\mathrm{MeV}/c^2$ and $10\,\mathrm{MeV}/c^2$ have been obtained for the two targets segments, respectively. Taking into account that the kaons have been selected from the data by requiring a primary vertex near but outside the target, the agreement is satisfactory.

While the absolute t' resolution at "low-t'" is with 2-3 $\cdot\, 10^{-3}\,\mathrm{GeV}^2/c^2$ much better than at "high-t'", the relative resolution is of the order of 100%. The shift towards too high reconstructed t' values is similar than in figure 5.25, but here it is significant. The residual distribution is actually not shifted systematically, but is rather asymmetric in shape. Thus the effect depends on the kinematics of the events and the ability of the spectrometer to reconstruct the scattering angle for them. Again it is worthwhile to compare with the K^- signal, which provides the t' resolution at $t' = 0$ (see figure 5.12). Consistently it is still better there (about $0.3 \cdot 10^{-3}\,\mathrm{GeV}^2/c^2$) and supports the general trend that the absolute resolution is better the smaller t' itself.

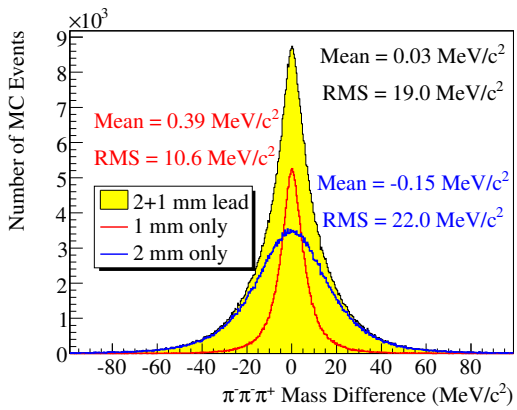

Figure 5.27: 3π mass resolution at "low-t'" for 2+1 mm target; standard deviations (RMS) given.

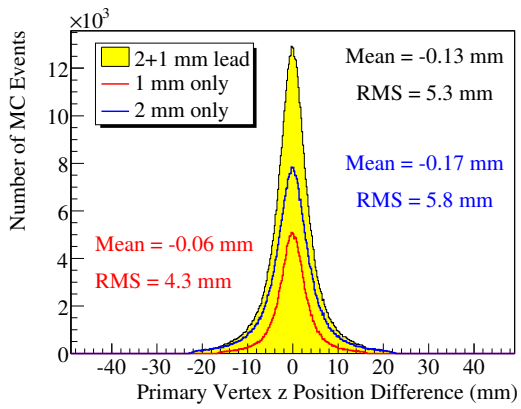

Figure 5.28: Vertex resolution at "low-t'" for 2+1 mm target; standard deviations (RMS) given.

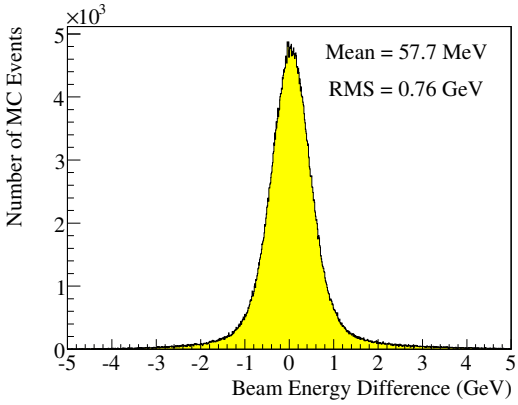

Figure 5.29: "Low-t'" energy resolution; standard deviation (RMS) given.

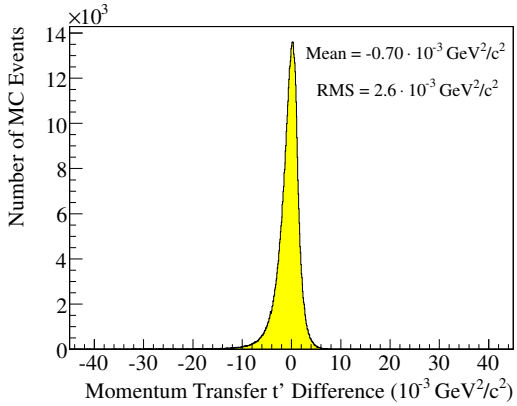

Figure 5.30: t' resolution at "low-t'"; standard deviation (RMS) given.

5.4 Mass-Independent Partial Wave Analysis

Based on the data selected according to sections 5.1 and 5.2 and using the Monte Carlo simulations presented in section 5.3, a PWA has been performed. As described in chapter 4 this task has been split into two parts, namely a mass-independent PWA followed by a mass-dependent fit. The former has been done for both the "high-t'" and the "low-t'" data and is detailed in this section. In particular the employed wave sets are summarized in a compact way, spin totals are presented to provide a first characterization of the data and several quality distributions are shown. The emphasis is on a comparison between the two t' regimes. Single wave intensities and relative phases are not discussed here, but in section 5.5 together with the mass-dependent "high-t'" fits. Also the interpretation of the produced resonances mostly takes place there.

The mass-independent PWA has been carried out in $40\,\mathrm{MeV}/c^2$ mass bins and from 0.5 - $2.5\,\mathrm{GeV}/c^2$. In order to take the effect of multiple solutions into account (see section 4.4.1), for most of the models 30 fits with different random start parameters have been attempted in each bin. Thus in such cases 1 500 separate fits have been done. The functions $f_i^\epsilon(t')$ introduced in section 4.1.4 are used only at "high-t'", mainly to respect the strong $M = 1$ content there (see section 5.4.1). A further difference arises from the rank N_r used for the fits. Following the discussion in sections 4.1.1 and 4.3.1 $N_r = 2$ is used as default for the scattering off nucleons (spin 1/2), while for the coherent scattering off the whole lead nuclei at "low-t'" $N_r = 1$ is set. Other ranks have been tried as well, for more details refer to section 5.6.1. In general the notations concerning isobars and spin states are used as described in section 4.1.3.

5.4.1 Partial Wave Sets

The spectrum of states produced in diffractive pion dissociation is very rich, limited only by the conservation laws of strong interactions: $I = 1$, $C = +1$ and $G = -1$ are dictated by the pion quantum numbers. Former $\pi^-\pi^-\pi^+$ analyses [60, 109, 113] showed furthermore that partial waves with negative reflectivity ϵ and/or spin projection $M > 1$ are much suppressed. Therefore the focus is on $\epsilon = +1$ and $M \leq 1$ states[14]. In this case the series of quantum numbers $J^{PC} = 1^{++}, 2^{-+}, 3^{++}, 4^{-+}, \ldots$ is consistent with both $M = 0$ and $M = 1$. For 0^{-+}, of course, only $M = 0$ is possible. States with $J^{PC} = 1^{-+}, 2^{++}, 3^{-+}, 4^{++}, \ldots$ require $M = 1$ if at the same time $\epsilon = +1$. This is independent from the fact that 1^{-+} and 3^{-+} are spin-exotic in the sense that they cannot come from a $q\bar{q}$ system (cf. section 2.1.1). Waves with $J > 4$ were tried for the large statistics "low-t'" sample, but didn't get any intensity. Considering only the main decay channels like $(\pi\pi)_s\pi$, $\rho\pi$ and $f_2\pi$ and different values for the orbital angular momentum L (see figure 4.1), already more than 50 possible partial waves with $\epsilon = +1$ and $M \leq 1$ exist.

5.4.1.1 "High-t'" Wave Set

Since the disputed spin-exotic 1^{-+} wave signals were reported at rather high values of t' (see section 2.4.1), the analysis concentrated on this data sample first. The initial set of partial waves was taken from [113] and consisted of 27 amplitudes. All of them happened to be significant and have been kept for the final PWA. The similarity between the BNL-E852 and the COMPASS 2004 "high-t'" events becomes thereby even more apparent, not only from the 3π mass spectrum (figure 5.9), but also from the spin totals of the major waves (see section 5.4.2.1). However, in the COMPASS case using lead targets, the $M = 1$ intensities contributing to the $J^{PC} = 1^{++}$ and 2^{-+} totals are about 50% relative to the $M = 0$ intensities. This compares to only about 10% in the BNL-E852 case. Therefore a total of eight additional $M = 1$ waves has been included for $1^{++}, 2^{-+}$ and even 3^{++}. Also some small $f_2\pi$ decay modes for 1^{++} and 2^{++} and two 4^{-+} partial waves have been added. Finally, two additional $2^{++} \to f_2\pi$ amplitudes have been found to be significant.

The final set comprises 42 partial waves and is summarized in table 5.5. The waves are ordered from $J = 0$ to $J = 4$, $M = 0$ to $M = 1$, $L = S$ to $L = G$ and from light to heavy isobars, respectively. First the 34 $\epsilon = +1$ states are listed, followed by the seven $\epsilon = -1$ ones and the flat wave. The latter is a background wave, which is characterized by a uniform distribution in the relevant decay angles and added incoherently to the other waves. Those partial waves which have been used also for the mass-dependent fit are marked as such. For most of the partial waves i a lower mass threshold m_i has been introduced. In other words the corresponding amplitude is assumed to contribute only in mass bins $m \geq m_i$. This stabilizes the fit a lot, since less parameters have to be considered. However, the choice of the m_i is not straightforward and has to be made with care. A general rule of thumb is that partial waves with high spin J should have higher thresholds than the low spin ones. Also heavy isobars in the decay chain like $\rho_3(1690)$

[14] Some $\epsilon = -1$ states, however, are also always tried. In addition, one of the systematic studies presented in section 5.6.2 included several $M = 2$ waves.

or $f_2(1275)$ give reason for a high m_i. Finally, very large L can justify a threshold. In practise the final m_i values have been obtained in an iterative procedure involving many fits. They are listed in the fourth column of table 5.5.

As mentioned previously, the functions $f_i^\epsilon(t')$ have been used for the "high-t'" PWA. They have been obtained once from the real data by dividing the events in t' bins instead of mass bins. Still three broad mass sub-divisions have been defined for this exercise, and for each of them a PWA has been performed in the t' bins. The resulting intensity for a particular $J^{PC}M^\epsilon$ state has then been fitted as a function of t', distinguishing between $M = 0$ and $M = 1$ spin projections[15]. The obtained functions $f_i^\epsilon(t')$ have been tabulated and used for the usual mass-independent fits according to equation (4.12). Those corresponding to the waves with $\epsilon = +1$ and $J \leq 2$ are shown in table 5.6.

5.4.1.2 "Low-t'" Wave Set

Finding a model for the "low-t'" data has been more difficult. Starting from not less than 74 waves, insignificant amplitudes have been sorted out step by step. In the end 55 waves remained, which included except for four still all the "high-t'" ones (cf. section 5.4.1.1). One more isobar has been introduced ($f_0(1500)$), but the corresponding partial waves do not show any signal. The final list of waves is presented in table 5.7. It is pointed out that neither this set nor the stated mass thresholds have been optimized to a level as in the "high-t'" case. Also the t' functions haven't been worked out here and were all set to $f_i^\epsilon(t') = 1$. For low values of t', however, $M = 1$ states are suppressed anyway, because the cross-section contains a factor $t'e^{bt'}$ for them in contrast to $e^{bt'}$ for $M = 0$ states.

5.4.2 Spin Totals

Before going into the details of single wave intensities and interferences between different waves, spin totals (see section 4.4.4) provide already a very useful characterization of the data. They are presented in this section for both the "high-t'" and the "low-t'" events. First the fraction of the background wave compared to all events is shown, followed by a confrontation of the $\epsilon = +1$ and the $\epsilon = -1$ spin totals. Then the major J^{PC} ($\epsilon = \pm 1$) totals are presented, eventually distinguishing also between $M = 0$ and $M = 1$. As always in this thesis, the results of the mass-independent fits are plotted as black (sometimes red) data points with statistical error bars. If the latter have been enlarged due to multiple solutions, this is visualized as thick green line.

5.4.2.1 "High-t'" Data

Figure 5.31 compares the total intensity (or overall spin total) at "high-t'" with the flat wave. Less than 5% of the data are recognized as background, the corresponding events having a mass around $1.3\,\mathrm{GeV}/c^2$. Although acceptance corrected, the total intensity reproduces well the shape of the 3π mass spectrum shown in figure 5.9 (left). This is not

[15] Based on equation (4.2), but with more parameters (see table 5.6).

$J^{PC}M^{\epsilon}$	L	Isobar π	Lower $m_{3\pi}$ Cut (GeV/c^2)	Mass-Dep. Fit
$0^{-+}0^+$	S	$f_0\pi$	1.40	X
$0^{-+}0^+$	S	$(\pi\pi)_s\pi$	-	
$0^{-+}0^+$	P	$\rho\pi$	-	
$1^{-+}1^+$	P	$\rho\pi$	-	X
$1^{++}0^+$	S	$\rho\pi$	-	X
$1^{++}0^+$	P	$f_2\pi$	1.20	
$1^{++}0^+$	P	$(\pi\pi)_s\pi$	0.84	
$1^{++}0^+$	D	$\rho\pi$	1.30	
$1^{++}1^+$	S	$\rho\pi$	-	
$1^{++}1^+$	P	$f_2\pi$	1.40	
$1^{++}1^+$	P	$(\pi\pi)_s\pi$	1.40	
$1^{++}1^+$	D	$\rho\pi$	1.40	
$2^{-+}0^+$	S	$f_2\pi$	1.20	X
$2^{-+}0^+$	P	$\rho\pi$	0.80	
$2^{-+}0^+$	D	$f_2\pi$	1.50	X
$2^{-+}0^+$	D	$(\pi\pi)_s\pi$	0.80	
$2^{-+}0^+$	F	$\rho\pi$	1.20	
$2^{-+}1^+$	S	$f_2\pi$	1.20	
$2^{-+}1^+$	P	$\rho\pi$	0.80	
$2^{-+}1^+$	D	$f_2\pi$	1.50	
$2^{-+}1^+$	D	$(\pi\pi)_s\pi$	1.20	
$2^{-+}1^+$	F	$\rho\pi$	1.20	
$2^{++}1^+$	P	$f_2\pi$	1.50	
$2^{++}1^+$	D	$\rho\pi$	-	X
$3^{++}0^+$	S	$\rho_3\pi$	1.50	
$3^{++}0^+$	P	$f_2\pi$	1.20	
$3^{++}0^+$	D	$\rho\pi$	1.50	
$3^{++}1^+$	S	$\rho_3\pi$	1.50	
$3^{++}1^+$	P	$f_2\pi$	1.20	
$3^{++}1^+$	D	$\rho\pi$	1.50	
$4^{-+}0^+$	F	$\rho\pi$	1.20	
$4^{-+}1^+$	F	$\rho\pi$	1.20	
$4^{++}1^+$	F	$f_2\pi$	1.60	
$4^{++}1^+$	G	$\rho\pi$	1.64	X
$1^{-+}0^-$	P	$\rho\pi$	-	
$1^{-+}1^-$	P	$\rho\pi$	-	
$1^{++}1^-$	S	$\rho\pi$	-	
$2^{-+}1^-$	S	$f_2\pi$	1.20	
$2^{++}0^-$	P	$f_2\pi$	1.30	
$2^{++}0^-$	D	$\rho\pi$	-	
$2^{++}1^-$	P	$f_2\pi$	1.30	
FLAT				

Table 5.5: Overview of the 42 partial waves used for the "high-t'" mass-independent PWA fit; listed mass cuts are lower boundaries for the 3π mass (see text). The partial wave notations are illustrated in figure 4.1 and the isobars are discussed in section 4.1.3; waves also used for the mass-dependent fit are marked.

$J^{PC}M^{\epsilon}$	Parameterization	Parameters
$0^{-+}0^{+}$	$a \cdot e^{-15t'} + b \cdot e^{-ct'} + d \cdot e^{-3t'}$	$a: 0.15, \quad b: -0.09, \quad c: 3.20, \quad d: 0.10$
$1^{++}0^{+}$		$a: -0.36, \quad b: 0.47, \quad c: 12.26, \quad d: 0.02$
$2^{-+}0^{+}$		$a: 0.13, \quad b: 0.10, \quad c: 9.55, \quad d: 0.18$
$1^{++}1^{+}$	$a \cdot t'e^{-15t'} + b \cdot t'e^{-ct'} + d \cdot t'e^{-3t'}$	$a: 0.49, \quad b: 0.10, \quad c: 9.57, \quad d: 0.04$
$2^{++}1^{+}$		$a: -0.19, \quad b: 0.25, \quad c: 9.29, \quad d: 0.02$
$2^{-+}1^{+}$		$a: -0.18, \quad b: 0.36, \quad c: 10.40, \quad d: 0.009$

Table 5.6: Parameterization of the t' dependence for different $J^{PC}M^{\epsilon}$; dominant examples with $\epsilon = +1$ and $J \leq 2$ shown.

$J^{PC}M^{\epsilon}$	L	Isobar π	Lower $m_{3\pi}$ Cut (GeV/c^2)
$0^{-+}0^{+}$	S	$f_0(980)\pi$	0.88
$0^{-+}0^{+}$	S	$(\pi\pi)_s\pi$	-
$0^{-+}0^{+}$	S	$f_0(1500)\pi$	1.60
$0^{-+}0^{+}$	P	$\rho\pi$	-
$0^{-+}0^{+}$	D	$f_2\pi$	1.20
$1^{-+}1^{+}$	P	$\rho\pi$	-
$1^{++}0^{+}$	S	$\rho\pi$	-
$1^{++}0^{+}$	P	$f_0(980)\pi$	0.88
$1^{++}0^{+}$	P	$f_2\pi$	1.00
$1^{++}0^{+}$	P	$(\pi\pi)_s\pi$	0.70
$1^{++}0^{+}$	P	$f_0(1500)\pi$	1.80
$1^{++}0^{+}$	D	$\rho\pi$	0.80
$1^{++}1^{+}$	S	$\rho\pi$	-
$1^{++}1^{+}$	P	$f_2\pi$	1.10
$1^{++}1^{+}$	P	$(\pi\pi)_s\pi$	0.90
$1^{++}1^{+}$	D	$\rho\pi$	1.00
$2^{-+}0^{+}$	S	$f_2\pi$	1.20
$2^{-+}0^{+}$	P	$\rho\pi$	0.80
$2^{-+}0^{+}$	P	$\rho_3\pi$	1.40
$2^{-+}0^{+}$	D	$f_2\pi$	1.50
$2^{-+}0^{+}$	D	$(\pi\pi)_s\pi$	0.80
$2^{-+}0^{+}$	F	$\rho\pi$	1.00
$2^{-+}1^{+}$	S	$f_2\pi$	1.10
$2^{-+}1^{+}$	P	$\rho\pi$	0.96
$2^{-+}1^{+}$	D	$(\pi\pi)_s\pi$	0.80
$2^{-+}1^{+}$	F	$\rho\pi$	1.20
$2^{++}1^{+}$	D	$\rho\pi$	-

$J^{PC}M^{\epsilon}$	L	Isobar π	Lower $m_{3\pi}$ Cut (GeV/c^2)
$3^{++}0^{+}$	S	$\rho_3\pi$	1.64
$3^{++}0^{+}$	P	$f_2\pi$	1.40
$3^{++}0^{+}$	D	$\rho\pi$	1.40
$3^{++}0^{+}$	F	$(\pi\pi)_s\pi$	1.50
$3^{++}1^{+}$	S	$\rho_3\pi$	1.80
$3^{++}1^{+}$	P	$f_2\pi$	1.40
$3^{++}1^{+}$	D	$\rho\pi$	1.10
$3^{++}1^{+}$	F	$(\pi\pi)_s\pi$	1.50
$4^{-+}0^{+}$	P	$\rho_3\pi$	1.80
$4^{-+}0^{+}$	D	$f_2\pi$	1.20
$4^{-+}1^{+}$	F	$\rho\pi$	1.24
$4^{++}1^{+}$	G	$\rho\pi$	1.50
$5^{++}0^{+}$	H	$\rho\pi$	1.40
$1^{-+}0^{-}$	P	$\rho\pi$	-
$1^{-+}1^{-}$	P	$\rho\pi$	-
$1^{++}1^{-}$	S	$\rho\pi$	-
$1^{++}1^{-}$	P	$f_2\pi$	1.20
$1^{++}1^{-}$	P	$(\pi\pi)_s\pi$	1.00
$1^{++}1^{-}$	D	$\rho\pi$	-
$2^{-+}1^{-}$	S	$f_2\pi$	1.20
$2^{-+}1^{-}$	P	$\rho\pi$	1.20
$2^{-+}1^{-}$	D	$(\pi\pi)_s\pi$	1.00
$2^{-+}1^{-}$	F	$\rho\pi$	1.20
$2^{++}0^{-}$	P	$f_2\pi$	1.32
$2^{++}0^{-}$	D	$\rho\pi$	-
$2^{++}1^{-}$	P	$f_2\pi$	1.20
$2^{++}1^{-}$	D	$\rho\pi$	-
FLAT			

Table 5.7: Overview of the 55 partial waves used for the "low-t'" mass-independent PWA fit; see also caption of table 5.5.

a surprise considering the flat acceptance in the 3π mass (see figure 5.13). In figure 5.32 the contribution of positive and negative reflectivity waves is shown, exhibiting the clear dominance of the former. The bump at about $1.6\,\mathrm{GeV}/c^2$ for $\epsilon = -1$ is discussed below.

The 0^{-+}, 1^{++}, 2^{-+} and 2^{++} spin totals (all with $\epsilon = +1$) are presented together in figure 5.33. The main dominant three resonances $a_1(1260)$, $a_2(1320)$ and $\pi_2(1670)$ are nicely separated according to their spin-parity quantum numbers (cf. table 5.4). Maybe a high-mass tail in the 1^{++} total is seen. Also the $\pi(1800)$ with $J^{PC} = 0^{-+}$ can be guessed already, but such small signals are much better resolved in individual partial waves (see section 5.5.1). In general the 0^{-+} spin total has a broad low-mass bump and a rather unstable shape, which is mostly due to the $0^{-+}0^+(\pi\pi)_s\pi S$ partial wave. This wave contains a very broad isobar and is actually not much different from the flat background wave. Therefore the interplay between these two is complicated[16].

A very striking and interesting feature of the data is displayed in figure 5.34, which shows next to each other the $M = 0$ and $M = 1$ spin totals for the 1^{++} and the 2^{-+} case. $M = 1$ is suppressed by a factor of about 2 only with respect to $M = 0$, which seems to be connected to the lead data[17] since for the free proton data [113] this suppression is about a factor of 5 higher. Another possible explanation for the increased $M = 1$ production could come back to the question about N^* excitations of the target (cf. section 5.1.4). This involves a change of $\Delta S = 1$ at the baryon (target) vertex, which could influence the meson vertex also. In the $1^{++}1^+$ spin total maybe the radial excitation $a_1(1640)$ is seen, but at "high-t'" no conclusions on its parameters can be made[18].

Finally, figure 5.35 shows two examples of $\epsilon = -1$ spin totals, namely those for 2^{-+} and 2^{++}. The latter is particularly significant and has a bump at $\sim 1.7\,\mathrm{GeV}/c^2$. This might be $a_2(1700)$ (see also sections 5.5.1.3 and 5.5.2) produced in negative naturality exchange (e. g. $b_1(1235)$), but unfortunately no interference to other partial waves is established in the $\epsilon = -1$ sector to study it further by means of a mass-dependent fit.

5.4.2.2 "Low-t'" Data

In figure 5.36 - 5.38 the spin totals shown in the previous section are presented for the "low-t'" events. The flat wave and the $\epsilon = -1$ amplitudes are of even lower significance here. The $0^{-+}(\epsilon = +1)$ total looks much smoother and contains a clean $\pi(1800)$ signal. Also the broad $\pi(1300)$ could be present in the broad low mass bump. The 1^{++} spin total has huge statistics and the radial excitation $a_1(1640)$ is visible (see also section 5.5.3). The 2^{-+} shape is sharper, indicating that $\pi_2(1670)$ is produced in a very distinguished way. Surprisingly also several thousand $a_2(1320)$ are obtained, which should be suppressed at "low-t'" because they can have $M = 1$ only. Part of them could have been produced by a photon instead of a Reggeon exchange, thus at $t' = 0$. Due to the finite t' resolution such events can migrate to higher values of t' (cf. figure 5.30). In general, the number of observed $M = 1$ with respect to $M = 0$ states is suppressed by a factor of 10 or higher.

[16] This becomes even more apparent in the studies involving different ranks (see section 5.6.1).
[17] More precisely, at "high-t'" the scattering occurs on the nucleons inside the lead nuclei.
[18] It is much better expressed in the "low-t'" data (section 5.5.3) and discussed there.

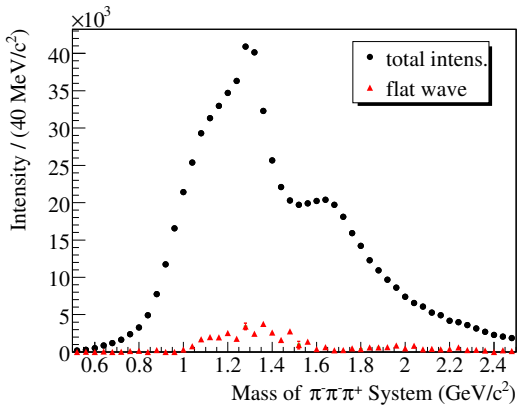

Figure 5.31: Comparison of total intensity with background wave at "high-t'"

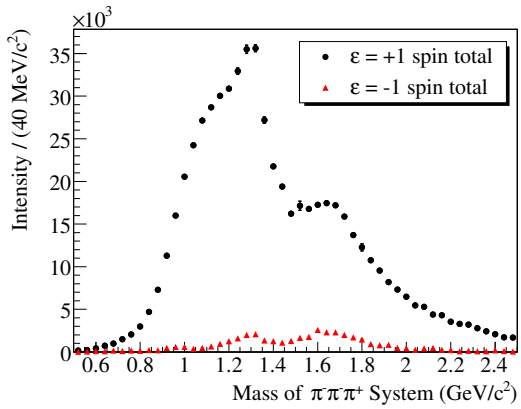

Figure 5.32: Comparison of positive and negative reflectivity totals ("high-t'").

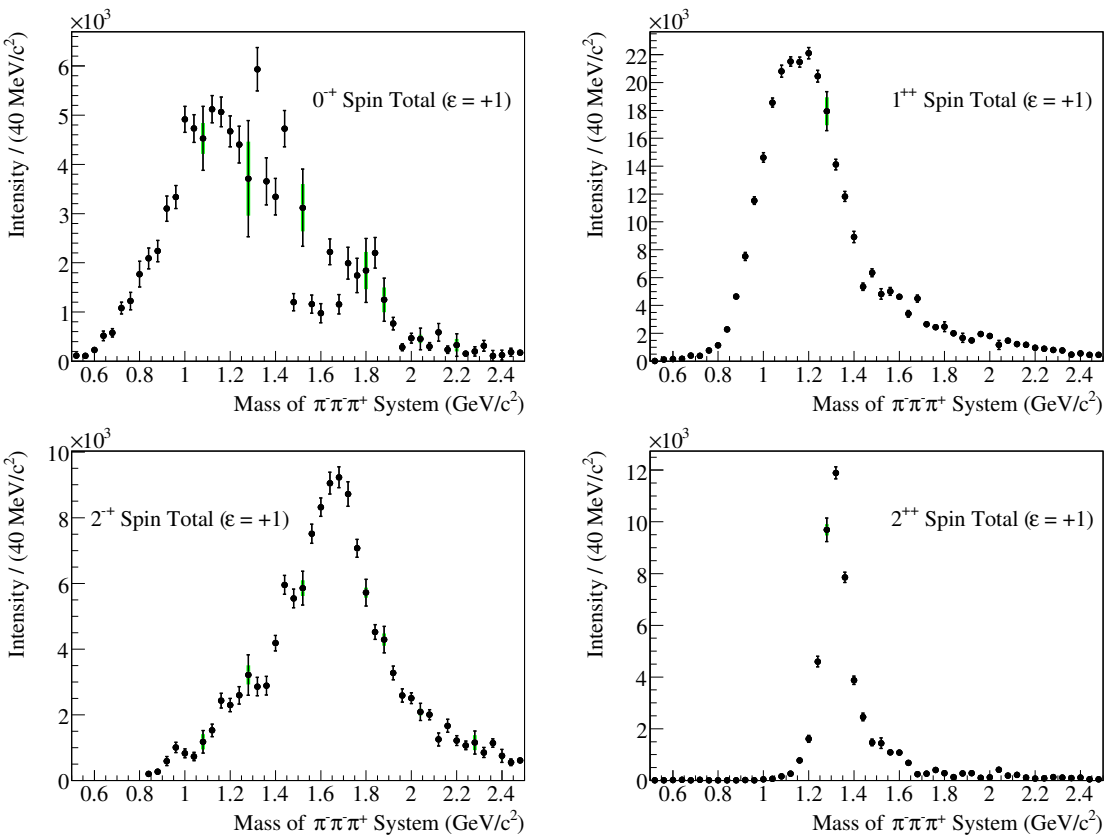

Figure 5.33: Spin totals of the four major J^{PC} ($\epsilon = +1$) states; from top left to down right: $0^{-+}, 1^{++}, 2^{-+}$ and 2^{++}; "high-t'" data shown.

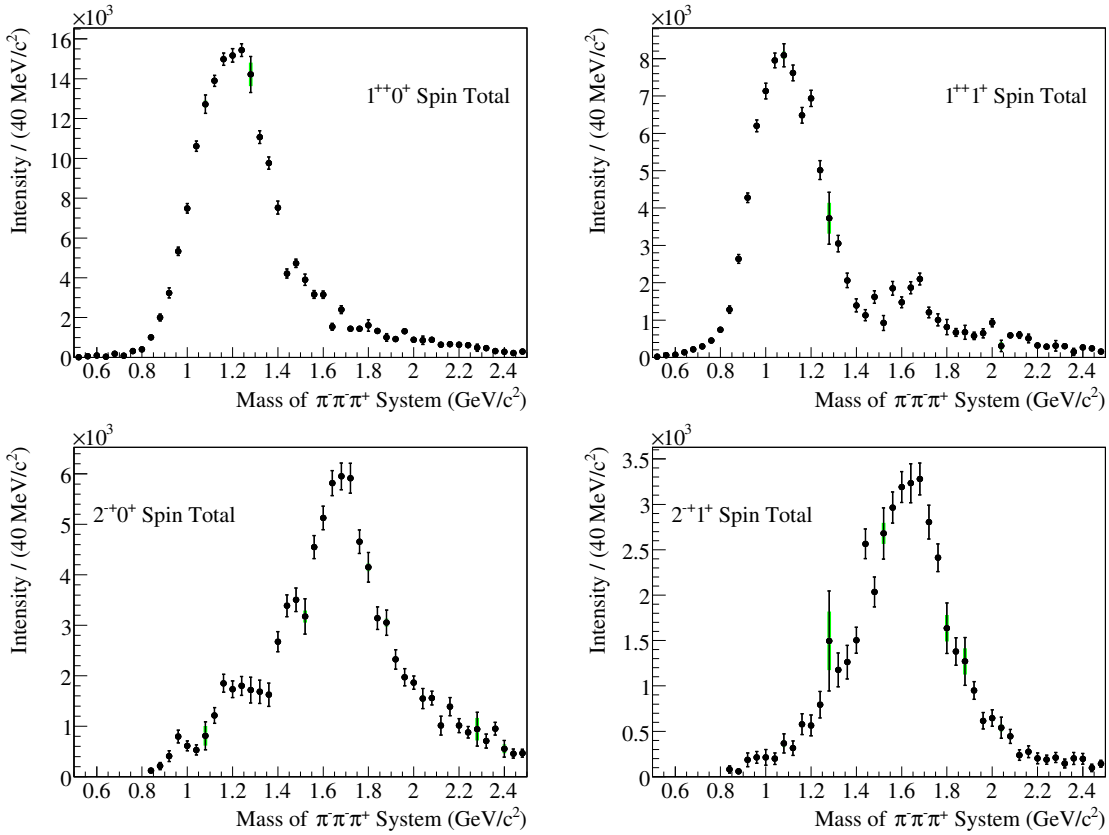

Figure 5.34: Comparison of $M = 0$ and $M = 1$ spin totals for $J^{PC} = 1^{++}$ and 2^{-+} ($\epsilon = +1$); "high-t'" data shown.

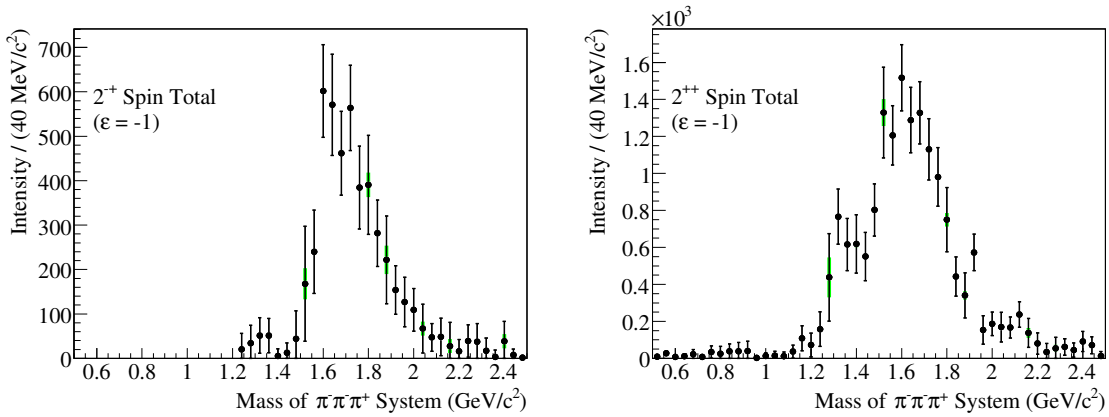

Figure 5.35: Most significant negative reflectivity spin totals: $J^{PC} = 2^{-+}$ and 2^{++}; "high-t'" data shown.

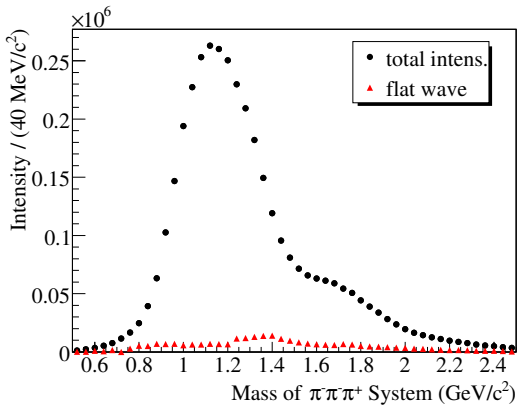

Figure 5.36: Comparison of total intensity with background wave at "low-t'"

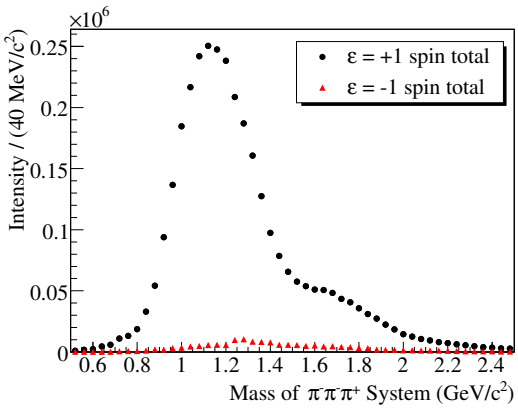

Figure 5.37: Comparison of positive and negative reflectivity totals ("low-t'").

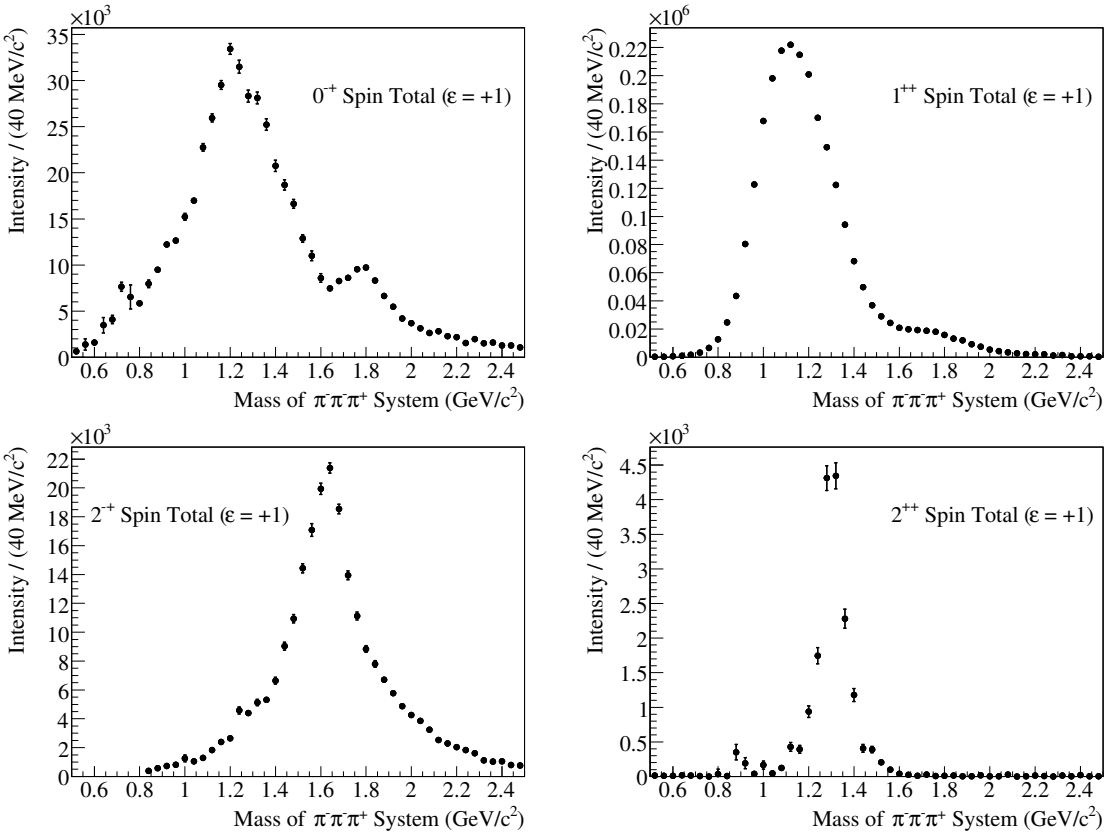

Figure 5.38: Spin totals of the four major J^{PC} ($\epsilon = +1$) states; from top left to down right: $0^{-+}, 1^{++}, 2^{-+}$ and 2^{++}; "low-t'" data shown.

5.4.3 Quality Assurance

In order to test the quality of the PWA model and the applied acceptance corrections, the procedure described in section 4.4.5 has been employed. For several important kinematical distributions or angles the data are compared to simulated and reconstructed Monte Carlo events, which have been weighted according to the obtained model. The latter are also referred to as predicted events and are always shown in red color, while the real events are plotted as yellow-filled histograms. Only a small selection of key distributions is presented here, some more can be found in appendix C.2.

5.4.3.1 "High-t'" Distributions

As pointed out in section 4.4.5, the comparison between data and weighted Monte Carlo (MC) in case of the 3π mass (figure 5.39, left) just checks the correct normalization of the MC events. The $\pi^+\pi^-$ mass distribution (same figure, right), however, is already important to see, because it clarifies whether all important isobars have been taken into account. This is obviously the case. Also $\cos\theta_{\mathrm{GJ}}$ and ϕ_{TY} are well described (figure 5.40) and so are many other angular distributions which are not shown here. The only found small obstacle arises from the description of the angle in the GJF between the recoil particle and one of the negative final state pions (figure 5.41, left)[19]. This behavior can maybe be explained from two arguments: First of all the "high-t'" range from 0.1 to 1.0 GeV^2/c^2 is rather large and the resonance production varies as a function of t'. This is partly covered by the $f_i^\epsilon(t')$ functions (see section 5.4.1.1), but certainly not in a perfect way. Secondly, there is significant background at "high-t'" below the exclusivity peak (see figure 5.7). Depending on the source of this background (see discussion in section 5.1.4), it can happen that the resonance decay is not much effected, while the description of the recoil particle is slightly wrong. An important cross-check for both arguments is to look at the corresponding distribution at "low-t'" (cf. figure 5.44, left), which indeed expresses a better agreement between data and MC.

5.4.3.2 "Low-t'" Distributions

At "low-t'" the agreement between data and weighted MC is in general very good. Figures 5.42 - 5.44 present the same distributions as shown for "high-t'", some of which look very different now. This is connected to the resonances produced, e. g. from the spin totals (see section 5.4.2) it is seen that the fraction of high ($J > 1$) spin and high ($M = 1$) spin projection states changes a lot between the two different t' ranges. In particular also the GJF angles between the recoil and one of the pions are shown again. The fact that those are better described here supports the arguments that the discrepancy at "high-t'" is due to either non-exclusive background or the large t' range. It should be remembered that at "low-t'" the functions $f_i^\epsilon(t')$ have not been used, which could explain the little remaining effect at $\cos(\mathrm{Recoil} - \pi^-)_{\mathrm{GJ}} \approx 1$.

[19]The fact that the corresponding distribution for the positive outgoing pion looks better could indicate that the bachelor pion is responsible for the discrepancy.

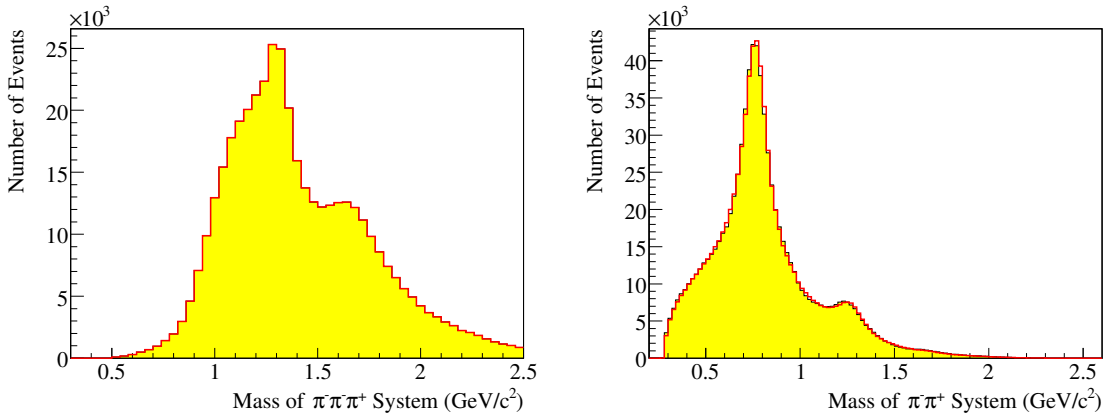

Figure 5.39: Weighted MC events (red color) compared to real data (yellow color) for 3π mass (left) and $\pi^+\pi^-$ pairs (right); "high-t'" case.

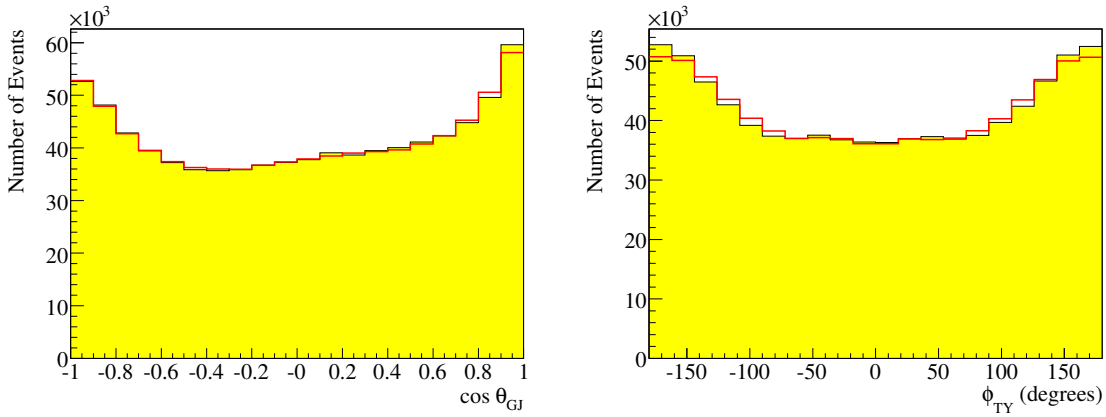

Figure 5.40: Weighted MC events (red color) compared to real data (yellow color) for $\cos\theta_{\mathrm{GJ}}$ (left) and ϕ_{TY} (right); "high-t'" case.

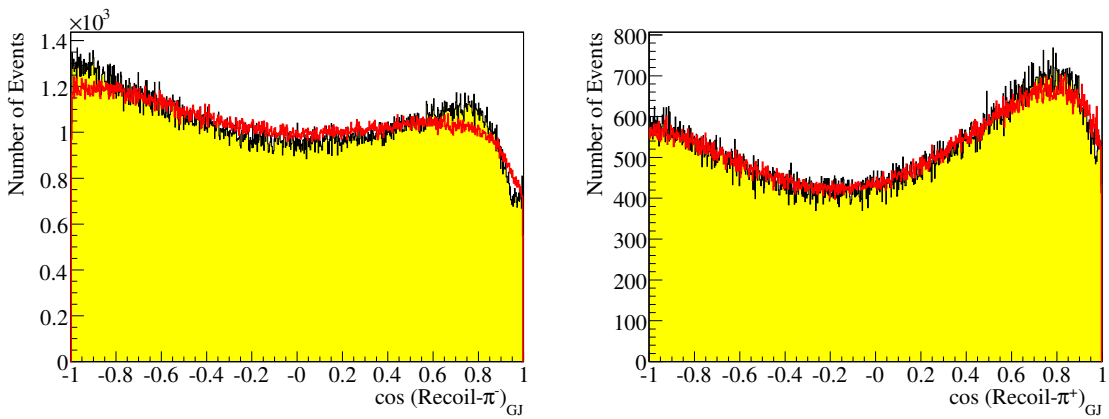

Figure 5.41: Weighted MC events (red color) compared to real data (yellow color) for $\cos(\mathrm{Recoil} - \pi^-)_{\mathrm{GJ}}$ (left) and $\cos(\mathrm{Recoil} - \pi^+)_{\mathrm{GJ}}$ (right); "high-t'" case.

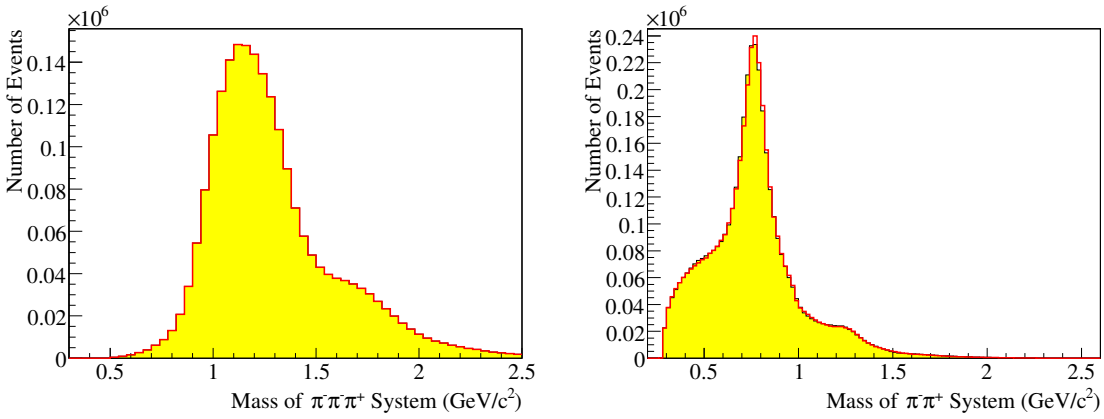

Figure 5.42: Weighted MC events (red color) compared to real data (yellow color) for 3π mass (left) and $\pi^+\pi^-$ pairs (right); "low-t'" case.

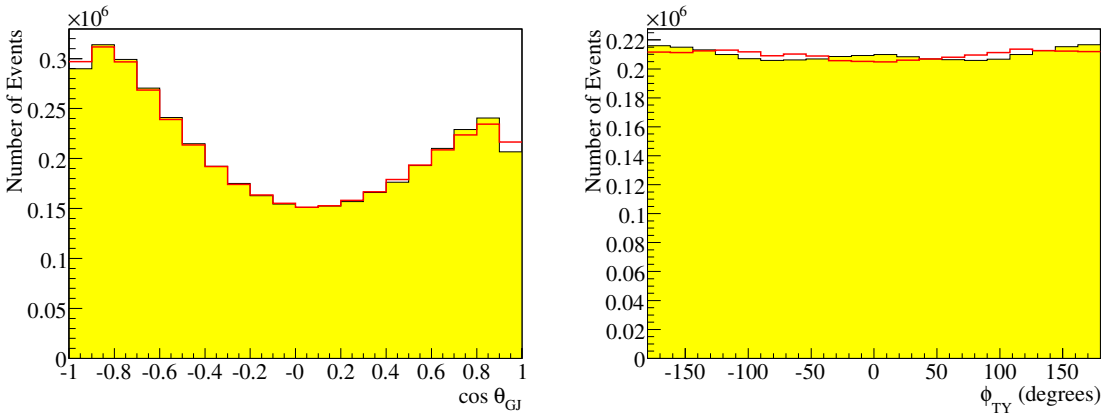

Figure 5.43: Weighted MC events (red color) compared to real data (yellow color) for $\cos\theta_{\mathrm{GJ}}$ (left) and ϕ_{TY} (right); "low-t'" case.

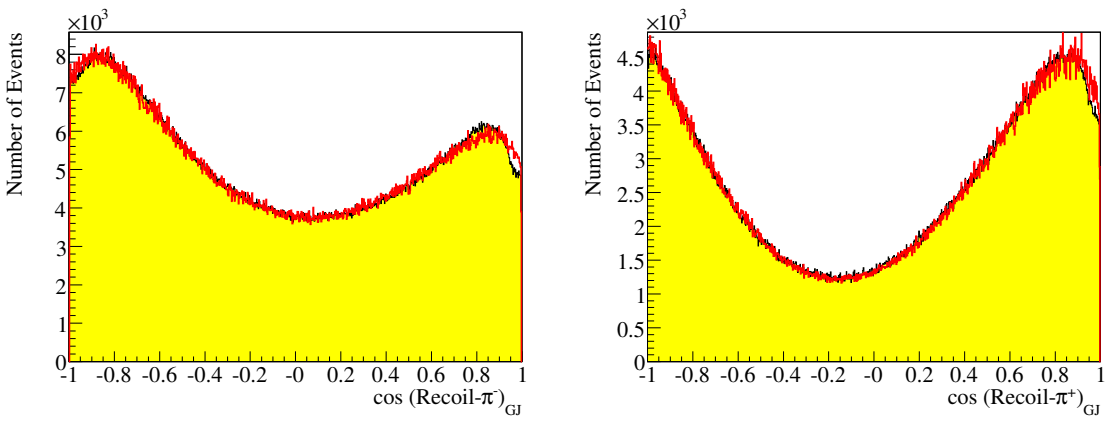

Figure 5.44: Weighted MC events (red color) compared to real data (yellow color) for $\cos(\mathrm{Recoil}-\pi^-)_{\mathrm{GJ}}$ (left) and $\cos(\mathrm{Recoil}-\pi^+)_{\mathrm{GJ}}$ (right); "low-t'" case.

5.5 Intensities, Phases and Mass-Dependent Fit

While in section 5.4 the results from the mass-independent fits are shown only in form of spin totals, this section presents single partial wave intensities and relative phases. In case of the "high-t'" data, a mass-dependent fit using seven out of the 42 waves from the mass-independent PWA has been performed. This fit is described first, including the details about the used Breit-Wigner parameterizations. The results and found states are then summarized and compared to the literature. This includes a discussion about the spin-exotic 1^{-+} wave, which is interpreted as the $\pi_1(1600)$ hybrid candidate. At the end of this section some selected waves and phase motions from the "low-t'" events are compiled, however, no mass-dependent fit exists yet. The latter turned out to be very difficult due to many overlapping resonances and complicated interference structures.

5.5.1 "High-t'" Mass-Dependent Fit

As explained in section 4.5, the mass-dependent fit is based on the outcome of the mass-independent PWA. From the known production amplitudes in each mass bin a global model is established, which describes the mass-dependence of the spin density matrix. According to equations (4.16) and (4.17) intensities and phases are derived from this matrix, and the fit results can therefore be visualized by overlaying a continuous curve (red colored) to the binned PWA data points (black colored). The spin density matrix elements are fitted altogether at the same time and not individual histograms. In practise a subset of the waves used in the mass-independent PWA has to be chosen for the mass-dependent fit. Otherwise the fit would have too many parameters, many of them describing meaningless amplitudes. For the results presented in this work the strategy has been to include only waves containing clean resonances, to set up a good interferometer for the exotic signal.

The selection of partial waves for the mass-dependent fit started out with the two dominant $M = 0$ amplitudes $1^{++}0^{+}\rho\pi S$ and $2^{-+}0^{+}f_2\pi S$. Since the aim of the "high-t'" analysis has been to study signals that are suppressed at "low-t'", i. e. the series with $J^{PC}M^{\epsilon} = 1^{-+}1^{+}, 2^{++}1^{+}, 3^{-+}1^{+}, 4^{++}1^{+}, \ldots$ the significant partial waves with such quantum numbers have been added. Those comprised the exotic $1^{-+}1^{+}\rho\pi P$, the $2^{++}1^{+}\rho\pi D$ and the $4^{++}1^{+}\rho\pi G$ waves. Two more from the series have actually been seen ($2^{++}1^{+}f_2\pi P$ and $4^{++}1^{+}f_2\pi F$) but happened to be very small. Finally, the $0^{-+}0^{+}f_0(980)\pi S$ and $2^{-+}0^{+}f_2\pi D$ waves have been considered because of their fast phase motions. Thus a total of seven waves has been selected for the mass-dependent fit (marked also in table 5.5). However, not all of their interferences with each other have been used, in particular not those between small amplitudes. In general, the two dominant waves have been considered to interfere with all other ones and also the $2^{++}1^{+}\rho\pi D$ with the $1^{-+}1^{+}\rho\pi P$.

The mass-dependent fit has been carried out from 0.80 to 2.32 GeV/c^2. Consistently the rank in (4.18) has been set to $N_r = 2$, as for the mass-independent fit. Furthermore, it has been made use of the possibility to multiply an overall mass-dependence on each amplitude (cf. section 4.5.1). Based on MC simulations of the one-Pomeron exchange

(parameterized as Regge trajectory) at a beam energy of 190 GeV, this term has been set to $1/m^{1.67}$ [181]. A total of 61 free parameters have been fitted by default, resulting in a reduced χ^2 of 2.17. In the following all seven partial wave intensities are shown one after the other, including the most expressed phase motions. Also the modelling in terms of Breit-Wigner (BW) and background functions is discussed, while the obtained resonance parameters are summarized in a compact form in section 5.5.2.

5.5.1.1 $1^{++}0^+\rho\pi S$

The dominant partial-wave intensity is the $1^{++}0^+\rho\pi S$ (figure 5.45). It has the shape of a rather broad bump centered at about 1.2 GeV/c^2 and can be dominantly described by one BW corresponding to the $a_1(1260)$ resonance. The parameterization of this BW has been taken from [182] and contains a dynamic (mass-dependent) width in the denominator (cf. equation (2.4)), taken as the integrated squared $1^{++}0^+\rho\pi S$ decay amplitude. In addition, an exponential background of the form $e^{-\alpha p^2}$ (cf. section 4.5.1) is needed, which could be due to the non-resonant Deck mechanism (see section 2.3.6). α has been a free parameter of the fit and a value of $(-1.01 \pm 0.24)\,(\mathrm{GeV}^2/c^2)^{-1}$ has been obtained. The $a_1(1260)$ parameters are listed in table 5.8.

5.5.1.2 $2^{-+}0^+f_2\pi S$

The second most significant amplitude is the $2^{-+}0^+f_2\pi S$ (figure 5.46). Its phase difference to the $1^{++}0^+\rho\pi S$ wave (figure 5.47) exhibits a clear resonating behavior around 1.7 GeV/c^2 consistent with the well-known $\pi_2(1670)$ meson. As an example, figure 5.48 shows the coherence between these two waves (see equation (4.17)), which is greater than 0.8 in the region of interest. The $2^{-+}0^+f_2\pi S$ partial wave has been described using one BW only and without any background contribution[20]. The total width of $\pi_2(1670)$ has been parameterized by taking its two main decay modes $f_2\pi S$ and $\rho\pi P$ into account, with a branching ratio of 60% and 40%, respectively. Other channels contribute with less than 10% and have been neglected.

5.5.1.3 $2^{++}1^+\rho\pi D$

The third well-established intensity, $2^{++}1^+\rho\pi D$ (figure 5.49), is large at "high-t'" only. It corresponds mostly to the $a_2(1320)$, however, the high-mass tail and especially the phase (figure 5.50) ask for a second resonance in the mass-dependent fit. Therefore this partial wave has been described with two BW functions, one for the $a_2(1320)$ and one for the $a_2(1700)$. For the standard seven waves fit, the parameters of the latter have been fixed to the PDG values [38] and only $a_2(1320)$ has been fitted (see table 5.8). A dynamic width BW based on the $\rho\pi D$ (80%) and the $\eta\pi D$ (20%) decay modes has been used, again neglecting other channels.

[20] It was tried to add coherent background, but it was not needed on the available level of statistics.

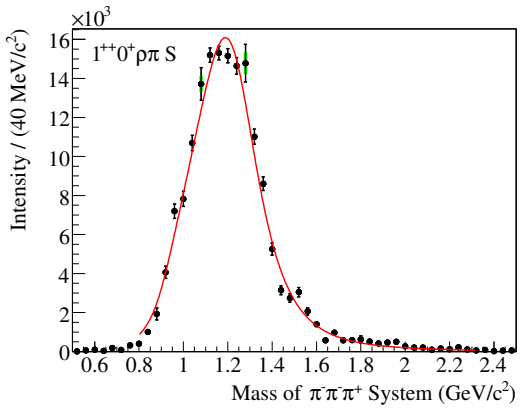

Figure 5.45: $1^{++}0^{+}\rho\pi S$ intensity.

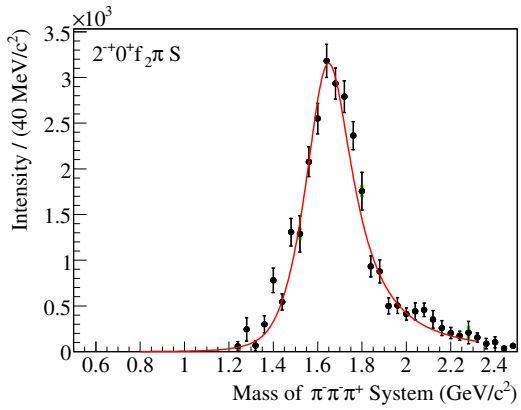

Figure 5.46: $2^{-+}0^{+}f_2\pi S$ intensity.

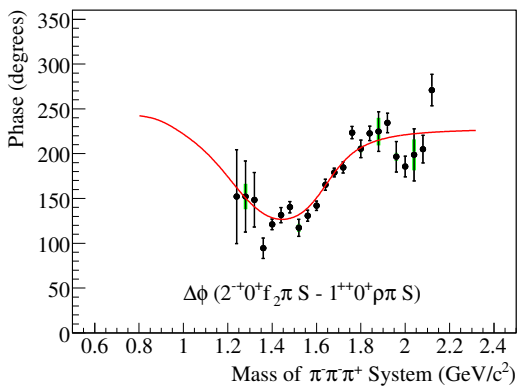

Figure 5.47: Phase difference between $2^{-+}0^{+}f_2\pi S$ and $1^{++}0^{+}\rho\pi S$.

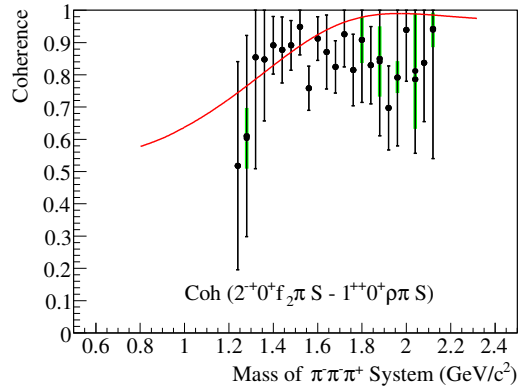

Figure 5.48: Degree of coherence between $2^{-+}0^{+}f_2\pi S$ and $1^{++}0^{+}\rho\pi S$.

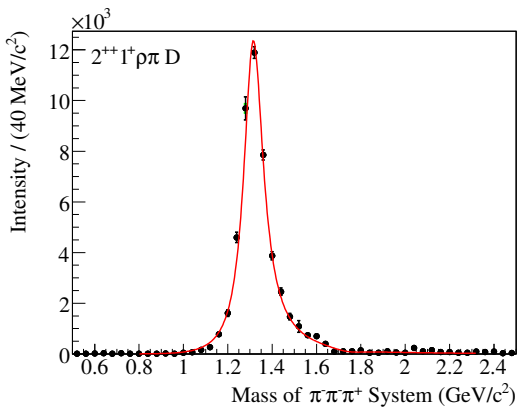

Figure 5.49: $2^{++}1^{+}\rho\pi D$ intensity.

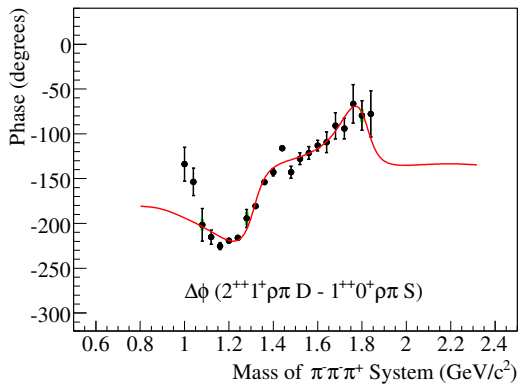

Figure 5.50: $2^{++}1^{+}\rho\pi D$ phase.

In the course of the systematic studies listed in section 5.6.2 it has been attempted also to fit $a_2(1700)$ instead of fixing its parameters. It turned out that this is difficult from the standard seven-waves fit and that the $2^{++}1^+ f_2\pi P$ wave has to be added as well[21]. This further wave puts in more information, and from an eight-waves mass-dependent fit some results for $a_2(1700)$ could be obtained (see section 5.5.2). However, also the standard fit describes the phase motion expressed in figure 5.50 very well. In the region around $1.3\,\mathrm{GeV}/c^2$ the phase of the narrow $a_2(1320)$ is rising, but the increase is less than 180° illustrating also the resonant behavior of $a_1(1260)$. The phase continues to rise around $1.7\,\mathrm{GeV}/c^2$, which demonstrates the discussed need for $a_2(1700)$.

5.5.1.4 $4^{++}1^+\rho\pi G$

Again produced dominantly at "high-t'", the $4^{++}1^+\rho\pi G$ signal (figure 5.51) represents the highest observed value of J. The peak intensity around $1.9\,\mathrm{GeV}/c^2$ is described by a BW function with a constant width in the denominator, because unfortunately no branching ratios for the corresponding $a_4(2040)$ meson have been published yet. Figure 5.52 presents the phase difference between this wave and the $1^{++}0^+\rho\pi S$ partial wave. The obtained $a_4(2040)$ mass is significantly smaller than the PDG average (see table 5.8), which has been identified to be connected to the constant width BW (see section 5.5.2).

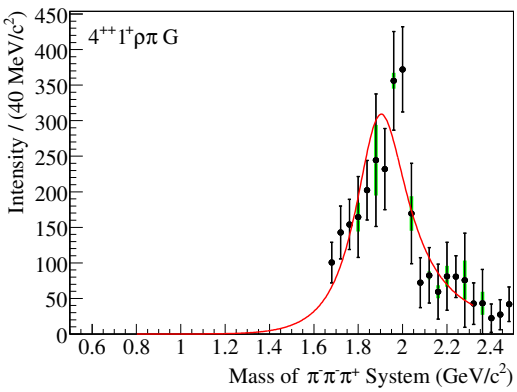

Figure 5.51: $4^{++}1^+\rho\pi G$ intensity.

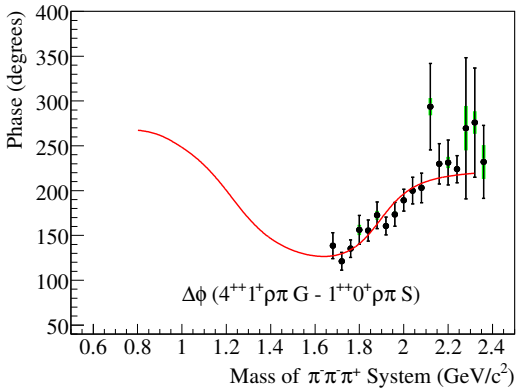

Figure 5.52: $4^{++}1^+\rho\pi G$ phase.

5.5.1.5 $0^{-+}0^+ f_0(980)\pi S$

Very small at "high-t'" (figure 5.53), the $0^{-+}0^+ f_0(980)\pi S$ amplitude is better pronounced by its phase motion relative to the $2^{-+}0^+ f_2\pi S$ wave (figure 5.54). The corresponding resonance is known as the $\pi(1800)$ meson. It is described by one constant width BW and some low mass background ($\alpha = (-0.98 \pm 0.56)\,(\mathrm{GeV}^2/c^2)^{-1}$), possibly needed due to the tail of $\pi(1300)$ (see also section 5.5.3). This relatively narrow signal (see table 5.8)

[21] Repeating first the mass-independent fit with a lowered threshold ($1.2\,\mathrm{GeV}/c^2$) for this wave.

helps to define the phase motion of the high-mass tail of the 2^{-+} wave and is therefore a useful component in the mass-dependent fit.

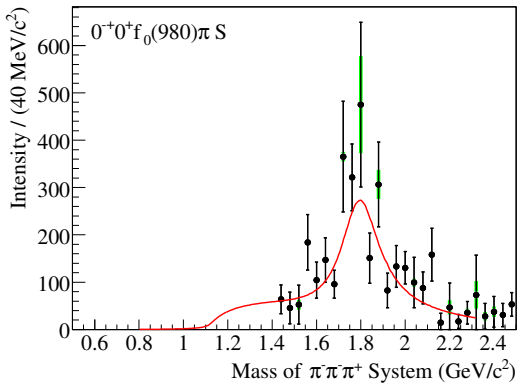

Figure 5.53: $0^{-+}0^{+}f_0(980)\pi S$ intensity.

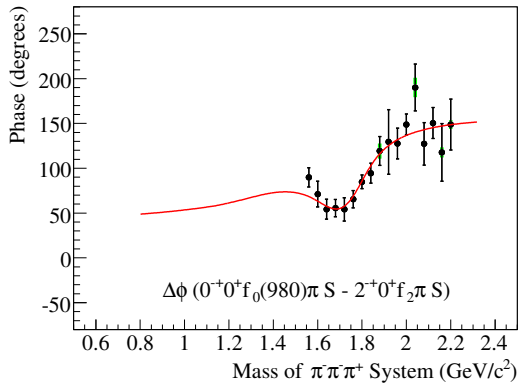

Figure 5.54: Phase difference between $0^{-+}0^{+}f_0(980)\pi S$ and $2^{-+}0^{+}f_2\pi S$.

5.5.1.6 $2^{-+}0^{+}f_2\pi D$

The $2^{-+}0^{+}f_2\pi D$ intensity (figure 5.55) shows a bump, which is clearly shifted to higher masses compared to the $2^{-+}0^{+}f_2\pi S$ case (figure 5.46). This bump cannot be explained as $\pi_2(1670)$, distorted by a D-wave barrier factor. In addition, the rising phase of this D wave relative to the S wave (figure 5.56) demonstrates that an additional 2^{-+} state is needed to explain the picture ($\pi_2(1880)$, see discussion in section 5.5.2). Using two resonances, $\pi_2(1670)$ parameterized as before (see section 5.5.1.2) and a second one higher in mass, provides a good description of both the intensity and the relative phase.

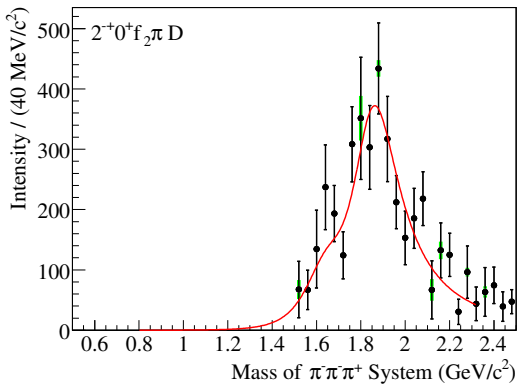

Figure 5.55: $2^{-+}0^{+}f_2\pi D$ intensity.

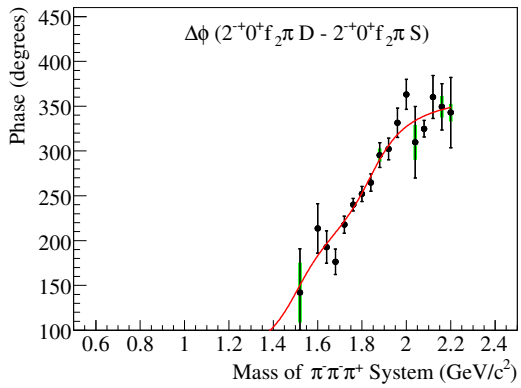

Figure 5.56: Phase difference between $2^{-+}0^{+}f_2\pi D$ and $2^{-+}0^{+}f_2\pi S$.

5.5.1.7 Spin-Exotic $1^{-+}1^+\rho\pi P$ Wave

The $1^{-+}1^+\rho\pi P$ intensity (figure 5.57) has the shape of a broad bump, centered at $1.6\,\mathrm{GeV}/c^2$, with a visible low-mass shoulder. One constant-width BW function (blue curve) and an exponential background (purple curve, $\alpha = (-1.13 \pm 0.28)\,(\mathrm{GeV}^2/c^2)^{-1}$) have been used to describe this wave. To clarify a possible resonant nature of this exotic amplitude, its interferences with well established states have been studied. Figure 5.58 shows the relative phase compared to the $1^{++}0^+\rho\pi S$ wave, which is difficult to measure because the tail of $a_1(1260)$ contains only $\sim 1\,000$ events at $1.6\,\mathrm{GeV}/c^2$. Nevertheless, this phase difference clearly rises. Also the degree of coherence is close to one in the region between 1.5 and $1.7\,\mathrm{GeV}/c^2$ (figure 5.59)[22]. More stable but less expressive is the phase relative to the $2^{-+}0^+f_2\pi S$ wave (figure 5.60), which has $\sim 3\,500$ events in the region of interest. This phase difference doesn't show any significant motion, indicating that two overlapping resonances might cancel each other. For further discussions on the nature of the 1^{-+} and also the obtained BW parameters, please refer to section 5.5.2.

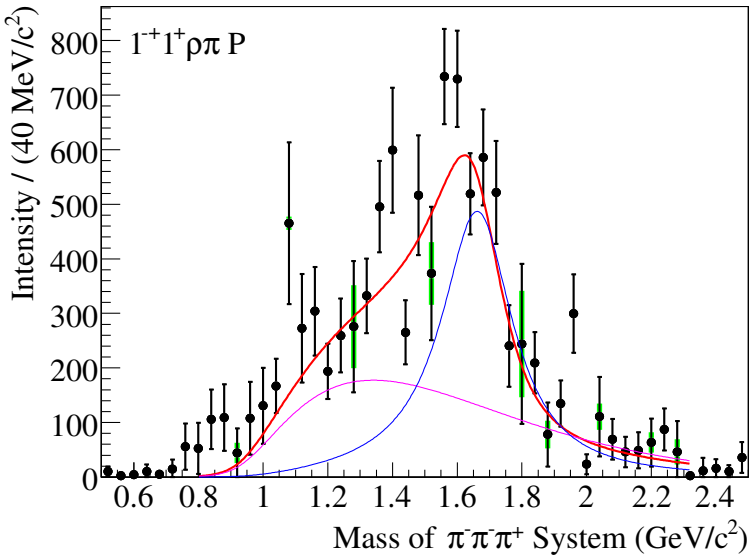

Figure 5.57: Spin-exotic $1^{-+}1^+\rho\pi P$ intensity; mass-dependent fit result shown as red curve. The blue and the purple curve illustrate the resonance and the background contribution, respectively (see text).

5.5.2 Summary and Discussion of "High-t'" Results

Table 5.8 and figure 5.61 summarize the resonance parameters obtained from the "high-t'" mass-dependent fit and compare them to the PDG values. In the table both mass M and width Γ are presented together with their statistical (from MINUIT, cf. section 4.5.2) and systematic errors. For the figures these errors have been added linearly. The system-

[22] The drop around $1.4\,\mathrm{GeV}/c^2$ is discussed later.

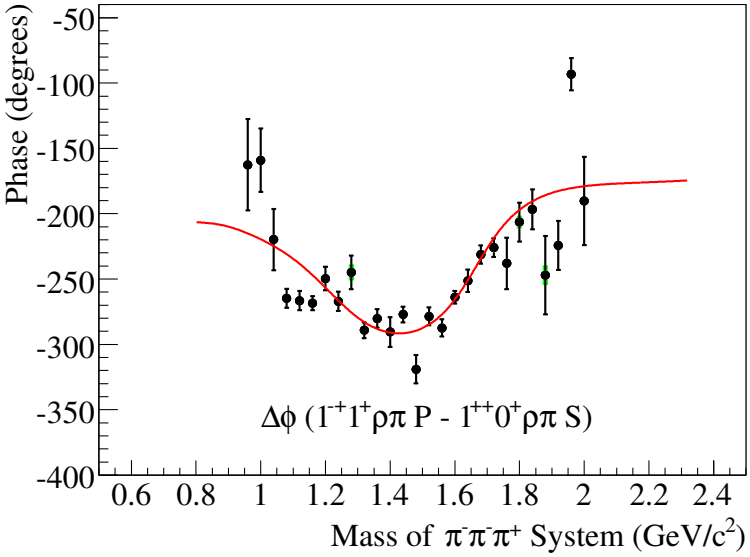

Figure 5.58: Phase difference $\Delta\phi$ between the spin-exotic $1^{-+}1^{+}\rho\pi P$ wave and the $1^{++}0^{+}\rho\pi S$ reference wave; mass-dependent fit shown in red color.

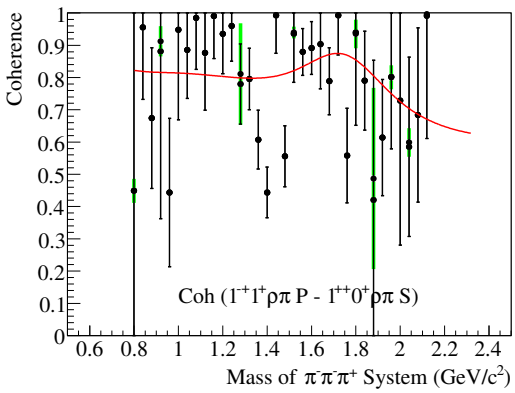

Figure 5.59: Degree of coherence between the $1^{-+}1^{+}\rho\pi P$ and the $1^{++}0^{+}\rho\pi S$ partial wave.

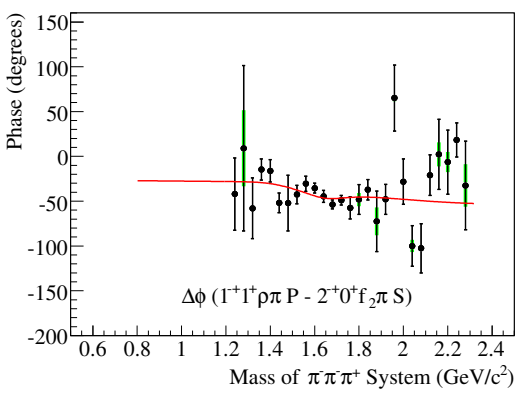

Figure 5.60: Compensation of the $1^{-+}1^{+}\rho\pi P$ and the $2^{-+}0^{+}f_2\pi S$ phase.

atic errors have been defined from a series of studies, which are listed in section 5.6.2. The last column of the table indicates the two studies out of the list responsible for the upper and lower limit, respectively. In addition to M and Γ, also the significance of a partial wave or resonance is important. This information has been compiled in table 5.9. Shown are the relative[23] intensity of each partial wave in percent and its statistical error (second column). The resonance part only, associated to a particular state, is presented in the fourth column. From this value N and its error σ, the given significance x has been defined according to $N = x\sigma$.

State	(GeV/c^2)	COMPASS ± stat ± syst	PDG	Study
$a_1(1260)$	M	1.256 ± 0.006 + 0.007 - 0.017	1.230 ± 0.040	2, 10
	Γ	0.366 ± 0.009 + 0.028 - 0.025	0.250 to 0.600	7, 6
$a_2(1320)$	M	1.321 ± 0.001 + 0.000 - 0.007	1.3183 ± 0.0006	1, 7
	Γ	0.110 ± 0.002 + 0.002 - 0.015	0.107 ± 0.005	7, 9
$\pi_1(1600)$	M	1.660 ± 0.010 + 0.000 - 0.064	$1.653^{+0.018}_{-0.015}$	1, 5
	Γ	0.269 ± 0.021 + 0.042 - 0.064	$0.225^{+0.045}_{-0.028}$	10, 8
$\pi_2(1670)$	M	1.659 ± 0.003 + 0.024 - 0.008	1.6724 ± 0.0032	2, 7
	Γ	0.271 ± 0.009 + 0.022 - 0.024	0.259 ± 0.009	2, 7
$\pi_2(1880)$	M	1.836 ± 0.013 + 0.000 - 0.044	-	1, 10
	Γ	0.263 ± 0.029 + 0.056 - 0.070	-	10, 8
$\pi(1800)$	M	1.785 ± 0.009 + 0.012 - 0.006	1.812 ± 0.014	7, 6
	Γ	0.208 ± 0.022 + 0.021 - 0.037	0.207 ± 0.013	7, 6
$a_4(2040)$	M	1.884 ± 0.013 + 0.050 - 0.002	2.001 ± 0.010	11, 2
	Γ	0.295 ± 0.024 + 0.046 - 0.019	0.313 ± 0.031	10, 4

Table 5.8: Results from mass-dependent fit of "high-t'" data compared to PDG values [38]; statistical and systematic errors shown separately (see text).

The well-known mesons $a_1(1260)$, $a_2(1320)$ and $\pi_2(1670)$ are resolved with high significance ($> 30\sigma$) and consistent with the PDG averages. $a_2(1320)$ is the most narrow resonance in the $\pi^-\pi^-\pi^+$ data and the only one which might be effected by the mass resolution of the spectrometer (cf. section 5.3.2.1). It has been estimated that its width could be up to $15\,\mathrm{MeV}/c^2$ smaller (see e. g. section 5.7), which is reflected in the systematic error. While $a_1(1260)$ interferes with a non-negligible background (probably Deck-like, cf. section 2.3.6), $a_2(1320)$ and $\pi_2(1670)$ are seen background free in the respective 2^{-+} and 2^{++} waves (sections 5.5.1.2 and 5.5.1.3). In the latter case a second resonance at around $1.7\,\mathrm{GeV}/c^2$ is needed to describe the observed phase behavior. In a dedicated study this second resonance has been fitted, resulting in a mass and width of $(1.660 \pm 0.030)\,\mathrm{GeV}/c^2$ and $(0.380 \pm 80)\,\mathrm{GeV}/c^2$, respectively. This is more or less

[23] Relative to the total intensity of the seven waves used in the mass-dependent fit. This includes overlaps between waves, thus the values in table 5.9 do not precisely sum up to 100%.

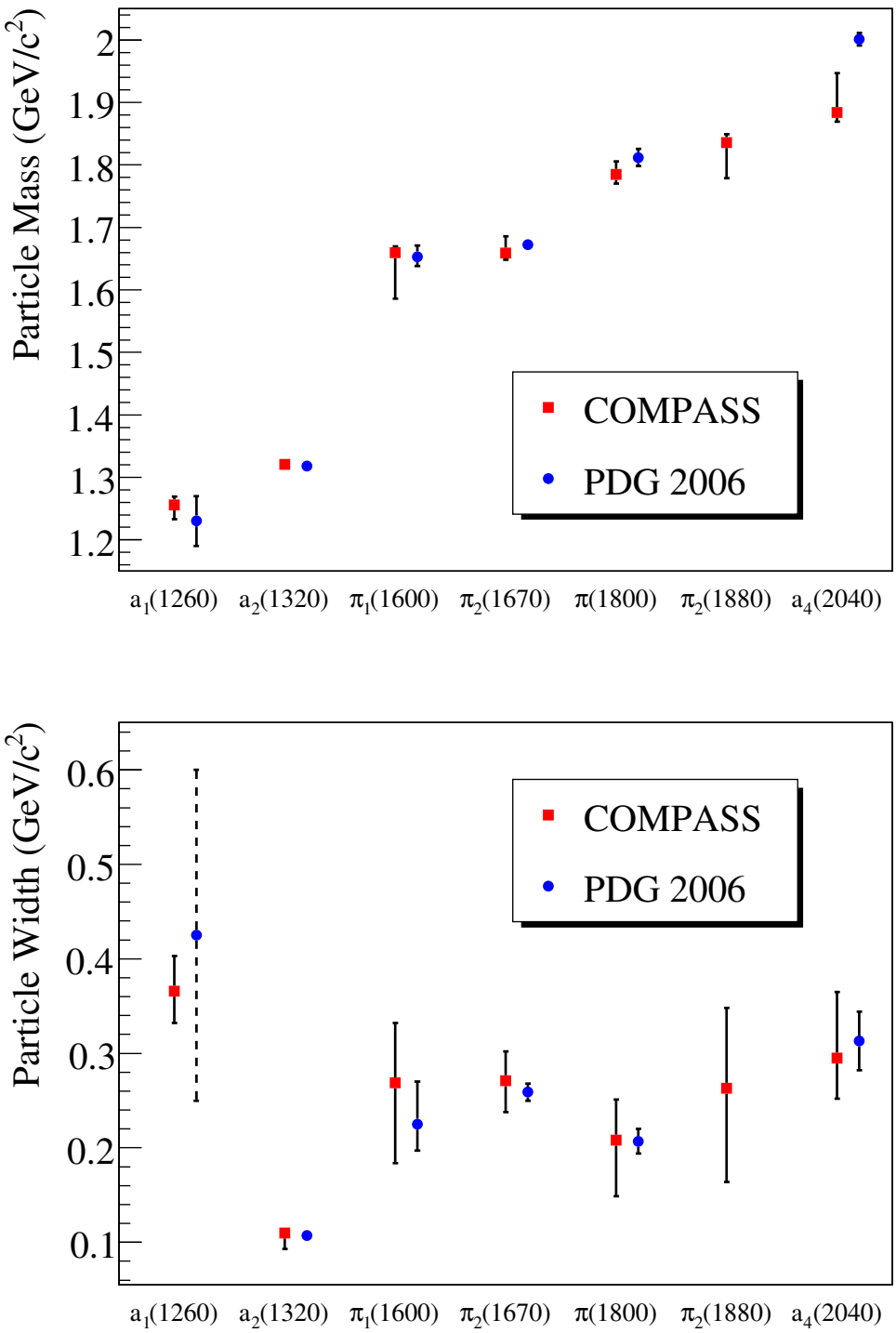

Figure 5.61: Overview of the resonance parameters (top: mass, bottom: width) from the "high-t'" mass-dependent fit and comparison to PDG values [38]. Sum of COMPASS statistical and systematic errors shown. For the $a_1(1260)$ width the PDG defines only a range, while $\pi_2(1880)$ is not yet listed at all (see text).

Wave	Intensity (%)	Resonance	Intensity (%)	Significance (σ)
$1^{++}0^+\rho\pi S$	61.5 ± 0.6	$a_1(1260)$	65 ± 2	32.5
$2^{++}1^+\rho\pi D$	17.9 ± 0.6	$a_2(1320)$	18.9 ± 0.6	31.5
$1^{-+}1^+\rho\pi P$	3.0 ± 0.2	$\pi_1(1600)$	1.6 ± 0.2	8.0
$2^{-+}0^+f_2\pi S$	9.8 ± 0.4	$\pi_2(1670)$	9.8 ± 0.3	32.7
$2^{-+}0^+f_2\pi D$	1.3 ± 0.4	$\pi_2(1880)$	2.3 ± 0.6	3.8
$0^{-+}0^+f_0\pi S$	1.0 ± 0.2	$\pi(1800)$	0.78 ± 0.11	7.1
$4^{++}1^+\rho\pi G$	1.0 ± 0.2	$a_4(2040)$	1.0 ± 0.2	5.0

Table 5.9: Relative intensity of each partial wave used in the mass-dependent fit; fraction and significance of the respective dominant resonance shown separately (see text).

consistent with the $a_2(1700)$ meson, which has been reported by several experiments[24]. The obtained width is by a factor of 2 larger than the PDG average of $(194 \pm 40)\,\mathrm{GeV}/c^2$, but is in good agreement with recent results [186]. Unfortunately, the COMPASS 2004 statistics is very limited here.

Less studied but nevertheless also well established are the $\pi(1800)$ and the $a_2(2040)$ mesons, which are both seen in the data but with lower significance (7σ and 5σ) compared to the dominant three states. $\pi(1800)$ can be fitted with a constant width BW, but a small background is needed to describe the corresponding 0^{-+} partial wave (section 5.5.1.5). This is possibly due to a tail of $\pi(1300)$, which has not been studied in the "high-t'" analysis. $\pi(1800)$ and $\pi(1300)$ are produced much more at "low-t'" (see section 5.5.3). The $a_4(2040)$ with $J = 4$ is the state with the highest total angular momentum. Compared to the PDG average the fitted mass is lower by about $100\,\mathrm{MeV}/c^2$. A dedicated study has indicated that this is probably due to the constant width BW parameterization used in the mass-dependent fit. By using instead a dynamic width based on just the $\rho\pi$ decay channel, immediately a $50\,\mathrm{MeV}/c^2$ higher mass has been obtained. This defines the upper systematic error on the $a_4(2040)$ mass in table 5.8.

Highlight of the "high-t'" PWA is certainly the 8σ exotic 1^{-+} signal (cf. section 5.5.1.7). The fitted BW resonance is consistent with the much disputed $\pi_1(1600)$ state, which is one of the most promising hybrid candidates (see section 2.4.1). Its phase has been studied with respect to both $a_1(1260)$ and $\pi_2(1670)$. While in the first case a clean motion around 1.6-1.7 GeV/c^2 is expressed (figure 5.58), the phase of π_1 and π_2 seem to compensate each other (figure 5.60). This behavior was observed by other experiments as well [113]. In summary, COMPASS confirms the $\pi_1(1600)$ in $\pi^-\pi^-\pi^+$ final states.

On the level of available statistics, it has been difficult to judge on the nature of the low-mass shoulder in the 1^{-+} wave. Effectively it has been described by introducing coherent background, but there are several possible explanations. First of all there is always the suspicion of dominant states leaking to the exotic wave. Previous experiments had in fact severe leakage problems, mostly below $1.4\,\mathrm{GeV}/c^2$ [110, 113]. The leakage study pre-

[24] See for example [183, 184, 185]; the state is still omitted from the PDG summary table.

sented in section 5.7, however, doesn't show any sign of leakage at COMPASS on the level of 5%. Interesting is also that the rank 1 fit looks cleaner in that respect[25]. In addition to this technical issue there are also two physics arguments: First of all, if the 1^{-+} wave is also affected by the Deck effect (like in the 1^{++} case), the standard background description would be perfectly right. More exciting but less probable is the possibility of having also the second known exotic 1^{-+} state in the data, namely the $\pi_1(1400)$ (cf. section 2.4.1). The drop in coherence in figure 5.59 immediately speaks against this, but one way out could be that for some reason $\pi_1(1400)$ and $a_1(1260)$ sit in the two different production vectors of the rank 2 fit. As one of the systematic studies (see section 5.6.2) the mass-dependent fit has been performed assuming a second resonance in the 1^{-+} wave. This results in a $\sim 60\,\mathrm{MeV}/c^2$ lower mass of the $\pi_1(1600)$ and is the reason for the very asymmetric systematic error in table 5.8.

The fitted width of $\pi_1(1600)$ is in principle consistent with theory predictions for a hybrid (cf. section 2.1.3.2). However, the total error is very large and doesn't impose any severe constraints. Also the unclear situation of the low-mass shoulder prevents a precise measurement of Γ. Having in mind that the presented analysis is based on the data of about two days only, COMPASS has an enormous potential to clarify all the raised questions.

Although not spin-exotic, the second 2^{-+} resonance above $1.8\,\mathrm{GeV}/c^2$ (section 5.5.1.6) is very interesting, too. There is in fact a discussed hadron with these properties, $\pi_2(1880)$, which is a hot candidate for a hybrid with normal quantum numbers [26]. The significance of this state is about 4σ only, but it is seen in the "low-t'" data also[26]. It is predicted to decay dominantly into $\rho\pi$ and $f_2\pi$ [52, 53, 187] and has been observed by several experiments [109, 118, 183, 188]. However, the $\pi_2(1880)$ is not yet established and therefore not listed by the PDG [38].

5.5.3 "Low-t'" Intensities and Phases

The "low-t'" data exceed the "high-t'" statistics by about a factor of 5 (see table 5.3) and are almost background free (see figure 5.4). They are very promising for meson spectroscopy, too, although no spin-exotic 1^{-+} signal is expected here, because the mandatory spin projection $M = 1$ is strongly suppressed. The same is true for the 2^{++} and the 4^{++} waves[27]. However, this event sample is ideal to study the 0^{-+}, 1^{++} and 2^{-+} waves. Indeed a first preliminary PWA brought forward very interesting results. The employed set of 55 partial waves is shown in table 5.7 and the major spin totals in figure 5.38. In this section a selection of individual intensities and phases is presented. On the one hand side they provide an interesting comparison to the "high-t'" results. On the other hand they prove the great potential of this different t' regime, which has been studied in few other experiments only [60, 109] by means of a $\pi^-\pi^-\pi^+$ PWA. No successful mass-dependent fit has been achieved for "low-t'" within this work, thus all interpretations have to be taken with care.

[25] But has other disadvantages; see section 5.6.1.

[26] In contrast to $\pi_1(1600)$; see section 5.5.3.

[27] Still some $a_2(1320)$ signal is observed at "low-t'"; see comments in section 5.4.2.2.

Figure 5.62 presents two of the $1^{++}0^+$ partial wave intensities, namely those with the $\rho\pi S$ (left) and the $f_2\pi P$ (right) decay chain. The former looks similar to the corresponding "high-t'" distribution (figure 5.45), but with the higher statistics maybe the radial excitation $a_1(1640)$ is seen in addition to $a_1(1260)$[28]. Moving to the $1^{++}0^+ f_2\pi P$ wave a clean $a_1(1640)$ signal is observed, however, at a mass higher than the PDG average of $(1.647 \pm 0.022)\,\mathrm{GeV}/c^2$ [38]. This is interestingly consistent with the other published $\pi^-\pi^-\pi^+$ data [113]. A further wave which contains the $a_1(1640)$ at "low-t'" is the $1^{++}0^+\rho\pi D$ (not shown here).

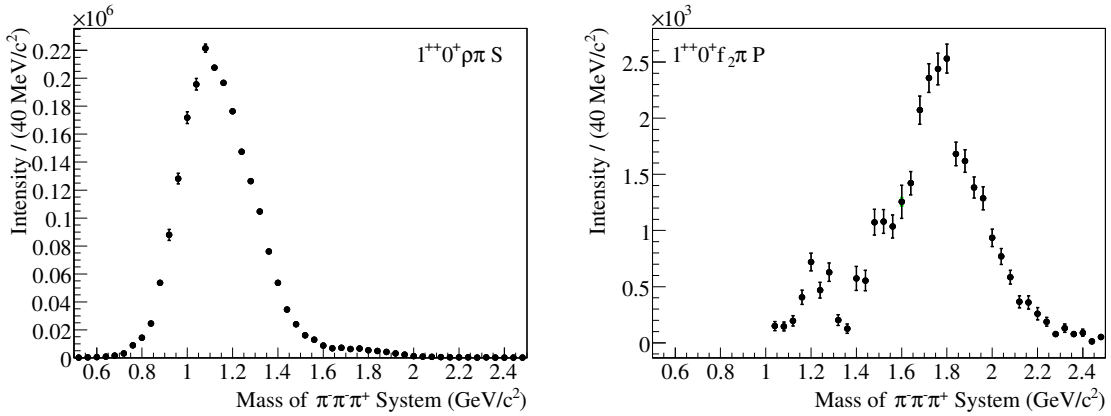

Figure 5.62: $1^{++}0^+\rho\pi S$ intensity (left) and $1^{++}0^+ f_2\pi P$ intensity (right); both obtained from the "low-t'" data.

Next the $2^{-+}0^+ f_2\pi S$ intensity is shown (figure 5.63) (left), which contains a perfect $\pi_2(1670)$ signal. Again this should be compared to the "high-t'" pendant (figure 5.46), because with high statistics a second peak at about $2.1\,\mathrm{GeV}/c^2$ is resolved. This could be the $\pi_2(2100)$ meson[29], which is supported by the beautiful phase motion seen in addition to the one of $\pi_2(1670)$ (figure 5.63, right).

The $0^{-+}0^+ f_0(980)\pi S$ intensity (figure 5.64, left) exhibits a strong $\pi(1800)$ signal. Its significance at "low-t'" is almost as high as for $\pi_2(1670)$ and its phase motion (same figure, right) is very well expressed between the motions of $\pi_2(1670)$ and $\pi_2(2100)$, respectively. Figure 5.65 (left) shows another 0^{-+} wave, $0^{-+}0^+\rho\pi P$, which is the only case where $\pi(1300)$ is maybe seen. This broad meson has a mass and width of $M = (1.3 \pm 0.1)$ and $\Gamma = 0.2$ - $0.6\,\mathrm{GeV}/c^2$, respectively.

On the right of figure 5.65 the $2^{-+}0^+ f_2\pi D$ wave intensity is presented. It contains a similar peak than is observed at "high-t'" (figure 5.55) in the same partial wave, but with much higher statistics. Also the (here not shown) phase motion with respect to the $2^{-+}0^+ f_2\pi S$ wave looks almost identical (figure 5.56). The potential hybrid $\pi_2(1880)$ is discussed at the end of section 5.5.2.

An important cross-check concerning the spin-exotic $\pi_1(1600)$ signal observed at "high-t'" is to prove its absence at "low-t'". This is done by figure 5.66, which shows the

[28] The PDG doesn't list $a_1(1640)$ in its meson summary table yet and states that it needs confirmation.
[29] Also this meson is not in the PDG summary table yet, but a few evidences exist [60, 109].

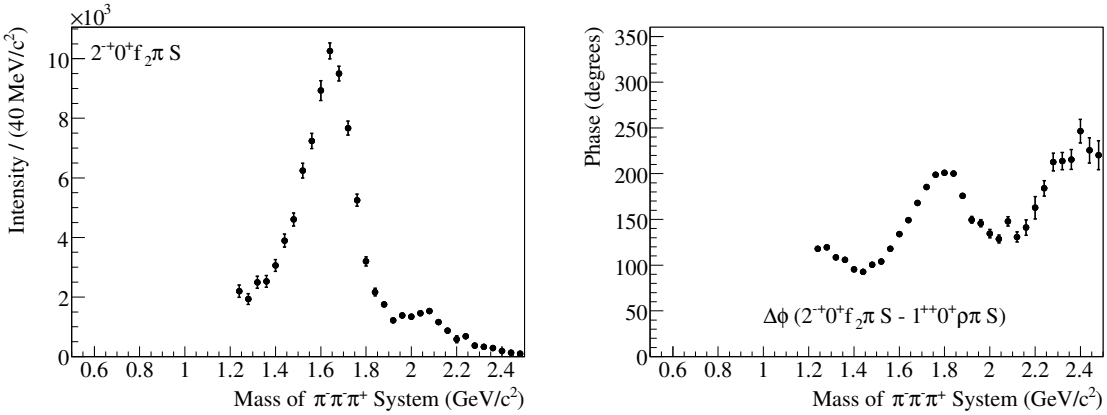

Figure 5.63: $2^{-+}0^{+}f_2\pi S$ intensity at "low-t'" (left) and its phase difference compared to $1^{++}0^{+}\rho\pi S$ (right).

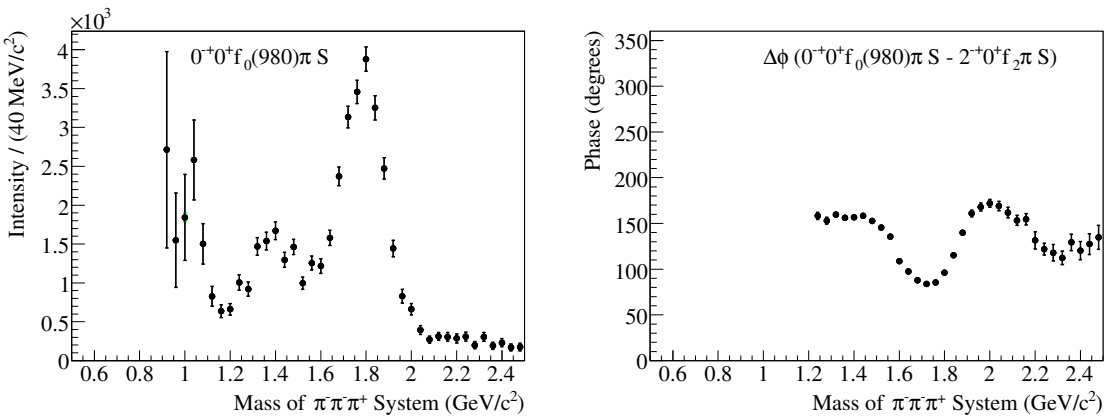

Figure 5.64: $0^{-+}0^{+}f_0(980)\pi S$ intensity at "low-t'" (left) and its phase difference compared to $2^{-+}0^{+}f_2\pi S$ (right).

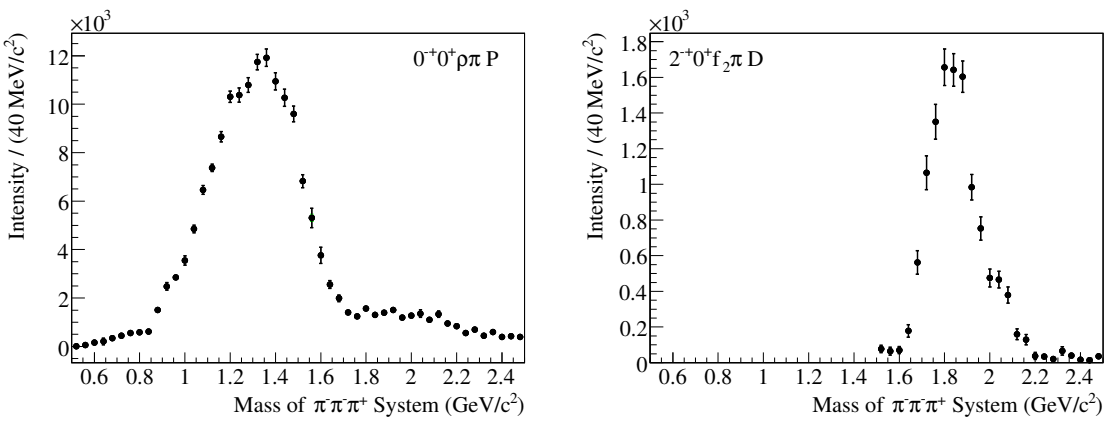

Figure 5.65: $0^{-+}0^{+}\rho\pi P$ (left) and $2^{-+}0^{+}f_2\pi D$ (right) intensities at "low-t'".

$1^{-+}1^+\rho\pi P$ intensity (left) and phase (right) at "low-t'". Only around $1.3\,\mathrm{GeV}/c^2$ there is some activity in the intensity, but it should be remembered that the "low-t'" statistics is larger by a factor of about 5 compared to "high-t'". The phase difference compared to the $2^{-+}0^+ f_2\pi S$ shows a more or less undisturbed $\pi_2(1670)$ motion, in contrast to figure 5.60 where $\pi_1(1600)$ and $\pi_2(1670)$ compensate each other.

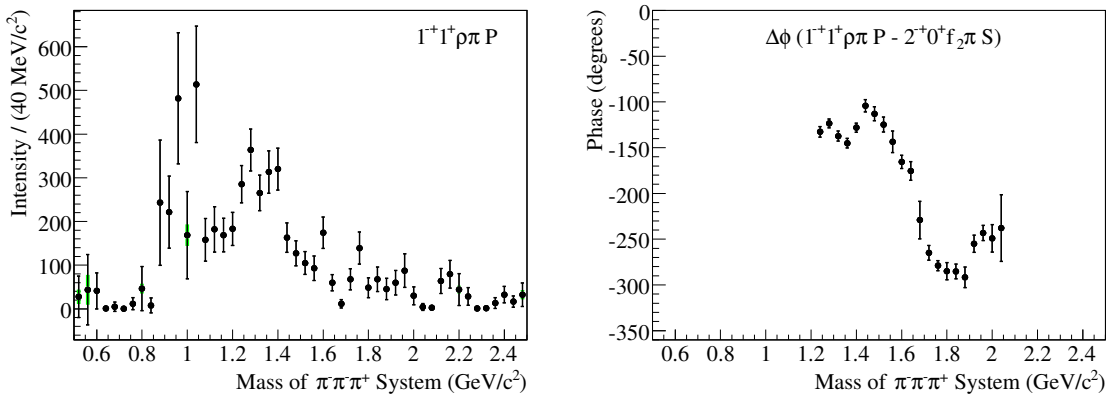

Figure 5.66: $1^{-+}1^+\rho\pi P$ intensity at "low-t'" (left) and its phase difference compared to $2^{-+}0^+ f_2\pi S$ (right).

5.6 Systematic Studies

In addition to the standard PWA described in sections 5.4 and 5.5, several studies have been performed to estimate the stability and the systematics of the analysis. Although in principle determined from physics, the rank of the mass-independent PWA has been varied for example, both for the "high-t'" and the "low-t'" case. The systematic errors presented in table 5.8 for the resonances observed at "high-t'" have been defined from a series of tests, which are listed in the second part of this section.

5.6.1 Effect of Different Rank in PWA

The choice of the rank N_r for the PWA has always led to many discussions within the spectroscopy community. It is not intended to enter this dispute, but some general comments can be made rather safely. First of all the degree of coherence of the fit naturally increases by lowering the rank, because less independent production amplitudes exist. Smoother resonance shapes could be obtained, but at the same time the background wave will grow and interesting signals will loose intensity. On the other hand, increasing N_r too much will always result in large fluctuations. Thus in addition to the physics arguments for $N_r = 2$ at "high-t'" and $N_r = 1$ at "low-t'" (cf. section 4.3.1), the available statistics and data quality plays a role. This is demonstrated in figure 5.67, which shows the flat wave at "high-t'" for $N_r = 1, 2, 3$ (left) and at "low-t'" for $N_r = 1, 2$ (right). Figure 5.68 (left) presents the exotic 1^{-+} wave, where the fluctuations and error bars grow

with N_r. In contrast, the 2^{-+} spin total (right) is much less effected. This is true for most of the waves, only the 0^{-+} intensity has been found to depend on the rank. In summary, it has been concluded that rank 2 is the most appropriate for "high-t'".

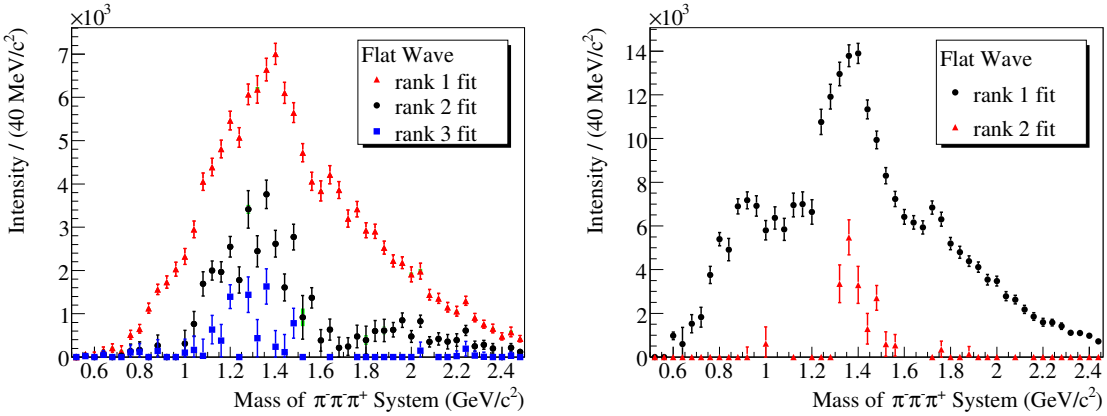

Figure 5.67: Variation of the background wave at "high-t'" (left) and "low-t'" (right) with the rank of the mass-independent PWA.

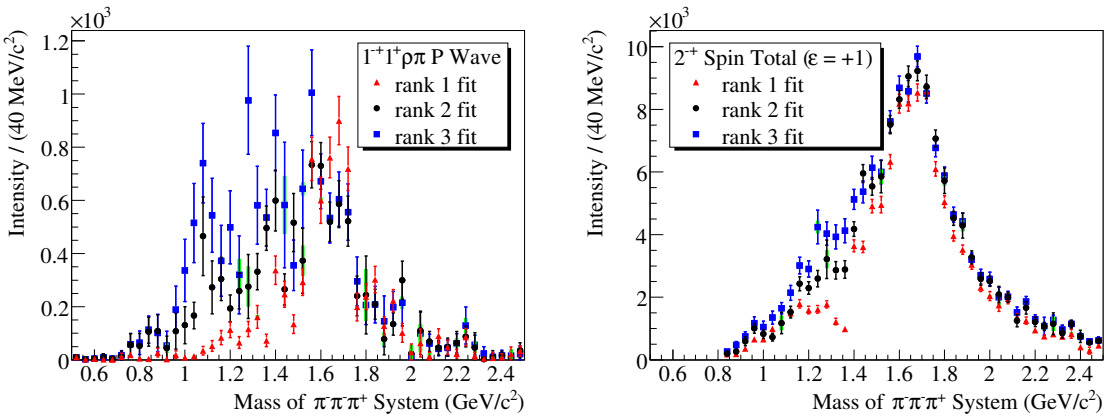

Figure 5.68: Exotic $1^{-+}1^{+}\rho\pi P$ partial wave (left) and 2^{-+} ($\epsilon = +1$) spin total (right) at "high-t'" for different ranks.

5.6.2 Systematic Error Estimates for "High-t'"

The following list summarizes and briefly describes the systematic studies which have been performed in addition to the standard analysis (repeated here as first item). Both the mass-independent and the mass-dependent fits have been varied. The lowest and the highest value obtained for a mass or width of a certain resonance have been taken to define the asymmetric systematic errors in table 5.8 (last column, same numbering as here). If a particular study is also discussed somewhere else in this chapter, a reference is given. Figure 5.69 illustrates the results of study number 5.

1. Standard analysis: 42 waves in mass-independent PWA, 7 waves in mass-dependent fit (0.8 - 2.32 GeV/c^2), parameters of $a_2(1700)$ fixed to PDG values
2. 42 waves in mass-independent fit with lowered mass threshold (1.2 GeV/c^2) for the $2^{++}1^+ f_2\pi P$ wave, $2^{++}1^+ f_2\pi P$ wave added to mass-dependent fit as eighth wave and parameters of $a_2(1700)$ released; see also section 5.5.1.3
3. Standard analysis with opened exclusivity cut: (189 ± 5) GeV
4. Standard analysis with tightened exclusivity cut: (189 ± 3) GeV
5. $\pi_1(1400)$ added as second constant width Breit-Wigner resonance to describe the exotic 1^{-+} wave in the mass-dependent fit, parameters of $\pi_1(1400)$ fixed to PDG values: $M = (1.376 \pm 0.017)$ GeV/c^2 and $\Gamma = (0.300 \pm 0.040)$ GeV/c^2, result shown in figure 5.69; see also sections 5.5.1.7 and 5.5.2
6. 1.6 mm target data completely removed from the analysis
7. 46 waves in mass-independent fit with four $M = 2$ waves included, thresholds adjusted
8. D-functions with relativistic factors instead of Zemach tensors used for mass-independent fit; cf. section 4.2
9. Experimental 3π mass resolution (from MC, section 5.3.2.1) included to mass-dependent fit; see also section 5.5.2
10. 40 MeV/c^2 mass bins shifted by 20 MeV/c^2 for mass-independent fit, mass-dependent fit then performed from 0.78 - 2.30/c^2
11. Dynamical width for $a_4(2040)$ used instead of constant one; see also section 5.5.2

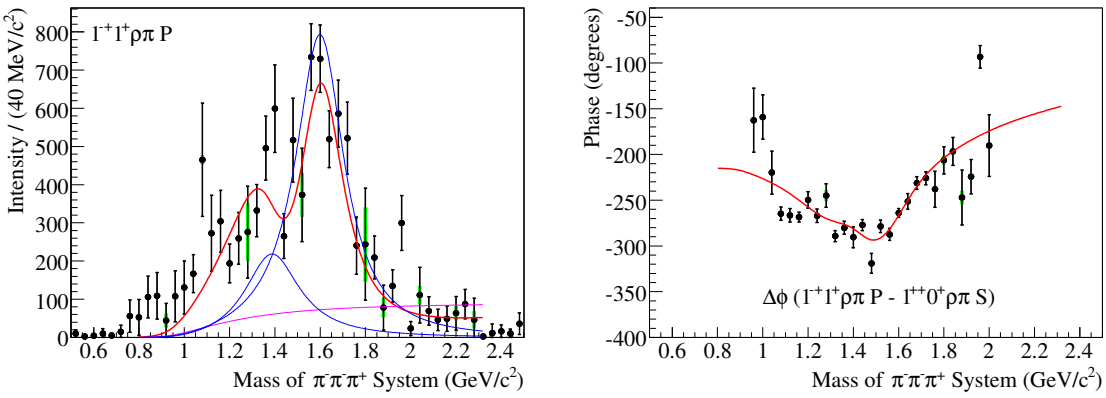

Figure 5.69: Illustration of systematic study number 5: $\pi_1(1400)$ added as second resonance (small blue curve) to describe the low-mass shoulder in the exotic wave intensity (left); the phase motion is almost unchanged compared to figure 5.58 (right).

5.7 Leakage Study for Exotic Wave at "High-t'"

For the leakage study 1 150 000 events following an optimized PWA model have been generated. First the 16 dominant partial waves obtained from the standard mass-independent fit have been fitted in terms of Breit-Wigner resonances and coherent backgrounds (mass-dependent fit for $0.80 \leq m \leq 2.32\,\mathrm{GeV}/c^2$). This included in particular several $J^{PC} = 2^{-+}$ waves, with both spin projections $M = 0$ and $M = 1$ and decay channels $f_2\pi S$, $f_2\pi D$, $\rho\pi P$ and $\rho\pi F$, which are potentially most dangerous concerning leakage to the exotic $1^{-+}1^{+}\rho\pi P$ wave [12]. The latter has also been one of the 16 fitted waves, but has then been excluded for the event generation to study the possibility of "fake" signals due to leakage. Thus 15 partial waves have been generated, using the mass-dependent cross-section formula (4.1). This cross-section comprised all relevant decay amplitudes plus the optimized production amplitudes and parameters for each Breit-Wigner term. It covered $\sim 75\%$ of the total number of events in the treated mass interval.

In a next step, the generated event sample has been subject to the full Monte-Carlo simulation and reconstruction as described in section 5.3. The obtained events have been selected or rejected based on the same cuts, which have been applied to the real data also. Afterwards a mass-independent PWA has been performed, using the standard wave set. Approximately two times more "high-t'" MC than real events have been simulated. If the leakage sample is normalized accordingly (figure 5.70), the amount of "fake" exotic intensity is found to be less than 5%. Also no significant non-diagonal elements of the spin density matrix have been observed, in other words no "fake" interference terms. Within the statistical errors, the parameters of the input resonances have furthermore been retrieved correctly from the standard seven-waves mass-dependent fit. The only significant finding has been an increased $a_2(1320)$ width (by $\sim 10\,\mathrm{MeV}/c^2$), reflecting the finite resolution. This is covered by the even larger corresponding error in table 5.8, which has been estimated based on a dedicated study (number 9 in section 5.6.2).

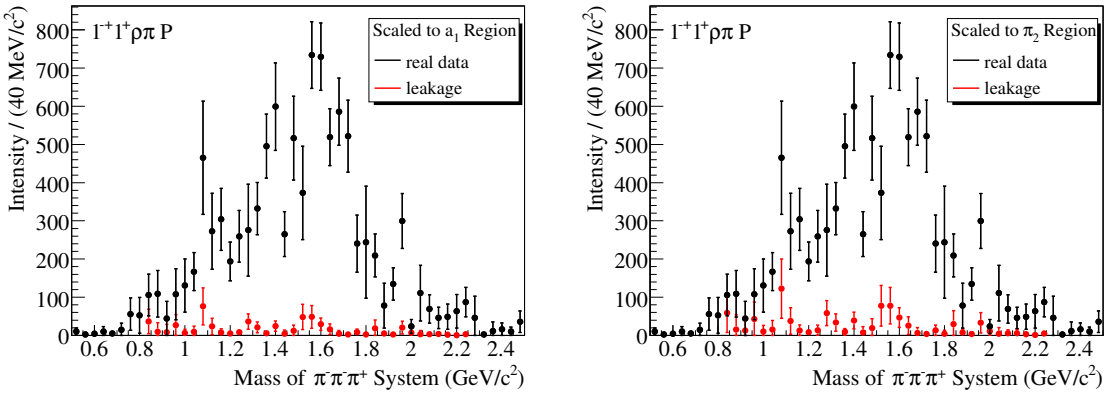

Figure 5.70: Simulated leakage to the $1^{-+}1^{+}\rho\pi P$ wave (red), compared to real data (black); MC events normalized to $a_1(1260)$ (left) or $\pi_2(1670)$ (right) region.

5.8 First Glimpse at the $\pi^-\pi^-\pi^-\pi^+\pi^+$ Data

As discussed in section 2.1.3, the flux tube model makes predictions for branching ratios of light-hybrid decays. In particular the partial widths for the $b_1(1235)\pi$ and the $f_1(1285)\pi$ channels are supposed to be much higher than those for a decay into $\rho\pi$. Since still in the latter case a strong $\pi_1(1600)$ signal has been observed in the presented $\pi^-\pi^-\pi^+$ PWA (cf. section 5.5.2), an obvious question is whether or not also the theory-favored channels could be studied. The $b_1(1235)$ decays dominantly into $\omega\pi$ [38], thus it would be necessary to reconstruct a π^0 in the final state by exploiting the information from the electromagnetic calorimeter of COMPASS (see chapter 3). More easy from the point of view of the event selection is to search for $f_1(1285)$ in the data, because it decays with a branching ratio of $(11 \pm 1)\%$ into four charged pions. In addition it is very narrow ($(\Gamma = 24.2 \pm 1.1)\,\mathrm{MeV}/c^2$, $M = 1.281.8 \pm 0.6\,\mathrm{MeV}/c^2$) and should therefore give a clean signature.

In order to estimate the potential of the $f_1(1285)\pi$ channel, the $\pi^-\pi^-\pi^+$ event selection as described in section 5.1 has been extended to $\pi^-\pi^-\pi^-\pi^+\pi^+$ final states. No cut optimizations have been performed[30] and also not exactly the same statistics have been processed. However, it is still possible to roughly compare the number of obtained exclusive 5π events to the 3π case, which is about a factor of 10 lower. Figure 5.71 shows the corresponding t' distribution, exhibiting a diffraction pattern similar to the one of figure 5.5. As expected the t' resolution is worse here, because five pions have to be reconstructed. Next figure 5.72 presents the invariant mass of the 5π system, which contains an enhancement of events around $1.8\,\mathrm{GeV}/c^2$ (possibly $\pi(1800)$). In general, higher masses are accessed compared to the 3π case (see e. g. figure 5.9).

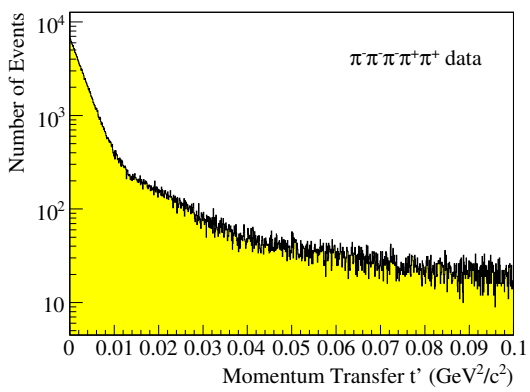

Figure 5.71: 4-momentum transfer t' for diffraction of beam pions on lead nuclei; $\pi^-\pi^-\pi^-\pi^+\pi^+$ final states.

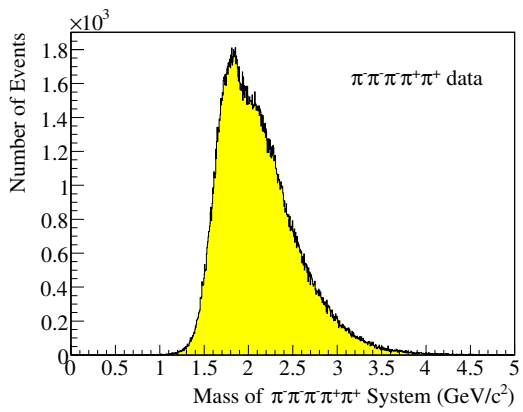

Figure 5.72: Invariant mass of the 5π system for all t'.

[30] Which would probably be necessary for the vertex and the exclusivity cut. The latter as well as the momentum transfer calculation have been performed here based on the total energy of the five pions.

The next step has been to plot in a 2-dim. histogram the mass of a neutral $\pi^-\pi^-\pi^+\pi^+$ subsystem versus the mass of a $\pi^-\pi^+$ sub-subsystem, which is shown on the left of figure 5.73. More precisely there are three combinations per event to form a neutral 4π system, and then four possibilities for each of them to define a $\pi^-\pi^+$ subsystem. Thus the histogram comprises a total of 12 entries per event. Indeed, a clear $f_1(1285)$ signal is seen in form of a sharp band around $m_{4\pi} = 1.280\,\mathrm{GeV}/c^2$. The 2-dim. histogram has been projected onto its x axis for $\pi^-\pi^+$ masses below $0.63\,\mathrm{GeV}/c^2$ (below the indicated black line). The resulting 4π mass distribution is presented on the right of figure 5.73, including a simple fit of the $f_1(1285)$ signal with a Gaussian[31] and a second order polynomial (blue curve). The amplitude of the Gaussian is $1\,186 \pm 32$ and its mean and σ are $(1.2829 \pm 0.0006)\,\mathrm{GeV}/c^2$ and $0.0217 \pm 0.0018\,\mathrm{GeV}/c^2$, respectively. Thus a significant amount of $f_1(1285)$ mesons is seen in the data and they are resolved with good precision[32]. It is therefore worthwhile to continue the study of the 5π system and, recently, the challenge has been started to set up a PWA also for this case [189].

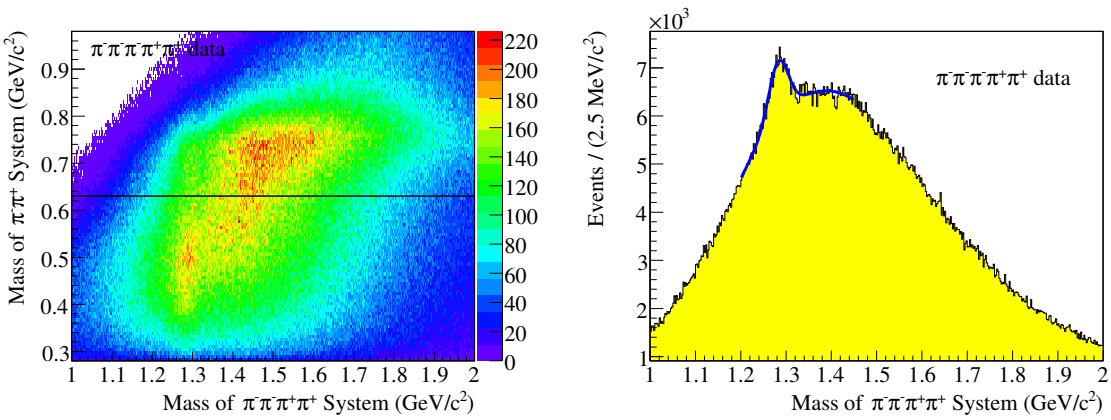

Figure 5.73: Mass of neutral 4π system vs. mass of $\pi^-\pi^+$ subsystem (left); 12 entries per event. The projection of this 2-dim. histogram onto the x axis for $\pi^-\pi^+$ masses below $0.63\,\mathrm{GeV}/c^2$ exhibits a clear $f_1(1285)$ signal (right). A fit to the distribution using a Gaussian and a second order polynomial has been performed (blue curve, see text).

[31]Since $f_1(1285)$ is so narrow, its width in the data is dominated by the experimental resolution. Therefore a Gaussian instead of a Breit-Wigner parameterization is sufficient.

[32]For comparison: the PDG mass and width are $m = (1.2818 \pm 0.0006)\,\mathrm{GeV}/c^2$ and $\Gamma = 0.0242 \pm 0.0011\,\mathrm{GeV}/c^2$, respectively [38]. If the fitted σ is translated into a "full-width-half-maximum", $\Gamma = (0.051 \pm 0.004)\,\mathrm{GeV}/c^2$ is obtained.

Chapter 6

The PANDA Experiment at FAIR

Based on the existing GSI[1] accelerators, an international Facility for Antiproton and Ion Research (FAIR) was proposed in 2001 [190] and approved in 2003. By exploiting new concepts in phase space cooling and fast cycling super-conducting magnets, intense high-quality antiproton ($\bar{p}$) and heavy ion beams will be available. On the fundamental research side FAIR will address questions of the strong interaction as well as topics in nuclear, astro, plasma and atomic physics. Cancer therapy is an example of its applied research program. The heart of this worldwide unique accelerator complex, shown schematically in figure 6.1, will be two new synchrotrons (SIS100, SIS300) which supply a system of production targets, separators, storage and cooling rings. An efficient parallel operation will allow up to five experiments to run at the same time [191]. According to the most recent planning, FAIR will be constructed between 2008 and 2016.

The antiProton ANnihilations at DArmstadt (PANDA) experiment has been proposed as a universal detector system to study hadron physics at large distances [32] (cf. section 6.1). Making use of $\bar{p}p$ annihilations PANDA will be located at the High Energy Storage Ring (HESR, cf. section 6.2), an $\bar{p}$ storage ring which will be part of the FAIR facility. The main goal of PANDA is to exceed the statistics and precision of past efforts by orders of magnitude, and it is therefore optimized for high luminosity. Section 6.3 gives an overview of the present PANDA layout including a discussion of the main technological challenges and the requirements on the particular detectors. A detailed description of all sub-components as well as the PANDA physics can be found in [192].

6.1 Physics Objectives

As pointed out in chapter 1, spectroscopy has always played a leading role for the establishment of QCD and related models. The charmonium sector offers the unique advantage to study open questions like confinement and the generation of hadron masses in an experimentally well controlled environment. PANDA will perform high-precision measurements in this field, both below and above the $D\bar{D}$ threshold and including the search

[1] Gesellschaft für SchwerIonenforschung, Darmstadt, Germany.

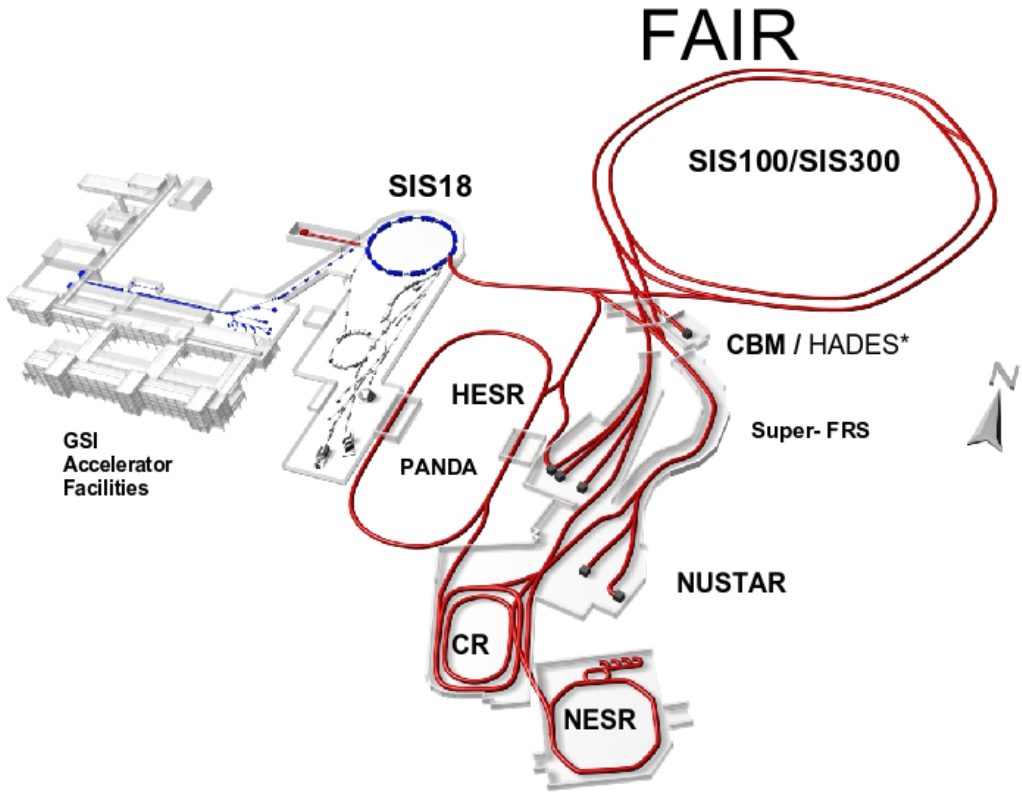

Figure 6.1: Schematic layout of the present GSI facilities (left, blue color) and the planned FAIR complex (right, red color). The PANDA experiment will be located at the antiproton storage ring HESR.

for hybrids and glueballs (cf. section 2.1). Also open-charm mesons will be addressed by performing near-threshold scans. A center-of-mass energy range from 2.2-5.5 GeV/c^2 will be accessible, defined by the $\bar{p}$ storage ring (see section 6.2). Furthermore, the properties of hadrons in media and hypernuclei will be studied. In this section only part of the PANDA physics program is discussed, focussing on the spectroscopy aspects. There is, for example, also growing interest to make use of electromagnetic probes in $p\bar{p}$ annihilations to measure Generalized Parton Distributions [193].

6.1.1 Charmonium Spectroscopy

The level scheme of lower-lying bound $c\bar{c}$ states can be described fairly well in terms of heavy-quark potential models (cf. section 2.1.3). Extensive measurements of the masses and widths of the $J^{PC} = 1^{--}$ states have been performed at e^+e^- machines, where they can be produced directly via an intermediate photon (cf. section 2.2). Other states, not carrying the same quantum numbers as the photon, can only be directly populated in $p\bar{p}$ annihilations. Through this formation mechanism, high-precision measurements of

e. g. the 0^{-+} ground state η_c [194] and its recently discovered radial excitation η_c' [17] are feasible. Also the existing data on the singlet P-resonance h_c [18, 19] need to be improved, to finally answer the question about the spin-dependence of the $q\bar{q}$ potential. As discussed in section 2.4, several evidences for narrow states above the $D\bar{D}$ threshold have been observed during the last years. It is stressed again that all these states need to be confirmed and scanned from $p\bar{p}$ annihilations. Only then proper and consistent interpretations of their nature will be in reach.

6.1.2 Search for Gluonic Excitations

The search for exotics at COMPASS naturally concentrates on the light meson sector (1-2 GeV/c^2). This thesis itself presents a positive signal of a spin-exotic state around 1.6 GeV/c^2, probably corresponding to the hybrid candidate $\pi_1(1600)$ (cf. section 5.5.1.7). However, the complexity of the performed PWA shows a general difficulty in that mass regime, namely that many broad (100-300 MeV/c^2) and overlapping resonances (mostly $q\bar{q}$) have to be disentangled. In this context PANDA will continue the work in the charmonium sector (3-5 GeV/c^2), with the big advantage that both the known conventional states as well as the predicted exotic states are very narrow there ($\sim$ MeV/c^2, see also section 2.1.3).

6.1.3 Open-Charm Physics

Besides the spectroscopy of charmonium states, PANDA will also provide the capability to address open-charm physics. While the former can be seen in analogy to positronium, the latter corresponds more to a hydrogen atom (heavy-light system). Severe discrepancies of recently discovered D_{sJ} states [28, 29, 30, 31] with model calculations have to be clarified, and precise measurements of masses and widths are needed.

6.1.4 Charm in Nuclear Media and Hypernuclei

For π, K and ω mesons it is established that their properties change in dense environments like nuclear matter [195, 196, 197]. PANDA will be able to extend these studies towards the heavy-quark sector, by exploiting reactions on nuclear targets ($\bar{p}A$). One approach will be to check whether the energy threshold to produce D mesons is different compared to their free mass. Also a lower in-medium D meson mass could move $c\bar{c}$ states, lying just below threshold in the $p\bar{p}$ case, above threshold for the $\bar{p}A$ reaction.

With a modified experimental setup, PANDA is expected to produce plenty of hypernuclei and survey them precisely. In these nuclei one or more nucleons are replaced by a hyperon, e. g. a Λ baryon. In particular double-Λ hypernuclei are of interest, because they give experimental access to Λ-Λ interactions. At PANDA they can be produced by impinging antiprotons of about 3 GeV/c^2 on a primary target, yielding among other things $\Xi\bar{\Xi}$ pairs. The Ξ particles are then stopped and captured in a secondary target, where the double-Λ hypernuclei are formed. An array of germanium γ-detectors, located as close as possible to the target, will be used to do precision spectroscopy on them [192].

6.2 In-Beam Installation at the Storage Ring

PANDA will be set up as an in-beam internal target experiment at the High Energy Storage Ring (HESR) [191]. Two modes of operation are foreseen for this antiproton storage ring: a high-resolution ($\Delta p/p \leq 4 \cdot 10^{-5}$) mode with reduced luminosity (up to $2 \cdot 10^{31}\,\mathrm{cm}^{-2}\mathrm{s}^{-1}$) and a low-resolution ($\Delta p/p \sim 10^{-4}$) mode with high luminosity (up to $2 \cdot 10^{32}\,\mathrm{cm}^{-2}\mathrm{s}^{-1}$). While in the former case a precise scanning of resonances is possible (cf. section 2.2.2), in the latter case new states can be search for more easily. $p\bar{p}$ annihilation rates of up to $2 \cdot 10^{7}/\mathrm{s}$ are expected.

6.2.1 The High Energy Storage Ring

The HESR will supply phase-space cooled $\bar{p}$ beams with momenta between 1.5 and 15 GeV/c. Both electron and stochastic cooling are foreseen, but only the latter can be used up to the maximum momentum. Electron cooling at momenta higher than 9 GeV/c is a real challenge, and a lot of development work is currently ongoing to achieve the best performance[2]. The HESR will have a circumference of 574 m and a total magnetic bending power of 50 Tm. The size of the beam at the PANDA target will be $\sim$ 1 mm, however, de-focussing might be necessary if a pellet target will be used (see section 6.2.2). In the high-resolution mode, the storage ring will be filled once at the beginning of a cycle with 10^{10} antiprotons[3] at an injection momentum of 3.8 GeV/c. A beam preparation period of typically 2-5 minutes follows, during which (de-)accelerating and cooling takes place. Depending on the mode of operation and the beam momentum, a measurement time of the order of an hour per cycle is provided. The above stated luminosities are thereby peak values; during a cycle the luminosity will typically drop by 30-40%.

6.2.2 Internal Target Systems

For the charm spectroscopy program two target options are discussed. With regard to luminosity a pellet target is favored, consisting of frozen hydrogen droplets with a diameter of 25 µm. A stream of these micro-spheres would traverse the $\bar{p}$ beam perpendicularly, with typical rates of 10-15 kHz. This technology was successfully used at the Wide Angle Shower Apparatus (WASA) at the CELSIUS facility, where a performance close to the PANDA needs was achieved [198, 199]. An effective target thickness of $3.8 \cdot 10^{15}\,\mathrm{atoms/cm}^2$ is required to match the maximum design luminosity of $2 \cdot 10^{32}\,\mathrm{cm}^{-2}\mathrm{s}^{-1}$. A single pellet would undergo about 100 interactions, which allows an efficient determination of the z position along the beam line of interaction points.

The second option relies on a hydrogen cluster-jet target [192]. Its advantage is a homogeneous density profile and the possibility to focus the antiproton beam to the maximum possible. Furthermore the gas density could be adjusted along with the beam consumption (cf. section 6.2.1) and thus the luminosity be kept constant throughout a whole stor-

[2] Based e. g. on the experiences with the COoler SYnchrotron (COSY) at Forschungszentrum Jülich.
[3] In the high-luminosity mode refilling will be necessary to achieve 10^{11} $\bar{p}$.

age cycle. However, reaching the design luminosity is a real challenge for this technology. Another disadvantage would be the less well-defined interaction points. Both the pellet and the cluster-jet target impose severe mechanical constraints on the PANDA detector design, due to the vertical crossing target vacuum pipe.

Concerning nuclear targets for the in-medium meson property measurements, a technique with fibers or wires may be used. Although beam heating is in principle a problem, they pose no additional constraints on the detector system. In contrast, the two-target setup in combination with the germanium array for the hypernuclei spectroscopy will involve major modifications [192].

6.3 Detector Components

In order to fulfill the envisaged rich physics program, an efficient detection and identification of charged particles (0.1-8 GeV/c) and photons is mandatory over the full solid angle. To this end, PANDA is based on the combination of two spectrometers (see figure 6.2). The interaction point is surrounded by a barrel-shaped target spectrometer (TS), consisting of a 2 T solenoid magnet, vertex detection, charged particle tracking, particle identification and electromagnetic calorimetry. A second, forward spectrometer (FS) with a dipole magnet (2 Tm max. bending power) will be used to analyze the particles emitted in the very forward direction. In the following some of the key components of the TS are briefly described (sections 6.3.1 to 6.3.4) and a summary of the FS and the data acquisition system is given (section 6.3.5 and section 6.3.6). For further details, please refer to [192].

6.3.1 Micro Vertex Detector

The design of the micro vertex detector (MVD) for the TS is optimized for the detection of secondary vertices (like D-meson decays) and maximum acceptance close to the interaction point. In addition, it will strongly improve the transverse momentum resolution. In the present layout the MVD consists of a four-layer barrel detector with an inner and outer radius of 2.5 and 13.5 cm, respectively. While the first two layers are planned to be made out of radiation-hard silicon pixels, the two outer layers will be based on strips of the same material. In order to support the tracking of forward going particles, six additional pixel-detector wheels with radii between 5 and 13.5 cm are foreseen. In total about 6.5 million pixels and 200 000 strips will be integrated, where at the same time the total material budget has to be kept below 4% of a radiation length. A spatial resolution for secondary vertices of about 50 μm and a time resolution of the order of 10 ns is required.

6.3.2 Central Tracker

The central tracker (CT) of the TS has to provide charged particle tracking for angles greater than $\sim 15^\circ$ w. r. t. the beam axis. Furthermore it should have a good detection efficiency for secondary vertices occurring outside the MVD (e. g. Λ decays). The CT will be constructed as a barrel around the MVD (see figure 6.2) with an inner and outer

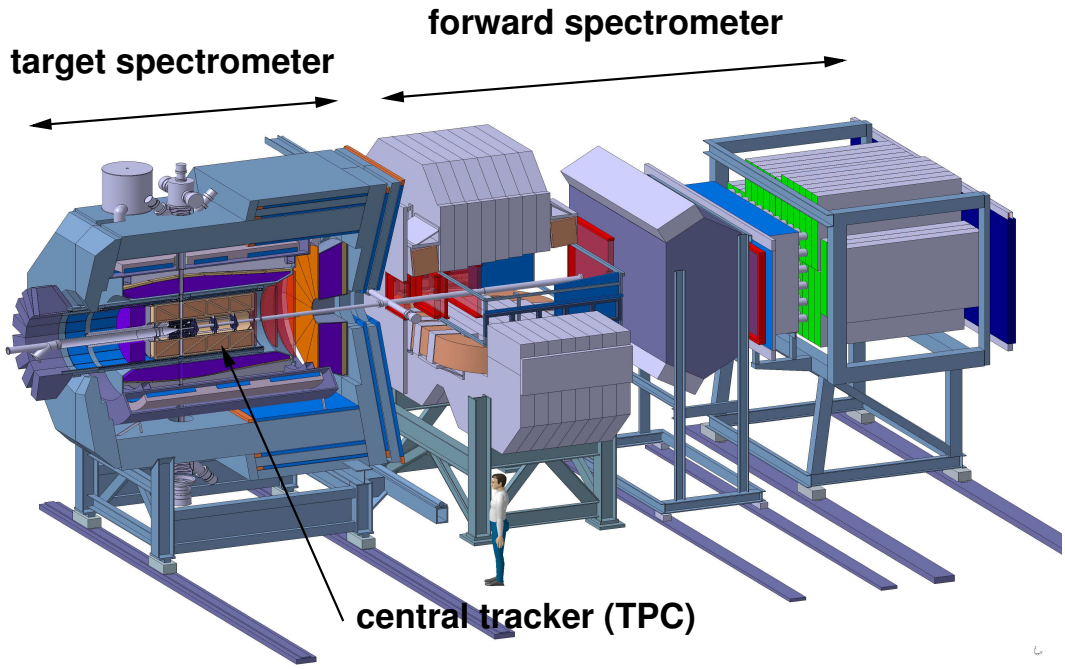

Figure 6.2: Target and forward spectrometer of PANDA with vertically crossing target pipe and antiproton beam coming from the left; central tracker marked (brown color).

radius of 15 and 42 cm, respectively. Two gas detector technologies are currently under discussion, a Straw Tube Tracker (STT) and a Time Projection Chamber (TPC). The TPC has several advantages compared to the STT and its continuous operation at the HESR would constitute a novel development in particle physics. In the following the common requirements on the CT are summarized and the STT and the TPC solution are briefly compared. The latter is described in detail in chapter 7.

6.3.2.1 Requirements from Physics

The maximum luminosity and $p\bar{p}$ annihilation rate at the HESR (cf. section 6.2) make a high-rate capability of the CT mandatory. In particular in the forward region, rates of the order of $10^4\,\mathrm{cm}^{-2}\,\mathrm{s}^{-1}$ have to be stand. Thus the device has to be very resistant against ageing effects. For reconstructed trajectories a momentum resolution $\delta p/p$ of the order of 1% is needed for the whole acceptance and momentum range. Here possible inhomogeneities of the magnetic field on the percent level have to be taken into account. Concerning the detection of e. g. K_S^0 or Λ vertices a spatial resolution of $\sigma_{r\phi} \sim 150\,\mu\mathrm{m}$ and $\sigma_z \sim 1\,\mathrm{mm}$ is required.

In order not to decrease the energy resolution of the electromagnetic calorimeter (section 6.3.4), the employed materials have to be kept as thin and light as possible. Especially γ-conversions significantly disturb the charmonium spectroscopy, but also multiple scattering and secondary background production have to be avoided. The requirement on

the total material budget is to stay in the range of 1% of a radiation length. In addition, the CT should contribute to the global particle identification, in particular for charged particles with momenta below 1 GeV/c.

6.3.2.2 TPC vs. STT

The TPC is in some regards the more challenging solution (see chapter 7), but its realization would feature several advantages compared to the STT. First of all the overall material budget will certainly be smaller, since a TPC is basically a gas-filled cylinder. The STT in contrast would consist of up to 10 000 tubes (about 30 µm in diameter), arranged in 10-12 double layers [192]. To avoid heavy support frames and provide instead a self-supporting structure, these tubes have to be operated at an over-pressure of $\sim$ 1 bar. Their walls need to hold this pressure and, in addition, individual tubes have to be electrically shielded against each other.

While the tracking capabilities in the 2-dim. $r\phi$ plane are probably similar, the TPC constitutes an ideal tracking device in all three dimensions. It is feasible to measure the z position of secondary vertices with an accuracy of $\sim$ 1 mm, which would be very difficult with the STT. The way out in the latter case is to introduce several skewed layers (2-3° skew angle), however, this is from a mechanical point of view not easy due to the crossing target pipe (cf. section 6.2.2).

The biggest advantage of the TPC would be that it allows the identification of charged particles via the measurement of their specific energy loss ($\mathrm{d}E/\mathrm{d}x$). This works in particular well for small momenta (below $\sim$ 1 GeV/c), where other dedicated detectors start to be inefficient (cf. section 6.3.3). Simulations show that about 100 hits on a given track, in combination with a truncated mean algorithm, provide a $\mathrm{d}E/\mathrm{d}x$ resolution of the order of 7% [189]. In particular the separation of kaons and pions, which is an important prerequisite for many physics channels, could be greatly improved.

6.3.3 Charged Particle Identification

Particle identification (PID) for hadrons and leptons over a large range of solid angle and momenta is an essential requirement for many of the physics objectives. In PANDA several technologies will be employed, the combination of which should guarantee a complete coverage. Being part of a global PID strategy, the TPC capabilities have been mentioned already in section 6.3.2.2. A similar performance could perhaps be achieved with a barrel-shaped Time-Of-Flight system, however, the short lever arm of $\sim$ 50 cm would require extremely good time resolutions.

Within the TS, the next outer device following the CT will be a Detector of Internally Reflected Cherenkov Light (DIRC). The DIRC is composed of 1.7 cm thick quartz slabs, arranged in a barrel at a radial position of 48 cm away from the beam pipe (thin grey line between the CT and the EMC (purple color) in figure 6.2). The Cherenkov photons are detected in photomultipliers sitting at the upstream end of PANDA (left in figure 6.2). Depending on the specifications of the employed radiator material, the DIRC will work

efficiently only for charged particles with momenta higher than 600 MeV/c.

Partly behind and partly integrated into the iron yoke of the solenoid magnet, several detectors for muon detection will be installed. Either gaseous mini-drift tubes, plastic scintillator counters or a combination of both could be used to perform the important task of identifying e. g. $c\bar{c} \rightarrow \mu^+\mu^-$ decays.

6.3.4 Electromagnetic Calorimeter

A central element of the PANDA detector will be the electromagnetic calorimeter (EMC). The planning for this device is very advanced[4] and foresees a barrel part as well as two end-caps (shown in purple in figure 6.2). A total of about 15 000 lead tungstate ($PbWO_4$) crystals with a front-size of $2.1 \times 2.1\,\text{cm}^2$ will be employed. This inorganic scintillator enables a time resolution of down to 1 ns and an energy resolution below 2.5% for 1 GeV photons, provided that the crystals are cooled to $-25°$ C to improve the light yield.

6.3.5 Forward Spectrometer

The forward part of PANDA will be set up as a dipole spectrometer and in a typical fixed-target geometry (cf. figure 6.2). Several tracking stations[5] will provide 2-dim. hit coordinates. Two Cherenkov counters (disc-DIRC and/or RICH) and a Time-Of-Flight system will take over the PID part. A hadronic calorimeter and a muon detector behind it constitute the downstream end of PANDA.

6.3.6 The "FutureDAQ" Concept

Most of the contemporary experiments rely on a traditional trigger and data acquisition (DAQ) scheme, which is based on a two-layer hierarchical approach[6]. A set of dedicated detectors is used to evaluate a first level trigger decision, which is broadcasted to all detector frontend electronics. The full event information is then transported to a higher trigger level or to a storage. Thus the decision time of the first level trigger is usually limited by the buffering capabilities of the frontends. In addition, the hard-wired trigger logics are not very flexible and only few different trigger schemes are possible.

For PANDA a completely new approach will be chosen, which is much better adapted to the needs of high-rate and high-precision experiments. All detector channels are considered to be self-triggering entities, capable of detecting and preprocessing signals themselves. The relevant data connected to a particle hit is marked by a precise absolute time stamp and buffered. A farm of computing nodes, which has access to these buffers via a high-bandwidth network, selects interesting events by combining the information from different detector components. In this scheme, trigger algorithms closely related to certain physics objectives can be programmed and eventually run in parallel.

[4] A Technical Design Report (TDR) for the EMC is currently being reviewed and close to be published.
[5] Probably GEM detectors based on the COMPASS design; see also chapter 7.
[6] E. g. COMPASS, although the online filter leaves already the classical structures (see section 3.3).

Chapter 7

A High-Rate TPC for PANDA based on the GEM

An ideal solution for the central tracker of PANDA would be a Time Projection Chamber (TPC). Such a device satisfies all requirements and, in addition, allows the identification of particles via $\mathrm{d}E/\mathrm{d}x$ measurements (cf. section 6.3.2). The continuous beam structure at the HESR in combination with interaction rates of up to $2 \cdot 10^7/s$, however, poses a big challenge for operating a TPC at PANDA (cf. section 6.2). After a short introduction to the basic principles of TPCs, the key issues are discussed in section 7.1. To cope with the high demands, it has been proposed to employ GEM structures for gas amplification. This technology, described in section 7.2, has proven at COMPASS to work extremely well for 2-dim. tracking devices, and the extension to a TPC application is very promising. Based on the experiences from other experiments and also simulations, a preliminary design for the PANDA TPC has been worked out. It is summarized in section 7.3. Finally, a summary and an outlook of developments and tests towards a TPC for PANDA is given in section 7.4. For more information about the project see also [34, 192].

7.1 Technological Challenges

After a general introduction, this section details the key challenges of developing a TPC for PANDA. All are connected to the mandatory high interaction rates, thus directly to the goal of performing precision spectroscopy (cf. section 6.1). Partly the hardware construction of the TPC is concerned, partly powerful reconstruction tools have to be developed. This section focusses on the former, but in any case there will not be a clear border between the online and the offline world. It is pointed out that the main detector concept of the proposed International Linear Collider (ILC) also foresees a TPC as tracking device [200], facing similar difficulties as described here.

7.1.1 The TPC Principle

A TPC is a 3-dim. tracking device capable of providing information on many points of a particle track and on the specific energy loss, dE/dx, of the particle [33]. It usually consists of a large gas-filled volume, which is in the case of PANDA a cylinder surrounding the interaction point and placed inside the solenoid magnetic field[1]. Figure 7.1 shows a schematic view of a TPC, drawn such that the cylinder axis coincides with the ($\bar{p}$-) beam direction. An electric field[2] along the same axis separates positive gas ions from electrons, both created by ionizing particles traversing the gas volume. The primary electrons then drift towards the readout anode end-cap, where they are amplified and induce signals on an arrangement of pad electrodes. From the position of the pads the 2-dim. projection of the particle track is obtained. The third coordinate comes from a measurement of the drift time of each primary electron cluster, which requires a precise knowledge of the electric field in the drift volume. Distortions of this field due to the accumulation of space charge from primary ions or avalanche ions drifting back into the drift volume deteriorate the resolution and have to be kept at a minimum. To this end all TPCs up to now have been operated in a pulsed mode, employing an electrostatic gate placed near to the amplification stage. This gate is opened only after an interaction has occurred and closed immediately thereafter to draw off the ions. Large-scale TPCs have been successfully operated in many experiments, e. g. [201, 202, 203, 204, 205].

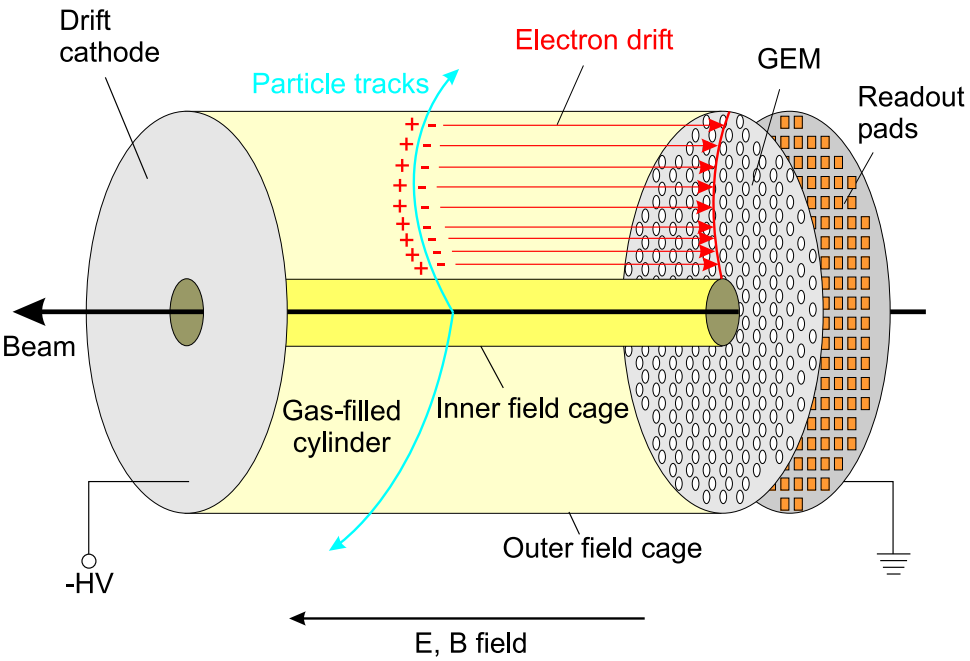

Figure 7.1: Schematic view of a TPC; primary electron drift from left to right. The gas amplification in the PANDA TPC will be performed with GEM foils, see section 7.2.

[1] In fact the TPC will have to be split into two halves to accommodate the target pipe (see section 7.3).
[2] Produced by an arrangement of two parallel plane electrodes and a cylindrical field cage.

7.1.2 Space Charge Built-Up and Track Distortions

The feasibility of the PANDA TPC will strongly depend on the question whether the accumulation of space charge inside the drift volume can be limited to a tolerable level. In addition to the primary ionization, there will be a constant back-flow of slow ions ($v_D \sim 1.7\,\mathrm{cm/ms}$, cf. section 7.3.2) from the amplification stage, which has to be suppressed as much as possible. Owing to the beam properties at the $\bar{p}$ storage ring, the classical technique of gating cannot be applied and the TPC has to be operated in a continuous mode. To estimate the magnitude of accumulated charge and the resulting distortions, dedicated simulations have been performed [189]. $p\bar{p}$ background events at $2\,\mathrm{GeV}/c$ beam momentum and at the maximum annihilation rate of $2 \cdot 10^7/\mathrm{s}$ have been generated. For each primary electron arriving at the amplification stage four back-drifting ions have been assumed[3]. Figure 7.2 (left) shows the simulated space charge distribution. Thus far cylindrical symmetry has been supposed and the TPC volume is therefore just described in rz-coordinates. The interaction point is located at $r = z = 0$. Due to the primary ionization, the charge density is higher in forward direction. At the innermost radius, where the track density is high, a space charge of up to $55\,\mathrm{fC/cm^3}$ is obtained. This translates into radial displacements of the drifting electrons of up to 6 mm, depending on their rz start position, as can be seen in figure 7.2 (right)[4]. It is important to note that such displacements have already been corrected for in other experiments [201, 206]. However, in the context of the discussion about event deconvolution (see section 7.1.3), the question is whether or not an online correction will be necessary. Currently, studies are carried out to evaluate the usage of a laser calibration system for this task.

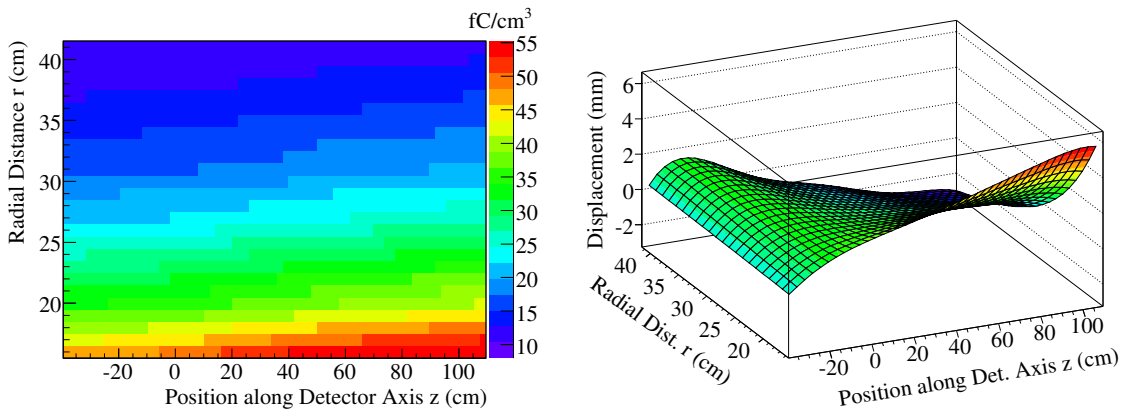

Figure 7.2: Simulated ion space charge density inside the PANDA TPC (left) and resulting radial displacements of drifting electrons depending on their rz start position (right) [189]. The readout end-cap is located in the plane $z = -40\,\mathrm{cm}$.

[3]Corresponding to e. g. a relatively low amplification factor of 2 000 and an ion suppression factor of 0.2%, which is feasible with GEM foils as discussed in section 7.2.2.

[4]Taking also $\sim 1\%$ inhomogeneities of the magnetic field and thus $\vec{E} \times \vec{B}$ effects into account; for further details see [189].

7.1.3 Event Mixing and Online Reconstruction

Due to the long electron drift time a TPC is a rather slow detector. Depending on the counting gas and the drift field of the PANDA TPC (see section 7.3), it will take of the order of 50 µs until the last signal electron of a particular event reaches the gas amplification stage. Thus at full luminosity about 1 000 events (3 000 tracks) will be superimposed inside the TPC at any time. Consequently, the signals of these tracks will arrive interleaved at the readout plane, which is called "event mixing". In order to deconvolute the events, it will be necessary to reconstruct already online track pieces. Based on topological considerations like target pointing or by matching the track pieces with other, fast detectors[5], an absolute time stamp can be assigned. The feasibility of the PANDA TPC will strongly depend on the availability of algorithms for event deconvolution.

7.2 The GEM Solution

The Gas Electron Multiplier (GEM) [35] consists of a thin polyimide foil (typically 50 µm) with a copper-clad on both sides (typically 5 µm). It is perforated by a large number of holes ($\sim 10^4/\mathrm{cm}^2$), which are arranged in a regular pattern[6]. In the so-called standard geometry, the holes have a double-conical cross-section with an inner diameter of 50 µm and an outer diameter of 70 µm at a hole pitch of 140 µm. Figure 7.3 (left) shows a photograph of a GEM foil taken with an electron microscope. Inserted between a pair of parallel plane electrodes, and upon the application of a potential difference between the two copper layers of the foil, an electric field as shown in figure 7.3 (right) is achieved. If e. g. a voltage of $\sim$ 400 V is applied, the field strength inside the holes is of the order of 50 kV/cm. The described configuration already makes up a working charge amplification device. Primary electrons created by a traversing particle are efficiently collected inside the holes, where they undergo avalanche multiplication. The resulting charge cloud is then extracted on the other side of the foil and can be collected on a readout anode (e. g. the TPC pads) or further amplified.

While the separation of the amplification stage from the readout anode is already a benefit on its own, the real advantage of the GEM technology is the possibility to cascade several foils. High amplification factors (gains) of several tenth of thousands can be achieved with a relatively low gain of the single foils, and thus with a discharge probability of practically zero [207]. A key feature concerning the TPC application is the intrinsic ion backflow suppression of multi-GEM structures (see section 7.2.2). Furthermore, laboratory tests have proven that the foils are resistant against aging effects [208]. In summary, the GEM technology perfectly suits the demands of the high-rate environment at PANDA.

[5] In most cases the micro vertex detector, but probably also the electromagnetic calorimeter; see section 6.3.
[6] Photolithographic technique, developed at CERN-EST-MT.

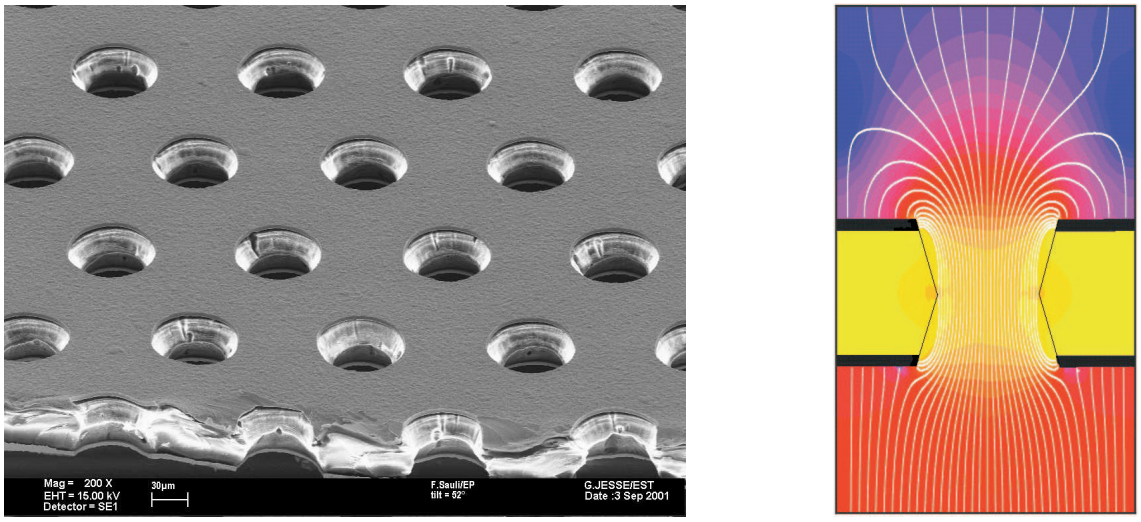

Figure 7.3: Electron microscope photograph of a GEM foil (left) and illustration of electric field lines in a GEM hole (right).

7.2.1 The COMPASS Triple-GEM Detectors

In the COMPASS experiment at CERN (cf. chapter 3), 22 GEM detectors with double-strip readout[7] have been operated successfully for many years. With a size of $31 \times 31\,\text{cm}^2$, they constitute the backbone of the near-beam tracking. Three GEMs are stacked on top of each other, separated by thin spacer grids [209]. An asymmetric sharing of the total gain between the three foils, gradually decreasing by $\sim 10\%$ at each amplification stage, and a segmentation of the foils on one side completely prevents gas discharges [210]. All detectors are operating stably at an average single projection efficiency $> 97\%$ and an average spatial resolution of $\sim 70\,\mu\text{m}$ [211, 212]. From the 2008 beam time onwards, also several triple-GEM detectors with a pixel readout will be employed as low-material beam tracking devices [213]. From the development of the two COMPASS GEM detector types, a lot of valuable knowledge has been transfered to the PANDA TPC design.

7.2.2 Ion Back-Drift Suppression

The field configuration shown in figure 7.3 (right) comprises a higher electric field on the "lower" than on the "upper" side of the GEM foil. In this case the "lower" side is meant to be the one closer to the readout anode of the detector. Thus ions created during the avalanche amplification inside the holes are collected with high probability on the upper side of the GEM, while electrons are efficiently extracted on the bottom side and guided to either the next foil or the anode. Figure 7.4 shows a schematic cross-section of a triple-GEM detector, introducing the drift, two transfer and the collection field, respectively. By optimizing these fields the number of back drifting ions can be limited, which is essential for a TPC application without ion gate (cf. section 7.1.2).

[7] Two orthogonal sets of 768 strips, measuring two projections of a particle track.

In order to quantify the involved charge transfer processes [214], the currents on all electrodes of the system have to measured with high precision during detector irradiation. To this end a small-size triple-GEM test detector was installed in front of an X-ray tube[8] as shown in figure 7.5. The ion back-flow has been defined as the ion current on the cathode (see figure 7.4) divided by the electron current on the anode[9]. With a high collection field of 5 kV/cm and a low second transfer field of 160 V/cm, a minimum ion back-flow of 0.8% has been achieved in an Ar/CO_2 (70/30) gas mixture [215]. A rather low, TPC-like drift field of 250 V/cm was used and the first transfer field set to 4-6 kV/cm. This still ensured a stable and safe operation.

There are several perspectives to further reduce the ion back-flow for the PANDA TPC. First of all the presence of the 2 Tm magnetic field will help, since it decreases the transverse diffusion in the GEM holes and therefore increases the electron transparency [216]. In addition, a GEM foil with unit gain could be added on top of the triple-GEM stack as pure ion blocker. Its transparency for electrons should, of course, be close to 100%. Here, geometrical parameters like thickness and hole shape were found to play a key role [217].

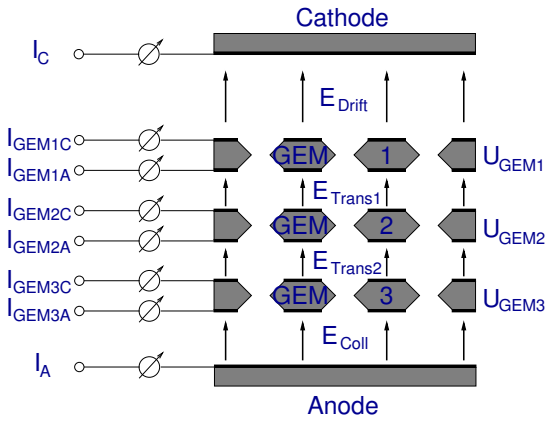

Figure 7.4: Definition of fields and currents in a triple GEM detector.

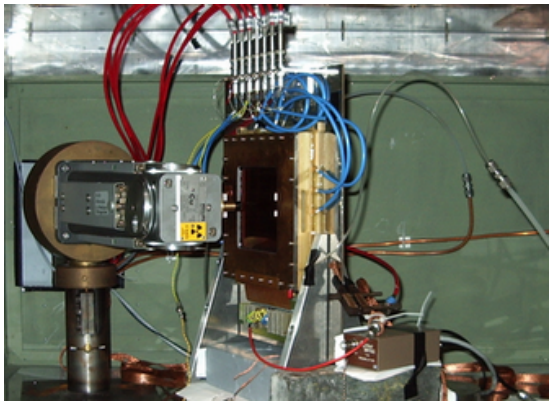

Figure 7.5: X-ray irradiation setup for ion back-flow studies.

7.3 TPC Design and Integration into PANDA

In this section an overview of the design and operational parameters of the PANDA TPC is given [192]. It is emphasized that certainly not all of them are final yet, because, in general, the layout of the PANDA experiment is still subject of ongoing optimizations.

[8]The same setup, including the current meters, has also been used for the gain measurements of the TPC test chamber (see section 8.3).

[9]Please note that due to the primary ionization this quantity is not exactly equal to the suppression factor used in section 7.1.2. Being precise, the measured ion back-flow is the sum of this factor and the inverse gain (thus 0.25% for the numerical example given in section 7.1.2).

7.3.1 Geometry and Mechanics

In the current design, the PANDA TPC consists of two half-cylinders to accommodate the target pipe, which intersects the beam pipe perpendicularly as shown in figure 7.6. Each of the chambers has an inner radius of 15 cm, an outer radius of 42 cm and an overall length of 150 cm. Due to the fixed-target nature of PANDA the geometrical center of these chambers is shifted by 35 cm downstream w. r. t. the interaction point. The total volume of the TPC is about 700 liter. A pad size of 4 - 6 mm^2 is foreseen, resulting in about 65 000 - 100 000 electronic channels. Simulations are currently carried out to decide on the pad shape (e. g. rectangular or hexagonal). The mechanical structure of each half-chamber will be composed of a vessel containing the field cage and the detector gas. Two end-flanges will house the high-voltage cathode (downstream end) and the multi-GEM structure and frontend electronics (upstream end). A light-weight, self-supporting sandwich structure will be employed, based on two skins of fiber glass composite material and a core of fiber honeycomb[10]. Possibly a thin layer of CO_2 gas will be inserted between the field cage and the support structure of the vessel for better electrical insulation.

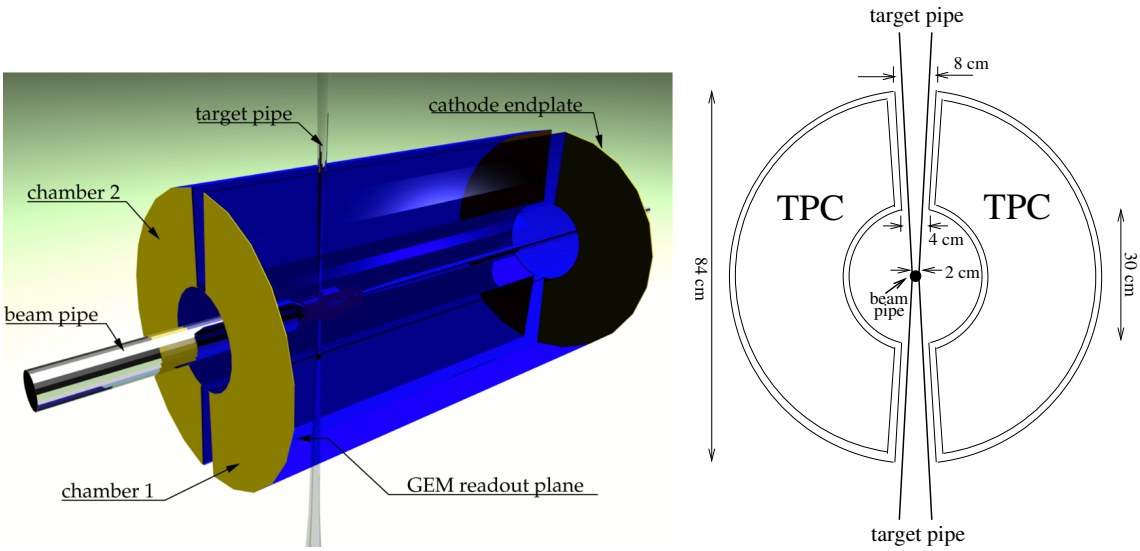

Figure 7.6: The two half-cylinders constituting the PANDA TPC, together with the target and the beam pipes; 3-dim. view (left) and vertical cross-section (right) shown.

7.3.2 Detector Gas and Operation

The choice of counting gas is crucial for the design and functionality of a TPC. Several requirements have to be fulfilled, examples are a high and saturated electron drift velocity, a low diffusion and a high ion mobility. In order to keep the accumulation of space charge low (cf. section 7.1.2), a small primary ionization is desirable[11]. As main components basically only the noble gases argon and neon qualify, with several possibilities for

[10] The TPC test chamber has been built in a similar way, cf. section 8.1.1.

[11] Which, however, contradicts partly the optimization of the dE/dx measurements.

a few % of organic admixtures like CO_2 and CH_4 [192]. Due to its large radiation length of 322 m and its low primary ionization rate of 16/cm, neon is preferred for the PANDA TPC. This, however, implies a closed gas system because neon is rather expensive. CO_2 is a very efficient and uncritical quencher[12], with the advantage of low diffusion but also the disadvantage of lower drift velocities. The chosen default gas mixture is Ne/CO_2 (90/10)[13], possibly enriched by a few % of CH_4 to make the gas faster. A drift field of 400 V/cm is foreseen, leading to an electron drift velocity of $\sim$ 2.8 cm / µs and an ion drift velocity of $\sim$ 1.7 cm / ms (without CH_4 admixture). A rather low gain of a few thousand will be set for the GEM stack, in order to keep the ion back-flow as low as possible. The whole gas system will have to be extremely clean, since e. g. oxygen contaminations in the order of a few tenth of ppm can already lead to significant losses of signal electrons due to attachment processes [219]. In general, any foreign substances different from the counting gas will effect the drift velocity and thus the tracking performance.

7.3.3 Readout Electronics

Contrary to wire chambers, the signal in a GEM detector is produced entirely from the motion and collection of electrons created in the last foil before the readout anode. The slow ions do not contribute to the signal, which is therefore intrinsically fast. Consequently, the sampling rate in time (equivalent to the z coordinate) will have to be considerably higher than the $\sim$ 10 MHz usually used for TPCs with wire chamber readout[14]. Highly integrated front-end electronics with low power consumption of a few mW per channel are needed. Following the general concept of the PANDA DAQ (cf. section 6.3.6), a data-driven self-triggering readout scheme is pursued. Massive data reduction by zero suppression and online feature extraction such as pulse charge, hit time and track segment definition will be employed.

7.4 Research and Development towards a PANDA TPC

The small-size TPC test chamber presented in this thesis (see chapter 8) marks the first step of hardware developments towards the PANDA TPC. There are several plans for further studies with this detector, which are detailed in section 8.7. Based on the experiences gained, a large-scale prototype with a drift length of 65 cm and a diameter of 30 cm is currently being designed. This device will be tested in experimental environments, namely as tracker in FOPI (from 4π [220]) and CB-ELSA (Crystal Barrel at the ELektronen-Stretcher-Anlage [221]). In parallel, a lot of work is ongoing on the simulation and track reconstruction side [189, 222]. First algorithms for event deconvolution have been developed and implemented in the PANDA software framework [223].

[12] Polyatomic molecules which absorb secondary photons and drain their energy into internal excitations.
[13] This mixture is used also for the ALICE TPC [218].
[14] Like for example the ALICE ALTRO electronics, see section 8.4.1.

Chapter 8

Test Chamber Measurements

The first hardware development in the line of feasibility studies of a GEM-based TPC for PANDA has been the construction of a small-size test chamber. After proofing the proper functioning of all components and a successful commissioning with X-rays, tracks from cosmic muons were recorded. Based on these data elementary measurements like space point resolution, cluster size distribution and signal shape analyses have been performed. Having been operated for many months the detector hereby also showed its stability.

Section 8.1 introduces the design and working principle of the test chamber. Here the general idea of operation is explained and all sub-components are described in detail. Their construction, test and assembly to the complete detector is presented in section 8.2, followed by a summary of the basic characterizations obtained during the X-ray commissioning in section 8.3. The readout electronics, trigger and data acquisition system used for the measurements with cosmic muons is discussed in section 8.4. The main emphasis of this chapter is placed on the analysis of these data: Section 8.5 explains the used reconstruction tools and algorithms, while in section 8.6 the results are presented. The following discussion focuses in particular on the impacts for the operation of the PANDA TPC. Finally, an outlook of possible future measurements with the test chamber is given (section 8.7).

8.1 Detector Description and Operation

In order to be able to exchange certain components without rebuilding the whole detector, much attention was paid to a flexible design. To this end, the TPC consists of three basic modules: the cathode plane, the field cage and the readout plane. The latter also hosts the GEM stack for gas amplification, which partly extends into the field cage volume. All modules are attached to each other with standardized flanges using rubber O-rings (Viton®, DuPont) to ensure gas tightness. The cathode and the field cage have a diameter of 20 cm, while the active area is only $10 \times 10\,\mathrm{cm}^2$, given by the dimensions of the GEM foils. The maximum drift length is defined by the distance between the cathode and the first GEM foil and has been 7.7 cm for all measurements presented. Figure 8.1 shows, to scale, a computer aided design (CAD) drawing of the detector. This section in-

troduces in detail the design and functionality of all sub-components of the test chamber, including the GEM stack. Dedicated parts describe the overall high voltage scheme and the gas system, which are closely connected to the operation of the TPC.

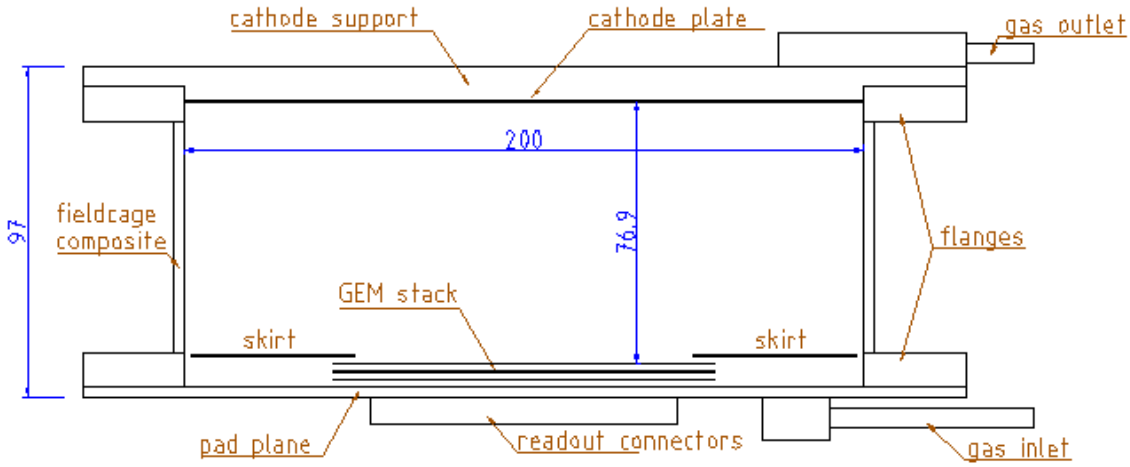

Figure 8.1: CAD drawing of the GEM-TPC test chamber, vertical cross-section shown. All dimensions (blue color) are in mm. The electron drift is from top to bottom.

8.1.1 Cathode Plane and Field Cage

The cathode (top of figure 8.1) is realized as a 0.3 mm thick copper plate, which is glued on a 10 mm fiberglass support (Vetronit G11). It also hosts the gas outlet of the TPC and a connector for its high voltage supply, as can be seen on the right of the photograph shown in figure 8.2. Both components are glued into a connector piece with two bores (also made out of fiberglass), which is glued to the backside of the cathode plane. A silver wire, fed through a small hole in the copper plate and the matching bore of the connector piece and soldered to the copper plate on the inside of the gas volume, is used to connect the cathode with its high voltage connector.

The cylindrical field cage (see figure 8.3) consists at its innermost layer of a 125 µm thick insulating polyimide foil, which has 18 µm-thick copper strips on both sides. The strips are 3 mm wide, have a pitch of 4 mm and are arranged in a way such that the inner strips are shifted by 2 mm w. r. t. the outer strips (cf. figure 8.4). In this way, a linear degrading of the potential and a seamless field shaping also in the regions close to the outer borders are achieved [224]. To protect and insulate the outer strips, a second 125 µm thick polyimide foil is glued on top of them. A 3 mm thick resin-soaked paper honeycomb, laminated with 200 µm sheets of glass-fiber reinforced plastic (GRP), is used as support structure. The outermost layer is a thin copper foil which shields the chamber from externally induced noise. The photograph presented in figure 8.3 was taken during the field cage construction, when just the first flange and GRP laminate were mounted. For more details concerning the composite design and assembly of the field cage see section 8.2.2.

A chain of 36 resistors, 10 MΩ each, connects field cage strips and defines their potentials. It is placed outside of the gas volume to avoid local heating and field distortions. The field cage also features a total of four thin windows for X-ray irradiation, which were employed during the commissioning and gain measurements presented in section 8.3. These windows have a thickness of $2 \times 125\,\mu\text{m}$ polyimide foil plus 18 µm copper (from the inner strips, cf. section 8.2.2). Taking into account the attenuation coefficients [225] of these materials, it was estimated that for e. g. 5.9 keV photons only $\sim 2\%$ of the intensity passes the windows. Therefore, ^{55}Fe for example can't be used as irradiation source and all commissioning measurements (section 8.3) have been performed with a copper X-ray tube. For its K_α line at 8.04 keV, about 30% intensity passes the field cage windows.

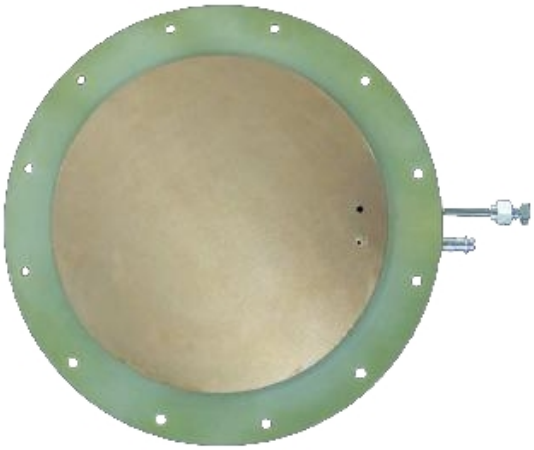

Figure 8.2: Photograph of the TPC cathode module. The gas outlet and high voltage connector apparent on the right are glued into a (not visible) connector piece with two bores.

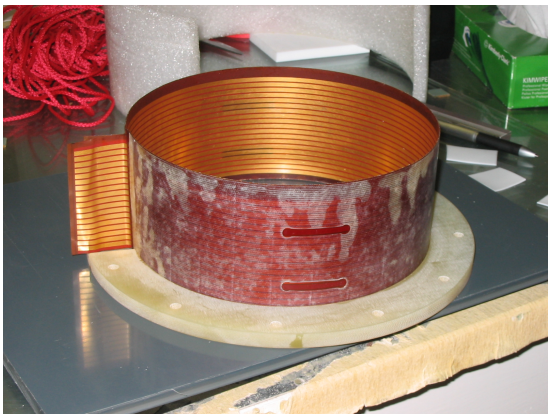

Figure 8.3: TPC field cage during construction. Upper flange, honeycomb, copper shielding and resistor chain not yet integrated. Two out of the four windows for irradiation visible in the front.

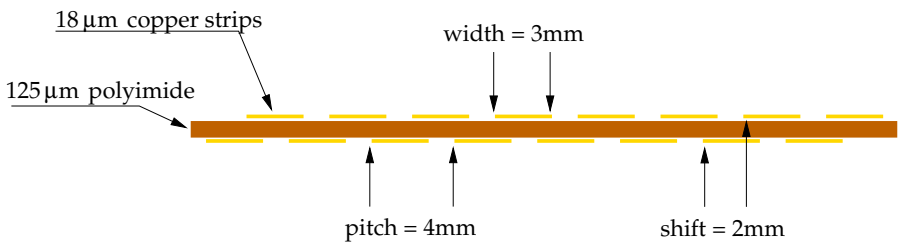

Figure 8.4: Schematic sketch showing the inner and outer field cage strips and their relative displacement.

8.1.2 Readout Plane

The readout plane is a multi-layer printed-circuit board (PCB) with a thickness of 3 mm and a diameter of 20 cm. It is based on four conducting layers and three insulating layers, with the topmost layer consisting of rectangular pads to collect the signal charges. Their size and pitch are $0.8 \times 6.0\,\mathrm{mm}^2$ and $1.0 \times 6.2\,\mathrm{mm}^2$, respectively. In total there are 1 536 pads, covering an area of $\sim 10 \times 10\,\mathrm{cm}^2$. The analog signals of always 64 of them are transferred to surface-mounted device (SMD) connectors, soldered on the backside of the PCB. To ensure gas tightness, the corresponding contact vias are displaced in the different layers.

Figure 8.5 displays, to scale, a detail of the PCB design, selecting such a group of 64 pads. Shown are the signal pad layer (dark blue), the two middle layers with the circuit paths (violet and light blue dashed lines) for the displaced vias (light blue circles) and the layer with the soldering pads for the high-density SMD connector (violet). Since the connector has in total 68 pins, the four outer ones are not needed for signal processing and are used instead to ground the four big soldering support pads (also violet). These four ground channels as well as the 64 signal channels are connected via flat-cables to the front-end electronics inputs (cf. section 8.4).

To cover all 1 536 pads, 24 of the connectors described above are needed. Figure 8.6 shows a photograph of a part of the readout plane, including three of the 14 feedthroughs for the high voltage supply of the GEM foils. In addition, the readout PCB features the gas inlet and four sinkholes, in which plastic pillars for the mounting of the GEM stack are inserted. The whole plane is on ground potential.

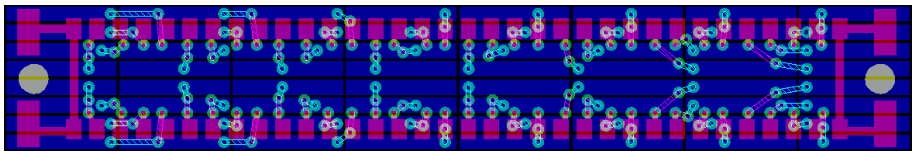

Figure 8.5: Detail from the four-layer readout PCB, showing a group of 64 signal pads (dark blue), which are connected by displaced vias (light blue) to the soldering pads (violet) of one high-density SMD connector. All layers are shown overlayed. Only 64 out of the 68 connector pins are used for signal readout, the remaining four for grounding purposes.

8.1.3 GEM Stack Geometry

As motivated and introduced in section 7.2, a multi-GEM structure is foreseen as gas amplification stage for the PANDA TPC. Therefore, the test chamber also features several cascaded GEM foils ($10 \times 10\,\mathrm{cm}^2$ area), with the possibility to vary their number and distances. This is achieved by framing all foils individually (cf. section 8.2.1) and mounting them to plastic pillars, which are fixed to the readout plane. Washers with a precision of 0.1 mm are used to define the separation distances. Additionally, all voltage

differences across the foils as well as the electrical fields between them can be set independently from outside (cf. section 8.1.4). Thus, optimizations concerning ion back flow can be introduced at any time and the effective gain can be adapted to different readout electronics.

For the measurements presented in this work, a triple-GEM configuration with 2 mm nominal spacings has always been used. On top of the GEM stack, a 20 cm diameter, 0.3 mm-thick copper plate with a $10 \times 10\,\mathrm{cm}^2$ hole is mounted to shield the region not covered by the GEM foils (cf. figure 8.1). This "skirt" ensures a proper termination of the electrical field lines outside the active area and thereby prevents drift field distortions. Its distance to the most upper GEM foil is also 2 mm and the total height of the GEM stack including the skirt was measured to be $\sim 9\,\mathrm{mm}$[1]. Thus it partly extends into the field cage volume. Figure 8.7 shows a photograph of the GEM stack mounted on the readout plane, the skirt just being added. Silver wires are used to connect the high voltage, which is supplied via feedthroughs in the readout plane, to the GEM foils.

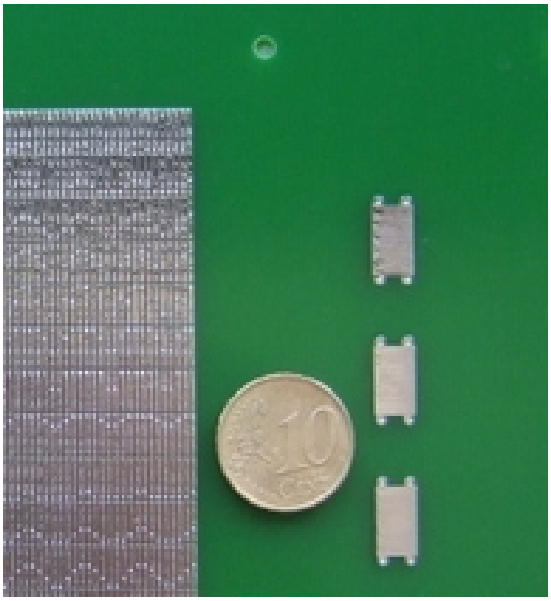

Figure 8.6: Detail of the readout plane showing part of the signal pads, three HV feedthroughs and one sink hole for a GEM stack pillar.

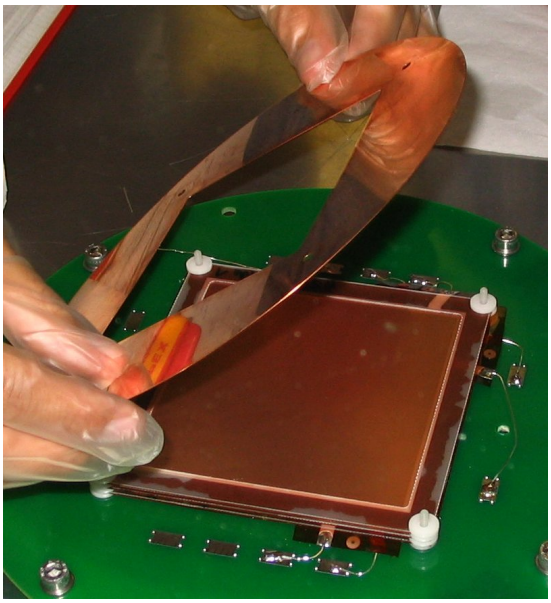

Figure 8.7: Photograph of the GEM stack, mounted to the readout plane; skirt just being added to it.

8.1.4 High Voltage System

In total, eleven negative high voltage (HV) potentials are supplied to operate the TPC test chamber. These are (from top to bottom in figure 8.1 and from high to low potential)

[1] This includes $\sim 0.5\,\mathrm{mm}$ due to the thicknesses of the GEM foils and the skirt. Also it should be noticed that the GEM stack is hold together by plastic screws, which could not be tightened completely

the drift cathode, the first and last strip of the field cage, the skirt, all top and bottom sides of the GEM foils and the readout plane. The HV system is illustrated in figure 8.8, which also introduces the drift, transfer and collection fields of the test chamber (see also section 7.2). While the drift field (few hundreds of V/cm) defines the primary electron drift in the TPC volume, the transfer and collection fields (few kV/cm) within the GEM stack influence the gas amplification and signal extraction [214]. To be able to correct for field distortions at the transition from the drift volume to the amplification stage, the field between the skirt and the first GEM foil is defined as a second, adjustable drift field.

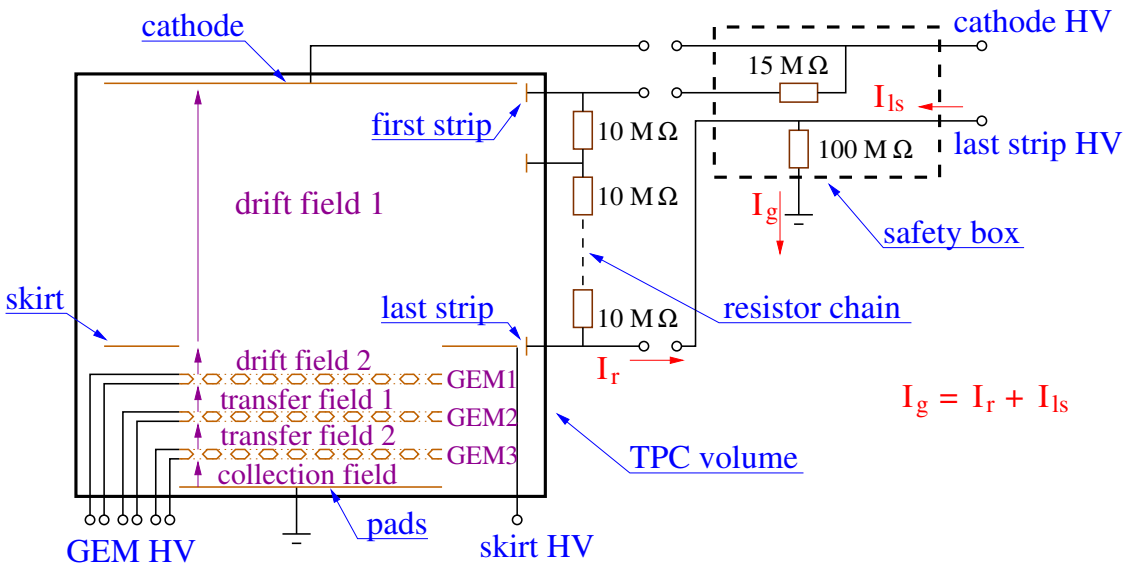

Figure 8.8: Overview of the test chamber high voltage system including the definition of the adjustable electrical fields (magenta color); HV connectors are marked as circles. Currents through resistor chain I_r and from last strip supply I_{ls} sum up to ground current I_g; e. g. for $U_c = 6\,\text{kV}$ and $U_{ls} = 3\,\text{kV}$: $I_c = 8\,\mu\text{A}$ and $I_{ls} = 22\,\mu\text{A}$, cf. figure 8.12.

The most negative potential is reached at the cathode, ranging from 5-7 kV depending on the desired drift field. Deduced from the same HV channel, the potential of the first field cage strip is defined via a 15 MΩ resistor, located in an external safety box (see figure 8.8). All subsequent strips are connected further by a chain of 10 MΩ resistors. Thus, only one HV channel above 5 kV is needed, which was provided for all measurements presented in this work by a C.A.E.N. N470 module [226] (max. 8 kV, 1 μA resolution). To reduce the noise coming from this device, a low-pass filter made out of two times a resistor (1 MΩ) and a capacitor (1.2 nF) to ground was included for this particular HV channel.

The potential of the last field cage strip could in principal be fixed by just another high-value resistor to ground. However, to keep the flexibility to change for example the gas amplification of the GEM foils, an additional independent HV channel for the last strip is added, injecting current to the system. In that way, the last strip potential can always be adapted to the actual height and settings of the GEM stack, while the desired drift field is kept at the same time. Still a 100 MΩ resistor to ground, again located in the safety box,

is needed to terminate the field cage HV subsystem and to limit the current which has to be provided for the last strip. Typical current values for both the last strip channel and the resistor chain can be found in figure 8.12 of section 8.2.3.

The skirt as well as all top and bottom sides of the GEM foils have their own voltage supplies, resulting in seven more HV channels. A C.A.E.N. A1833N module (max. 4 kV, 20 nA resolution) embedded in an SY2527 main frame has been used for those and also for the channel of the last field cage strip. The module features an internal trip bus, allowing to shut down all channels immediately if one of them exceeds a programmed current limit. This limit has usually been set to $\sim 1\,\mu$A for the GEM foils and the skirt and to $\sim 50\,\mu$A for the last field cage strip. The drift cathode is switched off also in case of a trip, by using the "kill" input line of its power supply module. For all GEM foils, 10 MΩ loading resistors have been incorporated as an additional protection in case of an over-current. As for the cathode's HV channel, a noise filter was added to the supply of the GEM foil closest to the pads.

The readout plane, where all electrons are finally collected, defines the zero potential of the test chamber. This potential is derived from the electronics ground and has to be connected to the ground of all HV channels (cf. section 8.4.3). In order to safely handle the whole HV system and also to conveniently operate the TPC, a Labview® control [227] has been programmed[2]. Via a user interface, all desired field and voltage settings can be entered. The program then calculates the required potentials for all HV channels, taking into account the chamber geometry. These values can then be loaded to the A1833N module, just for the one channel of the N470 it has to be done "by hand". If turned on, all channels are ramped up with a speed of 20 V/s. During operation, the Labview® program permanently updates all voltage and current readings of the HV channels and displays them on the screen. In addition, a status bar indicates whether e. g. a trip has occurred. A summary of the default settings used to operate the TPC can be found in Table 8.1 of section 8.1.5.

8.1.5 Default Voltage and Drift Field Settings

For most of the presented measurements, a moderate drift field of 250 V/cm was chosen, while the GEM settings have been taken over from the COMPASS triple-GEM detectors [212] (see also section 7.2.1). It should be noticed, that those chambers were optimized for minimal discharge probability rather than for ion back-drift suppression (cf. section 7.2.2). In particular, the settings include an asymmetric gain sharing between the three GEM foils, with the foil closest to the pads having the lowest voltage difference applied. However, for the test chamber measurements with cosmic muons at a rate of $\sim 1\,\mathrm{cm}^{-2}\mathrm{s}^{-1}$, space charge build-up is of course no issue. It has therefore been decided to gain from the experiences with the COMPASS chambers and use them also as reference for the TPC. Table 8.1 summarizes the TPC default settings, which are later also referred to as "100%".

[2]The communication is based on an OLE for Process Control (OPC) server, where both the program and the modules connect as clients.

Drift Field 1	Drift Field 2	Transf. Field 1	Transf. Field 2	Collect. Field
250 V/cm	250 V/cm	3.75 kV/cm	3.75 kV/cm	3.75 kV/cm
Voltage GEM1		Voltage GEM2	Voltage GEM3	
400 V		365 V	320 V	

Table 8.1: Default field and voltage settings for the TPC operation.

8.1.6 Gas Properties and Supply

As discussed also in section 7.3.2, a clean and tight gas system is a prerequisite for every TPC setup. Therefore, several rules have been strictly followed during the construction of the gas supply for the test chamber. First of all, stainless steel tubes have been used whenever possible. Only for the installation inside the X-ray shielding box (see section 8.3.1), bendable copper tubes became necessary. Plastic pipes were almost completely avoided, since water can easily penetrate them by diffusion. Just the last $\sim$ 10 cm of gas line before the inlet of the TPC, where flexibility is of course needed, are made out of plastic. Behind the detector, several meters of rolled up tubes are placed to avoid back diffusion. So far, the system has always been open at the very end, so the TPC is flushed with gas and operated at atmospheric pressure.

On the input side, two different alternatives have been installed to supply the counting gas to the TPC. One is to directly connect a pre-mixed gas bottle to the detector, the other to use a gas mixing system, which was especially designed for this application. Up to three gases can be mixed here, their relative fluxes as well as the total flux being controlled by digital flow-meters (Bronkhorst [228], multi-bus El-Flow series). With both setups a gas flow of 6-10 ℓ/h is usually adjusted, which corresponds to about two or three gas exchanges per hour. The detector has always been flushed for at least one day before switching it on. So far, it has been operated only with an Ar/CO_2 (70/30) mixture and due to cost reasons mostly from pre-mixed bottles (supplied by Linde or Air Liquide). The required degree of purity is 5.0 for argon and 4.5 for CO_2, which acts in this gas mixture as a "quencher" (cf. section 7.3.2). For the default drift field of 250 V/cm, the electron drift velocity is about 0.55 cm/µs. This corresponds to a maximum drift time of about 14 µs over the 7.7 cm drift length of the test chamber.

To check both the quality and the mixing ratio of the input gas, a mass spectrometer (VG ARGA by VG Quadrupoles) has been employed. Through a thin capillary, a small fraction of the flow is diverged from the main detector input line and sucked in an evacuated storage volume. There, the analyzer head is placed, which consists of three parts: an ion source, a quadrupole analyzer and an ion detector. Inside the ion source, gas particles are subjected to bombardment by electrons, which are generated from a hot wire filament. One or two electrons are stripped from the neutral gas atoms or molecules, leaving them single or doubly positively charged. These ions are then extracted into the quadrupole analyzing field, where they undergo stable or unstable oscillations in a trajectory, de-

pending on their mass. Only in case of stable trajectories, a current is measured on the ion detector, the signal height being proportional to the number of ions. Thus by performing a scan of the quadrupole voltage, a mass spectrum (in the range of 0-80 u for the VG ARGA) is obtained.

Figure 8.9 (left) shows an example of such a measurement, for the case of the pre-mixed gas. This spectrum has been compared to the corresponding one from the mixing system, exhibiting perfect agreement within the measurement sensitivity. In particular, no heavy contaminations from e. g. silicon oil or other valve lubricants are noticeable. The presented zoom (right of figure 8.9) enlarges the contribution of small components, mostly corresponding to doubly ionized gas particles or cracked CO_2 molecules. Even the tiny admixture of ^{36}Ar isotopes is resolved in this mass spectrum. The water contamination is to a large extend also visible in a residual gas measurement, performed with just the evacuated storage volume of the mass spectrometer setup. Thus most of the observed water evaporated from the walls of the vacuum chamber during the measurement and is actually not inside the gas system itself. The heaviest component has been found at a mass of 46 u, probably leftovers from cleaning parts of the system with ethanol (C_2H_5OH). In conclusion, the gas system has been found to be clean and suitable for a TPC operation.

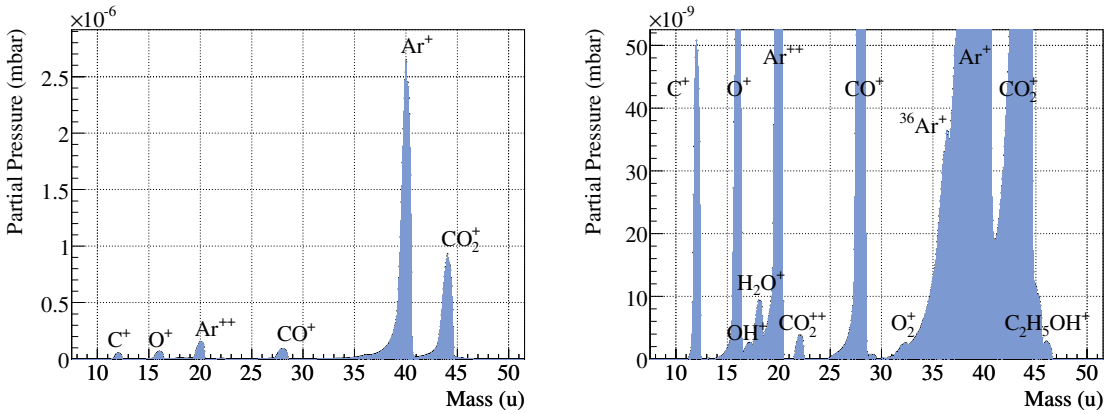

Figure 8.9: Left: mass spectrum of the Ar/CO_2 gas mixture used for the TPC operation, obtained by a quadrupole spectrometer. Right: same spectrum, but zoomed on the y axis to enlarge small components. For both plots, the black points indicate the step size during the spectrometer scan.

8.2 Construction and Component Tests

While in section 8.1 the design and functionality of the test chamber is described, this section details its mechanical construction. In particular the assembly and testing of the GEM-foils and the field cage are presented, since these are the most difficult and also interesting parts from a technical point of view. For the cathode just a floating high voltage test in air was performed, during which the voltage was ramped up to 7 kV without any stability problems.

8.2.1 GEM Foil Framing and Testing

To ensure a flexible handling of the GEM foils within the TPC, they are not glued together within one common support structure, but instead framed individually. Standardized fiber-glass frames have been designed for this, each with a thickness of 0.6 mm and four alignment holes in the corners. To stretch the foils, they are fixed to a Plexiglas® support plate and heated up in an oven to 80°. Thus, the different temperature expansion coefficients of polyimide materials and Plexiglas® are exploited. The foil is then centered between two aligned frames and glued to them with ARALDIT® "Standard", a two-component glue which doesn't show any out-gassing behavior [229]. A completed GEM module has a thickness of 1.3 mm and an active (inner) area of $10 \times 10\,\mathrm{cm}^2$.

Each GEM foil was carefully tested before it was mounted to the test chamber. First, a visual check with a microscope was performed to make sure that the foil is properly stretched and no glue leftovers or other impurities are present. Afterwards, high voltage was applied between the upper and lower copper-clad in a nitrogen environment. The high voltage is ramped up in steps of $\sim 50\,\mathrm{V}$ until finally each foil has to hold 550 V for at least 2 minutes with a leakage current of less than 10 nA. This test finally proves the operational readiness and stability of the GEM foil.

8.2.2 Field Cage Assembly

For the construction of the field cage, a 19.8 cm diameter aluminum tube was used as basic support structure during all glueing and assembling steps. Two layers of Teflon® (DuPont) tape on top of the aluminum guaranteed a smooth and clean work surface. The total diameter of the tube (including the Teflon®) was 20 cm, which at last defined the inner diameter of the field cage. In addition, two semicircular clamps with a slightly larger inner radius had been prepared and were used to press on the different composites during glueing. A two-component glue (ARALDIT® AY103/HY991, ratio 100/40) was chosen, since it is available in large quantities and, similar to the ARALDIT® "Standard", shows no out-gassing. The respective field cage parts have always been put to an oven at 50° C for the glue to harden.

In a first step, the field cage foil (described in section 8.1.1) was bent around the tube and a 125 µm polyimide foil was glued on top of it to insulate and protect the outer strips. To save material, these outer strips are reduced at the positions of the irradiation windows. As already mentioned before, the resistor chain had been decided to be located outside of the drift volume. Therefore, the strip foil was bent 90° on its two ends, as sketched in figure 8.10. Of course, one end has to stick out more than the other one, to make it possible to connect the inner and outer strips via the resistors.

Next, the first fiber-glass laminate (200 µm thick) was fixed, which has holes at the same positions where also the outer strips are reduced for the windows. Successively, the two flanges with which the field cage can be attached to the cathode and the readout plane were added (see figure 8.11). All joints were sealed with glue to ensure gas tightness, in particular the part where the field cage foil is bent over. There, two small reinforcement

bars had to be installed, so that afterwards the two foil ends could be glued to each other (see again figure 8.10). Once both flanges had been mounted, the 3 mm paper honeycomb structure (soaked with epoxy resin) was glued, followed by the second laminate (again with holes for the irradiation windows). The last layer of the field cage composite, a 100 µm copper foil, was then added as shielding against external noise. Finally, two adapter pieces hosting high voltage connectors for the first and the last field cage strip were assembled and 10 MΩ resistors were soldered between the inner and outer strips.

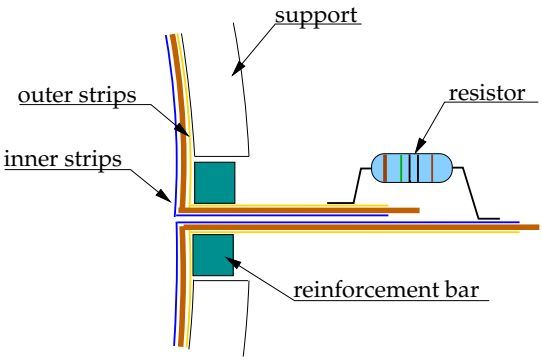

Figure 8.10: Schematic detail of the field cage, showing the connection of the inner and outer strips via the resistor chain.

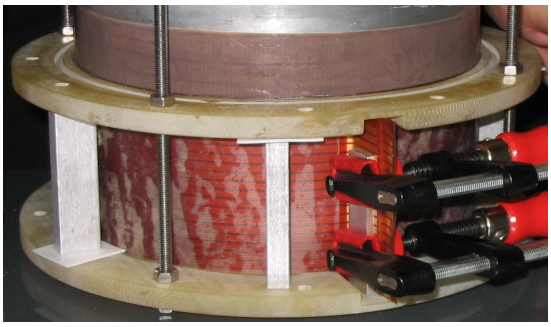

Figure 8.11: Photograph taken during the field cage construction; glueing of second flange.

8.2.3 Field Cage Test

To test the high voltage (HV) stability of the field cage, a potential difference between the first and the last strip was applied. The TPC had been closed before by attaching the readout plane and the drift cathode, but no GEM foils had been mounted yet. The safety box described in section 8.1.4 was connected and the readout pads were grounded to define the zero potential. Just 128 of them were combined to a single channel, amplified and monitored on the oscilloscope to check for discharges inside the detector. Thus apart from the GEM stack, which was not needed for this test, all nominal HV potentials were defined. In particular the currents within the resistor chain and on the last strip's HV channel could be measured and taken as reference for later operation. The measurement was done with a resolution of 0.1 µA in case of the resistor chain (see section 8.3.3 for more information about the used current meter). For the last strip just the 1 µA resolution current monitor of the power supply itself was regarded. During the whole field cage test, the TPC was flushed with nitrogen.

In total, ten measurement points were taken, which are summarized in figure 8.12. The potential of the drift cathode was varied between 1 000 V and 7 000 V and the last strip was set to always half this value. Thus, voltage differences between 500 V and 3 500 V were applied (for the 250 V/cm default drift field of the test chamber $\sim$ 1900 V difference

are needed). The field cage didn't show any problems during the test series, in particular no discharges were observed on the monitored pads and the measured currents increased linearly as expected. Consistently, the currents in the resistor chain and on the last strip summed up to the current to ground. The latter is, of course, always defined by the last strip potential and the 100 MΩ resistor inside the safety box (cf. figure 8.8).

8.2.4 Assembly and Test of the Complete Detector

After all components had been successfully tested, the test chamber was finally assembled including the GEM stack. Since for the latter seven high voltage (HV) supplies are needed, adequate connectors (SHV, max. 7 kV) were glued to the outer side of the readout plane. The loading resistors mentioned in section 8.1.4 were soldered between the SHV connectors and the HV feedthroughs of the readout. Although all open conductors were sealed with a silicone varnish (Dow Corning, 1-2577 CONFORMAL COATING), a protection plate made out of Plexiglas® was added on top of the detector. Figure 8.13 shows a photograph of the completely assembled TPC, yet without the readout electronics used for the cosmic muons tracking and an additional copper cover for shielding.

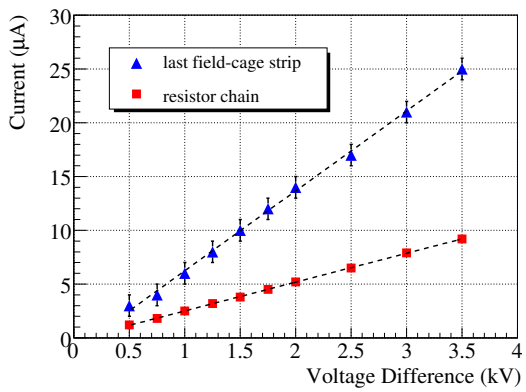

Figure 8.12: HV test of the field cage; voltage differences were applied between the cathode and the last field cage strip.

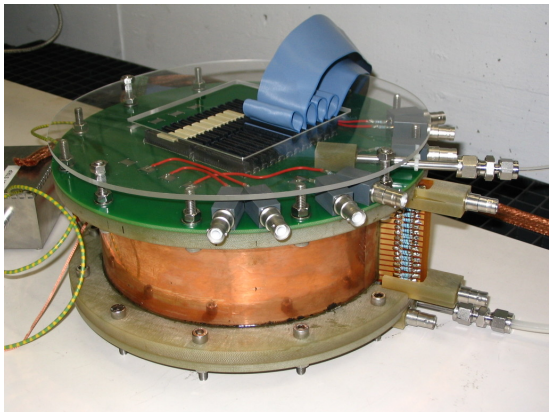

Figure 8.13: Assembled TPC test chamber with the readout plane (green) on top and the drift cathode at the bottom. field cage resistor chain, gas in and outlet and HV connectors visible.

In order to test the gas tightness of the test chamber, it was flushed with Ar/CO_2 and a LeakHunter® (Model 8065 by Matheson Tri-Gas) was used to carefully check for leaks. Neither at the O-ring sealings, nor at the gas inlet and outlet any detectable gas flow was found. Subsequently, the detector HV was ramped up slowly, first in a nitrogen and then again in an Ar/CO_2 environment. All currents were controlled and monitored with the Labview® program introduced in section 8.1.4, without showing any malfunction of the TPC. The last thing which was successfully tested before starting systematic measurements, was the interlock and safety system.

8.3 X-Ray Commissioning and Gain Calibration

Before using the test chamber for cosmic muons tracking, some elementary characterizations were performed. Since those required a known energy deposition at a fixed rate, a copper X-ray tube was taken as irradiation source. Section 8.3.1 describes this commissioning setup, while in sections 8.3.2 and 8.3.3 results from systematic studies and calibrations are presented. Altogether, these measurements helped to understand the detector and define its working point. In particular the knowledge of the detector's effective gas gain was an important input for setting up the readout electronics for the cosmic muons tracking.

8.3.1 Experimental Setup and Photon Detection

For all commissioning measurements presented in this section, an X-ray generator (Phillips, PW1120/90/96) with a copper anode (PW2213/20, fine focus) was used as irradiation source. Up to 60 kV can be applied to the anode, at a maximum electrical power of 1 500 W. Usually 10 mA and 15-16.5 kV were set for operation, the latter value being well above the $\sim$ 9 kV excitation voltage of copper. The $K_\alpha(88\%)$ and $K_\beta(12\%)$ emission lines, in turn, have an energy of 8.04 keV and 8.91 keV, respectively. To steer and control the X-ray rate, collimators with 1 mm and 2 mm bores were prepared. In addition, a filter with several copper foils of 5 µm thickness inside was used to clean up the X-ray spectrum. The initial intension here was to just reduce the fraction from Bremsstrahlung. However, it turned out later that it was even more important to cut off a second, non-copper X-ray peak at about 6 keV from the spectrum [215]. If needed, a shutter which is placed right after the opening of the tube (so even before the collimator) can be closed to completely block the beam. Figure 8.14 (left) shows a photograph of the TPC being set-up inside the shielding box of the X-ray generator, and a zoom (right) to the collimator pointing at one of the field cage windows.

Figure 8.14: Left: Experimental setup for X-ray irradiation of the test chamber, showing the generator and the lifted detector; both inside a shielding box. Right: Collimator pointing to one of the field cage windows.

In Ar/CO_2 (70/30), a copper X-ray photon creates on average 293 primary electrons through ionization (internal photoelectric effect) and subsequent electron avalanches. Here, both the ratio between K_α and K_β (see above) emission and the ratio between Ar (26 eV mean ionization potential) and CO_2 (33 eV) are taken into account. However, this number is only true if a complete conversion of the photon energy into electrons can be assumed. In case of Ar, excited ions can also re-arrange by emitting a photon instead of an (Auger) electron, which most likely escapes the detector without further interaction. The probability for this process is $\sim$ 15%, and the mean number of primary electrons per incident photon decreases to a value of 281. Furthermore, a characteristic "escape peak" appears in pulse spectra obtained from argon ionizations (cf. figure 8.17).

The readout of the TPC signals during the X-ray commissioning was not yet done with the multi-channel electronics chain, which is needed to extract three dimensional charged particle tracks (cf. section 8.4). Instead all pads were connected together and the whole charge, which was produced by the initial X-ray photon and then further amplified by the GEM foils, was collected together. It was either measured as a total current or processed in form of pulse signals, depending on the particular studies. In any case, a good noise shielding of the area close to the pads and of the signal cable was necessary. Therefore, a copper cover was designed, which just fits the detector but still leaves space at the position of the windows (cf. figure 8.14).

8.3.2 Rate Measurements and Pulse Height Spectrum

The studies presented in the following were performed by processing and analyzing the TPC signals as single pulses (instead of total current measurement). An ORTEC® [230] pre-amplifier (EG&G, Model 142IH) close to the detector was used, followed by an ORTEC® main amplifier in form of a NIM[3] module (EG&G, timing filter or 440A, selectable active filter). The amplified and shaped signals were either simply counted with a NIM discriminator and scaler logic, or sampled by a LeCroy 2259B module inside a CAMAC[4] crate and recorded. This module features an 11-bit, peak sensing analog-to-digital converter (ADC) with voltage input. To define a gate for the ADC, the TPC signal was split with a NIM linear fan in/fan out module, where one line defined the starting time for the gate and the other line was actually sampled. The X-ray was operated with the 1 mm collimator and the filter attached to the tube's opening, which gave a small enough intensity, such that no signal distortions due to pile-up were present.

Figure 8.15 displays the results of a rate scan, with systematically changed GEM stack voltage settings. "100%" refers to the settings listed in table 8.1, all other were scaled as indicated. The drift field was fixed during this scan to 250 V/cm. Apparently, the detection sets in at about "97%", while at "103%" an efficiency plateau is reached and all X-ray photons are detected. This expected behavior proves the proper function of the gas amplification part of the TPC. However, the absolute numbers cannot be taken over for the detection of cosmic muons, since there a different ionization process takes place.

[3]Nuclear Instrumentation Module, mechanical and electrical standard.

[4]Computer Automated Measurement And Control, standard including bus system for data acquisition.

Similarly, scans of both drift fields (cf. figure 8.8 for their definition) were performed to check the significance of theirs settings. The GEM stack was set to "105%" for this measurement, so well inside the efficiency plateau. First, both drift fields were varied simultaneously between 200 V and 300 V in 25 V steps, which is exhibited in figure 8.16. Afterwards, drift field 1 was fixed to 250 V/cm and only drift field 2 was varied between 240 V and 260 V in 5 V steps. In both cases, no systematic change in the X-ray count rate was observed and it was concluded that no fine adjustment between drift field 1 and 2 is needed.

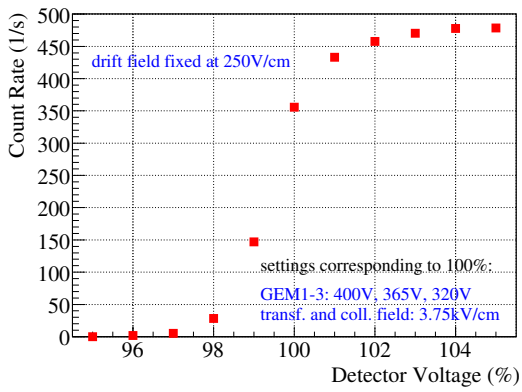

Figure 8.15: X-ray count rate vs. GEM stack voltage, given relative to the default settings indicated as "100%"; drift field fixed to 250 V/cm.

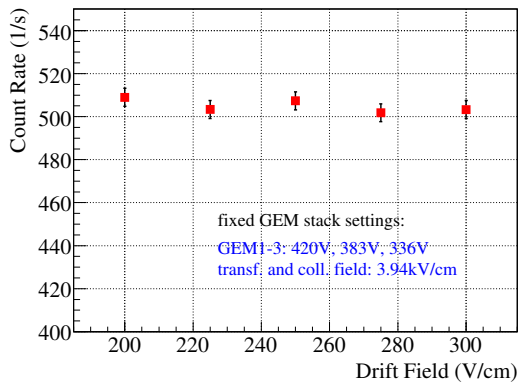

Figure 8.16: X-ray count rate vs. drift field; GEM stack settings fixed to "105%" (inside efficiency plateau). Errors are statistical.

In order to measure the energy resolution of the test chamber (and also to cross-check the gain calibration, see section 8.3.3), several pulse spectra at different voltage settings were taken. A shaping time of 0.25 µs was used for the ORTEC® 440A amplifier (see above), and the gate for the LeCroy ADC module was set to 1.4 µs. Figure 8.17 shows an example spectrum, corresponding to "105%" GEM stack settings and the default drift field of 250 V/cm. The main peak corresponds to the above discussed case, when the complete X-ray photon energy is translated into signal electrons (K_α and K_β lines not being resolved). Left to it, the argon "escape peak" shows up as a shoulder in the spectrum. Apparently, the energy resolution is worse than the potentially $\sim$ 20% of comparable GEM detectors [231]. A fit with two Gaussians and a background polynomial, which is also displayed in figure 8.17, results in a resolution of $\sim$ 30% ("photo-peak", full width half max.). This value can be partly explained by the fact that the X-rays enter the test chamber through one of the field cage windows and therefore parallel to the readout plane. Thus, the measurement suffers from local gain variations over the whole area of the GEM foils and also border effects. In addition, the TPC operation includes of course a much longer drift time for the electrons to actually reach the gas amplification stage, with a much higher probability of losses.

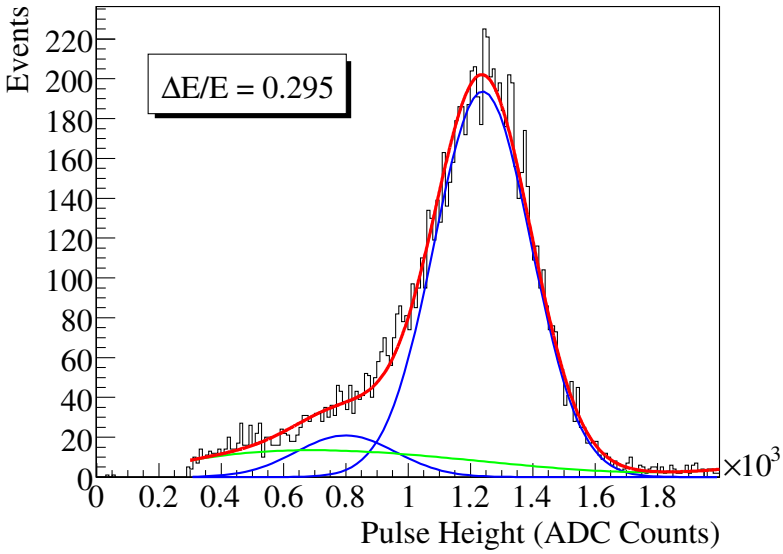

Figure 8.17: TPC pulse height spectrum recorded with copper X-rays. The red curve displays the result of a fit with two single Gaussians (blue) and some background polynomial (green). Resolution obtained from "photo peak" (FWHM).

8.3.3 Gain Calibration

For the gain calibration the total current on the readout pads was measured with 10 pA resolution. The current meter used for this was the first prototype of a series of custom-made devices[5], which were constructed to stand up to 7 kV of high voltage (HV) while still having an excellent resolution at the same time. The meters are based on an operational amplifier and a digital voltmeter and are powered by 9 V batteries. Depending on the existent current, four ranges are available which can measure up to 10 nA, 1 µA, 100 µA or 10 mA. The corresponding resolutions are 10 pA, 1 nA, 100 nA and 10 µA, respectively. While the following gain calibrations were performed with the best resolution mode, the 100 µA range was chosen during the field cage test (see section 8.2.3). For a detailed description of the current meters see section 7.2 of [215].

Once set up for the gain measurement, the input X-ray rate was determined by setting the TPC into the efficiency plateau (see figure 8.15) and counting the number of signals as described before. A stable value of $341 \pm 18\,\mathrm{s}^{-1}$ (statistical error) was obtained with the generator settings described in section 8.3.1 and using the filter followed by the 1 mm bore collimator. In addition, a background rate of $18 \pm 3\,\mathrm{s}^{-1}$ was measured (shutter closed), which was later subtracted. The GEM stack HV was then varied between "100%" and "105%" (cf. section 8.1.5), while the drift field was kept constant at 250 V/cm at the same time. For each setting, the total current on the pads was measured, which ranged from 130 pA to 310 pA. Since these are very small currents, the resolution of the meters

[5]Design by I. Konorov, Technische Universität München, Physik-Department E18; constructed by Electronics Workshop of TU München, Physik-Department.

showed up as fluctuations and 10 pA or even 20 pA errors had to be assumed. Again, a background current was measured (shutter closed), which was of the order of 30 pA.

The effective gain is defined as the ratio of the (measured) current on the readout plane and the "primary current". This "primary current" can be calculated as the product of the (measured) X-ray rate, the known elementary charge and the number of primary electrons per incident photon. For the latter, a value of 281 has been taken (see also discussion in section 8.3.1). The final results of this calibration are presented in figure 8.18, exhibiting an exponential dependence of the gain on the detector voltage as expected. The observed absolute values are similar to other triple-GEM detectors as for example the COMPASS chambers [210].

Since the effective gas gain can also be obtained from pulse spectra like the one shown in figure 8.17, this alternative was used as a cross-check. For this purpose a voltage calibration of the pulse heights is needed, which was done using a pulse generator. From the (calibrated) position of the "photo peak" V and the known number of primary electrons (293 in this case), the gain G can then be calculated according to $G = (V \cdot 1\,\mathrm{pF})/(293 \cdot e)$. Here the input capacitance (1 pF) of the pre-amplifier enters, and e is the elementary charge. It turned out that this "pulse height method" gives systematically smaller gain values compared to the "current method", independent of the particular voltage settings. The reason is that in the case of all pads being connected, the capacitance defined between the last GEM foil and the readout plane ($\sim$ 50 pF) is of the same order of magnitude than the capacitance of e. g. a 1 m 20 kV HV cable. Thus the power supply cannot maintain the potential of the last GEM foil while the signal electrons drift through the collection field and, effectively, a smaller current is created via the pre-amplifier. In the pulse height spectrum, the "photo peak" therefore shifts to lower values. This behavior was indeed reproduced for one GEM stack setting ("104%") by reducing the number of connected pads until the position of the peak didn't change anymore. The gain values calculated from these data are shown in figure 8.19 together with an error band corresponding to the "current method" result for this particular setting.

8.4 Electronics, Data Acquisition and Trigger for Cosmic Muons Detection

The tracking performance of the test chamber has been studied with muons from cosmic-ray air showers. These high-energetic charged particles leave an ionization track inside the detector, while still crossing it completely. Thus, apart from random coincidences, a background free trigger can be set up. To be able to completely reconstruct the obtained three dimensional tracks, dedicated readout electronics is needed. It has to provide a multi-channel signal processing including a pre-amplifier, shaper and analog-to-digital conversion. In addition, buffers are needed, which are large enough to cover the maximum time a signal electron might need to drift through the whole TPC volume. Once complete, the data corresponding to one trigger has to be shipped to an acquisition system, which stores it to disc.

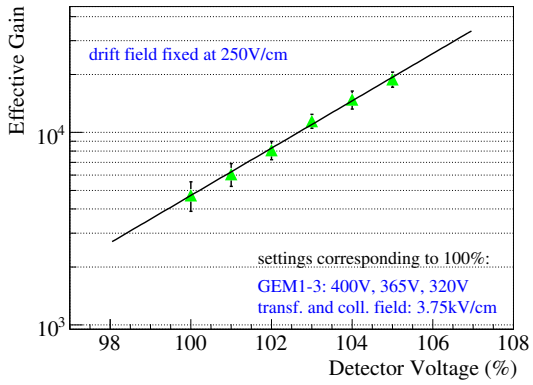

Figure 8.18: Results from gain measurement with the "current method", voltage settings are relative to default settings; logarithmic scale.

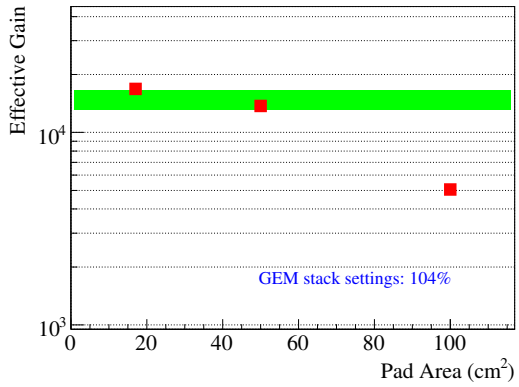

Figure 8.19: Dependence of gain obtained by the "pulse height method" on read out pad area; detector at "104%". Corresponding value from figure 8.18 drawn as green error band.

For all measurements presented in section 8.6, 128 channels of the test chamber have been equipped with the ALICE[6] TPC readout electronics [232]. A universal series bus (USB) device, also developed by the ALICE collaboration (CERN EP-ED) for small-scale laboratory applications, acts in this setup as interface to a data acquisition (DAQ) computer. This USB interface also receives and forwards the trigger, which is provided in this particular case by the coincidence of two scintillator detectors. On the DAQ computer, a custom-made program serves as run control and online event display. Figure 8.20 shows a photograph of the electronics chain including the interfaces to the detector, DAQ computer and trigger.

8.4.1 Frontend Electronics

The charge signals of the TPC are mainly processed by the PASA and ALTRO chips [232, 233]. Both are application specific integrated circuits (ASICs) and support 16 channels. Eight chips are placed on one frontend card (FEC), which consequently hosts a total of 128 channels. The FEC is identically used for the ALICE TPC readout, where it is directly connected to the detector. However, since the ALICE TPC features avalanche multiplication in wire-chambers, the FEC expects a positive polarity input signal. Thus the test chamber's negative electron signal has to be adapted first, which is done by a signal polarity inverter (SPI) card[7]. In the following, the main elements of the frontend electronics are briefly described, starting from the detector side (left of figure 8.20). For detailed and up-to-date manuals and layout schematics, please refer to [234].

[6] A Large Ion Collider Experiment, located at the Large Hadron Collider, CERN, Switzerland.

[7] Currently a new pre-amplifier ASIC with flexible polarity input is designed, which will make the SPI obsolete.

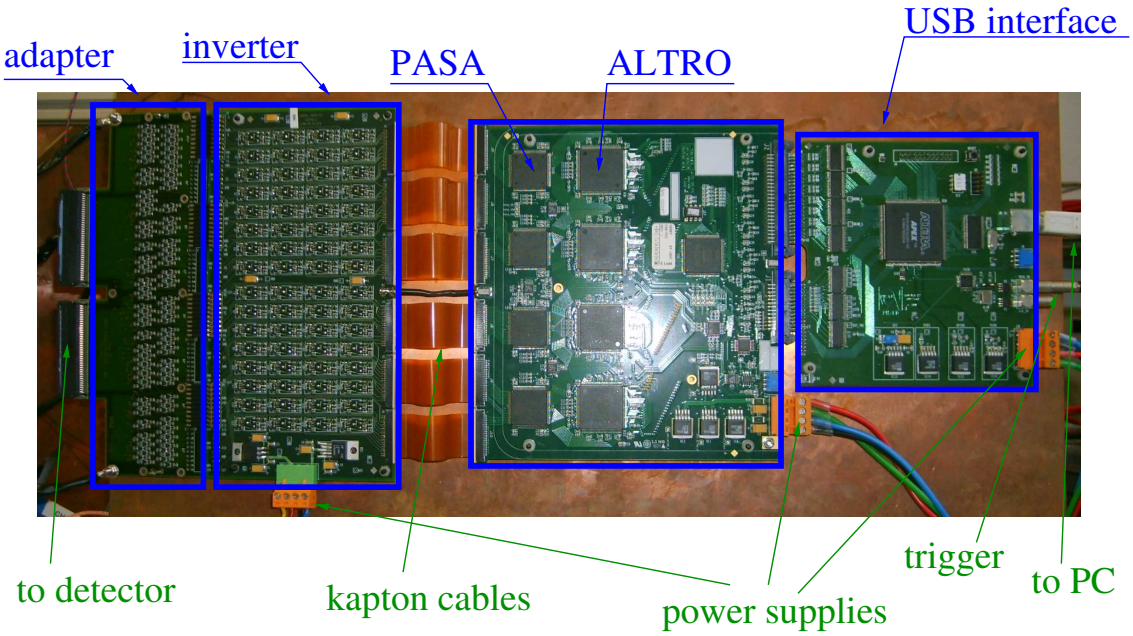

Figure 8.20: Overview photograph of the test chamber readout electronics chain. The basic processing elements are labeled in blue, while the green captions point out interfaces and connectors. All cards are mounted to a copper support plate.

About 10 cm long, screened flat cables are used to guide the analog signals of the test chamber from the readout plane (cf. section 8.1.2) to a printed circuit board (PCB). This first card[8] in the readout chain fulfills two functions. First of all, it contains protection circuits for all channels, which prevent the adjacent electronics components from damage in case of a gas discharge. Secondly, it acts as an adapter between the pitch of the flat cable connectors and those of the SPI, to which it is directly plugged. With this setup, it is much easier and efficient to shield the flat cables against externally induced noise and, in addition, the cables can be much shorter. The adapter card is a passive device, which doesn't need a voltage supply.

Next, the above introduced SPI card follows in the signal processing line. It is again a PCB with 128 independent circuits, which are active elements in the sense that only with supplied voltage, signals pass through and are inverted. Two versions of this card were tested, which differ mainly in the power supply part. It was finally decided to operate with the one featuring an on-board voltage regulator, simply because it showed a better noise performance (see section 8.4.3). This version needs a positive and a negative, ~ 7 V voltage channel and has a typical current consumption of 0.1-0.3 A. The SPI is connected by means of high-density Kapton® (DuPont) cables and a ground cord to the FEC.

On the FEC, each readout channel comprises four basic functional units: a charge sensitive pre-amplifier/shaper (PASA), a pipelined 25 MSamples/s analog-to-digital-converter (ADC), a digital circuit for further signal processing and a data memory

[8]Developed and employed for tests of the T2K (From Tokai To Kamioka) TPC, J-PARC, Japan.

(multiple-event buffer). Apart from the first one, all units are contained in the ALTRO chip. The 16-channel PASA has a conversion gain of 12 mV/fC, a dynamic range of 2 V and a shaping time (FWHM) of 190 ns. Its power consumption is 11 mW per channel and a single channel has a noise value below 570 e^- [232].

Immediately after the PASA, the signals are sampled inside the ALTRO chip by a 10-bit ADC with an (adjustable) rate of 10 MHz. When a level-1 trigger is received, a predefined number of samples (usually set to 150 in case of the test chamber) is processed and temporarily stored in the multiple-event buffer. The data processor contains a set of circuits that can perform a baseline correction, tail cancellation and zero suppression [233]. The tail cancellation is only needed in case of slow ion signals from a wire-chamber and was never employed for the GEM-TPC. Also the baseline correction and zero suppression were usually switched off during the measurements, to have more flexibility in the offline analysis. In particular the treatment of "common-mode noise"[9], which is not incorporated into the ALTRO, has then been feasible.

The ALTRO data memory (1024 × 40 bits) can hold up to four complete, 1 000-sample (10-bit words) acquisitions. Upon arrival of a level-2 trigger, the latest acquisition inside this multiple-event buffer is frozen and cannot be overwritten by a new level-1 trigger. Since the readout of the chip is performed via a 40-bit bus system on the FEC, the data has to be packed into 40-bit words. Details about this data format and instructions how to correctly decode it can be found in the ALTRO documentation [234]. If operated at a sampling rate of 10 MHz, the 16 channels of the ALTRO chip consume in total a power of 320 mW. The whole FEC needs two positive voltage supplies (3.3 V and 4.3 V) and consumes a current of about 1.1 A and 0.6 A, respectively, depending on the trigger rate.

8.4.2 Data Acquisition System

The data from the FEC is transfered to the DAQ computer via a custom-made USB device, also developed by the ALICE collaboration. This general interface can handle up to 12 FEC cards and distributes a common clock and the external hardware trigger. The level 1 and 2 trigger conditions are controlled here, too, but were simply equated for all test chamber measurements. On demand, the device can also create an internal trigger, which is exploited during noise tests and pedestal runs (see section 8.4.3). It furthermore allows an efficient programming of the FEC through the USB connection, using a set of basic register access functions[10]. The card requires its own voltage supply (+5 V and −5 V) and can consume several Ampère during data transmission, depending on the load.

To control the data taking during runtime, dedicated DAQ software has been developed, which provides also several online histograms and a graphical user interface (GUI). During start-up, the program establishes the connection to the USB interface and initializes the FEC. It also checks that a calibration file, including the baseline and noise values for each channel, is available. Before actually starting a "run", the number of samples to be read per trigger and channel, the trigger mode (internal or external) and the data taking

[9] Synchronous movement of all readout channels of one FEC or one chip, see also section 8.4.3.
[10] ANSI-C library and USB driver provided by CERN EP-ED.

mode (zero suppression on/off) have to be entered via the GUI. If an active zero suppression on the ALTRO level is chosen, individual thresholds for each channel are up-loaded, based on the values in the calibration file. In any case, the program decodes online the data and checks for each event (trigger) that at least 10 samples are above threshold, before it marks the event to be stored. This basic selection is necessary, since the acceptance of the trigger scintillators is much larger than the area covered by the 128 readout channels (see also section 8.4.4) and many "empty" events would be recorded otherwise. When a run is finished or stopped manually, a ROOT [155] file containing unique event numbers and all (already decoded) sample information is saved to disc.

8.4.3 Noise Optimization, Treatment and Performance

Before starting the data taking with muons, the noise of the system had to be optimized. This included the detector, the electronics, the high voltage (HV) power supplies and, as it turned out to be very important, also the low voltage power supplies. The strategy was to first start with only the FEC being attached to the USB interface (cf. sections 8.4.1 and 8.4.2), then add the inverter card, connect the TPC and, finally, ramp up the HV. For every step, the noise was monitored by using the previously described DAQ system in the internal trigger mode with baseline subtraction and zero suppression off. Of the order of 100 triggers and about 150 samples per trigger and channel were recorded and the mean and the root mean square (RMS) calculated for each channel. This calculation can be performed and updated online by the monitoring software, which served as a quick reference during the tests. Especially during the start-up phase, however, it was necessary to correct also for "common-mode noise", which, as mentioned before, cannot be done by the ALTRO chip and was therefore done offline.

The "common-mode noise" correction is based on the algorithm, which was developed and is used for the readout of the GEM and silicon detectors of the COMPASS experiment [235]. The algorithm runs on the raw analog samples, which are rearranged in time frames (usually 150 like the number of samples per trigger and channel). For each such frame, the sample values are sorted by amplitude and the median is calculated and subtracted from all values. Afterwards, the RMS can be again calculated for each of the 128 channels and stored to a "pedestal file" together with the mean of each channel which defines the baseline value. These two parameters, the "common-mode noise" corrected RMS and the baseline, are later read in for each channel by the reconstruction software (see section 8.5). To keep track of possible changes within the noise structure of the TPC, "pedestal runs" have been regularly taken and the "pedestal files"updated.

For data taking, the following grounding scheme was finally chosen: It comprises a first central grounding star point in form of the copper cover, which is mounted on top of the TPC. To this "detector ground", the outermost field cage layer (cf. section 8.1.1) is connected, as well as all HV connector grounds of the test chamber. A second star point is defined by the massive copper plate, on which all electronics cards are mounted (cf. figure 8.20). In particular the FEC ground is connected to this plate by means of a thick screw connection. All other PCBs get their ground via cable or plug-in connections from

the FEC. To this "electronics ground", also the shielding of the signal cables and the not read-out pads are directed. Finally, the "detector ground" and the "electronics ground" are put together to define one common grounding point. In addition, it turned out to be very important to add a ferrite core to the electricity cables of the SPI and thereby avoid noise fed-in from its power supply module. Also several HV filters are in use for the TPC, which have already been discussed in section 8.1.4.

Figure 8.21 displays two noise distributions, which were obtained with the described setup. For the left one only the FEC was attached, thus it shows more or less the noise coming from the PASA pre-amplifier. Averaged over all channels, 0.54 ADC counts were measured after the "common-mode noise" correction, which attributes to $\sim$ 2%. For the plot on the right-hand side, the whole electronics chain including the detector itself was connected. All devices were powered and the HV ramped up. For these data taking conditions, the average RMS noise is 1.88 ADC counts, with a (already corrected) "common-mode noise" contribution of $\sim$ 5%. The increase in noise of a factor 3.5 is almost completely due to the SPI card, the TPC itself adding just a few %.

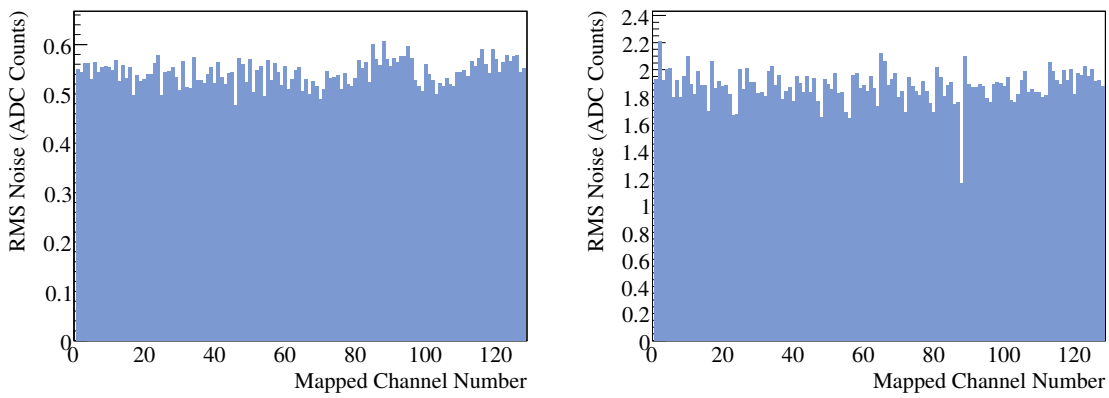

Figure 8.21: Noise performance of the TPC readout electronics, RMS for each channel shown. The 128 channels are mapped "left to right" if looking from the front to the SPI. Left: only ALTRO card connected, average noise 0.54 ADC counts. Right: everything including TPC connected and powered, average noise 1.88 ADC counts.

8.4.4 Cosmic Muons Trigger and Data Taking

The cosmic muons trigger is based on two plastic scintillator detectors (NE-110, blue-violet emitter), which were designed and fabricated especially for this application. Each of them has an active area of $10 \times 10\,\text{cm}^2$ and a thickness of 1 cm. Fishtale-shaped light-guides (Plexiglas®) couple the scintillator bulks to photomultipliers[11] (PMT). On the output side, the light-guide is circular with a diameter of 5.4 cm, which matches the cathode size of the PMTs. Each PMT has to be operated between -1.2 and -1.5 kV and has a current consumption of up to 0.3 mA.

[11] Former Thorn Emi, now Electron Tubes [236], 9236 series, 350-450 nm peak sensitivity.

To actually define a coincidence of the two trigger detectors, three NIM modules are employed. First of all, the PMT signals are processed by an amplifier module (LeCroy, 612A). Afterwards, a discriminator (LeCroy, 620D) with an adjusted threshold of the order of -30 to -40 mV follows, the logical outputs of which are then combined in a coincidence module (LeCroy, 622). If existing, the final trigger decision is forwarded to the readout electronics by means of a LEMO 00 cable, which is plugged into the USB interface (see section 8.4.2 and figure 8.20).

Depending on the position of the two trigger scintillators around the test chamber, the topology and number of the recorded muon tracks varies. In general, the muon rate is highest if the detectors are co-planar with their active area facing upwards. Also they should be mounted as close as possible to the TPC. For the presented measurements, the TPC was mounted with the drift direction vertical, to trigger on tracks crossing the chamber perpendicularly to the readout plane. This is illustrated schematically in figure 8.22 while figure 8.23 shows a photograph of the real setup. In fact, this geometry corresponds to the very abundant forward going tracks in PANDA (see section 6.3), which are the most difficult to reconstruct (see section 8.5).

After a coincidence trigger had occurred and been transmitted by the USB interface, the whole electron drift time of 14 µs (cf. section 8.1.6) was digitized for all read out pads. To be on the save side, 150 samples were stored (100 ns time intervals, cf. section 8.4.1). In order to be able to study in a flexible way the signal shapes, furthermore no online zero suppression was performed. Neither was the baseline correction, to allow for an offline "common-mode-noise" correction. As mentioned before, always 128 pads were connected: 16 with the 6.2 mm pitch and 8 with the 1.0 mm pitch. This corresponds to a sensitive volume of $99.2 \times 8 \times 77\,\mathrm{mm}^3$, which is indicated in figure 8.22.

8.5 Event Reconstruction and Analysis

The software to reconstruct the test chamber data is set up as a sub-branch inside the PANDA framework[12]. This has the advantage that all developed algorithms can be used for both real data and Monte Carlo data. Thus cross-checks and cross-calibrations are possible. In particular, the test chamber data provide a realistic environment concerning noise and fake hits, which of course challenges the pattern recognition much more. After an overview of the recorded data sets, this section describes in detail the employed analysis techniques. First a preprocessing of the data is performed, which are then reconstructed in four stages: the pulse shape analysis, the cluster finding, the track finding and, finally, the track fitting. All information needed for systematic studies are stored in a way such that the final analysis can be done very efficiently based on ROOT [155] macros.

[12]PandaROOT: full environment for simulations, event reconstruction and physics data analysis in PANDA, written in C++. For further details on the TPC implementation see [189, 222].

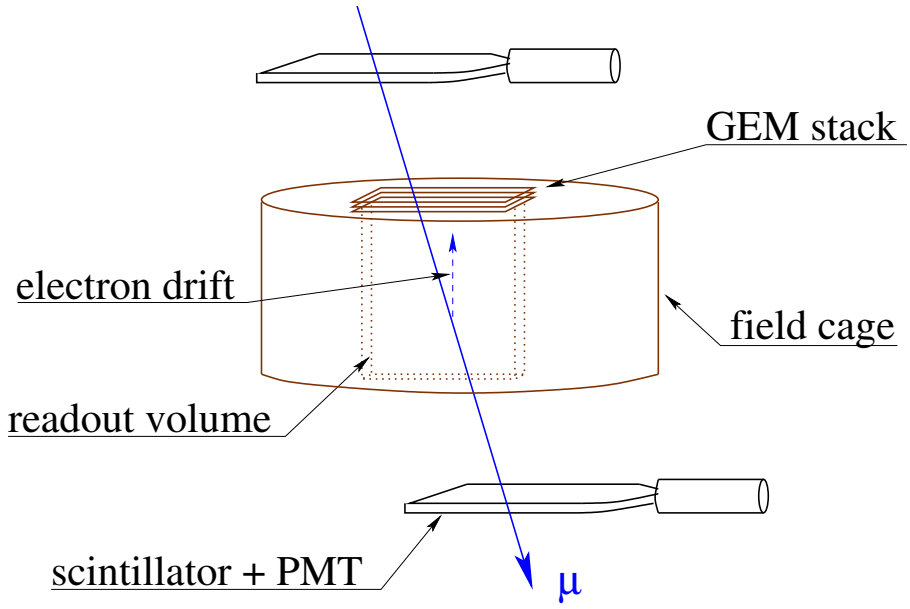

Figure 8.22: Position of trigger detectors with respect to the test chamber; TPC mounted horizontally (drift direction vertical), thus muons cross the readout plane and the GEM stack rather perpendicularly. The sensitive volume of $99.2 \times 8 \times 77\,\mathrm{mm}^3$, given by the area of the read out pads and the drift length, is indicated.

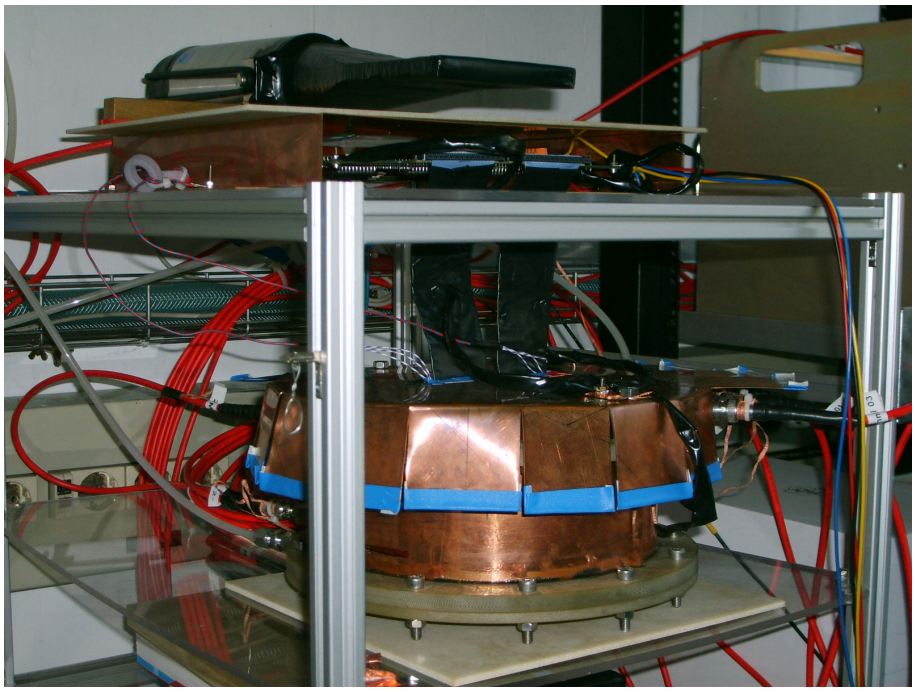

Figure 8.23: Photograph of the cosmic muons stand; case of horizontal TPC mounting. Only the top scintillator is visible, lying on the (covered) readout electronics.

8.5.1 Data Set and Preprocessing

The total data set, based on which the results presented in section 8.6 have been obtained, consists of $\sim$ 13 000 cosmic muon tracks. As summarized in table 8.2, seven data taking periods ("H1"-"H11") with different GEM stack settings were performed. The number of trigger attempts gives a rough estimate of the effective data taking time, since 1 000 attempts corresponded to about one hour. Usually single runs with a duration of the order of ten hours were taken. The number of good triggers represents the number of events which passed the online selection criterion of at least 10 samples over threshold (cf. section 8.4.2). Period "H6" comprises the largest statistics with one particular voltage setting, and has therefore often been used exclusively. During a pre-production step the data have been corrected for "common-mode-noise" and baseline shifts using the algorithm described in section 8.4.3. The corrected samples have then been passed to the PandaROOT framework for further processing.

Period name	H1	H2	H3	H4	H5	H6	H7
Trigger attempts	30 100	61 100	44 000	78 000	10 040	107 000	17 000
Number of runs	5	8	5	9	2	12	2
Good triggers	2 371	5 335	2 963	6 452	742	6 585	1 318
GEM settings (%)	106	103	100	98	106	100	98
Drift field (V/cm)	250	250	250	250	250	250	250

Table 8.2: Overview of the recorded data sets; time period 02.02.2007-02.03.2007.

8.5.2 Pulse Shape Analysis (PSA)

The PSA is carried out on each pad individually. The whole 150 samples per pad of one event are processed with an algorithm, which defines bunches of consecutive samples as pulses. A pulse begins when an ADC reading is greater than a threshold of $4 \times \sigma_i$, where σ_i is the "common-noise" corrected RMS-noise of pad i provided by a parameter file (see section 8.4.3). The pulse ends either when an ADC value is below threshold ("time-over-threshold") or if the wave form exhibits a local minimum. In the latter case the previous pulse is completed and its integrated amplitude and time t are calculated: $t = t_\mathrm{f} + 0.3(t_\mathrm{l} - t_\mathrm{f})$, where t_f and t_l are the time of the first and the last sample in the pulse, respectively. In addition, a new pulse is started. The performance of the PSA is illustrated in figure 8.24 for two topologically different events. While the left panel shows the charge structure on a pad corresponding to a muon track with a larger angle to the detector axis, the right panel visualizes what happens when a muon crosses the TPC perpendicular to the readout plane. The example pad receives a continuous signal, with just sufficient sub-structure such that the PSA can still distinguish different pulses. Thus the 10 MHz sampling frequency of the ALTRO seems to be enough for the slow Ar/CO_2 gas. For the PANDA TPC employing a neon-based mixture, however, clearly a better performance would be needed to provide e. g. precise $\mathrm{d}E/\mathrm{d}x$ information from many hits per track.

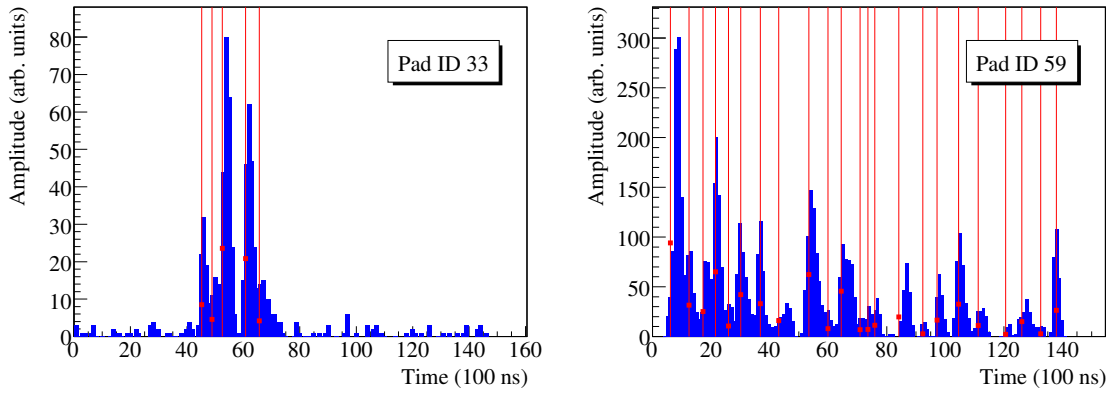

Figure 8.24: Time structure of the charge (blue, ADC units) as induced on a readout pad for one complete electron drift time. The situation of an oblique (left) and a perpendicular (right) muon track is compared. A pulse shape analysis performed for both pads yields a time (indicated by the red vertical lines) and an integrated amplitude (scaled down by a factor of 10, indicated by the red markers) for every pulse.

8.5.3 Cluster Finding

Based on the pulses found, the next task is to group neighboring pulses together into clusters, thereby improving the resolution of the measurement. This is performed in all three spatial dimensions, thus in the readout plane (x-y) as well as in time (corresponding to z). The algorithm first sorts all pulses by amplitude, and starts the first cluster with the time and amplitude of the largest pulse. It then goes through the list of pulses with descending amplitude and evaluates whether a pulse is adjacent in the pad plane and in time to an already started cluster. The latter is controlled by a maximum allowed time difference between the cluster and the "to-be-added" pulse. Usually a window of $\pm 0.5\,\mu s$ has been chosen[13]. Only if both the spatial and time condition are fulfilled the pulse is added to the cluster, otherwise a new cluster is started. Step by step all pulses are either assigned to one of the existing clusters or start a new cluster themselves. In case a pulse can be attributed to more than one cluster the charge is split equally. Finally, the center of gravity of charge and the corresponding errors are calculated for each cluster. The z position is obtained by taking into account the electron drift velocity v_D[14]. The spatial uncertainties are taken as the quadratic sum of the diffusion[15] and the variance of a rectangle function with a width of the pad pitch or the inverse sample frequency times v_D, respectively. The amplitude uncertainty is defined by the RMS noise σ_i (cf. section 8.5.2). Figures 8.25 and 8.26 illustrate the performance of the cluster finding for the same two events from which the single pad information displayed in figure 8.24 have been extracted. Shown are the unclustered pulses (top panels) in the x-z and y-z planes, as well as the obtained clusters (bottom panels). Open circles denote the relative pulse or cluster amplitudes.

[13] Once a new pulse has been added to a cluster, the center in time of this window is updated by the weighted mean of all pulse times in the cluster.

[14] About 0.57 cm / µs, calibrated in an iterative procedure (see section 8.6.1).

[15] $D_T = D_L = 0.016\sqrt{\text{cm}} = 160\,\mu\text{m}/\sqrt{\text{cm}}$, obtained from GARFIELD (version 7.04) [237].

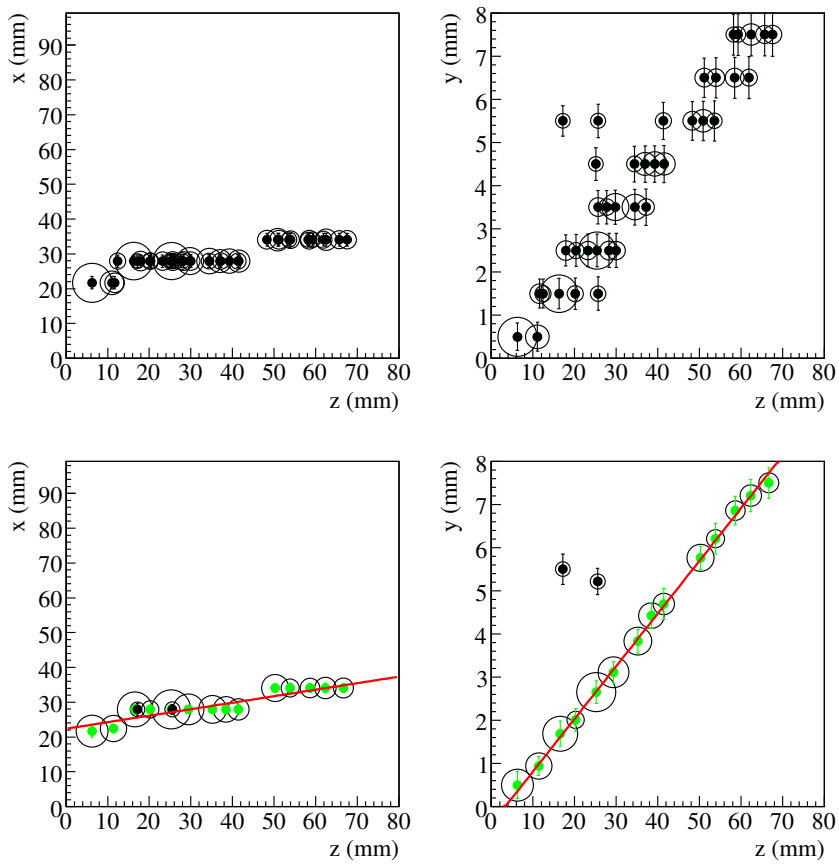

Figure 8.25: Cosmic muon event in the TPC test chamber; oblique angle of incidence w. r. t. the pad plane. The top panel presents the data before the clustering, the bottom panel the space points of the found clusters (cf. section 8.5.3); x-z (left) and y-z (right) projections shown, open circles indicate the relative amplitudes. The pad pitch is 6.2 mm in x and 1 mm in y direction, respectively. For the clustered data, the green markers denote hits selected by the pattern recognition for the track fit (cf. section 8.5.4), which is also shown as red line.

8.5.4 Pattern Recognition and Track Fitting

As can be seen from figures 8.25 and 8.26, the space points resulting from the cluster finding mostly align along the muon tracks. However, there is a certain number of outliers (due to noise or uncorrelated hits), which have to be excluded from the track fitting in order not to spoil the results. This pattern recognition is done solely in the y-z plane, which is sufficient due to the good y resolution and a track multiplicity of essentially unity. The employed method for the track finding is a Hough transform[16], where a particle track is described by the relation $y = a_y \cdot z + b_y$[17]. Every measured space point (y_k, z_k) is mapped to a straight line in the a_y-b_y plane, with $b_y = (-z_i) \cdot a_y + y_i$. Those

[16]Feature extraction technique [238], nowadays widely used in digital image processing.
[17]For the fitting also the relation $x = a_x \cdot z + b_x$ is used.

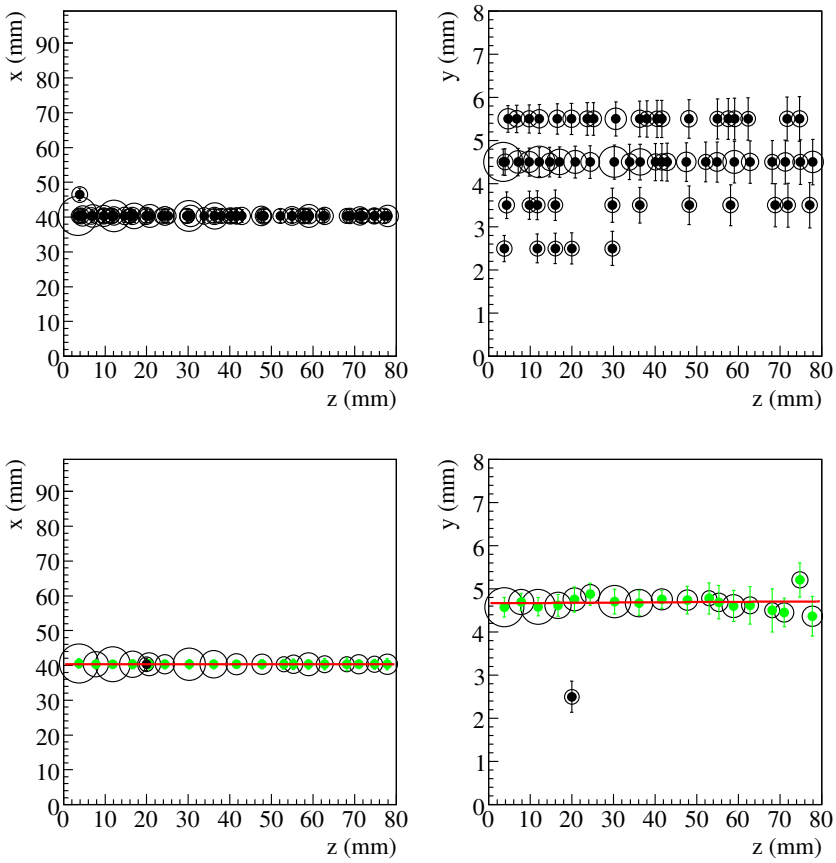

Figure 8.26: Cosmic muon event in the TPC test chamber; perpendicular angle of incidence w. r. t. the pad plane. See caption of figure 8.25.

lines corresponding to collinear points in the y-z plane intersect in one point in the a_y-b_y plane, based on which the "hits-on-track" can be selected. Figure 8.27 presents as an example the same event shown in figures 8.24 (left) and 8.25. Several hits (green lines in figure 8.27, green markers in figure 8.25 (bottom, right)) are selected, while two outliers (black colored) are rejected by the pattern recognition. Based on the selected hits, a 3-dim. straight-line least-squares fit is performed using the above introduced track parameterization (red lines in figures 8.25 and 8.26 (bottom)). This step concludes the track reconstruction, and the results such as the residual vectors for each selected hit and the track parameters are written to an output file for further analyses.

8.5.5 Further Analysis Tools

For the final data analysis a set of ROOT macros has been used. They take the output files from the described reconstruction procedure, which are usually organized as one file per run (cf. section 8.5.1). A loop over all reconstructed events and, eventually, all clusters of a track is performed. The quality of the analyzed tracks can be ensured by applying cuts on e. g. the minimum number of hits per track or the track angle w. r. t. the z axis.

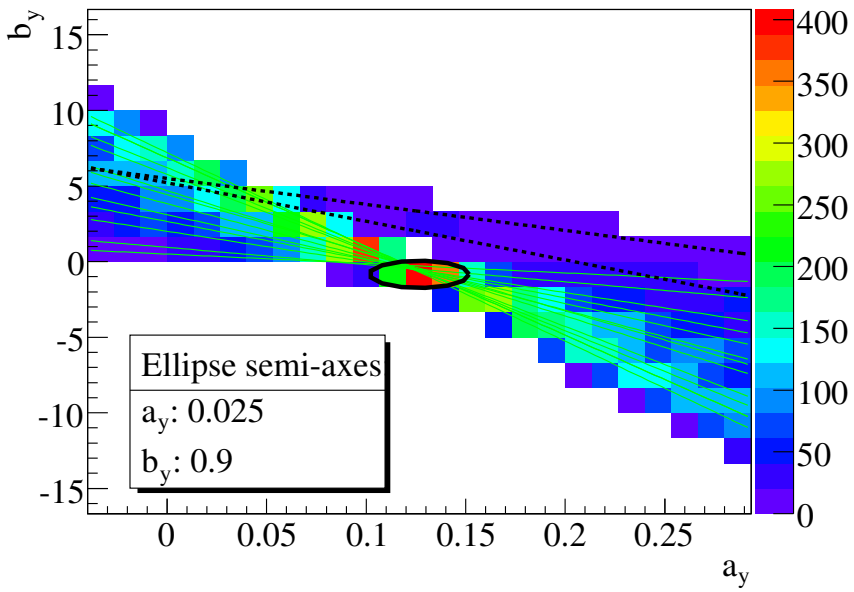

Figure 8.27: Pattern recognition in the TPC test chamber using the method of Hough transform (see text). An ellipse around the center of the bin with the maximum accumulated line length (indicated by the color scale) selects "hits-on-track" (green lines intersecting the ellipse). Outliers (black dashed) are rejected for the track fitting; same event as in figure 8.25.

8.6 Results from Measurements with Cosmic Muons

This section summarizes selected results obtained with the TPC test chamber, set up for tracking of cosmic muons as described in the section 8.4.4. The data set and reconstruction tools are described in section 8.5. It is emphasized that the analysis of the recorded data is still ongoing and subject to improvements (see also section 8.7).

8.6.1 Drift Velocity Calibration

For the calibration of the drift velocity the clustering has been deactivated. The pattern recognition has been applied to the single pulses, using the GARFIELD [237] value of 0.552 cm / µs as an estimate for the drift velocity. Due to the special trigger topology (see figure 8.22) many tracks traverse the TPC completely from top to bottom, thus crossing both the readout and the drift plane. The z distribution of the unclustered "on-track" pulses therefore exhibits two sharp edges at a distance d'. Since the true drift length d (77 mm, cf. section 8.1) is known, the initially assumed drift velocity can be corrected by the ratio of d and d'. The result is shown in figure 8.28 for about one month of operation, corresponding to the periods "H1" to "H7" introduced in table 8.2). About two calibrations have been performed for each day of data taking (one per run). The drawn errors contain both the uncertainties on d and d', which are of the order of 0.5 mm. A constant function fit to the points yields an average drift velocity of (0.569 ± 0.001) cm / µs.

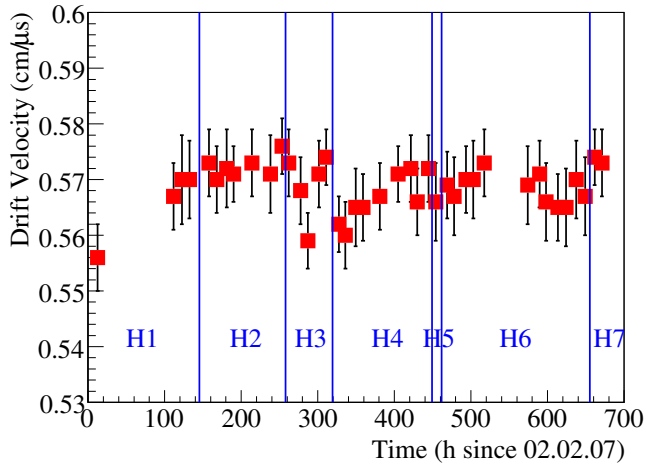

Figure 8.28: Drift velocity calibration for a TPC operation of one month. Temperature and pressure variations are not taken into account.

8.6.2 Cluster Size Distribution

As explained in section 8.5.3, the clustering proceeds in all three spatial dimensions (with a time window of $\pm 0.5\,\mu s$). The resulting cluster size distribution for "100%" GEM settings (see table 8.1) is presented on the left of figure 8.29. To clean up the event sample, a track angle of $< 30°$ with respect to the z axis and a minimum of four "hits-on-track" has been required[18]. A mean 3-dim. cluster size of 3.2 is obtained, where the mean number of contributing x (6.2 mm pitch) and y (1.0 mm pitch) pads is 1.1 and 2.1, respectively. Figure 8.29 also shows on the right the dependence of the mean 3-dim. cluster size and the RMS standard deviations (drawn as error bar) on the voltage settings. As expected the cluster size grows with increasing gain (cf. figure 8.18).

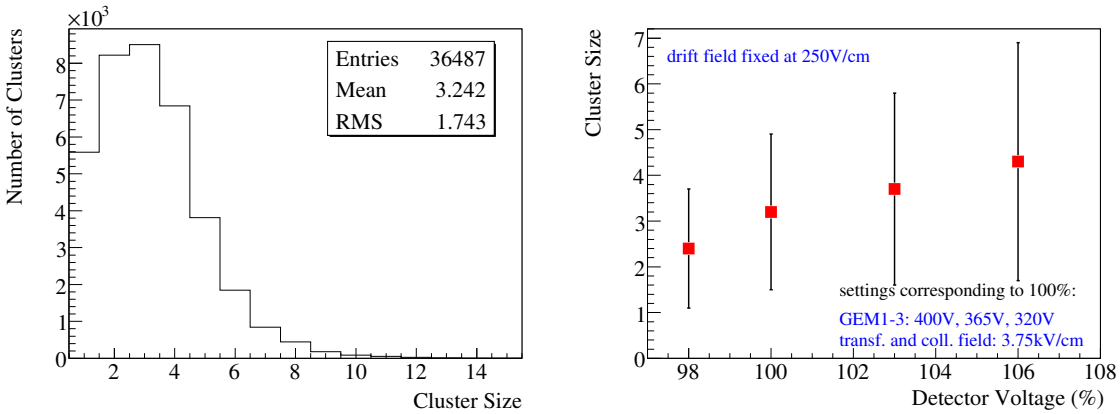

Figure 8.29: Left: Distribution of sizes of 3-dim. clusters for standard settings ("100%"). Right: Mean cluster size for different GEM stack settings, RMS of each corresponding distribution drawn as error bar.

[18] On average, the tracks comprise 10.4 selected hits.

8.6.3 Spatial Resolution

In figure 8.30 (left) the residual distribution for the y coordinate (1 mm pitch) is shown for the standard settings and cuts as described in section 8.6.2. One entry in this histogram corresponds to one cluster, more precisely to its distance in y direction to the fitted track it belongs to. Thus the same clusters which define the track and contribute to its fit are considered to evaluate the residuals. This introduces a small bias in the analysis, which is partly recovered by the requirement of a minimum of four clusters per track[19]. The residual distribution has been fitted with two Gaussians as indicated in the figure. From their standard deviations $\sigma_{1,2}$ and integrals $I_{1,2}$, a y resolution of $(203 \pm 2)\,\mu\text{m}$ has been calculated:

$$\Delta_y = \frac{\sqrt{I_1^2\sigma_1^2 + I_2^2\sigma_2^2}}{I_1 + I_2} \quad . \tag{8.1}$$

Due to diffusion the resolution is expected to depend on the z-position of the clusters. To study this effect, the TPC has been divided (in software) into eight regions along the drift axis, and an analysis has been performed for each region independently. The result is presented in the right panel of figure 8.30, showing a clear degradation of the resolution with increasing z. While in the region $0 < z < 10\,\text{mm}$ a resolution of $140\,\mu\text{m}$ is achieved, up to $250\,\mu\text{m}$ are observed for the longest drift distances. A fit to the data using equation (8.2) [239] has been performed to quantify the effect:

$$\sigma = \sqrt{\sigma_0^2 + \frac{D_\text{T}^2 \cdot z}{N_\text{eff}}} \quad . \tag{8.2}$$

In this formula σ_0 reflects the resolution at $z = 0$[20], while the second term takes the z-dependent transverse diffusion into account. It is parameterized by using the transverse diffusion coefficient D_T and an effective number of primary electrons per reconstructed cluster N_eff. The latter is a statistical factor, reflecting that the effect of the diffusion on the resolution is less severe the more electrons there are in a charge cloud. Since most of the tracks cross the pad plane perpendicularly, a third angle-dependent term in equation (8.2) is omitted [239].

For σ_0 and the ratio $D_\text{T}/\sqrt{N_\text{eff}}$ the fit shown in figure 8.30 obtains $(134 \pm 7)\,\mu\text{m}$ and $(78 \pm 4)\,\mu\text{m}/\sqrt{\text{cm}}$, respectively. While the value for σ_0 seems reasonable, the z dependence of the resolution is too strong (at least a factor of two) to be purely due to diffusion. If the known diffusion coefficient for Ar/CO_2 (70/30) is inserted ($D_\text{T} = 160\,\mu\text{m}/\sqrt{\text{cm}}$ [237]), a value of about four is calculated for N_eff. This is a rather small number compared to other measurements using Ar/CO_2, where $N_\text{eff} \approx$ 15-20 has been observed [239]. Thus there are systematic effects, which have not been taken into account so far. One problem is certainly the high noise of the readout electronics (see section 8.4.3), due to which broadened signals might fall below the 4σ threshold cut (cf. section 8.5.2). Also

[19]The spike at zero in the residual distribution, however, cannot be completely explained by this. It is partly connected also to very perpendicular muon tracks, which hit only one or few pad rows.

[20]Composed of several parts like the pad size, the intrinsic GEM resolution, electronics noise or calibration errors.

gas impurities, in particular oxygen contaminations, could play a role: If signal electrons are lost during their drift towards the readout plane due to attachment, a z-dependent degradation of the TPC performance would make sense. Finally, the 3-dim. clustering algorithm (see section 8.5.3) can influence the results, especially the choice of the $\pm 0.5\,\mu s$ time window[21]. To clarify these open questions it will be very important to set up a full simulation for the test chamber, including e. g. diffusion and noise. In addition, a monitoring system for the gas quality during measurements is needed.

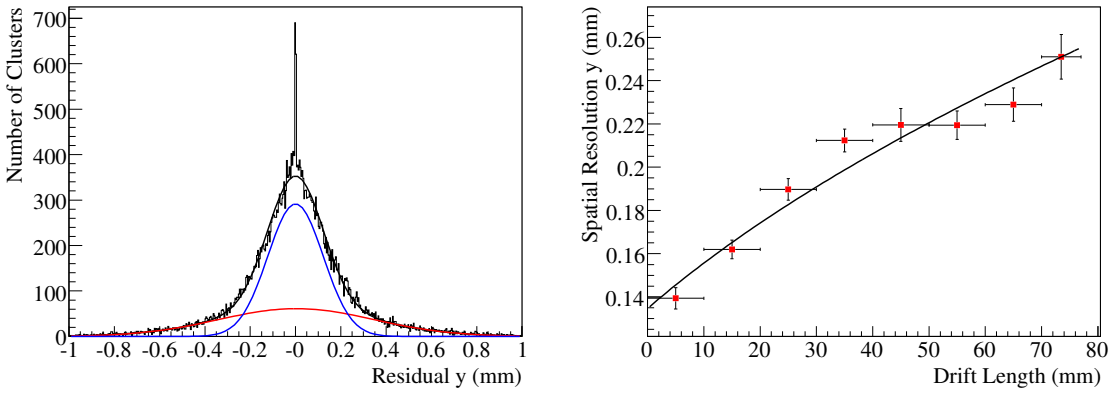

Figure 8.30: Left: Residual distribution of y coordinate for standard settings (see text). A double-Gaussian fit to the data is presented in black; the blue and red curve show the two single Gaussians. Right: y-resolution dependence on the drift distance z; horizontal error bars indicate the width of the eight defined z-regions. The black curve represents a fit to the data according to equation (8.2).

8.7 Future Prospects

There are several more measurements which can be performed with the TPC test chamber using the laboratory setup described in this chapter. The first one has actually already been performed, namely to rotate the detector by 90° and trigger on cosmic muon tracks parallel to the readout plane. Such events should be more easy to reconstruct, since the signal structure on the pads basically consists of one pulse only. The analysis of these data is ongoing. Furthermore the readout electronics will be changed soon to the one used for the T2K TPC [240]. At some point the Ne/CO_2 (90/10) gas mixture foreseen for the PANDA TPC will also be tested. Simulations of the test chamber have to be performed, too. In addition, a test beam at the ELSA ring in Bonn, Germany [221] is planned for fall 2008 [222], which will comprise an external tracking telescope.

[21] First tests with a varying time window have indeed shown that both the resolution and the z-dependence depend on this parameter: With an increasing window the performance improves until a plateau is reached. The chosen default value of $\pm 0.5\,\mu s$ marks the beginning of this plateau.

Chapter 9

Conclusions and Outlook

In the scope of this thesis, a partial wave analysis (PWA) of $\pi^-\pi^-\pi^+$ final state events from diffractive pion dissociation at COMPASS has been carried out. In the regime of high momentum transfer ($0.1 < t' < 1.0\,\mathrm{GeV}^2/c^2$) more than 400 000 events have been studied, employing a set of 42 partial waves in a mass-independent PWA ($40\,\mathrm{MeV}/c^2$ mass bins). A subsequent mass-dependent fit has been performed for seven out of the 42 waves. The well-known states $a_1(1260)$, $a_2(1320)$ and $\pi_2(1670)$ are resolved with high quality, confirming the Particle Data Group (PDG) average values for mass M and width Γ. Within the statistical uncertainties and the estimated systematics, the less established states $\pi(1800)$ and $a_4(2040)$ are furthermore seen with parameters consistent with the PDG. Also the $a_2(1700)$ meson is contained in the data. In addition, a resonance in the $2^{-+}0^+\,[f_2\pi]\,D$ wave with $M = 1.836^{+0.013}_{-0.057}$ and $\Gamma = 0.263^{+0.085}_{-0.099}\,\mathrm{GeV}/c^2$ is observed. It is identified with the discussed $\pi_2(1880)$ meson, which is a candidate for a hybrid with conventional quantum numbers. Highlight of the analysis certainly is the strong signal obtained in the spin-exotic $1^{-+}1^+\,[\rho\pi]\,P$ wave around $1.6\,\mathrm{GeV}/c^2$. The phase motion of the corresponding resonance is studied with respect to the tail of $a_1(1260)$ and to $\pi_2(1670)$, and the mass-dependent fit yields a mass and width of $M = 1.660^{+0.010}_{-0.074}$ and $\Gamma = 0.269^{+0.063}_{-0.085}\,\mathrm{GeV}/c^2$, respectively. These values are consistent with the claimed and much disputed $\pi_1(1600)$. Due to its exotic quantum numbers, this state cannot be a conventional $q\bar{q}$ meson and is a hot candidate for a $q\bar{q}g$ hybrid. Several theory models predict a 1^{-+} hybrid in the light-quark sector with a mass between 1.5 and $2.0\,\mathrm{GeV}/c^2$ and a width of the order of 200-250 MeV/c^2. Dedicated systematic studies have been carried out to probe the stability of the presented results. In particular a leakage study has been performed, which doesn't exhibit any significant leakage from the dominant waves to the 1^{-+} wave.

Also more than 2 000 000 events with small momentum transfer ($10^{-3} < t' < 10^{-2}\,\mathrm{GeV}^2/c^2$) have been analyzed by means of a mass-independent PWA. These data exhibit dominant $a_1(1260)$ and $\pi_2(1670)$ production, but also $\pi(1800)$ is present with high significance. The radial excitations $a_1(1640)$ and $\pi_2(2100)$ can be identified as well, especially through their clean phase motions. Also the $\pi_2(1880)$ meson, already observed in the high-t' regime, is seen here again. As expected no $1^{-+}1^+$ signal is obtained: Be-

cause of the $M = 1$ spin projection, this amplitude is suppressed for low values of t'. In summary, the regime of small momentum transfer t' is also very interesting and should be studied further. In particular a mass-dependent fit has to be developed, to allow the determination of the parameters of the found resonances.

The analysis presented in this thesis is effectively based on 2-3 days of data taking only. This demonstrates the great potential of COMPASS to contribute to the field of meson spectroscopy, in particular to the search for exotic states. COMPASS combines a high luminosity with an excellent acceptance and allows the reconstruction of charged and neutral particles in the final state. It will be very important to confirm the $\pi_1(1600)$ also in e. g. $\pi^-\pi^0\pi^0$, $\eta'\pi$ or $\pi^-\pi^-\pi^-\pi^+\pi^+$ and to investigate its different branching ratios. To this end a long-term hadron run is currently ongoing at CERN using a liquid-hydrogen target. Thus much more statistics, especially in the domain of large momentum transfers, will be available in the near future. Also the central production mechanism is envisaged, possibly enabling the search for glueballs.

On the hardware development side, measurements to prove the feasibility of a GEM-based time projection chamber (TPC) for PANDA are ongoing. For this thesis a small-size GEM-TPC test chamber with a drift length of 7.7 cm and a diameter of 20 cm has been built. After a successful commissioning with X-rays this detector has been operated stably for several months in a setup for tracking-performance tests with cosmic muons. It has been mounted in a way such that the angles between the particle trajectories and the readout plane approach 90°. These tracks are potentially the most difficult to reconstruct in a TPC and are particularly interesting regarding the abundant forward going particles in PANDA. The average space point resolution achieved in the presented measurements is 200 µm in the y projection, where small readout pads of 1 mm pitch are used. For a drift length less than 1 cm, a resolution as good as 140 µm has been accomplished.

Measurements with different track geometries, rather parallel to the readout plane and also using cosmic muons, have been taken out and are currently analyzed. A test beam at an accelerator facility is planned in the near future employing an external tracking telescope. These data will allow the investigation of the performance of the chamber in a harder radiation environment including the effect of space charge build-up. For 2009 a large-size prototype with a drift length of 65 cm and a diameter of 30 cm is currently being designed. This detector will be installed in the FOPI and CB-ELSA experiments and will mark an important step towards the decision to use the proposed TPC for the PANDA experiment.

Appendix A

Software Versions

In order to allow at least a partial reproduction of the analysis results presented in chapter 5, this appendix summarizes the versions of the main software programs and libraries which have been employed. It is distinguished between the real data processing, the simulations and the PWA program.

A.1 Real Data Processing

The analyzed mDST files were centrally produced at CERN from November 2005 to April 2006 with the following CORAL [14], PHAST [156] and ROOT [155] versions:

- CORAL CVS tag: hprod_nov05_1
- PHAST: 7.025
- ROOT: 4.03.02

For further processing at TU München, including the event selection, PHAST 7.036 has been used, compiled with ROOT 4.04.02.

A.2 Simulations

The MC simulations for the PWA acceptance corrections can be divided into four computational steps: event generation (1), GEANT simulation (2), CORAL reconstruction (3) and acceptance evaluation (4).

1. Performed in the PWA framework with version "22_11_2007" (see also appendices A.3 and C.1)
2. COMGEANT 7.02 using Geant 3.21 and CERNLIB 2002
   geometry files:

- 1.6 mm lead target: geom_hadron_2004.03.6.real.ffr_hp20_1.6mmPb
- 2+1 mm lead target: geom_hadron_2004.03.6.real.ffr_hp20_2+1mm_pion

3. CORAL CVS tag: hprod_nov05_1, mDST produced with PHAST 7.025 and ROOT 4.04.02

4. Done with PHAST 7.036, compiled with ROOT 4.04.02

A.3 PWA Program

The PWA program has no official versioning control yet. However, the two private versions, with which the "high-t'" and the "low-t'" results were obtained, have been frozen under the date labels "24_03_2008" and "09_05_2008", respectively. The phase-space event generation for the simulations was done with version "22_11_2007".

Appendix B

Recalculation of Beam Energy

In the following the formula to calculate the beam energy E_a, based on the scattering angle θ and the total 4-momentum of the outgoing three-pion system p_c (cf. figure 2.3), is shortly derived [241]. It is used during both the real data event selection ("step 3b", see section 5.1.4) and the Monte Carlo acceptance evaluation (see section 5.3.1). The underlying assumption is that the target mass is equal to the recoil particle mass: $m_b = m_d = m_0$. Since furthermore $m_a \ll E_a$, an approximation for the beam momentum $|\vec{p}_a|$ can be introduced:

$$|\vec{p}_a| = \sqrt{E_a^2 - m_a^2} \approx E_a - \frac{m_a^2}{2E_a} \quad . \tag{B.1}$$

Based on equation (B.1), the 4-momentum transfer $t = (p_a - p_c)^2$ can be written

$$t \approx m_a^2 + m_c^2 - 2E_a(E_c - |\vec{p}_c|\cos\theta) - m_a^2 \left(\frac{|\vec{p}_c|}{E_a}\right)\cos\theta \quad . \tag{B.2}$$

Alternatively, and using $m_b = m_d = m_0$, it holds that

$$t = (p_b - p_d)^2 = 2m_0(E_a - E_c) \quad . \tag{B.3}$$

By equating (B.2) and (B.3) a quadratic equation in the variable E_a is obtained:

$$2a_2E_a^2 - 2a_1E_a - a_0 = 0 \quad \text{with} \tag{B.4}$$

$$\begin{aligned} a_2 &= m_0\left\{1 - \left(\frac{E_c}{m_0}\right)\left[1 - \left(\frac{|\vec{p}_c|}{E_c}\right)\cos\theta\right]\right\} \quad , \\ a_1 &= m_0E_c\left[1 - \left(\frac{m_c^2 + m_a^2}{2m_0E_c}\right)\right] \quad \text{and} \\ a_0 &= m_a^2\,|\vec{p}_c|\cos\theta \quad . \end{aligned}$$

Solving equation (B.4) for E_a and exploiting the fact that $2a_0a_2 \ll a_1^2$ (see below) reveals

$$E_a \approx \left(\frac{a_1}{a_2}\right) + \left(\frac{a_0}{2a_1}\right) \quad \text{or} \quad E_a \approx -\left(\frac{a_0}{2a_1}\right) \quad . \tag{B.5}$$

Since a_0 and a_1 are positive for the COMPASS case only the first solution is physical, provided that $a_2 > 0$. For the case that $m_0 > E_c$ (lead target) this is true if merely $\cos\theta > 0$ or $\theta < 90°$. If $m_0 < E_c$ (proton target) it has to be required that

$$\theta < \theta_{\max} \quad \text{where} \quad \theta_{\max} = \arccos\left(\frac{E_c - m_0}{|\vec{p}_c|}\right) \quad , \tag{B.6}$$

which is still satisfied for COMPASS[1]. This justifies also the assumption that $2a_0a_2 \ll a_1^2$. Finally, from equations (B.4) and (B.5), the looked for formula can be written as:

$$\frac{E_a}{E_c} \approx \left[1 - \left(\frac{m_c^2 + m_a^2}{2m_0E_c}\right)\right]\left\{1 - \left(\frac{E_c}{m_0}\right)\left[1 - \left(\frac{|\vec{p}_c|}{E_c}\right)\cos\theta\right]\right\}^{-1} + \tag{B.7}$$

$$\left(\frac{m_a^2}{2m_0E_c}\right)\left(\frac{|\vec{p}_c|}{E_c}\right)(\cos\theta)\left[1 - \left(\frac{m_c^2 + m_a^2}{2m_0E_c}\right)\right]^{-1} \quad , \tag{B.8}$$

given in the LAB frame.

[1]The largest occurring scattering angles in the presented analysis are $\sim 14\,\text{mrad}$.

Appendix C

Simulations Supplement

This appendix complements the description of the simulations presented in section 5.3, by summarizing the input parameters of the event generator. Also further quality distributions for the PWA are shown, similar to those of section 5.4.3.

C.1 Event Generator Tuning

The event generator has been set up with the knowledge from the real data as summarized in table C.1. While the z position of the primary vertices has been distributed uniformly within the limits[1] stated in the first row of the table, a Gaussian has been assumed for the x and y positions[2] (second row). Also the beam divergence, i. e. the angle between the incoming beam particle and the z axis, has been described by a Gaussian (third row). The beam energy profile has been fitted from the "low-t'" data only, since those have much higher statistics and are nearly background free (c. f. section 5.1.4). Three Gaussians and one constant function have been used as parameterization, where two of the Gaussians are meant to describe the beam profile[3] and the third one and the constant function to collect background. The parameters of the two signal Gaussians for both data taking periods are shown in the fourth row of table C.1. It is emphasized that the treatment of the beam properties is simplified insofar as, in general, no correlations between the different parameters are taken into account. Finally, the "high-t'" and the "low-t'" t' distributions have been taken directly from the data and fitted with two exponential functions each (fifth and sixth row). Separately for the two t' ranges and also for the two target settings, events with 3π masses between $0.5\,\mathrm{GeV}/c^2$ and $2.5\,\mathrm{GeV}/c^2$ have been generated (in total 9 000 000 for "high-t'" and 7 200 000 for "low-t'", respectively). While the relative weight between the two segments of the 2+1 mm target has been fixed to two, the relative weight between the 2+1 mm and the 1.6 mm target has been fine adjusted based on the real data.

[1] Defined by the target positions as obtained from the data and the known target widths.

[2] Reflecting the beam profile in the x-y plane; stated parameters are the mean and the RMS of the reconstructed primary vertex x and y distributions.

[3] The second Gaussian accounts for the energy loss of some of the beam pions; see section 3.2.1.

Parameter / Period	1.6 mm	2+1 mm
Target position and width (cm)	$-310.238 \leq z \leq -310.078$	$-314.600 \leq z \leq -314.400$ $-304.602 \leq z \leq -304.502$
Beam Position and spread (cm)	$x_0 = 0.074, \sigma_x = 0.35$ $y_0 = 0.067, \sigma_y = 0.28$	$x_0 = 0.10, \sigma_x = 0.35$ $y_0 = 0.10, \sigma_y = 0.27$
Beam divergence and spread (mrad)	$\mathrm{d}x/\mathrm{d}z = 0.25, \sigma = 0.10$ $\mathrm{d}y/\mathrm{d}z = 0.05, \sigma = 0.18$	$\mathrm{d}x/\mathrm{d}z = 0.26, \sigma = 0.10$ $\mathrm{d}y/\mathrm{d}z = 0.01, \sigma = 0.18$
Beam energy profile (GeV): $a \cdot e^{-0.5(\frac{E-b}{c})^2} + d \cdot e^{-0.5(\frac{E-e}{f})^2}$	$a : 0.31, b : 187.4, c : 1.04$ $d : 0.69, e : 190.1, f : 1.07$	$a : 0.29, b : 187.5, c : 1.01$ $d : 0.71, e : 190.0, f : 1.04$
"Low-t'" distribution $a \cdot e^{bt'} + e^{ct'}$ (GeV$^2/c^2$)	$a : 760.7$ $b : -389.2, c : 217.0$	$a : 2231$ $b : -390.2, c : 330$
"High-t'" distribution $a \cdot e^{bt'} + e^{ct'}$ (GeV$^2/c^2$)	$a : 2.47$ $b : -10.77, c : -2.79$	$a : 2.65$ $b : -10.48, c : -2.71$

Table C.1: Summary of the event generator parameters used for the simulations of the two analyzed data taking periods; see text for more details.

C.2 Further PWA Quality Distributions

Figure C.1 ("high-t'") and figure C.2 ("low-t'") present PWA quality distributions, obtained according to the procedure described in section 4.4.5 and additional to those presented in section 5.4.3. Shown are the three components of the single pion momenta, both for the two negative pions (left histograms) and the positive pion (right histograms) of the final states. As usual, the real data are represented by a yellow-filled histogram and the MC events are overlayed in red. A small dip at $p_y = 0$ is seen in the real data for both t' ranges and independent of the pion charge, which is not completely described by the weighted MC. This could indicate an inaccuracy in the geometry or trigger description of the simulations, showing up for very forward going particles. The low momentum discrepancy in the "high-t'" p_z distributions is probably connected to non-exclusive background events[4], since it almost disappears for low values of t'. In general, the agreement between weighted MC and data is very good.

[4]See the corresponding energy distributions in section 5.1.4.

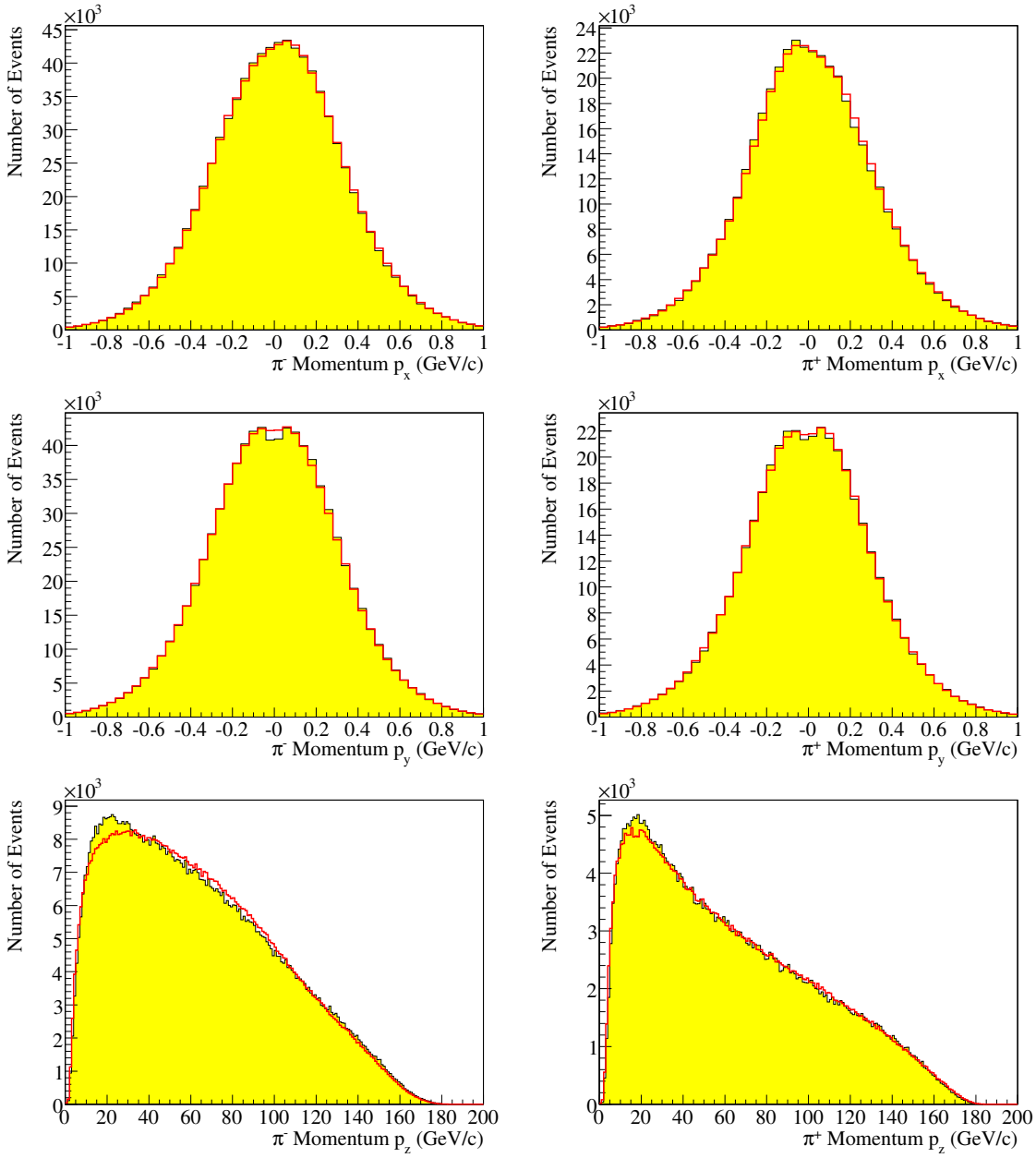

Figure C.1: Comparison of real data (yellow, filled) with PWA-model weighted MC distributions (red) at "high-t'"; single pion momentum components shown. From top to bottom: x, y and z components; from left to right: π^- (two entries per event) and π^+ case.

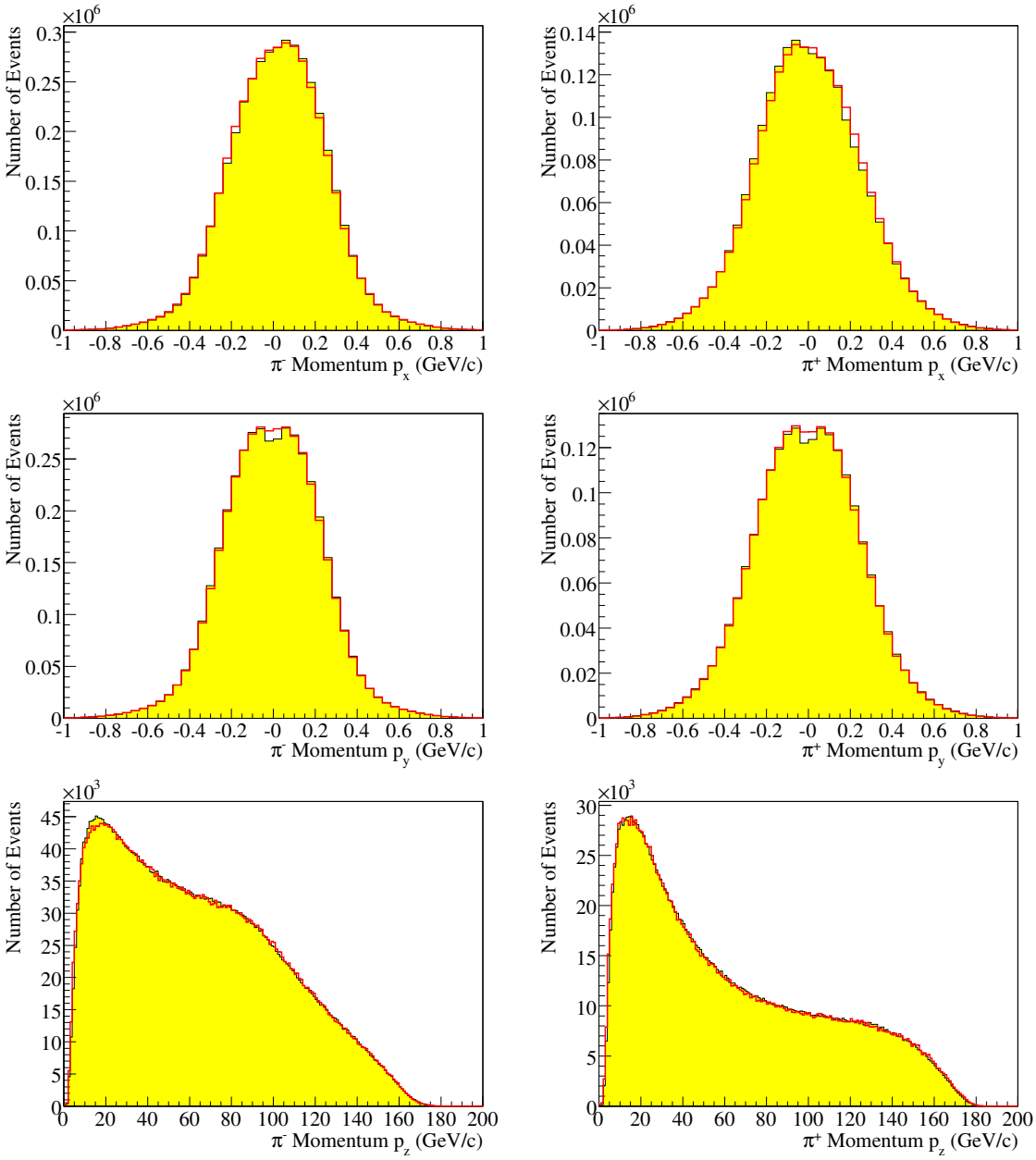

Figure C.2: Comparison of real data (yellow, filled) with PWA-model weighted MC distributions (red) at "low-t'"; single pion momentum components shown. From top to bottom: x, y and z components; from left to right: π^- (two entries per event) and π^+ case.

Bibliography

[1] H. Fritzsch and M. Gell-Mann. *Current algebra: Quarks and what else?* Proceedings of 16th International Conference on High-Energy Physics, Batavia, Illinois, 6 - 13 Sep 1972, pages 135–165. hep-ph/0208010. *cited in chapter 1 (p. 1), 2.1.3 (p. 7)*

[2] D. J. Gross and F. Wilczek. *Ultraviolet Behavior of Non-Abelian Gauge Theories*. Phys. Rev. Lett. **30** (1973) 1343–1346. *cited in chapter 1 (p. 1), 2.1.3 (p. 7)*

[3] H. D. Politzer. *Reliable Perturbative Results for Strong Interactions?* Phys. Rev. Lett. **30** (1973) 1346–1349. *cited in chapter 1 (p. 1), 2.1.3 (p. 7)*

[4] K. G. Wilson. *Confinement of Quarks*. Phys. Rev. **D10** (1974) 2445–2459. *cited in chapter 1 (p. 1), 2.1.3 (p. 8)*

[5] M. Gell-Mann. *Symmetries of baryons and mesons*. Phys. Rev. **125** (1962) 1067–1084. *cited in chapter 1 (p. 1), 2.1.1 (p. 6)*

[6] N. Isgur and J. E. Paton. *A Flux Tube Model for Hadrons in QCD*. Phys. Rev. **D31** (1985) 2910. *cited in chapter 1 (p. 1), 2.1.3 (p. 8)*

[7] C. J. Morningstar and M. J. Peardon. *Efficient glueball simulations on anisotropic lattices*. Phys. Rev. **D56** (1997) 4043–4061. *cited in chapter 1 (p. 1)*

[8] D. Alde et al. *Evidence for a 1^{-+} Exotic Meson*. Phys. Lett. **B205** (1988) 397–400. *cited in chapter 1 (p. 1), 2.4.1 (p. 18)*

[9] D. R. Thompson et al. *Evidence for exotic meson production in the reaction $\pi^- p \to \eta\pi^- p$ at 18 GeV/c*. Phys. Rev. Lett. **79** (1997) 1630–1633. *cited in chapter 1 (p. 1), 2.4.1 (p. 18)*

[10] A. Abele et al. *Exotic $\eta\pi$ state in $\bar{p}d$ annihilation at rest into $\pi^-\pi^0\eta p_{spectator}$*. Phys. Lett. **B423** (1998) 175–184. *cited in chapter 1 (p. 1), 2.4.1 (p. 18)*

[11] G. S. Adams et al. *Observation of a new $J^{PC} = 1^{-+}$ exotic state in the reaction $\pi^- p \to \pi^+\pi^-\pi^- p$ at 18 GeV/c*. Phys. Rev. Lett. **81** (1998) 5760–5763. *cited in chapter 1 (p. 1), 2.4.1 (p. 19)*

[12] A. R. Dzierba et al. *A partial wave analysis of the $\pi^-\pi^-\pi^+$ and $\pi^-\pi^0\pi^0$ systems and the search for a $J^{PC} = 1^{-+}$ meson*. Phys. Rev. **D73** (2006) 072001. *cited in chapter 1 (p. 2), 2.4.1 (p. 19), 2.4.1 (p. 20), 5.7 (p. 99)*

[13] G. Baum et al. *COMPASS: A Proposal for a COmmon Muon and Proton Apparatus for Structure and Spectroscopy*. CERN SPSLC **96-14** (1996).
cited in chapter 1 (p. 2), 3.0.2 (p. 23), 3.1.6 (p. 26)

[14] P. Abbon et al. *The COMPASS experiment at CERN*. Nucl. Instrum. Meth. **A577** (2007) 455–518. *cited in chapter 1 (p. 2), 3.0.2 (p. 23), 3.0.2 (p. 24), 3.2 (p. 27), 3.2.1 (p. 28), 3.2.1 (p. 29), 3.3 (p. 30), 3.3.3 (p. 32), A.1 (p. 153)*

[15] J. J. Aubert et al. *Experimental Observation of a Heavy Particle J*. Phys. Rev. Lett. **33** (1974) 1404–1406. *cited in chapter 1 (p. 2)*

[16] J. E. Augustin et al. *Discovery of a Narrow Resonance in e^+e^- Annihilation*. Phys. Rev. Lett. **33** (1974) 1406–1408. *cited in chapter 1 (p. 2)*

[17] S. K. Choi et al. *Observation of the $\eta_c(2S)$ in exclusive $B \to KK_SK^-\pi^+$ decays*. Phys. Rev. Lett. **89** (2002) 102001. *cited in chapter 1 (p. 2), 6.1.1 (p. 105)*

[18] J. L. Rosner et al. *Observation of the $h_c(^1P_1)$ state of charmonium*. Phys. Rev. Lett. **95** (2005) 102003. *cited in chapter 1 (p. 2), 6.1.1 (p. 105)*

[19] P. Rubin et al. *Observation of the $^1P_1$ state of charmonium*. Phys. Rev. **D72** (2005) 092004. *cited in chapter 1 (p. 2), 6.1.1 (p. 105)*

[20] E. Eichten et al. *The Spectrum of Charmonium*. Phys. Rev. Lett. **34** (1975) 369–372.
cited in chapter 1 (p. 2)

[21] T. Appelquist, A. De Rujula, H. D. Politzer, and S. L. Glashow. *Charmonium Spectroscopy*. Phys. Rev. Lett. **34** (1975) 365–369. *cited in chapter 1 (p. 2)*

[22] S. K. Choi et al. *Observation of a new narrow charmonium state in exclusive $B^\pm \to K^\pm\pi^+\pi^- J/\psi$ decays*. Phys. Rev. Lett. **91** (2003) 262001.
cited in chapter 1 (p. 2), 2.4.2 (p. 21)

[23] B. Aubert et al. *Observation of a broad structure in the $\pi^+\pi^- J/\psi$ mass spectrum around 4.26 GeV/c^2*. Phys. Rev. Lett. **95** (2005) 142001. *cited in chapter 1 (p. 2), 2.4.2 (p. 21)*

[24] K. Abe et al. *Observation of a near-threshold $\omega J/\psi$ mass enhancement in exclusive $B \to K\omega J/\psi$ decays*. Phys. Rev. Lett. **94** (2005) 182002. *cited in chapter 1 (p. 2), 2.4.2 (p. 21)*

[25] K. Abe et al. *Observation of a new charmonium state in double charmonium production in e^+e^- annihilation at $\sqrt{s} \sim 10.6$ GeV*. Phys. Rev. Lett. **98** (2007) 082001.
cited in chapter 1 (p. 2), 2.4.2 (p. 21)

[26] E. Klempt and A. Zaitsev. *Glueballs, hybrids, multiquarks. Experimental facts versus QCD inspired concepts*. Phys. Rept. **454** (2007) 1–202.
cited in chapter 1 (p. 2), chapter 2 (p. 5), 2.1 (p. 5), 2.4 (p. 18), 2.4.2 (p. 21), 5.5.2 (p. 93)

[27] E. S. Swanson. *The new heavy mesons: A status report*. Phys. Rept. **429** (2006) 243–305. *cited in chapter 1 (p. 2), 2.4 (p. 18)*

[28] B. Aubert et al. *Observation of a narrow meson decaying to $D_s^+\pi^0$ at a mass of 2.32 GeV/c^2*. Phys. Rev. Lett. **90** (2003) 242001. *cited in chapter 1 (p. 2), 6.1.3 (p. 105)*

[29] P. Krokovny et al. *Observation of the $D_{sJ}(2317)$ and $D_{sJ}(2457)$ in B decays*. Phys. Rev. Lett. **91** (2003) 262002. *cited in chapter 1 (p. 2), 6.1.3 (p. 105)*

[30] D. Besson et al. *Observation of a narrow resonance of mass 2.46 GeV/c^2 decaying to $D_s^+\pi^0$ and confirmation of the $D_{sJ}(2317)$ state*. Phys. Rev. **D68** (2003) 032002. *cited in chapter 1 (p. 2), 6.1.3 (p. 105)*

[31] J. Brodzicka et al. *Observation of a new D_{sJ} meson in $B^+ \to \bar{D}^0 D^0 K^+$ decays*. Phys. Rev. Lett. **100** (2008) 092001. *cited in chapter 1 (p. 2), 6.1.3 (p. 105)*

[32] M. Kotulla et al. *Strong interaction studies with antiprotons. Letter of intent for: PANDA (Antiproton Annihilations at Darmstadt)*. GSI-ESAC/Pbar (2004) . *cited in chapter 1 (p. 2), 2.2.2 (p. 13), chapter 6 (p. 103)*

[33] D. R. Nygren and J. N. Marx. *The Time Projection Chamber*. Phys. Today **31N10** (1978) 46–53. *cited in chapter 1 (p. 2), 7.1.1 (p. 112)*

[34] Q. Weitzel et al. *Development of a High-Rate GEM-Based TPC for PANDA*. Conference Record of the IEEE Nuclear Science Symposium (NSS 2007), Honolulu, Hawaii, 27 Oct - 03 Nov 2007, pages 227–233. *cited in chapter 1 (p. 2), 7.0.6 (p. 111)*

[35] F. Sauli. *GEM: A new concept for electron amplification in gas detectors*. Nucl. Instrum. Meth. **A386** (1997) 531–534. *cited in chapter 1 (p. 3), 7.2 (p. 114)*

[36] C. Amsler and N. A. Tornqvist. *Mesons beyond the naive quark model*. Phys. Rept. **389** (2004) 61–117. *cited in chapter 2 (p. 5)*

[37] D. V. Bugg. *Four Sorts of Mesons*. Phys. Rept. **397** (2004) 257–358. *cited in chapter 2 (p. 5)*

[38] W.-M. Yao et al. *Review of Particle Physics*. J. Phys. **G33** (2006) 1–1232. *cited in chapter 2 (p. 5), 2.4.2 (p. 21), 4.1.3 (p. 38), 5.1.4 (p. 58), 5.2.1 (p. 61), 5.2.3 (p. 63), 5.2.4 (p. 64), 5.5.1 (p. 84), 5.5.2 (p. 90), 5.5.2 (p. 91), 5.5.2 (p. 93), 5.5.3 (p. 94), 5.8 (p. 100), 5.8 (p. 101)*

[39] F. Von Hippel and C. Quigg. *Centrifugal-Barrier Effects in Resonance Partial Decay Widths, Shapes, and Production Amplitudes*. Phys. Rev. **D5** (1972) 624–638. *cited in 2.1.2 (p. 7)*

[40] R. L. Jaffe and K. Johnson. *Unconventional States of Confined Quarks and Gluons*. Phys. Lett. **B60** (1976) 201–204. *cited in 2.1.3 (p. 7)*

[41] M. S. Chanowitz and S. R. Sharpe. *Hybrids: Mixed States of Quarks and Gluons*. Nucl. Phys. **B222** (1983) 211–244. *cited in 2.1.3 (p. 7)*

[42] V. Bernard and U.-G. Meissner. *Chiral perturbation theory*. Ann. Rev. Nucl. Part. Sci. **57** (2007) 33–60. *cited in 2.1.3 (p. 8)*

[43] G. S. Bali. *QCD forces and heavy quark bound states*. Phys. Rept. **343** (2001) 1–136. *cited in 2.1.3 (p. 8)*

[44] C. J. Morningstar and M. J. Peardon. *The Glueball spectrum from an anisotropic lattice study*. Phys. Rev. **D60** (1999) 034509. *cited in 2.1.3 (p. 8)*

[45] J. N. Hedditch et al. 1^{-+} *exotic meson at light quark masses*. Phys. Rev. **D72** (2005) 114507. *cited in 2.1.3 (p. 8)*

[46] C. Bernard et al. *Lattice calculation of* 1^{-+} *hybrid mesons with improved Kogut-Susskind fermions*. Phys. Rev. **D68** (2003) 074505. *cited in 2.1.3 (p. 8)*

[47] P. Lacock, C. Michael, P. Boyle, and P. Rowland. *Hybrid mesons from quenched QCD*. Phys. Lett. **B401** (1997) 308–312. *cited in 2.1.3 (p. 8)*

[48] C. McNeile and C. Michael. *Decay width of light quark hybrid meson from the lattice*. Phys. Rev. **D73** (2006) 074506. *cited in 2.1.3 (p. 8)*

[49] T. Manke et al. *Hybrid quarkonia on asymmetric lattices*. Phys. Rev. Lett. **82** (1999) 4396–4399. *cited in 2.1.3 (p. 8)*

[50] G. S. Bali. *Lattice calculations of hadron properties*. Eur. Phys. J. **A19** (2004) 1–8. *cited in 2.1.3 (p. 8)*

[51] N. Isgur, R. Kokoski, and J. E. Paton. *Gluonic Excitations of Mesons: Why They Are Missing and Where to Find Them*. Phys. Rev. Lett. **54** (1985) 869–872. *cited in 2.1.3 (p. 9)*

[52] T. Barnes, F. E. Close, and E. S. Swanson. *Hybrid and conventional mesons in the flux tube model: Numerical studies and their phenomenological implications*. Phys. Rev. **D52** (1995) 5242–5256. *cited in 2.1.3 (p. 9), 5.5.2 (p. 93)*

[53] F. E. Close and P. R. Page. *The Production and decay of hybrid mesons by flux tube breaking*. Nucl. Phys. **B443** (1995) 233–254. *cited in 2.1.3 (p. 9), 5.5.2 (p. 93)*

[54] S. Godfrey and N. Isgur. *Mesons in a Relativized Quark Model with Chromodynamics*. Phys. Rev. **D32** (1985) 189–231. *cited in 2.1.3 (p. 9)*

[55] T. Barnes, S. Godfrey, and E. S. Swanson. *Higher charmonia*. Phys. Rev. **D72** (2005) 054026. *cited in 2.1.3 (p. 9), 2.1.3 (p. 10), 2.4.2 (p. 21)*

[56] T. Regge. *Introduction to complex orbital momenta*. Nuovo Cim. **14** (1959) 951–976. *cited in 2.1.3 (p. 9)*

[57] G. F. Chew and S. C. Frautschi. *Principle of Equivalence for all Strongly Interacting Particles within the S Matrix Framework*. Phys. Rev. Lett. **7** (1961) 394–397. *cited in 2.1.3 (p. 9)*

[58] R. J. Eden. *Regge poles and elementary particles*. Rept. Prog. Phys. **34** (1971) 995–1053. *cited in 2.1.3 (p. 10)*

[59] A. C. Irving and R. P. Worden. *Regge Phenomenology*. Phys. Rept. **34** (1977) 117–231. *cited in 2.1.3 (p. 10)*

[60] C. Daum et al. *Diffractive Production of 3π States at 63 and 94 GeV*. Nucl. Phys. **B182** (1981) 269–336.
cited in 2.2.1 (p. 12), 4.1.4 (p. 40), 4.5.1 (p. 50), 5.4.1 (p. 72), 5.5.3 (p. 93), 5.5.3 (p. 94)

[61] D. Alde et al. *Production of $G(1590)$ and Other Mesons Decaying Into η Pairs by 100 GeV/c π^- on Protons*. Nucl. Phys. **B269** (1986) 485–508. *cited in 2.2.1 (p. 12)*

[62] S. I. Bityukov et al. *Observation of resonance with mass $M = 1814$ MeV, decaying into $\pi^-\eta\eta$*. Phys. Lett. **B268** (1991) 137–141. *cited in 2.2.1 (p. 12)*

[63] S. Teige et al. *Properties of the $a_0(980)$ meson*. Phys. Rev. **D59** (1999) 012001.
cited in 2.2.1 (p. 12)

[64] F. E. Close and G. A. Schuler. *Central production of mesons: Exotic states versus pomeron structure*. Phys. Lett. **B458** (1999) 127–136. *cited in 2.2.1 (p. 12)*

[65] T. A. Armstrong et al. *Spin Parity Analysis of the E Meson Centrally Produced in the Reactions $\pi^+p \to \pi^+(K_L^0K^\pm K^\mp)p$ and $pp \to p(K_L^0K^\pm\pi^\mp)p$ at 85 GeV/c*. Phys. Lett. **B146** (1984) 273–278. *cited in 2.2.1 (p. 12)*

[66] D. Barberis et al. *A kinematical selection of glueball candidates in central production*. Phys. Lett. **B397** (1997) 339–344. *cited in 2.2.1 (p. 12)*

[67] F. Bradamante, G. Mallot, and S. Paul (Eds.). *Workshop on Future Physics @ COMPASS*. CERN Yellow Report **2004-011** (2004). *cited in 2.2.1 (p. 12), 3.1 (p. 24)*

[68] E. Aker et al. *The Crystal Barrel spectrometer at LEAR*. Nucl. Instrum. Meth. **A321** (1992) 69–108. *cited in 2.2.1 (p. 12)*

[69] C. Amsler. *Proton antiproton annihilation and meson spectroscopy with the Crystal Barrel*. Rev. Mod. Phys. **70** (1998) 1293–1340. *cited in 2.2.1 (p. 12)*

[70] P. Salvini et al. *$\bar{p}p$ annihilation into four charged pions at rest and in flight*. Eur. Phys. J. **C35** (2004) 21–33. *cited in 2.2.1 (p. 12), 2.4.1 (p. 18)*

[71] B. Aubert et al. *The BaBar detector*. Nucl. Instrum. Meth. **A479** (2002) 1–116.
cited in 2.2.1 (p. 12)

[72] A. Abashian et al. *The Belle detector*. Nucl. Instrum. Meth. **A479** (2002) 117–232.
cited in 2.2.1 (p. 12)

[73] B. Aubert et al. *Measurements of the mass and width of the η_c meson and of an $\eta_c(2S)$ candidate*. Phys. Rev. Lett. **92** (2004) 142002. *cited in 2.2.1 (p. 12)*

[74] X. L. Wang et al. *Observation of Two Resonant Structures in $e^+e^- \to \pi^+\pi^-\psi(2S)$ via Initial State Radiation at Belle*. Phys. Rev. Lett. **99** (2007) 142002. *cited in 2.2.1 (p. 12)*

[75] B. Aubert et al. *Measurement of double charmonium production in e^+e^- annihilations at $\sqrt{s} = 10.6\,GeV$*. Phys. Rev. **D72** (2005) 031101. *cited in 2.2.1 (p. 12)*

[76] W. Braunschweig et al. *Observation of the Two Photon Cascade 3.7 GeV $\rightarrow$ 3.1 GeV + $\gamma\gamma$ via an Intermediate State P_c*. Phys. Lett. **B57** (1975) 407–412. *cited in 2.2.2 (p. 13)*

[77] T. Himel et al. *Observation of the $\eta_c(2980)$ produced in the Radiative Decay of the $\psi'(3684)$*. Phys. Rev. Lett. **45** (1980) 1146–1149. *cited in 2.2.2 (p. 13)*

[78] R. Partridge et al. *Observation of an η_c Candidate State with Mass 2978 MeV $\pm$9 MeV*. Phys. Rev. Lett. **45** (1980) 1150–1153. *cited in 2.2.2 (p. 13)*

[79] J. Z. Bai et al. *The BES upgrade*. Nucl. Instrum. Meth. **A458** (2001) 627–637. *cited in 2.2.2 (p. 13)*

[80] D. Peterson et al. *The CLEO III drift chamber*. Nucl. Instrum. Meth. **A478** (2002) 142–146. *cited in 2.2.2 (p. 13)*

[81] S. Van Der Meer. *Stochastic Cooling and the Accumulation of Anti-Protons*. Rev. Mod. Phys. **57** (1985) 689–697. *cited in 2.2.2 (p. 13)*

[82] C. Baglin et al. *Charmonium Spectroscopy by Anti-Proton Annihilation with Protons from an Internal H_2 Gas Jet Target*. Contribution to the EPS Int. Europhysics Conf. on High Energy Physics, Bari, Italy, 18 - 24 July 1985 . *cited in 2.2.2 (p. 13)*

[83] M. Ambrogiani et al. *Measurements of the magnetic form factor of the proton in the timelike region at large momentum transfer*. Phys. Rev. **D60** (1999) 032002. *cited in 2.2.2 (p. 13)*

[84] S. Bagnasco et al. *New measurements of the resonance parameters of the $\chi_{c0}(1^3P_0)$ state of charmonium*. Phys. Lett. **B533** (2002) 237–242. *cited in 2.2.2 (p. 13)*

[85] U. Amaldi, M. Jacob, and G. Matthiae. *Diffraction of Hadronic Waves*. Ann. Rev. Nucl. Part. Sci. **26** (1976) 385–456. *cited in 2.3 (p. 13), 2.3.2 (p. 14), 2.3.2 (p. 15), 2.3.4 (p. 16), 2.3.5 (p. 17), 5.1.4 (p. 57)*

[86] K. Goulianos. *Diffractive Interactions of Hadrons at High-Energies*. Phys. Rept. **101** (1983) 169–219. *cited in 2.3 (p. 13)*

[87] G. Alberi and G. Goggi. *Diffraction of Subnuclear Waves*. Phys. Rept. **74** (1981) 1–207. *cited in 2.3 (p. 13), 2.3.5 (p. 17)*

[88] J. Saudinos and C. Wilkin. *Proton Nucleus Scattering at Medium-Energies*. Ann. Rev. Nucl. Part. Sci. **24** (1974) 341–378. *cited in 2.3.2 (p. 14)*

[89] M. L. Good and W. D. Walker. *Diffraction disssociation of beam particles*. Phys. Rev. **120** (1960) 1857–1860. *cited in 2.3.2 (p. 14)*

[90] C. Bemporad et al. *Coherent production of pions on nuclei. Determination of unstable boson-nucleon total cross-sections*. Nucl. Phys. **B33** (1971) 397–420. *cited in 2.3.2 (p. 15)*

[91] V. N. Gribov and I. Y. Pomeranchuk. *Complex orbital momenta and the relation between the cross-sections of various processes at high-energies*. Phys. Rev. Lett. **8** (1962) 343–345. *cited in 2.3.4 (p. 16)*

[92] R. Webb et al. *Double Diffraction Dissociation and Test of Pomeron Factorization at the CERN ISR*. Phys. Lett. **B55** (1975) 336–340. *cited in 2.3.4 (p. 16), 2.3.5 (p. 17)*

[93] R. T. Deck. *Kinematical interpretation of the first $\pi - \rho$ resonance*. Phys. Rev. Lett. **13** (1964) 169–173. *cited in 2.3.6 (p. 17)*

[94] C. Daum et al. *Experimental Proof of the Existence of the A1 Meson*. Phys. Lett. **B89** (1980) 281–284. *cited in 2.3.6 (p. 17)*

[95] Shi-Lin Zhu. *New Hadron States*. Int. J. Mod. Phys. **E17** (2008) 283–322. *cited in 2.4 (p. 18)*

[96] E. Eichten, S. Godfrey, H. Mahlke, and J. L. Rosner. *Quarkonia and their transitions*. hep-ph/0701208. *cited in 2.4 (p. 18)*

[97] N. Brambilla et al. *Heavy quarkonium physics*. CERN Yellow Report **2005-005** (2005). *cited in 2.4 (p. 18)*

[98] W. D. Apel et al. *Analysis of the Reaction $\pi^- p \to \pi^0 \eta n$ at 40 GeV/c Beam Momentum*. Nucl. Phys. **B193** (1981) 269–286. *cited in 2.4.1 (p. 18)*

[99] G. M. Beladidze et al. *Study of $\pi^- N \to \eta \pi^- N$ and $\pi^- N \to \eta' \pi^- N$ reactions at 37 GeV/c*. Phys. Lett. **B313** (1993) 276–282. *cited in 2.4.1 (p. 18), 2.4.1 (p. 19)*

[100] H. Aoyagi et al. *Study of the $\eta\pi^-$ system in the $\pi^- p$ reaction at 6.3 GeV/c*. Phys. Lett. **B314** (1993) 246–254. *cited in 2.4.1 (p. 18)*

[101] S. U. Chung et al. *Evidence for exotic $J^{PC} = 1^{-+}$ meson production in the reaction $\pi^- p \to \eta \pi^- p$ at 18 GeV/c*. Phys. Rev. **D60** (1999) 092001. *cited in 2.4.1 (p. 18)*

[102] A. R. Dzierba et al. *A study of the $\eta\pi^0$ spectrum and search for a $J^{PC} = 1^{-+}$ exotic meson*. Phys. Rev. **D67** (2003) 094015. *cited in 2.4.1 (p. 18)*

[103] G. S. Adams et al. *Confirmation of a π_1^0 Exotic Meson in the $\eta\pi^0$ System*. Phys. Lett. **B657** (2007) 27–31. *cited in 2.4.1 (p. 18)*

[104] W. Dünnweber and F. Meyer-Wildhagen. *Exotic states in Crystal Barrel analyses of annihilation channels*. AIP Conf. Proc. **717** (2004) 388–393. *cited in 2.4.1 (p. 18)*

[105] A. Donnachie and P. R. Page. *Interpretation of experimental J^{PC} exotic signals*. Phys. Rev. **D58** (1998) 114012. *cited in 2.4.1 (p. 19)*

[106] A. P. Szczepaniak, M. Swat, A. R. Dzierba, and S. Teige. *Study of the $\eta\pi$ and $\eta'\pi$ spectra and interpretation of possible exotic $J^{PC} = 1^{-+}$ mesons*. Phys. Rev. Lett. **91** (2003) 092002. *cited in 2.4.1 (p. 19)*

[107] S. U. Chung, E. Klempt, and J. G. Körner. *SU(3) classification of p-wave $\eta\pi$ and $\eta'\pi$ systems*. Eur. Phys. J. **A15** (2002) 539–542. *cited in 2.4.1 (p. 19)*

[108] E. I. Ivanov et al. *Observation of exotic meson production in the reaction $\pi^- p \to \eta'\pi^- p$ at 18 GeV/c*. Phys. Rev. Lett. **86** (2001) 3977–3980. *cited in 2.4.1 (p. 19)*

[109] D. V. Amelin et al. *Study of resonance production in diffractive reaction $\pi^- A \to \pi^+\pi^-\pi^- A$*. Phys. Lett. **B356** (1995) 595–600.
cited in 2.4.1 (p. 19), 4.1.3 (p. 38), 5.1.4 (p. 55), 5.4.1 (p. 72), 5.5.2 (p. 93), 5.5.3 (p. 93), 5.5.3 (p. 94)

[110] Y. Khokhlov. *Study of $X(1600)$ 1^{-+} hybrid*. Nucl. Phys. **A663** (2000) 596–599.
cited in 2.4.1 (p. 19), 5.1.4 (p. 57), 5.5.2 (p. 92)

[111] I. A. Kachaev et al. *Study of reaction $\pi^- A \to \pi^+\pi^-\pi^- A$ at VES setup*. AIP Conf. Proc. **619** (2002) 577–581. *cited in 2.4.1 (p. 19)*

[112] D. V. Amelin et al. *Investigation of hybrid states in the VES experiment at the Institute for High Energy Physics (Protvino)*. Phys. Atom. Nucl. **68** (2005) 359–371.
cited in 2.4.1 (p. 19), 2.4.1 (p. 20)

[113] S. U. Chung et al. *Exotic and $q\bar{q}$ resonances in the $\pi^+\pi^-\pi^-$ system produced in $\pi^- p$ collisions at 18 GeV/c*. Phys. Rev. **D65** (2002) 072001.
cited in 2.4.1 (p. 19), 2.4.1 (p. 20), 4.1.3 (p. 38), 5.1.4 (p. 55), 5.1.4 (p. 57), 5.2.1 (p. 60), 5.2.1 (p. 62), 5.3.1 (p. 65), 5.4.1 (p. 72), 5.4.2 (p. 76), 5.5.2 (p. 92), 5.5.3 (p. 94)

[114] D. V. Amelin et al. *Investigation of the reaction $\pi^- + A \to \omega\pi^-\pi^0 + A$*. Phys. Atom. Nucl. **62** (1999) 445–453. *cited in 2.4.1 (p. 20)*

[115] V. Dorofeev et al. *The $J^{PC} = 1^{-+}$ hunting season at VES*. AIP Conf. Proc. **619** (2002) 143–154. *cited in 2.4.1 (p. 20)*

[116] M. Lu et al. *Exotic meson decay to $\omega\pi^0\pi^-$*. Phys. Rev. Lett. **94** (2005) 032002.
cited in 2.4.1 (p. 20)

[117] C. A. Baker et al. *Confirmation of $a_0(1450)$ and $\pi_1(1600)$ in $\bar{p}p \to \omega\pi^+\pi^-\pi^0$ at rest*. Phys. Lett. **B563** (2003) 140–149. *cited in 2.4.1 (p. 20)*

[118] J. Kuhn et al. *Exotic meson production in the $f_1(1285)\pi^-$ system observed in the reaction $\pi^- p \to \eta\pi^+\pi^-\pi^- p$ at 18 GeV/c*. Phys. Lett. **B595** (2004) 109–117.
cited in 2.4.1 (p. 20), 5.5.2 (p. 93)

[119] P. Pakhlov et al. *Production of new charmonium-like states in $e^+e^- \to J/\psi D^*\bar{D}^*$ at $\sqrt{s} \approx 10.6\,GeV$*. Phys. Rev. Lett. **100** (2008) 202001. *cited in 2.4.2 (p. 21)*

[120] B. Aubert et al. *Evidence of a broad structure at an invariant mass of 4.32 GeV/c^2 in the reaction $e^+e^- \to \pi^+\pi^-\psi(2S)$ measured at BaBar*. Phys. Rev. Lett. **98** (2007) 212001.
cited in 2.4.2 (p. 21)

[121] B. Aubert et al. *Study of the $B \to J/\psi K^-\pi^+\pi^-$ decay and measurement of the $B \to X(3872)K^-$ branching fraction*. Phys. Rev. **D71** (2005) 071103. *cited in 2.4.2 (p. 21)*

[122] D. E. Acosta et al. *Observation of the narrow state $X(3872) \to J/\psi\pi^+\pi^-$ in $\bar{p}p$ collisions at $\sqrt{s} = 1.96$ TeV*. Phys. Rev. Lett. **93** (2004) 072001. *cited in 2.4.2 (p. 21)*

[123] V. M. Abazov et al. *Observation and properties of the $X(3872)$ decaying to $J/\psi\pi^+\pi^-$ in $p\bar{p}$ collisions at $\sqrt{s} = 1.96$ TeV*. Phys. Rev. Lett. **93** (2004) 162002. *cited in 2.4.2 (p. 21)*

[124] S. Uehara et al. *Observation of a χ'_{c2} candidate in $\gamma\gamma \to D\bar{D}$ production at Belle*. Phys. Rev. Lett. **96** (2006) 082003. *cited in 2.4.2 (p. 21)*

[125] S. Okubo. *ϕ-meson and unitary symmetry model*. Phys. Lett. **5** (1963) 165–168. *cited in 2.4.2 (p. 21)*

[126] E. J. Eichten, K. Lane, and C. Quigg. *Charmonium levels near threshold and the narrow state $X(3872) \to \pi^+\pi^- J/\psi$*. Phys. Rev. **D69** (2004) 094019. *cited in 2.4.2 (p. 21)*

[127] Q. He et al. *Confirmation of the $Y(4260)$ resonance production in ISR*. Phys. Rev. **D74** (2006) 091104. *cited in 2.4.2 (p. 21)*

[128] K. Abe et al. *Observation of a resonance-like structure in the $\pi^\pm\psi'$ mass distribution in exclusive $B \to K\pi^\pm\psi'$ decays*. Phys. Rev. Lett. **100** (2008) 142001. *cited in 2.4.2 (p. 21)*

[129] J. Ashman et al. *A measurement of the spin asymmetry and determination of the structure function g_1 in deep inelastic muon proton scattering*. Phys. Lett. **B206** (1988) 364–370. *cited in 3.1.1 (p. 25)*

[130] E. S. Ageev et al. *Measurement of the spin structure of the deuteron in the DIS region*. Phys. Lett. **B612** (2005) 154–164. *cited in 3.1.1 (p. 25)*

[131] V. Y. Alexakhin et al. *The deuteron spin-dependent structure function g_1^d and its first moment*. Phys. Lett. **B647** (2007) 8–17. *cited in 3.1.1 (p. 25)*

[132] E. S. Ageev et al. *Spin asymmetry A_1^d and the spin-dependent structure function g_1^d of the deuteron at low values of x and Q^2*. Phys. Lett. **B647** (2007) 330–340. *cited in 3.1.1 (p. 25)*

[133] M. Alekseev et al. *The Polarised Valence Quark Distribution from semi-inclusive DIS*. Phys. Lett. **B660** (2008) 458–465. *cited in 3.1.1 (p. 25)*

[134] E. S. Ageev et al. *Gluon polarization in the nucleon from quasi-real photoproduction of high-p_T hadron pairs*. Phys. Lett. **B633** (2006) 25–32. *cited in 3.1.1 (p. 25)*

[135] R. Kuhn. *Gluon Polarization in the Nucleon - A Measurement of Spin Asymmetries in Quasi-Real Photo-Production of Hadrons with High Transverse Momentum at COMPASS*. PhD thesis, TU München, Physik-Department E18, 2007. *cited in 3.1.1 (p. 25), 3.3 (p. 30)*

[136] R. L. Jaffe and X.-D. Ji. *Chiral odd parton distributions and polarized Drell-Yan*. Phys. Rev. Lett. **67** (1991) 552–555. *cited in 3.1.2 (p. 25)*

[137] V. Y. Alexakhin et al. *First measurement of the transverse spin asymmetries of the deuteron in semi-inclusive deep inelastic scattering*. Phys. Rev. Lett. **94** (2005) 202002. *cited in 3.1.2 (p. 25)*

[138] E. S. Ageev et al. *A new measurement of the Collins and Sivers asymmetries on a transversely polarised deuteron target*. Nucl. Phys. **B765** (2007) 31–70. *cited in 3.1.2 (p. 25)*

[139] M. Wiesmann. *A Silicon Microstrip Detector for COMPASS and a First Measurement of the Transverse Polarization of Λ^0-Hyperons from Quasi-Real Photo-Production*. PhD thesis, TU München, Physik-Department E18, 2004. *cited in 3.1.3 (p. 25)*

[140] B. Grube. *A Trigger Control System for COMPASS and a Measurement of the Transverse Polarization of Λ and Ξ Hyperons from Quasi-Real Photo-Production*. PhD thesis, TU München, Physik-Department E18, 2006. *cited in 3.1.3 (p. 25), 3.3 (p. 30)*

[141] J. M. Friedrich. *Measurement of transverse Λ polarisation at COMPASS*. Proceedings of the 16th International Spin Physics Symposium (SPIN 2004), Trieste, Italy, 10 - 16 Oct 2004, pages 396–399. *cited in 3.1.3 (p. 25)*

[142] V. Y. Alexakhin. *Longitudinal Polarization of Λ and $\bar{\Lambda}$ Hyperons in Deep-inelastic Scattering at COMPASS*. Proceedings of the 16th International Spin Physics Symposium (SPIN 2004), Trieste, Italy, 10 - 16 Oct 2004, pages 393–395. *cited in 3.1.3 (p. 25)*

[143] U. Bürgi. *Charged Pion Polarizabilities to two Loops*. Phys. Lett. **B377** (1996) 147–152. *cited in 3.1.4 (p. 25)*

[144] J. Gasser, M. A. Ivanov, and M. E. Sainio. *Revisiting $\gamma\gamma \to \pi^+\pi^-$ at low energies*. Nucl. Phys. **B745** (2006) 84–108. *cited in 3.1.4 (p. 25)*

[145] Y. M. Antipov et al. *Measurement of π^--Meson Polarizability in Pion Compton Effect*. Phys. Lett. **B121** (1983) 445–448. *cited in 3.1.4 (p. 25)*

[146] J. Ahrens et al. *Measurement of the π^+ meson polarizabilities via the $\gamma p \to \gamma\pi^+ n$ reaction*. Eur. Phys. J. **A23** (2005) 113–127. *cited in 3.1.4 (p. 25)*

[147] A. Dinkelbach. *to be published*. PhD thesis, TU München, Physik-Department E18. *cited in 3.1.4 (p. 25)*

[148] L. Ametller, M. Knecht, and P. Talavera. *Electromagnetic corrections to $\gamma\pi^\pm \to \pi^0\pi^\pm$*. Phys. Rev. **D64** (2001) 094009. *cited in 3.1.4 (p. 25)*

[149] T. Nagel. *to be published*. PhD thesis, TU München, Physik-Department E18. *cited in 3.1.4 (p. 26)*

[150] M. A. Moinester. *How to search for doubly charmed baryons and tetraquarks*. Z. Phys. **A355** (1996) 349–362. *cited in 3.1.6 (p. 26)*

[151] M. Mattson et al. *First observation of the doubly charmed baryon Ξ_{cc}^+*. Phys. Rev. Lett. **89** (2002) 112001. *cited in 3.1.6 (p. 26)*

[152] J. Friedrich and L. Gatignon. private communication. friedrich@e18.physik.tu-muenchen.de. *cited in 3.2.1 (p. 28)*

[153] Japan Atomic Energy Agency, Japan, Nuclear Data Center. `http://wwwndc.jaea.go.jp/NuC/index.html`. *cited in 3.2.1 (p. 29)*

[154] T. Nagel. *Cinderella: an Online Filter for the COMPASS Experiment*. Master's thesis, TU München, Physik-Department E18, 2005. *cited in 3.3 (p. 30)*

[155] ROOT: An Object-Oriented Data Analysis Framework. `http://root.cern.ch`. *cited in 3.3.3 (p. 32), 8.4.2 (p. 139), 8.5 (p. 141), A.1 (p. 153)*

[156] Phast web page. `http://ges.home.cern.ch/ges/phast`. *cited in 3.3.3 (p. 32), A.1 (p. 153)*

[157] R. Frühwirth. *Application of Kalman filtering to track and vertex fitting*. Nucl. Instrum. Meth. **A262** (1987) 444–450. *cited in 3.3.3 (p. 32)*

[158] S. U. Chung and T. L. Trueman. *Positivity conditions on the spin density matrix: A simple parametrization*. Phys. Rev. **D11** (1975) 633–646. *cited in 4.1.1 (p. 37), 4.1.2 (p. 37), 4.2.1 (p. 41), 4.3.1 (p. 43)*

[159] J. D. Hansen et al. *Formalism and Assumptions involved in Partial-Wave Analysis of three-Meson Systems*. Nucl. Phys. **B81** (1974) 403–430. *cited in 4.1.1 (p. 37), 4.2.1 (p. 40), 4.3.1 (p. 43), 4.3.3 (p. 44)*

[160] S. U. Chung. *Techniques of amplitude analysis for two pseudoscalar systems*. Phys. Rev. **D56** (1997) 7299–7316. *cited in 4.1.2 (p. 37)*

[161] K. Buchner et al. *Application of a unitarized veneziano model to the reaction $K^+n \to k^+\pi^-p$ at 3 GeV/c*. Nucl. Phys. **B34** (1971) 292–306. *cited in 4.1.2 (p. 37)*

[162] W. Rarita and J. S. Schwinger. *On a theory of particles with half integral spin*. Phys. Rev. **60** (1941) 61. *cited in 4.2 (p. 40)*

[163] M. Jacob and G. C. Wick. *On the general theory of collisions for particles with spin*. Ann. Phys. **7** (1959) 404–428. *cited in 4.2 (p. 40)*

[164] S. U. Chung. *A General formulation of covariant helicity coupling amplitudes*. Phys. Rev. **D57** (1998) 431–442. *cited in 4.2 (p. 40)*

[165] S. U. Chung and J. Friedrich. *Covariant Helicity-Coupling Amplitudes: A New Formulation*. 0711.3143. *cited in 4.2 (p. 40)*

[166] S. U. Chung. *Spin Formalisms*. CERN Yellow Report **1971-08** (1971). *Lectures given in the Academic Training Program of CERN 1969-1970*. *cited in 4.2 (p. 40), 4.2.1 (p. 41), 4.2.2 (p. 42)*

[167] K. Gottfried and J. D. Jackson. *On the Connection between production mechanism and decay of resonances at high-energies*. Nuovo Cim. **33** (1964) 309–330. *cited in 4.2.1 (p. 40)*

[168] S. B. Treiman and C.-N. Yang. *Tests of the Single Pion Exchange Model*. Phys. Rev. Lett. **8** (1962) 140–141. *cited in 4.2.1 (p. 41)*

[169] C. Zemach. *Three pion decays of unstable particles*. Phys. Rev. **133** (1964) B1201–B1220. *cited in 4.2.2 (p. 42)*

[170] C. Zemach. *Use of angular momentum tensors*. Phys. Rev. **140** (1965) B97–B108. *cited in 4.2.2 (p. 42)*

[171] J. Orear. *Notes on Statistics for Physicists, Revised*. CLNS **82/511** (1982). *cited in 4.3.2 (p. 44)*

[172] G. Ascoli et al. *Partial Wave Analysis of the 3π Decay of the A_2*. Phys. Rev. Lett. **25** (1970) 962–965. *cited in 4.3.3 (p. 44)*

[173] B. D. Hall. *On the propagation of uncertainty in complex-valued quantities*. Metrologia **41** (2004) 173–177. *cited in 4.4.1 (p. 45)*

[174] I. J. R. Aitchison and M. G. Bowler. *Rescattering effects in the Deck model*. J. Phys. **G3** (1977) 1503–1512. *cited in 4.5.1 (p. 50)*

[175] MINUIT: Function Minimization and Error Analysis. `http://wwwasdoc.web.cern.ch/wwwasdoc/minuit/minmain.html`. *cited in 4.5.2 (p. 50)*

[176] T. Nagel. private communication. thiemo.nagel@ph.tum.de. *cited in 5.1.1 (p. 52)*

[177] V. V. Molchanov et al. *Radiative decay width of the $a_2(1320)^-$ meson*. Phys. Lett. **B521** (2001) 171–180. *cited in 5.1.4 (p. 56)*

[178] S. Grabmüller. *Studies of Diffractive Particle Production at COMPASS*. Master's thesis, TU München, Physik-Department E18, 2005. *cited in 5.1.4 (p. 57)*

[179] C. Daum et al. *Diffractive Production of Strange Mesons at 63 GeV*. Nucl. Phys. **B187** (1981) 1–41. *cited in 5.2.4 (p. 64)*

[180] G. W. Brandenburg et al. *Evidence for a New Strangeness 1 Pseudoscalar Meson*. Phys. Rev. Lett. **36** (1976) 1239–1242. *cited in 5.2.4 (p. 64)*

[181] D. Ryabchikov. private communication. Dmitri.Riabtchikov@cern.ch. *cited in 5.5.1 (p. 84)*

[182] M. G. Bowler. *The Parameters of the a_1 Meson*. Phys. Lett. **B209** (1988) 99–102. *cited in 5.5.1 (p. 84)*

[183] M. Lu et al. *Exotic meson decay to $\omega\pi^0\pi^-$*. Phys. Rev. Lett. **94** (2005) 032002. *cited in 5.5.2 (p. 92), 5.5.2 (p. 93)*

[184] K. Abe et al. *Measurement of K^+K^- production in two-photon collisions in the resonant-mass region*. Eur. Phys. J. **C32** (2003) 323–336. *cited in 5.5.2 (p. 92)*

[185] C. Amsler et al. *Proton anti-proton annihilation at 900 MeV/c into $\pi^0\pi^0\pi^0$, $\pi^0\pi^0\eta$ and $\pi^0\eta\eta$*. Eur. Phys. J. **C23** (2002) 29–41. *cited in 5.5.2 (p. 92)*

[186] I. Uman et al. *Light Quark Resonances in $\bar{p}p$ Annihilations at 5.2 GeV/c*. Phys. Rev. **D73** (2006) 052009. *cited in 5.5.2 (p. 92)*

[187] P. R. Page, E. S. Swanson, and A. P. Szczepaniak. *Hybrid meson decay phenomenology*. Phys. Rev. **D59** (1999) 034016. *cited in 5.5.2 (p. 93)*

[188] C. Daum et al. *3π Resonances in 2^- Partial Waves*. Phys. Lett. **B89** (1980) 285. *cited in 5.5.2 (p. 93)*

[189] S. Neubert. *to be published*. PhD thesis, TU München, Physik-Department E18. *cited in 5.8 (p. 101), 6.3.2 (p. 109), 7.1.2 (p. 113), 7.4 (p. 118), 8.5 (p. 141)*

[190] L. Äystö et al. *Conceptual Design Report: An International Accelerator Facility for Beams of Ions and Antiprotons*. Technical report, Gesellschaft für Schwerionenforschung, Darmstadt, Germany, 2001. *cited in chapter 6 (p. 103)*

[191] H. H. Gutbrod (Editor in Chief) et al. *FAIR Baseline Technical Report: An International Accelerator Facility for Beams of Ions and Antiprotons*. Technical report, Gesellschaft für Schwerionenforschung, Darmstadt, Germany, 2006. *cited in chapter 6 (p. 103), 6.2 (p. 106)*

[192] M. Kotulla et al. *Technical Progress Report for PANDA: Strong Interaction Studies with Antiprotons*. Technical report, Gesellschaft für Schwerionenforschung, Darmstadt, Germany, 2005. *cited in chapter 6 (p. 103), 6.1.4 (p. 105), 6.2.2 (p. 106), 6.2.2 (p. 107), 6.3 (p. 107), 6.3.2 (p. 109), 7.0.6 (p. 111), 7.3 (p. 116), 7.3.2 (p. 118)*

[193] A. Freund, A. V. Radyushkin, A. Schäfer, and C. Weiss. *Exclusive annihilation $p\bar{p} \to \gamma\gamma$ in a generalized parton picture*. Phys. Rev. Lett. **90** (2003) 092001. *cited in 6.1 (p. 104)*

[194] J. Z. Bai et al. *A measurement of the mass and full width of the η_c meson*. Phys. Rev. **D62** (2000) 072001. *cited in 6.1.1 (p. 105)*

[195] M. Kotulla et al. *Modification of the ω-Meson Lifetime in Nuclear Matter*. Phys. Rev. Lett. **100** (2008) 192302. *cited in 6.1.4 (p. 105)*

[196] K. Suzuki et al. *Precision spectroscopy of pionic 1s states of Sn nuclei and evidence for partial restoration of chiral symmetry in the nuclear medium*. Phys. Rev. Lett. **92** (2004) 072302. *cited in 6.1.4 (p. 105)*

[197] F. Laue et al. *Medium effects in kaon and antikaon production in nuclear collisions at subthreshold beam energies*. Phys. Rev. Lett. **82** (1999) 1640–1643. *cited in 6.1.4 (p. 105)*

[198] C. Ekstrom et al. *Hydrogen pellet targets for circulating particle beams*. Nucl. Instrum. Meth. **A371** (1996) 572–574. *cited in 6.2.2 (p. 106)*

[199] O. Nordhage, I. Lehmann, J. Lith, C.-J. Friden, and U. Wiedner. *Tracked pellets - a way to improve the efficiency of charmonium studies*. Nucl. Instrum. Meth. **A568** (2006) 561–565. *cited in 6.2.2 (p. 106)*

[200] J. Brau (Ed.) et al. *International Linear Collider reference design report*. Technical report, 2007. *ILC-REPORT-2007-001*. *cited in 7.1 (p. 111)*

[201] W. B. Atwood et al. *Performance of the ALEPH time projection chamber*. Nucl. Instrum. Meth. **A306** (1991) 446–458. *cited in 7.1.1 (p. 112), 7.1.2 (p. 113)*

[202] C. Brand et al. *The Delphi Time Projection Chamber*. Nucl. Instrum. Meth. **A283** (1989) 567–572. *cited in 7.1.1 (p. 112)*

[203] S. Afanasev et al. *The NA49 large acceptance hadron detector*. Nucl. Instrum. Meth. **A430** (1999) 210–244. *cited in 7.1.1 (p. 112)*

[204] K. H. Ackermann et al. *The STAR time projection chamber*. Nucl. Phys. **A661** (1999) 681–685. *cited in 7.1.1 (p. 112)*

[205] C. Garabatos. *The ALICE TPC*. Nucl. Instrum. Meth. **A535** (2004) 197–200. *cited in 7.1.1 (p. 112)*

[206] G. Van Buren et al. *Correcting for distortions due to ionization in the STAR TPC*. Nucl. Instrum. Meth. **A566** (2006) 22–25. *cited in 7.1.2 (p. 113)*

[207] S. Bachmann et al. *Discharge mechanisms and their prevention in the gas electron multiplier (GEM)*. Nucl. Instrum. Meth. **A479** (2002) 294–308. *cited in 7.2 (p. 114)*

[208] M. C. Altunbas et al. *Aging measurements with the gas electron multiplier (GEM)*. Nucl. Instrum. Meth. **A515** (2003) 249–254. *cited in 7.2 (p. 114)*

[209] M. C. Altunbas et al. *Construction, test and commissioning of the triple-GEM tracking detector for COMPASS*. Nucl. Instrum. Meth. **A490** (2002) 177–203. *cited in 7.2.1 (p. 115)*

[210] B. Ketzer et al. *Triple GEM Tracking Detectors for COMPASS*. IEEE Trans. Nucl. Sci. **495** (2002) 2403–2410. *cited in 7.2.1 (p. 115), 8.3.3 (p. 135)*

[211] Q. Weitzel. *Triple GEM Detectors in COMPASS - A Performance Study*. Master's thesis, TU München, Physik-Department E18, 2003. *cited in 7.2.1 (p. 115)*

[212] B. Ketzer et al. *Performance of triple GEM tracking detectors in the COMPASS experiment*. Nucl. Instrum. Meth. **A535** (2004) 314–318. *cited in 7.2.1 (p. 115), 8.1.5 (p. 125)*

[213] F. Haas. *to be published*. PhD thesis, TU München, Physik-Department E18. *cited in 7.2.1 (p. 115)*

[214] M. Killenberg et al. *Modelling and measurement of charge transfer in multiple GEM structures*. Nucl. Instrum. Meth. **A498** (2003) 369–383. *cited in 7.2.2 (p. 116), 8.1.4 (p. 124)*

[215] T. Huber. *Ion Backflow Studies with a Triple GEM Detector*. Master's thesis, TU München, Physik-Department E18, 2007. *cited in 7.2.2 (p. 116), 8.3.1 (p. 131), 8.3.3 (p. 134)*

[216] M. Killenberg et al. *Charge transfer and charge broadening of GEM structures in high magnetic fields*. Nucl. Instrum. Meth. **A530** (2004) 251–257. *cited in 7.2.2 (p. 116)*

[217] F. Sauli, S. Kappler, and L. Ropelewski. *Electron collection and ion feedback in GEM-based detectors*. IEEE Trans. Nucl. Sci. **50** (2003) 803–808. *cited in 7.2.2 (p. 116)*

[218] G. Dellacasa et al. *ALICE technical design report of the time projection chamber*. Technical report. *CERN-OPEN-2000-183*. *cited in 7.3.2 (p. 118)*

[219] M. Huk, P. Igo-Kemenes, and A. Wagner. *Electron Attachment to Oxygen, Water, and Methanol, in Various Drift Chamber Gas Mixtures*. Nucl. Instrum. Meth. **A267** (1988) 107–119. *cited in 7.3.2 (p. 118)*

[220] The FOPI Experiment, Gesellschaft für Schwerionenforschung, Darmstadt, Germany. `http://www-fopi.gsi.de`. *cited in 7.4 (p. 118)*

[221] The CB-ELSA Experiment, Rheinische Friedrich-Wilhelms-Universität, Bonn, Germany. `http://wwwnew.hiskp.uni-bonn.de/cb`. *cited in 7.4 (p. 118), 8.7 (p. 150)*

[222] C. Höppner. *to be published*. PhD thesis, TU München, Physik-Department E18. *cited in 7.4 (p. 118), 8.5 (p. 141), 8.7 (p. 150)*

[223] PandaROOT web page. `http://panda-wiki.gsi.de/cgi-bin/view/Computing/PandaRoot`. *cited in 7.4 (p. 118)*

[224] D. Decamp et al. *ALEPH: A Detector for Electron-Positron Annihilations at LEP*. Nucl. Instrum. Meth. **A294** (1990) 121–178. *cited in 8.1.1 (p. 120)*

[225] National Institute of Standards and Technology, USA, Physical Reference Data. `http://physics.nist.gov/PhysRefData/`. *cited in 8.1.1 (p. 121)*

[226] Costruzione Apparecchiature Elettroniche Nucleari, Italy. `http://www.caen.it`. *cited in 8.1.4 (p. 124)*

[227] National Instruments, USA. `http://www.ni.com`. *cited in 8.1.4 (p. 125)*

[228] Bronkhorst, Netherlands. `http://www.bronkhorst.com`. *cited in 8.1.6 (p. 126)*

[229] R. Bouclier, M. Capeans, C. Garabatos, F. Sauli, and K. Silander. *Effects of outgassing from some materials on gas chamber aging*. Nucl. Instrum. Meth. **A350** (1994) 464–469. *cited in 8.2.1 (p. 128)*

[230] AMETEK, USA, ORTEC Division. `http://www.ortec-online.com`. *cited in 8.3.2 (p. 132)*

[231] B. Ketzer et al. *GEM Detectors for COMPASS*. IEEE Trans. Nucl. Sci. **484** (2001) 1065–1069. *cited in 8.3.2 (p. 133)*

[232] L. Musa et al. *The ALICE TPC Front End Electronics*. Conference Record of the IEEE Nuclear Science Symposium (NSS 2003), Portland, Oregon, 19 - 25 Oct 2003, pages 3647–3651. *cited in 8.4 (p. 136), 8.4.1 (p. 136), 8.4.1 (p. 138)*

[233] R. Este Bosch et al. *The ALTRO Chip: A 16-Channel A/D Converter and Digital Processor for Gas Detectors*. IEEE Trans. Nucl. Sci. **506** (2003) 2460–2469. *cited in 8.4.1 (p. 136), 8.4.1 (p. 138)*

[234] Documentation web page of the ALICE TPC frontend electronics. `http://ep-ed-alice-tpc.web.cern.ch/ep-ed-alice-tpc`. *cited in 8.4.1 (p. 136), 8.4.1 (p. 138)*

[235] B. Grube. *The Trigger Control System and the common GEM and Silicon Readout for the COMPASS Experiment*. Master's thesis, TU München, Physik-Department E18, 2001. *cited in 8.4.3 (p. 139)*

[236] Electron Tubes, UK. `http://www.electrontubes.com`. *cited in 8.4.4 (p. 140)*

[237] R. Veenhof. *GARFIELD: Simulation of gaseous detectors*. CERN Program Library Writeup **W5050** (created 1984, last update 2008). *cited in 8.5.3 (p. 144), 8.6.1 (p. 147), 8.6.3 (p. 149)*

[238] R. O. Duda and P. E. Hart. *Use of the Hough transformation to detect lines and curves in pictures*. Commun. ACM **151** (1972) 11–15. *cited in 8.5.4 (p. 145)*

[239] R. K. Carnegie et al. *Resolution studies of cosmic-ray tracks in a TPC with GEM readout*. Nucl. Instrum. Meth. **A538** (2005) 372–383. *cited in 8.6.3 (p. 149)*

[240] P. Baron et al. *AFTER, an ASIC for the readout of the large T2K time projection chambers*. Conference Record of the IEEE Nuclear Science Symposium (NSS 2007), Honolulu, Hawaii, 27 Oct - 03 Nov 2007, pages 1865–1872. *cited in 8.7 (p. 150)*

[241] S. U. Chung. private communication. The derivation can be found also in an unpublished COMPASS note. *cited in chapter B (p. 155)*

Own Contributions

The data handling, event selection and simulations for the presented analysis were mostly my responsibility alone. Here I could rely to a large extend on the infrastructure provided by the COMPASS collaboration and the existing know-how within the E18 group. The PWA was done in close collaboration with Dmitri Ryabchikov, who brought the employed program with him. Together we interfaced it to the COMPASS data, worked out the partial wave sets and performed, complementary, a series of systematic studies.

Once the main results of the analysis had been obtained, I defended them during several meetings at CERN in front of the COMPASS collaboration until they got released for the public. Afterwards I presented my work at two international conferences.

In addition, I took hardware responsibilities at COMPASS, where I was one of the persons responsible for the maintenance of the GEM detectors. This included amongst others the commissioning at the beam time start-up and the duty of being "expert on call" at CERN for several weeks per year. I also took regularly shifts for the complete spectrometer operation during physics data taking.

My task within the PANDA TPC project was the construction of a TPC test chamber and the installation of all necessary laboratory infrastructure for operating such a detector. During the initial phase I was helped by Sebastian Neubert, Jochen Kaminski and Florian Haas. Further contributions from my side concerned the set up of the high-voltage control system, the integration of the ALTRO readout electronics and the programming of the DAQ and online monitor software. Also the cosmic muons stand was built by me, including the employed scintillator detectors. The reconstruction software, which I used for the analysis of the recorded tracks, has been developed by Christian Höppner.

I presented the TPC development at PANDA collaboration meetings and conferences. Also I participated in the writing of the Technical Progress Report for PANDA.

Acknowledgements

In the first place I would like to thank Prof. Stephan Paul for giving me the opportunity to work on these interesting subjects. He always supported my work and gave in the right moments the right impulses. I had the fun of joining several international conferences and workshops, which were not always in the closest corners of the world.

I am very grateful to my tutor Bernhard Ketzer, who guided and supervised me throughout all these years. From him I learned what it means to work in a scientific way, and his accuracy has always been an ideal for me.

Sincerest thanks to Dmitri Ryabchikov and Suh-Urk Chung. Their experience and help was substantial for the successful completion of the analysis. Dima never got tired to explain me again and again the secrets of PWA and it was great fun to work with him. Jan Friedrich had always time for discussions on my subject and physics in general.

Furthermore I thank Sebastian Neubert and Florian Haas for their help during the construction of the TPC test chamber. Thanks to Christian Höppner I also had the tools to analyze the data I took with this detector.

E18 has a long tradition of excellent computer administrators, to whom I am indebted for their work and patience with me. Roland Kuhn, Thiemo Nagel and Markus Krämer did this job during the time of my PhD. Alexander Mann, Anna-Maria Dinkelbach, Stefanie Grabmüller, Igor Konorov, Hans-Friedrich Wirth and Joachim Hartmann helped me at many different occasions, with discussions, technical support or the annual tax declaration. Many thanks also to my master's and technical students for their contributions: Tina Huber, Christian Hesse, Rupert Huber, Hans Eiter and Alexander Austregesilo. For the nice working atmosphere here at E18 I want to thank all its members very much: the COMPASS and PANDA group, the UCNs, the workshop and, most important, our secretary Karin Frank.

For information concerning the ALICE electronics I want to thank Luciano Musa and Federico Sánchez. Jochen Kaminski kindly helped to build the field cage of the TPC test chamber.

My parents have been a great support for me during these years, and their interest in my research has always been a great motivation for me. Thanks a lot! A ti Teresa te doy las gracias por haberme apoyado en todo momento, especialmente en estos últimos meses. En miles de situaciones, discussiones de física, ensayar charlas, motivarme, has sido una gran ayuda. Muchísimas gracias!